From molecular architecture and electrostatic interactions to underwater adherence of hydrogels

Francisco Javier Cedano Serrano

Sorbonne Université
ED 397 : Physique et Chimie des Matériaux
Laboratoire Sciences et Ingénierie de la Matière Molle (SIMM) – ESPCI Paris

From molecular architecture and electrostatic interactions to underwater adherence of hydrogels

Par Francisco J. CEDANO-SERRANO

Thèse de doctorat de Chimie et Physico-chimie des Polymères

Dirigée par Yvette TRAN, Dominique HOURDET et Costantino CRETON

Présentée et soutenue publiquement le 13/05/2019

Devant un jury composé de :

RESTAGNO, Frédéric	Chargé de recherche CNRS. Université Paris-Saclay.	Rapporteurs
GEOGHEGAN, Mark	Professeur. University of Sheffield.	
DEL CAMPO BÉCARES, Aránzazu	Professeur. Saarland University.	Examinatrices
LINDNER, Anke	Professeur. Université Paris Diderot.	
CRETON, Costantino	Directeur de recherche CNRS. ESPCI Paris.	Directeur de thèse
HOURDET, Dominique	Professeur. Sorbonne Université. ESPCI Paris.	Co-directeurs de thèse
TRAN, Yvette	Maître de Conférences. ESPCI Paris.	

From molecular architecture and electrostatic interactions to underwater adherence of hydrogels

Francisco J. CEDANO-SERRANO

Yvette TRAN, Dominique HOURDET and Costantino CRETON

May 13th, 2019

Acknowledgments

At the end of this doctoral thesis. I would like to express my gratitude to all the different people who have encouraged and supported me during these years.

I would like to start by acknowledging my principal supervisor Costantino. First, for gave me his confidence and his guidance during my PhD, but also his friendship during these years. I am also very grateful to Dominique and Yvette. I admire them very much and I greatly appreciate the discussions and all their academic and non-academic advices during these 3 years. I believe the three of them form an excellent team of supervisors that can guide several PhD students in different areas of research in the SIMM lab at ESPCI.

During my dissertation, it was an honour for me to have professor Mark Geoghegan, Frederic Restagno, Anke Linder and Arancha del Campo as members of the jury in the dissertation of my doctoral thesis. Thank you very much for accepting to review my thesis and for the valuable discussion during this. In particular, thanks to professors Frédéric and Mark for accepting to write the respective report of the manuscript and for Anke to be president of the jury committee.

I would like to thank all the members of the BioSmartTrainee network. This innovative training network led by Alla Synytska in Dresden, gave me the opportunity to pursue a PhD in a unique environment of fantastic collaboration and outstanding scientific and soft skills training in the field of adhesion science. As a fellow researcher in this network, I was able to collaborate with remarkable researchers and to share memorable experiences during these years. I would like to thank professors Marleen Kamperman and Alla Synytska, since the conclusions of this doctorate would not be the same if it were not for our collaborations. I want to highlight the ESRs Marco Dompé, Ugo Sidoli and Mehdi Vahdati with who I had the honour of working together and shared treasured moments. I also want to thank the long and valuable

discussions with Victor Kang, Justine Tavera, Dimitris Mintis and Maria Villou, and also the rest of the ESRs, Aurelie Feat, Vaishali Chopra and Maciej Chudak.

During the preparation of this manuscript and my PhD, I have been help by many. I am particularly grateful to my friends in the lab; Robert Gurney, Pierre Millereau, Jingwen Zhao, Helen Minsky and Gabriel Sanoja who made valuable comments for improving my scientific writing and oral presentations skills. I want to thank all of them as well for their friendship and for making my life easier and more enjoyable inside and outside ESPCI.

I would like to thank all the permanents in SIMM Lab and all the students and postdocs for their friendship, discussions, help, encouragements, and more important, for all the football and tennis games. Especially, I want to thank, Bruno, Valentine, Paul E., Paul F., Cécile M, Cécile C, Antoine F., Giorgia, Cyprian, Pascal, Anne-Charlotte, Juliette, Nassim, Xavier, Melanie, Milena, Julien, Louis, Yinjun, Josh, Ekkchai…

I want to thank my friends outside the lab. The Parisian group; Madda, Pekka, Connie and Sibell, and also my Colombian friends; Susana, Diana, Coloso, Juan, Manu, Juli, and Harry. Thank you for enriching my life with unforgettable moments during these years.

I want to thank my parents and my family for their loving and continuous support during my PhD. Above all I want to thank Leonie for all the hours she dedicated to listen to all my excited stories of underwater glues and for her loving and constant support during our time together, especially during the days of writing the manuscript.

Muchas gracias,

Francisco CEDANO – 20/05/2019

Table of Contents

Chapter 1

1. Underwater adhesion: context and objectives.

This first Chapter serves as a general introduction to the challenge of adhesion in aqueous environments, and gives a few examples of how nature has overcome this problem. To do this, we briefly review the intermolecular interactions present in different natural systems and the state of art of techniques developed to properly measure underwater adhesion due to specific molecular interactions. We also briefly present a few current bio-inspired materials based on electrostatic interactions, with promising adhesion properties in aqueous environments. The motivation of this research is based on both academic interest and potential applications in the medical field. It originates from the lack of understanding of the properties controlling adhesion of soft materials to hard surfaces when fully immersed in water, to the full development and characterization of a new "proof of concept" underwater adhesive system. Following the objectives of this research, we will give an outline of this thesis at the end of this chapter, which deals with underwater adhesion between functionalized surfaces and either soft elastic hydrogels (synthetic or bio-based) or complex coacervates adhesive systems.

Contents

1.1. Introduction

Adhesives have become a fundamental part of our daily lives as well as of many modern technologies. The design of a proper adhesive requires the optimization of intermolecular interactions and the maximization of the energy dissipation in the bulk of the adhesive.[1] The intermolecular interactions forces may be electrostatic in nature but may also involve specific mechanisms such as acid-base interactions, hydrogen-bond interactions, dispersion forces, chemical bonding, and hydrophobic interactions.[2] Except for hydrophobic interactions the majority of these interactions are screened or made irrelevant when water is present, which is the main cause of adhesive failure with most synthetic adhesives.[3] Therefore, water, even in the form of moist air, is the most common enemy of adhesion as J.H. Waite puts it simply, "Water and adhesives are in conflict".[4]

There are, however, significant advantages to develop adhesive systems that work in aqueous environments, particularly in the engineering industry and medical fields. Strong aquatic adhesives would be valuable in the construction and maintenance of water storage and transportation systems, and enable the reliable attachment of subaqueous sensors. In addition, they could be used for the repair of wet living tissues inside the body without the need for sutures, screws, or staples. Despite multiple applications for underwater adhesion, the ability to develop adhesives has been severely impaired by the presence of water between the adherend and the adhesive. It is well known that water affects adhesion through at least four pathways (**Figure 1-1**): (i) the presence of water at the interfaces, even between hydrophobic surfaces,[5] (ii) the wicking or absorbing water by capillary action into interfaces, (iii) the hydrolysis or erosion of the adhesive and (iv) the swelling or plasticization of the adhesive by water absorption.[4]

This introductive chapter begins with a brief overview of various strategies developed by natural organisms to overcome the problem of water. We then summarize the intermolecular

interactions that are commonly present in condensed matter and we discuss their adaptability for surface interactions in underwater conditions. Since we aim to understand the role of specific molecular interactions on adhesion properties of soft materials, we review the different proposed techniques and the state of the art to measure underwater adherence by controlling specific molecular interactions.

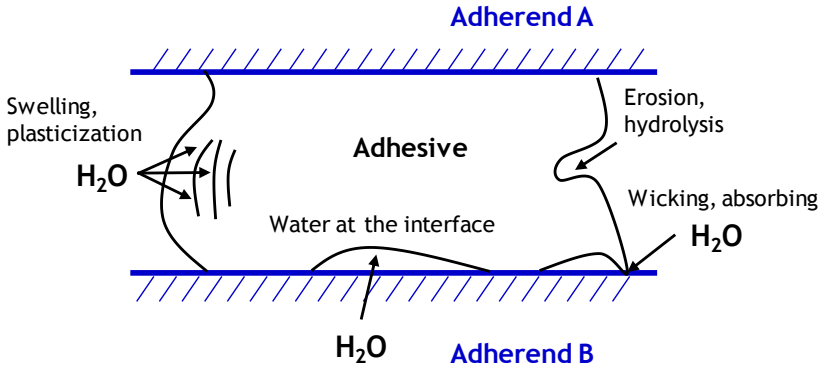

Figure 1-1. Four pathways by which water undermines the performance of adhesive bonds as adapted from J. H. Waite.[4]

1.2. Underwater adhesion in nature

The answers to overcome all the challenges for underwater adhesion can be found in nature. In the sea, there is a diversity of organisms that specialize in sticking to all types of wet surfaces. Barnacles, oysters, octopi, limpets and mussels are a few familiar examples. Recently, extensive efforts have been made towards understanding these natural adhesive systems.[6–11] Briefly, these organisms are able to bond materials underwater using protein-based adhesives: barnacles use secretions to glue calcareous base plates to rocks,[11,12] mussels use a network of threads to attach their soft invertebrate body to hard surfaces,[13,14] and both sandcastle worm and caddisfly larvae assemble a protective tubular shell by gluing together mineral particles underwater.[11,15] In each case, nature has created effective adhesives that exhibit the following traits: (i) minimal

preparation of the resident surface either by displacing competing ions or forming coordination complexes, (ii) repulsion of surface bound water, (iii) just-in-time and in situ setting reaction, (iv) strong cohesive and elastic properties to withstand significant shear forces, (v) ability to remain insoluble in water due to crosslinking.[11,16] In this section we present the most widely studied natural adhesive systems; the marine mussel (*Mytulis edulis*) and the sandcastle worm (*Phragmatopoma californica*) (**Figure 1-2**). Between these two species, there are several differences, yet, the adhesive chemistries show several similarities.

Figure 1-2. (Left) The mussel byssus contains hundreds of threads proximally fused to muscle at the base of the foot and distally attached to the substratum as highly studied by J.Herbert Waite and coworkers.[17] (Right) A sandcastle worm (*Phragmatopoma californica*) making a tube out of sand (yellow) and beads of zirconium oxide (white) as highly studied by R. Stewart.[18] Both photographs are of public domain.

1.2.1. Adhesives of Mussels and Sandcastle Worms

Mussel byssus formation is a tightly coupled choreography of chemistry and processing steps.[17] Briefly, mussels adhere to surfaces by using structures referred to as byssal threads, which terminate at the substrate surface in a plaque in which it secretes a protein-based

adhesive.[4,19] The strong attachment of this adhesive enables the mussel to survive in the turbulent, wet and saline habitat of intertidal zones and is attributed to the post-translational modification of tyrosine to 3,4-dihydroxypolyalanine (DOPA). To date, 25–30 different mussel foot proteins have been identified to contribute to the water-resistant adhesive and coating properties of the byssus.[20] However, all proteins contain DOPA, which is a distinctive functionality of the mussel byssus. DOPA is highly repeated within the amino acid sequence of the adhesive proteins found in the plaque.[6,21] The protein is secreted in a liquid form, which then solidifies to form a byssal thread and an adhesive plaque. The byssal threads are engineered to withstand elevated mechanical loads applied by waves and currents. A byssal thread connects a mussel to the adhesive plaque that is anchored to a foreign surface.[6]

On the other side, the sandcastle worm secretes small quantities of adhesive to join together mineral grains, such as sand, to form a protective tube underwater, which it uses in a similar fashion to a shell.[11,18] After an initial curing period of less than 30 s, the adhesive is strong enough to hold the particles in place. In the next hours, a second curing step follows which darkens the color. The resulting cement is a porous solid where the pores are filled with liquid. The adhesive compounds of the sandcastle worms are rich in nonpolar and ionic groups. Enhanced by nonpolar amino acids, complex coacervates and metal ion–polyelectrolyte complexes are formed from oppositely charged compounds. As a result, of complexation, which is a cohesive feature, the adhesive material is concentrated and insoluble in water (**Figure 1-3**).[6,17,22]

Both organisms co-secrete catechol oxidase with their proteins, resulting in the conversion of DOPA into DOPA-quinone. Consequently, covalent bonds are formed between DOPA-quinone groups or other amino acids that promote cohesion, such as cysteine or lysine.[6,15,23] A variety of such interactions and possible chemical reactions have been used (either separately

or in combination) in the development of several successful materials with promising underwater adhesion properties.[24–31]

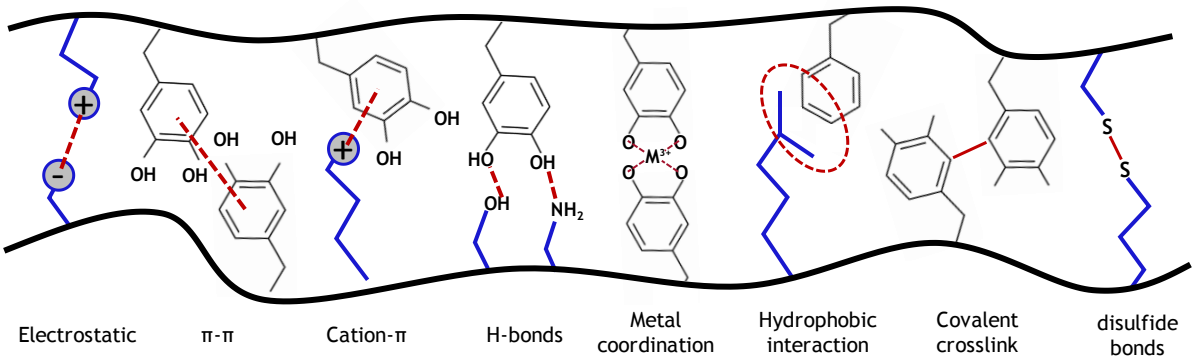

Figure 1-3. Overview of some of the different adhesive and cohesive interactions as found or hypothesized for wet adhesion by sandcastle worms and mussels. There are more interactions such as hydrophobic, disulfide bonds, metal coordination and covalent crosslinks.[32]

1.3. Bio-inspired adhesive systems

Inspired by sandcastle worms and mussels, several research groups have developed adhesive materials relying on electrostatic interactions, because these interactions play an important role in the adhesive processing and performance of these animal species. The strength of electrostatic interactions can be controlled by varying the ionic strength or pH and can thus be used to tune the mechanical properties of the adhesive systems.[32,33] In this section, synthetic adhesive materials based on electrostatic interactions will be discussed, including hydrogels and complex-coacervates.

1.3.1. Adhesive systems based on well crosslinked hydrogels

As introduced before, the design of a strong adhesive requires the optimization of intermolecular interactions at the interface and maximizing the energy dissipation in the bulk

of the adhesive. To address this challenge, highly stretchable and tough double network hydrogels (DN), as first reported by Suo and coworkers,[34] serve as good candidates to tackle this problem. Combining the ideas of DN hydrogels and molecular electrostatic interactions, several groups have designed hydrogels with a bulk dissipative mechanisms and interactions at the interface that can adhere to soft wet human tissues. For instance, Karami et al,.[35] reported a DN gel composed of covalently cross-linked poly(ethylene glycol)dimethacrylate and ionically crosslinked alginate reinforced with nanofibrillated cellulose. No tissue surface modification was needed to obtain high adhesion properties underwater with the developed hydrogel. Additionally, Li et al.[25] reported a tough hydrogel with adhesive properties consisting of two layers: a positively charged adhesive surface based on either chitosan or poly(acrylic acid) and a dissipative matrix based on the tough double network hydrogel of acrylamide-alginate of Suo and coworkers.[34] The former adheres to the substrate mainly by electrostatic interactions, as wet tissues are mostly negatively charged.[36] The two layers synergistically lead to higher adhesion energies on wet surfaces containing blood such as porcine skin. For short contact times (~1 min) they reported values in the order of ~250 J/m^2, however, for contact times higher than 20 min, they extraordinarily reached values in the order of 10^3 J/m^2.[25] Therefore, this novel hydrogel adhesives may be useful in many areas of application, including tissue adhesives, wound dressings, and tissue repair.

1.3.2. Adhesive systems based on complex coacervates

As introduced before, one of the phenomena, which is believed to play a fundamental role in the adhesive delivery of natural adhesive systems, is complex coacervation. In practice, it is an associative liquid-liquid phase separation of oppositely charged polyelectrolyte solutions.[15,23] Complex coacervates are particularly suitable for underwater adhesion, because of their fluid-like, yet water immiscible properties[33,37] and good wettability.[38] In natural

systems, after establishing molecular contact upon delivery, the complex coacervate liquid transforms into a solid-like material by the introduction of covalent or non-covalent but strong interactions activated by a change in environmental conditions (e.g. higher pH in seawater, metal ions coordination).[32]

This principle has been mimicked in synthetic systems by designing polyelectrolyte material systems either responsive to a particular trigger (pH,[29,39,40] ionic strength,[41,42]) or reinforced via a crosslinking reaction.[29,31,43,44] For instance, Zhao et al. designed a fully synthetic underwater adhesive that was applied to a water immersed surface via solvent exchange.[19] The adhesive consisted of oppositely charged polymers: a random copolyanion containing anionic acrylic acid and catechol-functionalized acrylic acid (7:3), and a polycation composed of quaternized chitosan ion-paired with bis(trifluoromethane)sulfonamide (Tf2N−). The use of Tf2N−counterions allowed chitosan to dissolve in dimethyl-sulfoxide (DMSO). Without complex formation taking place, the polymers were combined in a single DMSO solution and subsequently applied onto a water-immersed glass slide. Miscibility of DMSO and water enabled solvent exchange, which resulted in deprotonation of acrylic acid by water, followed by complexation of acrylic acid and chitosan. After 25 seconds, the complex turns into a viscoelastic material with strong underwater adhesive properties. This polyelectrolyte complex adhesive attached to a wide variety of surfaces, ranging from glass to hydrophobic plastics and as well as metals and wood, making it a multifunctional underwater glue.

This adhesive systems are very encouraging, however, our understanding is still very poor in terms of the specific role played by one single type of molecular interactions in the macroscopic underwater adhesion of these very complex systems (natural or synthetic). Therefore, the central topic of the following section will be to briefly describe the types of molecular interactions that can occur within the adhesives system. We specifically focus on H-bonds, charge-charge interactions, and cation-π interactions.

1.4. Molecular interactions involved in underwater adhesion

Molecular interactions (also known as non-covalent interactions) are attractive or repulsive forces between molecules and between non-bonded atoms. Molecular interactions were first described by the Dutch scientist Johannes Diderik van der Waals.[45,46] They are important in diverse fields of protein folding, drug design, material science, sensors, nanotechnology, separations, and even origins of life.[2] All molecular interactions are fundamentally electrostatic in nature and can be described by some variation of Coulomb's laws. However, we reserve the term 'electrostatic interaction' to describe interactions between formally charged species. Interactions between partial charges are given by other names.

1.4.1. Hydrogen bonding

Hydrogen bonding is an important type of interaction that defines the strength of several natural adhesives systems. For instance, hydrogen bond interactions are partially responsible for strong surface bonding via DOPA. However, the investigation of the impact of just the hydrogen bonding of DOPA's catechol group on the adhesive performance remains rather complex as it can undergo various types of other interactions.[32]

Historically, the idea that a single hydrogen atom could interact simultaneously with two other atoms was proposed in 1920 by Wendell M. Latimer and Wroth H. Rhodebush[47] and their advisor, G. N. Lewis.[48] Maurice Huggins (who was a student in Lewis' laboratory) has also described the hydrogen bond in his dissertation in 1919. The hydrogen bond is a short ranged and directional interaction between an electronegative atom (such as oxygen, nitrogen or fluorine) and a hydrogen atom covalent to another electronegative atom.[2] The hydrogen bond is commonly classified as an electrostatic effect since the hydrogen is partially positively charged when linked to a very electronegative atom, which leads to strong local dipoles. The strengths of hydrogen bonds form an entire continuum. Strong hydrogen bonds (82 to 164

kJ/mol), generally formed between charged donors and acceptors, are nearly as strong as covalent bonds, Weak hydrogen bonds (4 - 21 kJ/mol), sometimes formed with carbon as the proton donor, are no stronger than conventional dipole-dipole interactions. Moderate hydrogen bonds (12 - 50 kJ/mol), which are the most common, are formed between neutral donors and acceptors.[2]

1.4.2. Electrostatic interactions

Electrostatic interactions are among charged species and can be either attractive or repulsive, depending on the signs of the charges. However, it is important to clarify that electrostatic interactions within a pair of atoms (such as the ones in sodium chloride molecules) are called ionic bonds. But when a single cation and a single anion are close together, within a protein, between polymer chains or within a folded RNA, those interactions are considered to be non-covalent electrostatic interactions. Non-covalent electrostatic interactions can be strong, and act at long range. Electrostatic forces decrease gradually with distance ($1/r^2$, where r is the distance between the ions).[2]

The inverse-square Coulomb force between two charged atoms, or ions, is by far the strongest of the physical forces, even than most chemical binding forces. The free energy for the Coulomb electrostatic force (E_C) between two point formal charges Q_1 and Q_2 is given by:

$$E_C = \frac{Q_1 Q_2}{4\pi\varepsilon_0\varepsilon_r r} = \frac{z_1 z_2 e_0^2}{4\pi\varepsilon_0\varepsilon_r r} \qquad (1)$$

where r is the distance between the point charges (in meters), ε_r is the dielectric constant of the medium, also called relative permittivity. The dielectric constant reflects the tendency of the medium to shield charged species from each other. ε_r is 1 in vacuum, around 4 in the interior of a protein and 80 in water without salt. The expression on the right is commonly used for ionic interactions, where the magnitude and sign of each ionic charge is given in terms of the

elementary charge (e_0=1.602 x 10^{-19} C) multiplied by the ionic valency z. The Coulomb force F_C is given by

$$F_C = -\frac{E_S}{\mathrm{d}r} = \frac{Q_1 Q_2}{4\pi\varepsilon_0\varepsilon_r r^2} = \frac{z_1 z_2 e_0^2}{4\pi\varepsilon_0\varepsilon_r r^2} \quad (2)$$

For like charges, both E_C and F_C are positive and the force is repulsive, while for unlike charges they are negative and the force is attractive.

Water is very efficient in screening charges, reducing electrostatic forces between ions. The problem of calculating electrostatic effects in biological systems is complex, in part, because of non-uniformity of the dielectric environment. The dielectric micro-environments are complex and variable, with less shielding of charges in regions of hydrocarbon side chains and greater shielding in regions of polar side chains.[49]

1.4.3. Cation-π interactions

Intermolecular interactions play a major role in determining the structures of biological macromolecules. Although hydrogen-bonding and electrostatic interactions have been extensively studied and discussed, there is another important but generally underappreciated non-covalent binding force. Cations, from simple ions like Na+ to more complex amino acids such as lysine and tyrosine, are strongly attracted to the π face of benzene and other aromatic structures (**Figure 1-4**).[50,51] Cation–π interactions are, therefore, electrostatic in origin and occur between cations and electron-rich π orbitals. Particularly strong cation–π binding occurs when cations interact with the delocalized π orbitals perpendicular to the plane of aromatic rings, such as that of benzene, tryptophan, phenylalanine or tyrosine. A cation can interact favorably with this partial negative charge when the cation is near the face of the π-system. Although cation–π interactions are much stronger in the gas phase than in condensed phases, they still exceed the strength of hydrogen bonds, and possibly even charge–charge interactions, in aqueous solutions.[2,22,50] As a result, cation–π interactions provide an attractive molecular

design model to develop molecules that can function as adhesives in underwater environments. Recently, J.N. Israelachvili and coworkers[22] provide a first strong evidence to support the importance of cation–π interactions in marine bioadhesion. In this research, they argued that cation–π interactions between DOPA and Lysine amino acid is the dominant mechanism that mediates molecular cohesion in mussel foot proteins containing DOPA. Therefore, he suggested that molecules incorporating Lysine and DOPA could provide an attractive alternative for developing underwater adhesives.[22]

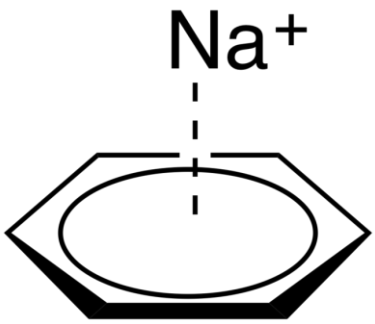

Figure 1-4. The cation-π interaction, showing a positive charge (Na+) interacting with the center of the ring of benzene. The distance from the charge to the benzene is about 2.4 Å (ionic radius of Na+ = 0.9 Å).

1.5. Measurement of adhesion underwater

Measuring adhesion energy is indeed an experimental challenge, especially underwater. Adhesion is not some objective part of a joint. Instead, it is a property of the bonded system. Therefore, it depends on several properties of the system such as; temperature, contact time, debonding rate, pulling direction, contact area, elastic and shear moduli of tested materials, surface energy and the solvent medium. In short, measuring adhesion energy underwater requires controlling all of these variables, but most importantly, the areal density of bonds formed at the interface and the structure of the soft material.

Developments of different adhesion measurement methods allowed the study of macro- and micro- scale-contact phenomena: macro-scale contacts are in general characterized using probe-tack, peel tests, shear tests[1,52,53] and through JKR technique with soft hydrogels.[54] The advantage of macro-scale methods is the well-defined contact area. However, these methods are limited to smooth and chemically homogenous samples over a few hundred μm^2.[55] On the micro-scale side, the main advantage is the knowledge of the interaction forces between colloidal particles (micron-sized particle), single molecules and surfaces. During the last 50 years, various direct force-measuring techniques have been developed, which allow for the full force-laws to be measured between two solid surfaces at a nanometric resolution.[2] Direct measurement of intermolecular forces has benefited greatly from the introduction of the surface force apparatus (SFA)[56–58] and the atomic force microscopy (AFM).[59] These techniques have made possible the direct measurement of different interaction forces between several types of surfaces and molecular structures ranging from hydrophobic colloids,[60] charged colloids,[61,62] covalent bonds[63] and to complete strands of DNA.[64] There is, therefore, an encouraging progress in the problem of measuring adhesion energy from specific molecular interactions in different aqueous environments. In the next section, we will describe briefly some results obtained with these techniques.

1.5.1. The Surface Force Apparatus (SFA)

One of the most used technique is the surface force apparatus (SFA) developed by D. Tabor together with R. Winterton in the late 60s[58] and with J. Israelachvili[57] in 1972. Later, J. Israelachvili and G. E. Adams adapted this technique to measure nanoscale forces in aqueous environments,[65] which opened up a whole new field of science.[2] Several modified versions of the instrument have been developed since the 80s keeping the same measurement principle.[66,67] The SFA contains two curved molecularly smooth surfaces of mica (of radius ~1 cm) between

which the interaction forces are measured. The two surfaces are in a crossed cylinder configuration, which is locally equivalent to a sphere near a flat surface or to two spheres close together. A typical SFA has a normal and a lateral distance resolution of 0.1 nm and 1 µm, respectively. The force sensitivity is about 10 nN and given the geometry of this technique, the sensitivity in measuring adhesion and interfacial energies is approximately 10^{-3} mJ/m^2.[2]

Over the past few years. SFAs have identified and quantified most of the fundamental interactions occurring between surfaces in air and under aqueous environments. Remarkably, repulsions resulting from electrostatic "double-layer" forces have been extensively studied with the surface force apparatus.[14,68,69] and more recently, with the inclusion of the Electrochemical Surface Forces Apparatus (EC-SFA),[70] attractive forces due to electrostatic interactions have been measured between an atomically smooth gold electrode (with controllable surface potential by the EC-SFA) and a mica surface covered with a self-assembled amino monolayer. Remarkably, with this new set-up, they were able to measure precisely attractive and repulsive electrostatic forces validating experimentally the DLVO theory (which will be explained more in detail in the Chapter 3) for electrostatic forces. A limitation of the SFA technique is the need for an extremely particle free condition of the medium near the surfaces, and its low lateral resolution (which is no better than that of an ordinary optical microscope). However, it has a significant advantage in the direct visualization of the contact region with the Multiple Beam Interferometry (MBI). Another limitation, and one currently shared with most other techniques at this scale, is that there is not direct link between the measured forces and the molecular composition and structure (e.g., molecular orientations) of the tested materials.

1.5.2. Atomic Force Microscopy (AFM)

One of the methods available for direct measurement of surface forces is the atomic force microscope (AFM) introduced in 1986 by Binnig, Quate and Gerber.[71] The surprising

simplicity of the microscope, capability of measuring in air and practically in any gas and liquid environment, makes it indispensable both in scientific research and in industry. The AFM is in principle similar to the SFA except that forces are measured not between two macroscopic surfaces but between a surface and either a fine tip or a colloidal probe (AFM-CP).[72,73] Moreover, there are several advantages of the AFM over the SFA. In addition to its versatility and ability to perform force measurements with both high normal and lateral resolution,[62] the AFM can work with many different materials (soft or hard) and under any aqueous environment as it allows a precise control of several parameters such as temperature, pH, solvent, humidity.[59] Furthermore, the principles of measurements of the AFM and the AFM-CP will be covered and explained in more detailed in the introduction of Chapter 3 (**Section 3.1**).

In the last 10 years, different groups including Synytska and coworkers[74–76] have extensively used the AFM-colloidal probe technique to measure different molecular forces underwater at a nanometric force scale between oppositely charged polyelectrolyte brushes.[33,53,77] The main focus of these previous works was to successfully achieve reversible adhesion by changing environmental variables such as pH[54] or by adding salt.[53] Furthermore, Spruijt and coworkers[61,78] used the AFM-CP technique to determine the strength of the cohesive ion–ion pair forces between positively and negatively charged polyelectrolytes brushes attached to the solid surfaces of a colloidal probe and of a silicon flat wafer, respectively (**Figure 1-5.a**). The surfaces were immersed in an aqueous solution with varying salt concentrations. During a typical experimental approach-and-retract cycle, the brushes come into contact and form a thin complex layer. When the surfaces were separated again, the polyelectrolyte chains were stretched until enough energy is stored to break all the formed ion–ion pairs between the brushes.

They found that the electrostatic force depends linearly on the logarithm of the pulling rate (**Figure 1-5**) and they gave solid evidence on the effect of varying the ionic strength in the

medium and its effect on the attractive electrostatic forces. Remarkably, they fit their data with a molecular rupture model for ionic bonds that quantitatively estimates the mean rupture force of a single ionic bond as a function of ionic strength and pulling rate. This model was inspired mainly by the model developed by Evans and Ritchie[79,80] of mean rupture force of single molecules as a function of temperature and loading rate, and by the Debye-Hückel theory of electrostatic double-layer forces.[2,78]

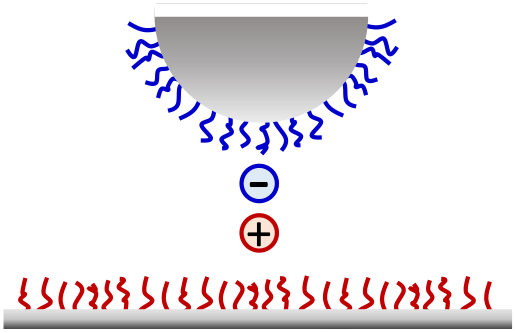

Figure 1-5. Schematic picture showing the AFM-CP measurement of the interactions between two oppositely charged polyelectrolyte brushes.[61,81]

1.5.3. JKR approach

Recently, Geoghegan and coworkers[54,82,83] reported quantitative values of underwater adhesion energies between oppositely charged, weak polyelectrolyte materials. Adhesion underwater was measured using the so-called Johnson–Kendall–Roberts (JKR) analysis between a silicon flat surface covered with polymer brushes and hemispheres of macroscopic hydrogels, both prepared from weak polyelectrolytes (**Figure 1-6**). The JKR technique, which will be explained in more detail in the introduction of Chapter 3 (**Section 3.2.1**), provides a mean of directly probing the adhesion at the interface, whereas other methods, such as tack, peel or shear tests measure the adherence, which is also dependent on the bulk-material properties.

Their work focused mainly on the reversibility and repeatability of the adhesive interactions and remarkably, they showed in various systematic studies, the dependence of work of adhesion on the charge density between hydrogels (including with double network hydrogels) and polymer brushes based on weak polyelectrolytes. For instance, a hemisphere piece of a poly(methacrylic acid) (PMAA) hydrogel was brought in contact to a flat surface covered with poly[2-(diethyl-amino)ethyl methacrylate] (PDEAEMA) brushes. At low pH, the brush is fully swollen but the gel excludes water and contains limited charge. At pH 6, both the brush and the gel are swollen, while at high pH the brush layer loses most of its charge and collapses to exclude water. The adhesion is maximized when both of these are charged, i.e. at pH close to 6. For this system, the work of adhesion was reported to be around 20-50 mJ/m^2 at pH 5.8.[54]

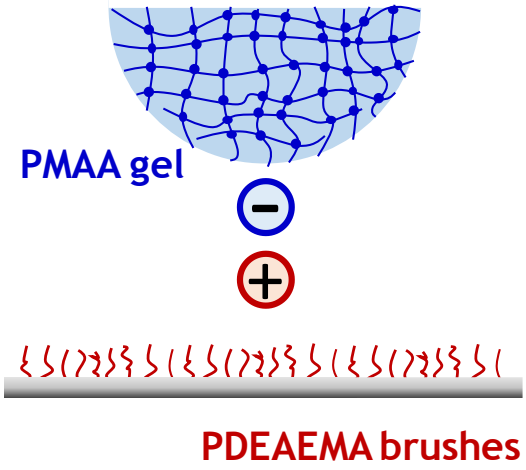

Figure 1-6. Schematic diagram of the process for a negatively charged hemisphere hydrogel being brought into contact with a positively charged polymer bushes layer. In this model system proposed by Geoghegan and coworkers, the adhesion was found to be maximized when both of these are charged, i.e. at pH close to 6.[54,83]

However, under these conditions, measuring the contact area between the gel and the substrate cannot be carried out through the gel because of the very close refractive index of the

gel and water, but the contact area was extrapolated from a side-view of the system. This research is very encouraging, but did not addressed the effect of all the parameters that are important in controlling and predicting the adhesion energy from a specific type of molecular interactions. Examples include a better estimate of the areal density of charges at the interface and the contribution of the macroscopic hydrogel network architecture to the macroscopic underwater adhesion.

1.5.4. Underwater probe-tack test for soft hydrogels

Measuring underwater adhesion while avoiding the problem of visualization of the contact during the measurement, was first proposed by Sudre et al.[84] He proposed to use a custom-built probe-tack test setup between a soft material and a hard surface. The device can be used in both air and water. In submerged configuration, the pH, ionic strength and temperature of the aqueous media are controlled *in situ*. When both surfaces are properly aligned, through direct visual control, the contact area during the compression and detachment phases is equal to the area of the functionalized hard surface, which is attached to the mobile probe. With this experimental setup, he succeeded to obtain quantitative values of the macroscopic adhesion energies under immersed conditions in a reproducible way.

The chamber in which the adhesion test is carried out is made of anodized aluminum alloy (**Figure 1-7**). The setup consists of two compartments hermetically separated. In the sample chamber where the contact test takes place, a special location has been designed for holding a glass slide, on which the hydrogel will be placed. The setup is attached to an Instron model 5565 traction machine on which a 10 N force cell is fitted. The noise on the force cell is of the order of 0.1 mN. Before immersion in solution, both surfaces are aligned in air. The contact is visualized by means of two windows for a deformation corresponding to approximately 20% of the deformation applied during the adhesion test. This technique will be used for all

macroscopic underwater adhesion experiments in this thesis. The precise experimental methodology and the different recommendations to measure the adhesion energy with this test will be presented in detail in the methodology section of Chapter 2 (**Section 2.3.7**).

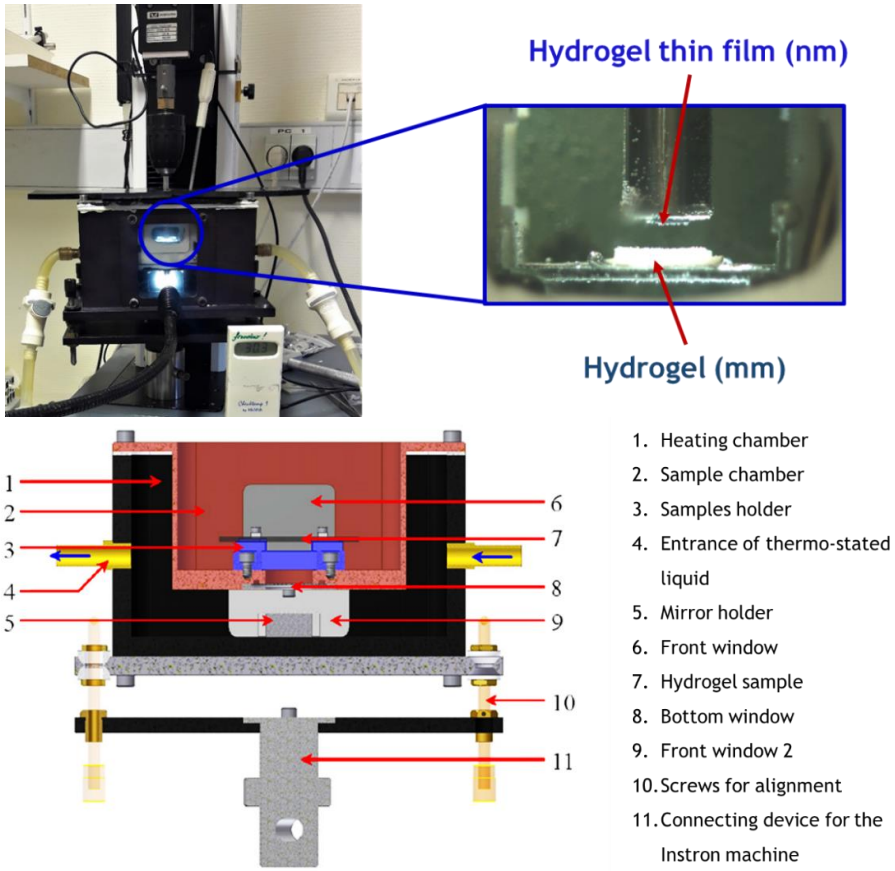

Figure 1-7. (Top) Photographs of the experimental setup developed to measure underwater adhesion between a solid surface and a soft material. (Down) Detailed parts and components of the probe-tack setup developed by Sudre et al. to measure underwater adhesion of soft materials.[84]

From hydrogen bonds interactions to macroscopic underwater adherence

Guillaume Sudre[85] investigated the macroscopic adhesion underwater between poly(N,N-dimethylacrylamide) (PDMA) hydrogels at swelling equilibrium and a surface covered with a

layer of poly(acrylic acid) (PAA) brushes.[84] The PDMA/PAA couple was chosen since PDMA and PAA can form hydrogen-bond specific interactions at the interface and this interaction can be modulated by tuning the pH of the medium. Therefore, he studied the effect of pH, and therefore, the effect of H-bonds on the macroscopic underwater adhesion of swollen materials.

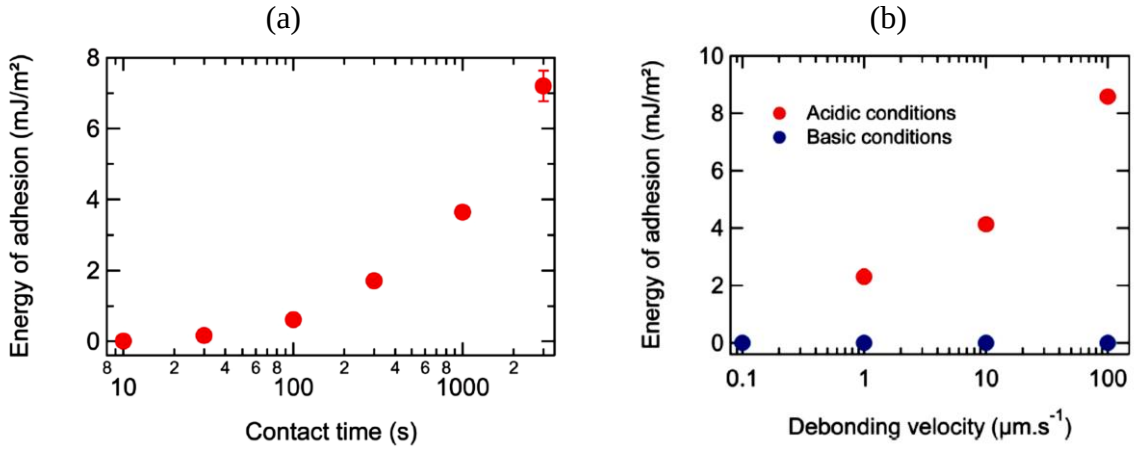

Figure 1-8. Key findings of Sudre et al. (a) Energy of adhesion between a PAA brush and a PDMA hydrogel equilibrated and immersed at pH 2, as a function of contact duration. The measurement at a contact time of 10 s did not show any adhesion peak.[84] (b) Energy of adhesion between a PAA brush and a PDMA hydrogel as function of the debonding velocity, equilibrated and immersed at pH 2 (acidic condition) and pH 9 (basic condition).[84]

They found that adhesion increased as the pH decreased and this was attributed to the formation of hydrogen bonds at the interface. Remarkably, they demonstrated that the time of contact and the debonding velocity, even for very elastic gels, were key parameters controlling the measured energies of adhesion with this technique (**Figure 1-8**). Varying systematically the equilibration time, contact time and debonding velocity gave access to (i) the kinetics of the formation of the complexes at the interface, (ii) their dissociation times and (iii) the diffusion properties of acid or base inside the gels. They showed that the formation of H-bonded

interactions is a particularly long process since the energy of adhesion continues to increase as a function of contact time for at least one hour.

It is interesting to highlight that for this system in equilibrated conditions, a minimum of 100 seconds of contact time was necessary to obtain a clear adhesion peak. By using a shorter contact time, only noise was measured with the 10 N load cell. Moreover, the results of the adhesion tests show that the measured values were in the order of 10 mJ/m^2. These values are in good agreement with the literature given the conditions under which the test was conducted.

Effect of swelling equilibrium on underwater adherence

Synthetic hydrogels are normally composed of flexible water-soluble polymer chains which are crosslinked in the presence of a fixed concentration of water (corresponding to the preparation conditions) and which, if left immersed in excess water, will swell to equilibrium. This equilibration with the environment until the chemical potentials of the water and mobile species inside and outside the gel are equal, has been well studied and leads to changes in mechanical properties such as the elastic modulus and also to changes in the large strain properties.[86]

In this context, the underwater probe-tack test methodology developed by Sudre et al.[84] was used by Macron et al.[87] to measure the work of adhesion between a poly(N,N-dimethylacrylamide) (PDMA) hydrogel and poly(acrylic acid) (PAA) polymer brushes while the PDMA hydrogel was swelling from its preparation state to equilibrium. Experiments were carried out systematically between a neutral PDMA gel and a PAA brush at pH 2 (forming hydrogen bonds at the interface). The key finding in this research was that regardless of the composition of the gels, the measured value of the adherence energy systematically decreased with increasing immersion time, i.e. as the gel swells to equilibrium (**Figure 1-9**). Moreover, in both equilibrated and non-equilibrated conditions the work of adhesion increased linearly

with the elastic modulus of the gel i.e. with the bulk density of elastic chains (**Figure 1-10.b**). Finally, it was reported that the adhesion energy at swelling equilibrium scaled linearly as a function of the logarithm of the detachment rate (**Figure 1-10.b**).

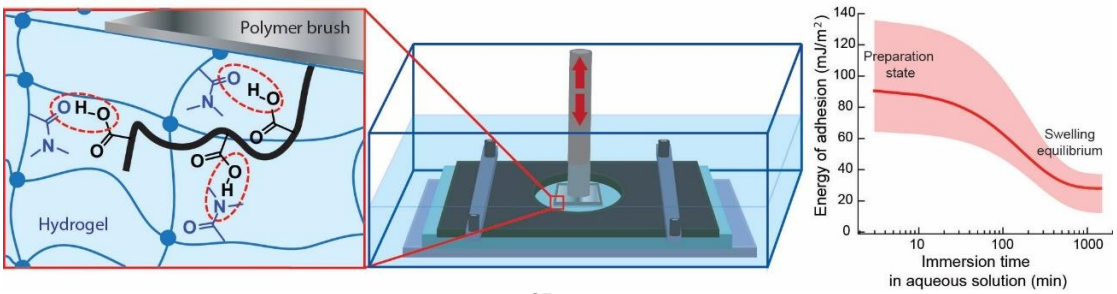

Figure 1-9. Key findings of Macron et al. [87] Underwater adherence test between a PDMA hydrogel and a PAA brush. Illustration of the setup used to mechanically hold the hydrogel layer with a Teflon-coated plate during the adherence test. On the left are represented the H-bond interactions formed between the PDMA hydrogel and the PAA polymer brush. On the right, is displayed the work of adhesion of the system measured as a function of the immersion time, the dispersion (pink area) and the best fit of the data points with an arbitrary function guiding the eye (red line).

Given these findings, they proposed to link the adhesion energy with the molecular architecture of the macroscopic hydrogels. Since they found that the adhesion energy increased with increasing elastic modulus of the hydrogels, they concluded that the dissipated energy upon debonding depends on the areal density of H-bonds formed at the interface (which was not measured) and not on the molecular weight of the polymer strands of the hydrogel.

They also found that the work of adhesion at equilibrium increased linearly with the logarithm of the pulling rate, suggesting that polymer chain stretching occurs before the rupture of the H-bond interactions, which means that indeed the length of the chains will affect the result on the dissipated energy. To resolve these two results, they argued that the decrease in

work of adhesion as the gel approached equilibrated conditions was attributed to the slowdown of the kinetics of formation of multiple H-bond interactions as the gel approached its equilibrated state. Nevertheless, despite the inspiring results from this research, the direct link between the macroscopic underwater adhesion energy and both the molecular weight of the polymer strands between crosslinks and the areal density of interactions at the interface is still generally unknown.

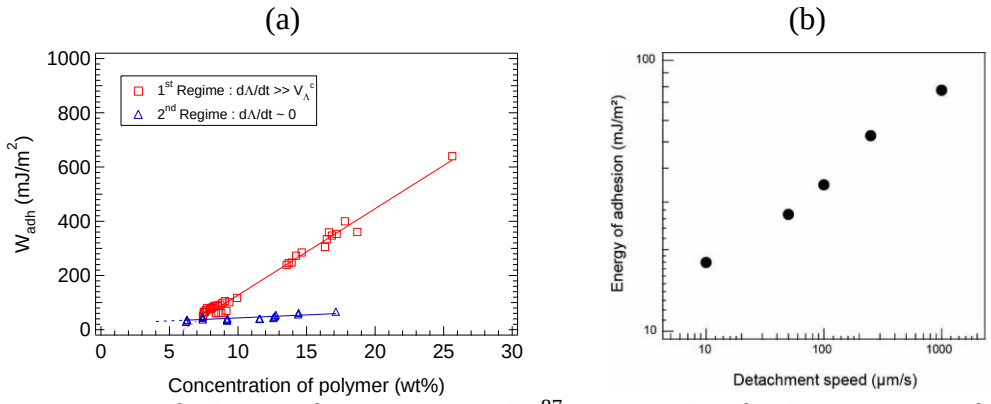

Figure 1-10. Key findings of Macron et al. [87] (a) Work of adhesion as a function of concentration of polymer for the PDMA hydrogel system. Red points corresponds to gels out-of-equilibrium and blue points to gels at equilibrium swelling. (b) Work of adhesion as a function of detachment speed at pH 2 between PDMA gels at swelling equilibrium and PAA brushes.[87]

From electrostatic interactions to macroscopic adherence: preliminary experiments

Jennifer Macron, who followed up on Guillaume Sudre's work, carried out preliminary experiments of macroscopic adhesion between charged gels, i.e. due to the electrostatic interactions. She used 1 mm thick macroscopic hydrogels of poly(methacryloyloxyethyl trimethyl ammonium chloride-*co*-acrylamide) [poly(MAETAC-*co*-AAm)] and hard surfaces coated with polymer brushes of poly(acrylic acid).[88] In the last chapter of her PhD manuscript, she showed systematic adhesion experiments between different poly(MAETAC-*co*-AAm)

hydrogels (changing the ratio between the cationic and neutral monomer) and poly(acrylic acid) brushes as function of immersion time. Remarkably, she found that the work of adhesion of a hydrogel containing 25% of cationic charges (in weight at preparation state), remained constant as a function of immersion time (**Figure 1-11**), i.e. during equilibration. In addition, the adhesion based on electrostatic interactions was marked by a significantly higher work of adhesion (~120 mJ/m^2) compared to H-bond interactions (~30 mJ/m^2), in particular when the hydrogels reached swelling equilibrium.

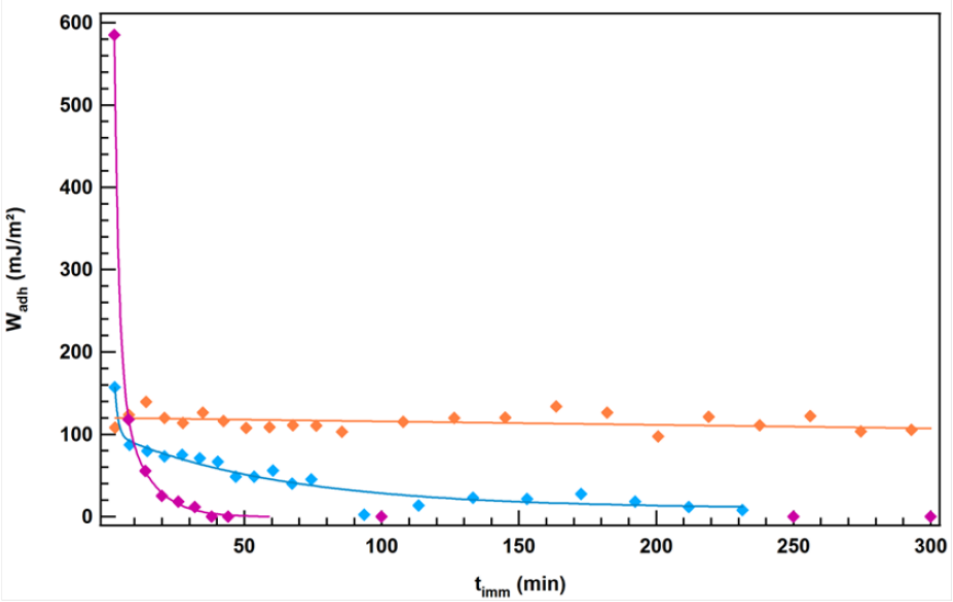

Figure 1-11. Adhesion energy as a function of immersion time of a poly(MAETAC-*co*-AAm) macroscopic hydrogel against a polymer brush of PAA in aqueous solution at pH 6, for a weight percentage of charges in the gel equal to 25% (orange), 50% (blue) and 75% (purple). The less charged polymer maintain its adhesion energy between preparation and equilibrium conditions.[88]

Finally, J. Macron conducted the first preliminary underwater probe-tack experiments of adhesion energy between the poly(MAETAC-*co*-AAm) hydrogel and a poly(acrylic acid) hydrogel thin film (dry thickness of ~200 nm) reporting higher values of adhesion energy in the order of ~10^3 mJ/m^2 in both equilibrated and non-equilibrated conditions.[88] These

experiments were preliminary, since no replicates were conducted and the same hydrogel thin film surface was used for both conditions.

Nevertheless the use of these novel poly(acrylic acid) hydrogel thin films as charged counter surfaces rather than brushes, was found very promising. The technique of thin film synthesis as first reported in the PhD dissertation of Mengxing Li,[89] is very simple (with less steps than polymer brushes) and versatile, which allows easily the adjustment of chemical (e.g. functional groups, responsiveness) and physical properties (e.g. size, structure) of the polymer films. The general synthesis of hydrogel thin films consists on grafting and crosslinking reactive polymer chains through thiol-ene click chemistry, which takes place efficiently without extensive precautions of controlled atmosphere and without addition of any initiator.[89,90] Briefly, the films are obtained by spin-coating ene-functionalized polymers in the presence of dithiol molecules as cross-linkers on thiol-modified substrate (**Figure 1-12**). The thiol-ene reaction allows both the chemical cross-linking of the polymer chains and their covalent attachment to the surface. Therefore, this technique will be used all along this thesis and the detailed procedure to prepare poly(acrylic acid) hydrogel thin films will be presented in more detailed in Chapter 2 (**Section 2.3.3**).

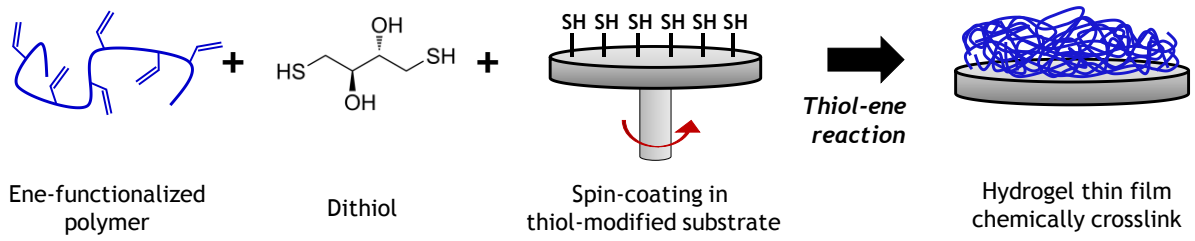

Figure 1-12. Synthesis of hydrogel thin films based on thiol-ene reaction.

1.6. Objectives of the thesis

This introduction has briefly touched upon different natural and synthetic systems that have managed to overcome the challenge of underwater adhesion to different extents. We have also

emphasized the research of several groups, which have contributed to the understanding of these natural adhesive systems and successful attempts to replicate them. In addition, we briefly review some of the intermolecular interactions presented in different natural systems, and above all, the state of the art of techniques developed to properly measure underwater adhesion at different scales due to specific molecular interactions.

Despite the significant progress in the field of underwater adhesion, there are still several open questions when linking specific molecular interactions to adhesion energy. Until now, no general relation has been established between a specific molecular interaction at the interface, soft hydrogel bulk mechanical properties and their macroscopic adhesion energy. Consequently, the direct link between the mesh size of the gel, the bond formation kinetics or the areal density of interactions at the interface and the macroscopic underwater adhesion energy remains unknown. We are therefore motivated in bridging the gap between specific molecular interactions and adhesion energy, and based on the previous progress in our research group and the previous studies presented in this introduction, we will focus our research on electrostatic molecular interactions.

Forces due to electrostatic interactions are well described by Coulomb's law in vacuum and molecular theories describing adhesion between charged molecules and surfaces, or in polymer science between polyelectrolytes, have been developed and verified experimentally.[91] The presence of thin polymer films or polymer brushes on surfaces causes additional complexity related to the counterion condensation and local pH change.[78,92] In addition, macroscopic hydrogels are soft solids that can store elastic energy upon deformation, causing long range effects that, in turn, affect macroscopic adhesive properties in a similar way as for classical soft elastomers where adherence is due to a balance between adhesive forces and strain energy.[52] However, for swollen hydrogels underwater, molecular forces and elastic strain energy are both

much weaker and the way molecular interactions causing short range attractive forces are coupled with gel mechanics to control macroscopic adhesion is still poorly understood.

Since the adhesion energy is the energy necessary to separate two surfaces, it may also contain an irreversible component, which in turn depends on the bulk mechanical properties of the macroscopic hydrogel. This is predicted by fracture models, such as the Lake and Thomas model,[93] where the energy to break a soft material is predicted to scale with the inverse square root of the elastic modulus.[1] In other words, the irreversible contribution to work of adhesion is expected to increase as the elastic modulus of the gels decreases. However, the Lake-Thomas model is not suitable for studying adhesion in our system since it assumes that bond scission and hence the fracture energy are rate independent, while previous work[83,84] on hydrogel/brush adhesion suggests that the adhesion energy is likely to be debonding rate dependent.

In the late 90s, Manoj Chaudhury[94–96] proposed an adhesion model in which the fracture energy of an interface is rate-dependent due to the rate dependent nature of the scission of weak individual bonds at the interface according to the description of Evans et al.[79,80] The adhesion energy can then be estimated as a function of kinetic parameters of bond scission of weak interactions and the polymer strand in the hydrogel is seen as a linear spring with a spring constant that is inversely proportional to the length of the chain. Accordingly, this model suggests that the adhesion energy should be directly related to the interfacial areal density of weak interactions and to the bulk mechanical properties of the macroscopic polymeric material. Therefore, it is interesting for us to see, through experimental measurements, if this model developed for elastomer adhesion can be extended to the case of underwater adhesion with macroscopic swollen hydrogels (**Section 2.2.2**).

In addition to the bulk mechanical properties, the ionic strength is a key variable for underwater adhesion experiments between oppositely charged polymeric materials. It is well known that the screening process of an electrostatic interaction can be described quantitatively

as a salt-enhanced activated process. In general, at low salt concentrations, the attraction of opposite charges is strong enough to keep two colloidal particles together. However, with increasing salt concentration, the electrostatic attraction is progressively screened and the colloidal particles will separate.[2] How the combination of these effects modifies the short-range attractive force of ions connected to soft polymeric materials is still poorly understood. As a result, the strength of ionic bonds between two soft surfaces carrying opposite charges as a function of different salt concentrations in the medium and their contribution to macroscopic underwater adhesion is still understudied.

To summarize, despite the vast progress in this field, there is no general model describing the link between specific molecular interactions used in naturally occurring adhesive systems and underwater macroscopic adhesion energy. In this context, and inspired by the recent developments of direct force measurements of intermolecular forces, and the progress on underwater probe-tack measurements, we are therefore, interested in bridging the gap between molecular electrostatic interactions. Especially, the link between interfacial areal density of electrostatic interaction, the hydrogel network architectures and the ionic strength of the medium with the macroscopic underwater adhesion of soft swollen materials. During the course of this manuscript, we will address these challenges by using a model synthetic system of oppositely charged gels, which will be described in the following section.

1.6.1. Model synthetic system

The first general objective of this manuscript is to develop a synthetic model system to explore systematically the relation between molecular electrostatic interactions at the interface, hydrogel network architecture and underwater adhesion energy between hydrogels at swelling equilibrium. The underwater probe-tack test is chosen to measure the macroscopic underwater adhesion in this model system. The advantage of this technique is the precise control over the

contact area between the tested materials. Moreover, apart from the variables on the probe-tack test that affect the measurements of adhesion (i.e. rate-dependence, contact time and pressure), two main parameters that are expected to contribute to the prediction and control of macroscopic adhesion are the interfacial areal density of electrostatic interactions and the elastic modulus of the macroscopic hydrogel.

On the surface side, we seek to synthetize surfaces functionalized with poly(acrylic acid) hydrogel thin films instead of simple polymer brushes, since the technique to prepare thin films as previously presented is more simple, robust and versatile (**Figure 1-12**). Additionally, these films serve our purpose of tuning the interfacial areal density of electrostatic interactions, as they can be tuned by either the pH or the ionic strength of the medium. However, in previous studies, the areal density of interactions at the interface has only been assumed (in the order of $\sim 10^{18}$ bonds/m^2)[87] but has not been properly measured. Furthermore, on the hydrogel side, the objectives are to explore systematically different hydrogel network architectures by varying the concentration of charged groups and the degree of crosslinking in preparation conditions to enable the exploration of different bulk mechanical properties of the hydrogels at swelling equilibrium.

We aim as well to make a comparison between macroscopic scale measurements using (underwater probe-tack) and microscopic underwater adhesion experiments using an AFM colloidal probe technique. In both experiments, the macroscopic positively charged hydrogel and the negatively charged weak polyacid on the surface (acrylic acid) were kept the same. Therefore, we aim to link the same molecular interaction to adhesion energy but at two different length scales. We aim to study the same parameters as in the probe-tack (i.e. debonding rate, contact time, pH, ionic strength, hydrogel network architecture) and we expect to achieve comparable rupture forces of molecular electrostatic interactions at both scales.

1.6.2. Bio-based system

Since we based our motivation on the inspiration of natural occurring adhesive systems, we seek to expand this study to a bio-based system by using hydrogels based on gelatin. Gelatin is derived from the hydrolysis of collagen, and depending on the solution-treated precursor, it can be either positively or negatively charged in the pH range between 5 and 8.[97–99] Moreover, the formation of thermoreversible physical gels in water is one of gelatin's most important features. Yet, these physically crosslinked gels neither are thermally nor mechanically stable. Therefore, a method to chemically crosslink gelatin is needed to improve its stability, necessary to prepare macroscopic gelatin hydrogels and to both graft and crosslink gelatin hydrogel films on silicon wafers.

Several questions arise when using chemically crosslinked gelatin networks. Since most chemical reactions use the free amino groups of the gelatin polymer chains to create a chemically crosslinked network, it is not clear whether the free amino groups left after crosslinking are sufficient to achieve measurable macroscopic adhesion. Therefore, the main objective of this bio-based system is to study achieve measurable underwater adhesion between oppositely charged gelatin hydrogels. Consequently, we will investigate whether the concept developed for the synthetic system of controlling and predicting underwater adhesion by tuning the interfacial charge density and the bulk mechanical properties, will be transposable to a gelatin-based system.

1.6.3. Complex-coacervate underwater adhesive

Following inspirations from natural adhesive systems, a third general objective pursued in this thesis is evaluating the underwater adhesion energy of a fully synthetic *in situ* setting adhesive based on a combination of complex coacervation and thermoresponsive domains. The adhesive consists of oppositely charged polyelectrolytes grafted with thermoresponsive side

chains mixed at a high salt concentration. Briefly, this adhesive system starts out as a fluid-like material that can be injected at room temperature. Upon increasing the temperature (*temperature switch*) or decreasing the salt concentration (*salt switch*) in an aqueous environment resembling biological conditions, the complex coacervate transitions into a non-flowing viscoelastic hydrogel with promising adhesive properties. Therefore, this final part of the thesis aims to adapt the underwater probe-tack test to measure, in a reproducible way, the underwater adhesion properties of complex coacervates adhesives after being exposed to either a temperature or a salt switch, or a combination of both setting mechanisms. We will therefore explore the underwater adhesion properties by changing different parameters in the test, including the temperature, ionic strength in the medium and the stretch rate.

1.7. Outline of this manuscript

This thesis will be divided into three parts. The first two parts will be related to the objective of linking electrostatic interactions to macroscopic adhesion with soft and solid-like materials, and the third part will focus on the adhesion properties of complex coacervate adhesives. In PART I, we will systematically look into the design of a model synthetic system to measure underwater adhesion at macro and micro scales by means of Probe-Tack and AFM-CP experiments, respectively. In PART II, we will present the extension of the synthetic system into a bio-based system including a possible new gelatin-based system that can be used for underwater adhesion. Finally, PART III focuses on the systematic study of a novel in situ underwater adhesive based on complex coacervation. Each chapter will be written individually as an article-like document, however, it will include a general introduction and state of the art, a theoretical section relevant to the specific chapter, experimental and results sections specific and concluding remarks. This manuscript will finish with general concluding remarks and

further perspectives for each of the three parts of this thesis, and finally a general abstract of the key findings will be presented.

References

(1) Ciccotti, M.; Creton, C. Fracture and Adhesion of Soft Materials : A Review. *Reports Prog. Phys.* **2016**, *79*, 046601.

(2) Israelachvili, J. N. *Intermolecular and Surface Forces*, 3 edition.; Academic Press, 2011.

(3) Nyarko, A.; Barton, H.; Dhinojwala, A. Scaling down for a Broader Understanding of Underwater Adhesives – a Case for the Caulobacter Crescentus Holdfast. *Soft Matter* **2016**, *12* (45), 9132–9141.

(4) Waite, J. H. Nature's Underwater Adhesive Specialist. *Int. J. Adhes. Adhes.* **1987**, *7* (1), 9–14.

(5) Defante, A. P.; Burai, T. N.; Becker, M. L.; Dhinojwala, A. Consequences of Water between Two Hydrophobic Surfaces on Adhesion and Wetting. *Langmuir* **2015**, *31* (8), 2398–2406.

(6) Kord Forooshani, P.; Lee, B. P. Recent Approaches in Designing Bioadhesive Materials Inspired by Mussel Adhesive Protein. *J. Polym. Sci. Part A Polym. Chem.* **2017**, *55* (1), 9–33.

(7) Mehdizadeh, M.; Yang, J. Design Strategies and Applications of Tissue Bioadhesives. *Macromol. Biosci.* **2013**, *13* (3), 271–288.

(8) Hofman, A. H.; van Hees, I. A.; Yang, J.; Kamperman, M. Bioinspired Underwater Adhesives by Using the Supramolecular Toolbox. *Adv. Mater.* **2018**, *1704640*.

(9) Scognamiglio, F.; Travan, A.; Rustighi, I.; Tarchi, P.; Palmisano, S.; Marsich, E.; Borgogna, M.; Donati, I.; De Manzini, N.; Paoletti, S. Adhesive and Sealant Interfaces for General Surgery Applications. *J. Biomed. Mater. Res. - Part B Appl. Biomater.* **2016**, *104* (3), 626–639.

(10) Duarte, A. P.; Coelho, J. F.; Bordado, J. C.; Cidade, M. T.; Gil, M. H. Surgical Adhesives: Systematic Review of the Main Types and Development Forecast. *Prog. Polym. Sci.* **2012**, *37* (8), 1031–1050.

(11) Stewart, R. J.; Ransom, T. C.; Hlady, V. Natural Underwater Adhesives. *J. Polym. Sci. Part B Polym. Phys.* **2011**, *49* (11), 757–771.

(12) Walker, G. The Histology, Histochemistry and Ultrastructure of the Cement Apparatus

of Three Adult Sessile Barnacles, Elminius Modestus, Balanus Balanoides and Balanus Hameri. *Mar. Biol.* **1970**, *7* (3), 239–248.

(13) Waite, J. H.; Andersen, N. H.; Jewhurst, S.; Sun, C. Mussel Adhesion: Finding the Tricks Worth Mimicking. *J. Adhes.* **2005**, *81* (3–4), 297–317.

(14) Wei, W.; Yu, J.; Gebbie, M. A.; Tan, Y.; Martinez Rodriguez, N. R.; Israelachvili, J. N.; Waite, J. H. Bridging Adhesion of Mussel-Inspired Peptides: Role of Charge, Chain Length, and Surface Type. *Langmuir* **2015**, *31* (3), 1105–1112.

(15) Stewart, R. J.; Wang, C. S.; Shao, H. Complex Coacervates as a Foundation for Synthetic Underwater Adhesives. *Adv. Colloid Interface Sci.* **2011**, *167*, 85–93.

(16) Brubaker, C. E.; Messersmith, P. B. The Present and Future of Biologically Inspired Adhesive Interfaces and Materials. *Langmuir* **2012**, *28* (4), 2200–2205.

(17) Waite, J. H. Mussel Adhesion – Essential Footwork. *J. Exp. Biol.* **2017**, *220* (4), 517–530.

(18) Stewart, R. J.; Weaver, J. C.; Morse, D. E.; Waite, J. H. The Tube Cement of Phragmatopoma Californica: A Solid Foam. *J. Exp. Biol.* **2004**, *207* (26), 4727–4734.

(19) Zhao, Q.; Lee, D. W.; Ahn, B. K.; Seo, S.; Kaufman, Y.; Israelachvili, J.; Waite, J. H. Underwater Contact Adhesion and Microarchitecture in Polyelectrolyte Complexes Actuated by Solvent Exchange. *Nat. Mater.* **2016**, *15* (4), 407–412.

(20) Yang, J.; Włodarczyk-Biegun, M. K.; Filippov, A.; Akerboom, S.; Dompé, M.; van Hees, I. A.; Mocan, M.; Kamperman, M. Functional Polymeric Materials Inspired by Geckos, Mussels, and Spider Silk. *Macromol. Chem. Phys.* **2018**, *219* (16), 1–13.

(21) Vreeland, V.; Waite, J. H.; Epstein, L. Polyphenols and Oxidases in Substratum Adhesion by Marine Algae and Mussels. *J. Phycol.* **1998**, *34* (1), 1–8.

(22) Gebbie, M. A.; Wei, W.; Schrader, A. M.; Cristiani, T. R.; Dobbs, H. A.; Idso, M.; Chmelka, B. F.; Herbert Waite, J.; Israelachvili, J. N. Tuning Underwater Adhesion with Cation-φ Interactions. *Nat. Chem.* **2017**, *9* (5), 473–479.

(23) Stewart, R. J.; Wang, C. S.; Song, I. T.; Jones, J. P. The Role of Coacervation and Phase Transitions in the Sandcastle Worm Adhesive System. *Adv. Colloid Interface Sci.* **2017**, *239*, 88–96.

(24) Barrett, D. G.; Bushnell, G. G.; Messersmith, P. B. Mechanically Robust, Negative-Swelling, Mussel-Inspired Tissue Adhesives. *Adv. Healthc. Mater.* **2013**, *2* (5), 745–755.

(25) Li, J.; Celiz, A. D.; Yang, J.; Yang, Q.; Wamala, I.; Whyte, W.; Seo, B. R.; Vasilyev, N. V.; Vlassak, J. J.; Suo, Z.; et al. Tough Adhesives for Diverse Wet Surfaces. *Science (80-*

. *).* **2017**, *357* (6349), 378–381.

(26) Zhang, H.; Bré, L.; Zhao, T.; Newland, B.; Da Costa, M.; Wang, W. A Biomimetic Hyperbranched Poly(Amino Ester)-Based Nanocomposite as a Tunable Bone Adhesive for Sternal Closure. *J. Mater. Chem. B* **2014**, *2* (26), 4067.

(27) Rahimnejad, M.; Zhong, W. Mussel-Inspired Hydrogel Tissue Adhesives for Wound Closure. *RSC Adv.* **2017**, *7* (75), 47380–47396.

(28) Yang, X.; Zhu, L.; Tada, S.; Zhou, D.; Kitajima, T.; Isoshima, T.; Yoshida, Y.; Nakamura, M.; Yan, W.; Ito, Y. Mussel-Inspired Human Gelatin Nanocoating for Creating Biologically Adhesive Surfaces. *Int. J. Nanomedicine* **2014**.

(29) Shao, H.; Stewart, R. J. Biomimetic Underwater Adhesives with Environmentally Triggered Setting Mechanisms. *Adv. Mater.* **2010**, *22* (6), 729–733.

(30) Shao, H.; Bachus, K. N.; Stewart, R. J. A Water-Borne Adhesive Modeled after the Sandcastle Glue of P. Californica. *Macromol. Biosci.* **2009**, *9* (5), 464–471.

(31) Ahn, B. K.; Das, S.; Linstadt, R.; Kaufman, Y.; Martinez-Rodriguez, N. R.; Mirshafian, R.; Kesselman, E.; Talmon, Y.; Lipshutz, B. H.; Israelachvili, J. N.; et al. High-Performance Mussel-Inspired Adhesives of Reduced Complexity. *Nat. Commun.* **2015**, *6*, 1–7.

(32) Hofman, A. H.; van Hees, I. A.; Yang, J.; Kamperman, M. Bioinspired Underwater Adhesives by Using the Supramolecular Toolbox. *Adv. Mater.* **2018**, *1704640*, 1–38.

(33) Gucht, J. van der; Spruijt, E.; Lemmers, M.; Cohen Stuart, M. A. Polyelectrolyte Complexes: Bulk Phases and Colloidal Systems. *J. Colloid Interface Sci.* **2011**, *361* (2), 407–422.

(34) Sun, J.-Y.; Illeperuma, W. R. K.; Zhao, X.; Mooney, D. J.; Vlassak, J. J.; Chaudhuri, O.; Suo, Z.; Oh, K. H. Highly Stretchable and Tough Hydrogels. *Nature* **2012**, *489* (7414), 133–136.

(35) Karami, P.; Wyss, C.; Khoushabi, A.; Schmocker, A.; Broome, M.; Moser, C.; Bourban, P.-E.; Pioletti, D. Composite Double-Network Hydrogels to Improve Adhesion on Biological Surfaces. *ACS Appl. Mater. Interfaces* **2018**, acsami.8b10735.

(36) Artzi, N.; Shazly, T.; Baker, A. B.; Bon, A.; Edelman, E. R. Aldehyde-Amine Chemistry Enables Modulated Biosealants with Tissue-Specific Adhesion. *Adv. Mater.* **2009**, *21* (32–33), 3399–3403.

(37) Spruijt, E.; Westphal, A. H.; Borst, J. W.; Cohen Stuart, M. A.; Van Der Gucht, J. Binodal Compositions of Polyelectrolyte Complexes. *Macromolecules* **2010**, *43* (15),

6476–6484.

(38) Spruijt, E.; Sprakel, J.; Lemmers, M.; Stuart, M. A. C.; Van Der Gucht, J. Relaxation Dynamics at Different Time Scales in Electrostatic Complexes: Time-Salt Superposition. *Phys. Rev. Lett.* **2010**, *105* (20), 1–4.

(39) Lawrence, P. G.; Lapitsky, Y. Ionically Cross-Linked Poly(Allylamine) as a Stimulus-Responsive Underwater Adhesive: Ionic Strength and PH Effects. *Langmuir* **2015**, *31* (4), 1564–1574.

(40) Seo, S.; Das, S.; Zalicki, P. J.; Mirshafian, R.; Eisenbach, C. D.; Israelachvili, J. N.; Waite, J. H.; Ahn, B. K. Microphase Behavior and Enhanced Wet-Cohesion of Synthetic Copolyampholytes Inspired by a Mussel Foot Protein. *J. Am. Chem. Soc.* **2015**, *137* (29), 9214–9217.

(41) Wang, Q.; Schlenoff, J. B. The Polyelectrolyte Complex/Coacervate Continuum. *Macromolecules* **2014**, *47* (9), 3108–3116.

(42) Jones, J. P.; Sima, M.; O'Hara, R. G.; Stewart, R. J. Water-Borne Endovascular Embolics Inspired by the Undersea Adhesive of Marine Sandcastle Worms. *Adv. Healthc. Mater.* **2016**, *5* (7), 795–801.

(43) Kaur, S.; Weerasekare, G. M.; Stewart, R. J. Multiphase Adhesive Coacervates Inspired by the Sandcastle Worm. *ACS Appl. Mater. Interfaces* **2011**, *3* (4), 941–944.

(44) Huang, Y.; Lawrence, P. G.; Lapitsky, Y. Self-Assembly of Stiff, Adhesive and Self-Healing Gels from Common Polyelectrolytes. *Langmuir* **2014**, *30* (26), 7771–7777.

(45) Wu, S. *Polymer Interface and Adhesion*; Marcel Dekker, INC., 1982.

(46) Israelachvili, J.; Ruths, M. Brief History of Intermolecular and Intersurface Forces in Complex Fluid Systems. *Langmuir* **2013**, *29* (31), 9605–9619.

(47) Latimer, W. M.; Rodebush, W. H. Polarity and Ionization from the Standpoint of the Lewis Theory of Valence. *J. Am. Chem. Soc.* **1920**, *42* (7), 1419–1433.

(48) Smith, D. A. *A Brief History of the Hydrogen Bond*; ACS Symposium Series, 1994.

(49) Nelson, D. L.; Cox, M. M. *Lehninger Principles of Biochemistry*, 7th ed.; W. H. Freeman, 2017.

(50) Dennis A Dougherty. Cation-π Interactions in Chemistry and Biology: A New View of Benzene, Phe, Tyr and Trp. *Science (80-.).* **1996**, *271* (12 January), 163–169.

(51) Hwang, D. S.; Lu, Q.; Lee, Y.; Oh, D. X.; Zeng, H.; Jho, Y. Nanomechanics of Cation-π Interactions in Aqueous Solution. *Angew. Chemie Int. Ed.* **2013**, *52* (14), 3944–3948.

(52) Shull, K. R. Contact Mechanics and the Adhesion of Soft Solids. *Mater. Sci. Eng. R*

Reports **2002**, *36* (1), 1–45.

(53) Kobayashi, M.; Terada, M.; Takahara, A. Reversible Adhesive-Free Nanoscale Adhesion Utilizing Oppositely Charged Polyelectrolyte Brushes. *Soft Matter* **2011**, *7*, 5717–5722.

(54) La Spina, R.; Tomlinson, M. R.; Ruiz-pørez, L.; Chiche, A.; Langridge, S.; Geoghegan, M. Controlling Network – Brush Interactions to Achieve Switchable Adhesion **. *Angew. Chemie Int. Ed.* **2007**, *46*, 6460–6463.

(55) Erath, J.; Schmidt, S.; Fery, A. Characterization of Adhesion Phenomena and Contact of Surfaces by Soft Colloidal Probe AFM. *Soft Matter* **2010**, *6* (7), 1432–1437.

(56) Israelachvili, J.; Adams, G. Measurement of Forces between Two Mica Surfaces in Aqueous Electrolyte Solution. *J. Chem. Soc. Fard. Trans. I* **1978**, *74*, 975–1001.

(57) Israelachvili, J. N.; Tabor, D. The Measurement of Van Der Waals Dispersion Forces in the Range 1.5 to 130 Nm. *Proc. R. Soc. A Math. Phys. Eng. Sci.* **1972**, *331*, 19–38.

(58) Tabor, D.; Winterton, R. H. S. Surface Forces: Direct Measurement of Normal and Retarded van Der Waals Forces. *Nature* **1968**, *219* (5159), 1120–1121.

(59) Butt, H. J.; Cappella, B.; Kappl, M. Force Measurements with the Atomic Force Microscope: Technique, Interpretation and Applications. *Surf. Sci. Rep.* **2005**, *59* (1–6), 1–152.

(60) Rabinovich, Y. I.; Yoon, R. H. Use of Atomic Force Microscope for the Measurements of Hydrophobic Forces between Silanated Silica Plate and Glass Sphere. *Langmuir* **1994**, *10* (6), 1903–1909.

(61) Spruijt, E.; Stuart, M. a C.; Van Der Gucht, J. Dynamic Force Spectroscopy of Oppositely Charged Polyelectrolyte Brushes. *Macromolecules* **2010**, *43*, 1543–1550.

(62) Hu, K.; Fan, F.-R. F.; Bard, A. J.; Hillier, A. C. Direct Measurement of Diffuse Double-Layer Forces at the Semiconductor/Electrolyte Interface Using an Atomic Force Microscope. *J. Phys. Chem. B* **1997**, *101* (41), 8298–8303.

(63) Grandbois, M.; Beyer, M.; Rief, M.; Clausen-schaumann, H.; Gaub, H. E. How Strong Is a Covalent Bond ? *Science (80-.).* **1999**, *283* (3), 1727–1731.

(64) Boland, T.; Ratner, B. D. Direct Measurement of Hydrogen Bonding in DNA Nucleotide Bases by Atomic Force Microscopy. *Proc. Natl. Acad. Sci.* **1995**, *92* (12), 5297–5301.

(65) Israelachvili, J. N.; Adams, G. E. Direct Measurement of Long Range Forces between Two Mica Surfaces in Aqueous KN03 Solutions. *Nature* **1976**, *262*, 774–776.

(66) Ruths, M.; Israelachvili, J. Surface Forces and Nanorheology of Molecularly Thin Films.

In *Springer Handbook of Nanotechnology*; Springer Berlin Heidelberg, 2007; pp 859–924.

(67) Restagno, F.; Crassous, J.; Charlaix, É.; Cottin-Bizonne, C.; Monchanin, M. A New Surface Forces Apparatus for Nanorheology. *Rev. Sci. Instrum.* **2002**, *73* (6), 2292.

(68) Dunlop, I. E.; Briscoe, W. H.; Titmuss, S.; Jacobs, R. M. J.; Osborne, V. L.; Edmondson, S.; Huck, W. T. S.; Klein, J. Direct Measurement of Normal and Shear Forces between Surface-Grown Polyelectrolyte Layers. *J. Phys. Chem. B* **2009**, *113* (12), 3947–3956.

(69) Hayashi, S.; Abe, T.; Higashi, N.; Niwa, M.; Kurihara, K. Polyelectrolyte Brush Layers Studied by Surface Forces Measurement: Dependence on PH and Salt Concentrations and Scaling. *Langmuir* **2002**, *18* (10), 3932–3944.

(70) Valtiner, M.; Kristiansen, K.; Greene, G. W.; Banquy, X.; Israelachvili, J. N. The Electrochemical Surface Forces Apparatus: The Effect of Surface Roughness, Electrostatic Surface Potentials, and Anodic Oxide Growth on Interaction Forces, and Friction between Dissimilar Surfaces in Aqueous Solutions. *Langmuir* **2012**, *28* (36), 13080–13093.

(71) Binning, G.; Quate, C. F.; Gerber, C. Atomic Force Microscope. *Phys. Rev. Lett.* **1986**, *56* (9), 930–934.

(72) Ducker, W. A.; Senden, T. J.; Pashley, R. M. Direct Measurement of Colloidal Forces Using an Atomic Force Microscope. *Lett. to Nat.* **1991**, *353*, 239–241.

(73) Butt, H. J. Measuring Electrostatic, van Der Waals, and Hydration Forces in Electrolyte Solutions with an Atomic Force Microscope. *Biophys. J.* **1991**, *60* (6), 1438–1444.

(74) Synytska, A.; Svetushkina, E.; Martina, D.; Bellmann, C.; Simon, F.; Ionov, L.; Creton, C. Intelligent Materials with Adaptive Adhesion Properties Based on Comb-like Polymer Brushes. *Langmuir* **2012**, *28*, 16444−16454.

(75) Chem, J. M.; Kamperman, M.; Synytska, A. Switchable Adhesion by Chemical Functionality and Topography. **2012**.

(76) Drechsler, A.; Synytska, A.; Uhlmann, P.; Elmahdy, M. M.; Stamm, M.; Kremer, F. Interaction Forces between Microsized Silica Particles and Weak Polyelectrolyte Brushes at Varying PH and Salt Concentration. *Langmuir* **2010**, *26* (9), 6400–6410.

(77) Drechsler, A.; Synytska, A.; Uhlmann, P.; Stamm, M.; Kremer, F. Tuning the Adhesion of Silica Microparticles to a Poly (2-Vinyl Pyridine) Brush : An AFM Force Measurement Study. *Langmuir* **2012**, *28*, 15555–15565.

(78) Spruijt, E.; Van Den Berg, S. A.; Cohen Stuart, M. A.; Van Der Gucht, J. Direct

Measurement of the Strength of Single Ionic Bonds between Hydrated Charges. *ACS Nano* **2012**, *6* (6), 5297–5303.

(79) Evans, E. A.; Ritchie, K. Strength of a Weak Bond Connecting Flexible Polymer Chains. *Biophys. J.* **1999**, *76* (5), 2439–2447.

(80) Merkel, R.; Nassoy, P.; Leung, A.; Ritchie, K.; Evans, E. Energy Landscapes of Receptor-Ligand Bonds Explored with Dynamic Force Spectroscopy. *Nature* **1999**, *397* (6714), 50–53.

(81) Spruijt, E. Strength, Structure and Stability of Polyelectrolyte Complex Coacervates. PhD Thesis, Wageningen University, 2012.

(82) Alfhaid, L.; Seddon, W. D.; Williams, N. H.; Geoghegan, M. Double-Network Hydrogels Improve PH-Switchable Adhesion. *Soft Matter* **2016**, *12*, 5022–5028.

(83) Alfhaid, L.; La Spina, R; Tomlinson, M. R.; Hall, A. R.; Seddon, D.; Williams, N. H.; Cousin, F.; Gorb, S.; Geoghegan, M. Adhesion between Oppositely Charged Polyelectrolytes. *J. Adhes.* **2016**, *94* (1), 58–76.

(84) Sudre, G.; Olanier, L.; Tran, Y.; Hourdet, D.; Creton, C. Reversible Adhesion between a Hydrogel and a Polymer Brush. *Soft Matter* **2012**, *8*, 8184–8193.

(85) Sudre, G. Adhésion Stimulable d'hydrogels. PhD Thesis, Université Pierre et Marie Curie (UPMC) Paris VI, 2011.

(86) Obukhov, S. P.; Rubinstein, M.; Colby, R. H. Network Modulus and Superelasticity. *Macromolecules* **1994**, *27* (12), 3191–3198.

(87) Macron, J.; Bresson, B.; Tran, Y.; Hourdet, D.; Creton, C. Equilibrium and Out-of-Equilibrium Adherence of Hydrogels against Polymer Brushes. *Macromolecules* **2018**, *51* (19), 7556–7566.

(88) Macron, J. Hydrogels En Milieux Immergés : De l'adhesion Macroscopique Aux Mécanismes Moléculaires. PhD Thesis, Université Pierre et Marie Curie (UPMC) Paris VI, 2014.

(89) Li, M. Films Minces d'hydrogels Stimulables. PhD Thesis, Université Pierre et Marie Curie (UPMC) Paris VI, 2014.

(90) Chollet, B.; Li, M.; Martwong, E.; Bresson, B.; Fretigny, C. Multiscale Surface-Attached Hydrogel Thin Films with Tailored Architecture. *ACS Appl. Mater. Interfaces* **2016**, *8*, 11729–11738.

(91) Dobrynin, A. V.; Rubinstein, M. Theory of Polyelectrolytes in Solutions and at Surfaces. *Prog. Polym. Sci.* **2005**, *30* (11), 1049–1118.

(92) Tagliazucchi, M.; de la Cruz, M. O.; Szleifer, I. Self-Organization of Grafted Polyelectrolyte Layers via the Coupling of Chemical Equilibrium and Physical Interactions. *Proc. Natl. Acad. Sci.* **2010**, *107* (12), 5300–5305.

(93) Lake, G. J.; Thomas, A. G. The Strength of Highly Elastic Materials. *Proc. R. Soc. A Math. Phys. Eng. Sci.* **1967**, *300* (1460), 108–119.

(94) Chaudhury, M. K. Rate-Dependent Fracture at Adhesive Interface. *J. Phys. Chem. B* **1999**, *103*, 6562–6566.

(95) Ghatak, A.; Vorvolakos, K.; She, H.; Malotky, D. L.; Chaudhury, M. K. Interfacial Rate Processes in Adhesion and Friction. *J. Phys. Chem. B* **2000**, *104* (17), 4018–4030.

(96) Hui, C. Y.; Tang, T.; Lin, Y. Y.; Chaudhury, M. K. Failure of Elastomeric Polymers Due to Rate Dependent Bond Rupture. *Langmuir* **2004**, *20* (14), 6052–6064.

(97) Solorio, L.; Zwolinski, C.; Lund, A. W.; Farrell, M. J.; Jan, P. Gelatin Microspheres Crosslinked with Genipin for Local Delivery of Growth Factors. *J Tissue Eng Regen Med.* **2011**, *4* (7), 514–523.

(98) Aramwit, P.; Jaichawa, N.; Ratanavaraporn, J.; Srichana, T. A Comparative Study of Type A and Type B Gelatin Nanoparticles as the Controlled Release Carriers for Different Model Compounds. *Mater. Express* **2015**, *5* (3), 241–248.

(99) Ofner, C. M.; Bubnis, W. A. Chemical and Swelling Evaluations of Amino Group Crosslinking in Gelatin and Modified Gelatin Matrices. *Pharmaceutical Research*. 1996, pp 1821–1827.

PART I

Model Synthetic System

Chapter 2

2. From molecular electrostatic interactions to macroscopic underwater adherence.

In this Chapter, we investigate the macroscopic adhesion energy (W_a) in pure water between a positively charged hydrogel of varying crosslink density made from (methacryloyloxyethyl)trimethylammonium chloride and acrylamide [poly(MAETAC-co-AAm)] and a negatively charged and crosslinked poly(acrylic acid) (PAA) thin film gel on a silicon wafer. Adhesion tests were carried out on a custom-built probe-tack setup fully immersed in pure water. The interfacial charge density on the PAA hydrogel thin film was estimated from streaming potential measurements and the molecular architecture of the thick hydrogel was obtained from mechanical testing. For a fixed interfacial charge density, W_a increased weakly with contact time (in stark contrast with the case where adhesion is due to H-bonds) but strongly with debonding rate. For a given gel, the work of adhesion increased linearly with the interfacial charge density of the thin PAA film while at constant interfacial charge density, W_a was found to decrease with the modulus of the gel. Results were analysed with a simple model proposed by Chaudhury for weak adhesion of elastomers. Using realistic values of the spring constant of the polymer chain and of the characteristic time of bond dissociation, we demonstrate that the work of adhesion can be rationalized by a combination of strain rate dependent bond breaking kinetics combined with a pH dependent areal density of electrostatic interactions.

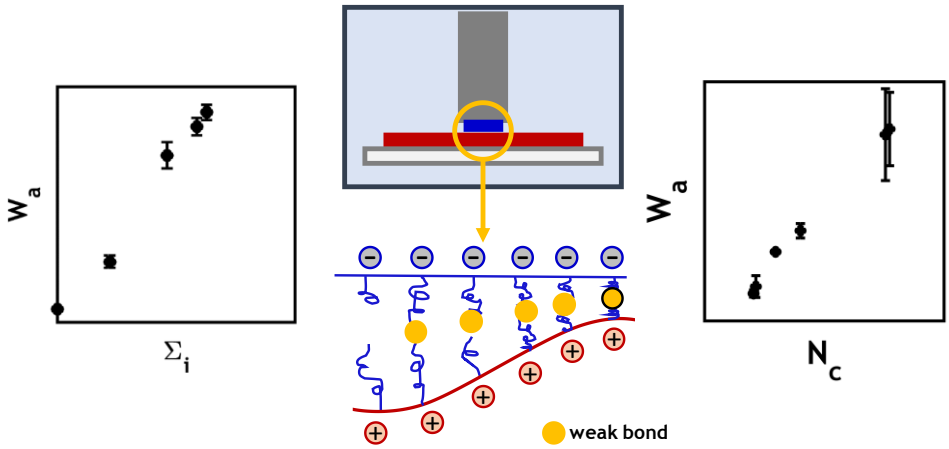

Part of content of this chapter is the result of a collaboration with Ugo Sidoli and Dr. Alla Synytska at the Leibniz Institute of Polymer Research, Dresden, Germany. The content of this chapter is already accepted for publication.

Contents

2.1. Introduction

Molecular electrostatic interactions play a key role in many macromolecular assemblies for bioadhesives systems.[1] There is a growing interest in using ionic bonds for a broad range of applications in medicine, such as tissue engineering,[2] drug delivery systems,[3] and surgical adhesives[4] because of their strength and tunability. For the latter application, adhesives systems using electrostatic interactions to achieve promising levels of adhesion for medical applications have been reported.[5] Yet, despite several previous studies,[6–8] the control and quantitative prediction of macroscopic adhesion properties from molecular electrostatic interactions is still poorly understood for soft materials fully immersed in an aqueous environment.

Forces due to electrostatic interactions are well described by Coulomb's law in vacuum and molecular theories describing adhesion between charged molecules and surfaces, or in polymer science between polyelectrolytes, have been developed and verified experimentally.[9] The presence of thin polymer films or polymer brushes on surfaces causes additional complexity related to the counterion condensation and local pH change.[10,11] In addition macroscopic hydrogels are soft solids that can store elastic energy upon deformation, causing long range effects that in term affect macroscopic adhesive properties in a similar way than for classical soft elastomers where adherence is due to a balance between adhesive forces and strain energy.[12] However for swollen hydrogels underwater, molecular forces and elastic strain energy are both much weaker and the way molecular interactions causing short range attractive forces are coupled with gel mechanics to control macroscopic adhesion is still poorly understood.

Initial investigations of this problem have measured the underwater adhesion energy at a nanometric force scale between oppositely charged polyelectrolyte brushes by using the AFM-colloidal probe technique.[13–15] The main focus of this previous work was to achieve reversible adhesion by changing environmental variables such as pH[6] or by adding salt.[13] Additionally, repulsions resulting from electrostatic interactions have been extensively studied with the

surface force apparatus.[16–18]. However, adhesion between molecules or monolayers focuses only on the molecular interactions but fails to consider the effect of the bulk mechanical properties of the tested materials. Recently, Geoghegan and coworkers[6,8] reported underwater adhesion experiments between oppositely charged polymer brushes and macroscopic hydrogel hemispheres using the so-called Johnson–Kendall–Roberts (JKR) analysis. They focused on the reversibility and repeatability of the adhesive interactions but did not vary systematically charge density and hydrogel structure. Rose et al.[19] obtained weak and reversible adhesion between highly swollen hydrogels by mediating the contact with nanoparticle able to adsorb on both surfaces with non-specific interactions.

Our group has recently developed a novel methodology to measure the underwater adhesion energy (W_a) between hydrogels and polymer brushes.[20] The first objective was to obtain pH-responsive and reversible adhesion of a hydrogel on a hard surface.[20] This technique was used to explore the effect of hydrogen bonding interactions on the W_a between a poly(acrylic acid) brush and a poly(N,N-dimethyl acrylamide) hydrogel, and a maximum W_a of about 100 mJ/m^2 was reported. This methodology was also used to measure W_a as the poly(N,N-dimethylacrylamide) hydrogel swelled from its preparation state until equilibrium.[21] This study showed that adhesion always decreases as the gels equilibrate with their surroundings regardless of the initial hydrogel polymer concentration and degree of crosslinking. In this article, we investigate the adhesion between negatively charged surfaces and positively charged highly elastic hydrogels. Because our gels are well crosslinked we expect to minimize viscoelastic dissipation and maximize the sensitivity of the adhesion test to the specific interfacial interactions.

In this work, model polyelectrolyte hydrogels were selected to measure W_a between a positively charged hydrogel and a negatively charged hydrogel thin film (**Figure 2-1**). Specifically, we investigated the effect of the hydrogel network architecture and of the

interfacial charge density on W_a with the intention of bridging the gap between a specific molecular interaction and the macroscopic underwater adherence energy.

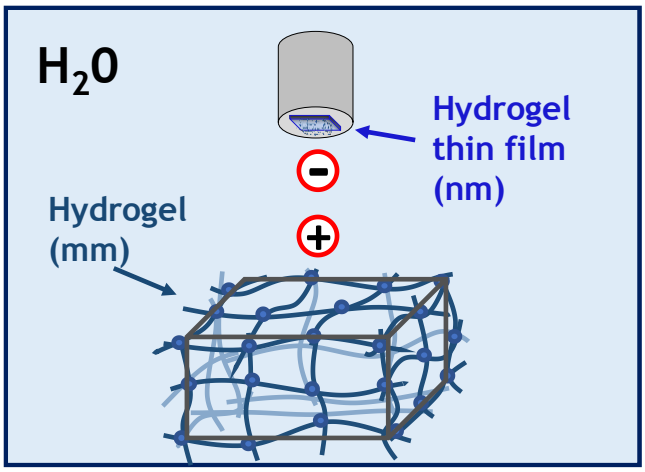

Figure 2-1. Simplified scheme of a tack test underwater between a hydrogel (Thickness < 2 mm) positively charged and a hydrogel thin film (Thickness < 0.5 µm) negatively charged.

2.2. Theory

2.2.1. Lake and Thomas model

Since the adhesion energy is the energy necessary to separate two surfaces it may also contain an irreversible component which in turn depends on the bulk mechanical properties of the macroscopic hydrogel, as predicted by fracture models, such as the Lake and Thomas model.[22] Lake and Thomas suggested that when a soft material is stretched to fracture, the bond that actually fractures is not the only bond in the material to store energy. To extend a bond to the point of rupture, most of the other bonds in that chain will also be nearly fully extended, and store the same energy. They proposed that the macroscopic fracture energy of the crosslinked network material (Γ_0) is proportional to the energy absorbed prior to rupture for a C-C bond (U_c) multiplied by the number of bonds between crosslinks (N_b). However, in a bulk polymer,

there will be multiple chains in the plane of crack propagation, and the fracture energy is an energy per unit surface (e.g. J/m^2). Therefore, they added to the model the number of strands crossing the interface per unit area given by ½$L\nu$, where L is the end to end distance of a strand ($\sim bN_b^{1/2}$), b is the length of a C-C bond (1.54 Å), N_b is the number of bonds in the polymer chain and (ν) is the number of elastically effective strands per unit volume. From this, Γ_0 is then given by:

$$\Gamma_0 \approx \frac{1}{2}\frac{U_c \nu b N_b^{3/2}}{N_{av}} \tag{1}$$

Moreover, ν can be estimated from the shear modulus of the hydrogel (G) using the phantom network model [23]

$$G = \nu k_B T\left(1-\frac{2}{f}\right) = \frac{\rho_0 \phi_p RT}{M_c}\left(1-\frac{2}{f}\right) \tag{2}$$

$$\nu = \frac{\rho_0 \phi_p N_{av}}{M_c} \tag{3}$$

where k_B is Boltzmann's constant, T is the temperature, f is the crosslink functionality, ρ_0 is the bulk polymer density, ϕ_p is the polymer volume fraction and R is the universal gas constant. N_b can be written as function of the molecular weight between crosslink (M_c) writing that it is twice the number of vinyl monomers in the elastic chain as follows:

$$N_b = \frac{2M_c}{M_0} \tag{4}$$

where M_0 is the molar mass of a monomer unit. Finally, unifying all equations above, the fracture energy Γ_0 in J/m^2 can be rewritten as function of M_c as:

$$\Gamma_0 \approx \sqrt{2}U_c\left(\frac{b\rho_0\phi_p}{M_0^{3/2}}\right)M_c^{1/2} \tag{5}$$

Consequently, the fracture energy Γ_0 is predicted to scale with the square root of the molecular weight between crosslinks multiplied by a constant.

2.2.2. Chaudhury model

The Lake-Thomas model is not suitable to study adhesion of our system since it assumes that bond scission and hence the fracture energy, are rate independent, and previous work[8,20] on hydrogel/brush adhesion suggests that the adhesion energy is likely to be debonding rate dependent. Chaudhury[24] proposed a weak adhesion model in which the fracture energy of an interface is rate-dependent due to the rate dependent nature of the scission of individual bonds at the interface adapting the work of Evans on single molecules to the case of non dissipative elastomers.[25,26]

In his model, he assumes that the macroscopic rate dependence of the adhesion energy is due to the rate dependence of the scission of a weak bond attached to a polymeric chain. He assumed that tethered chains composed by strong bonds and with a terminal weak bond attached to a network across the interface, would be stretched before this latter bond fails (**Figure 2-2**).

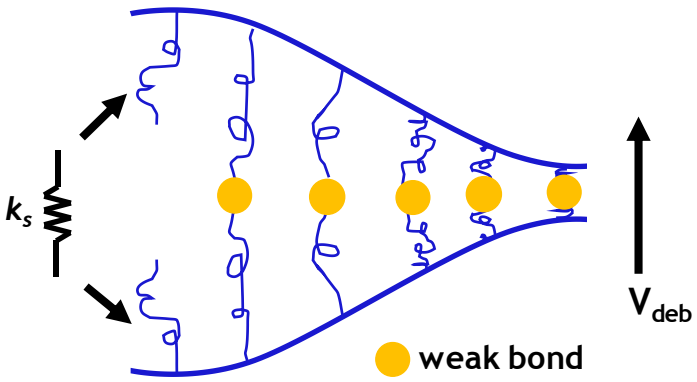

Figure 2-2. Schematic representation of the crack tip region soft polymeric material k_s represents the linear spring constant of a single polymer chain.

Essentially, since the probability of failure of the weak bond increases with force, the time of failure increases with the logarithm of the pulling rate. According to his model, the interfacial fracture energy (W_a) for relatively fast debonding rates can be described as follows:

$$W_a = \left(\frac{\Sigma_i}{2k_s}\right)\left[\left(\frac{k_B T}{\lambda}\right)\ln\left(\frac{k_s V \lambda \tau_-}{n k_B T}\right)\right]^2 \quad (6)$$

where Σ_i is the areal density of weak bonds crossing the fracture plane. λ is the activation length of the bond, which we assume normally to be 0.1 nm, that is, a typical ionic bond lengths.[27] τ_- is the characteristic time of bond dissociation, k_B is the Boltzmann's constant and n is the number of weak bonds in the polymer chain. k_s is the linear spring constant of the polymer chain which is inversely proportional to the length the chain. However, a polymer chain has a markedly non-linear behavior since at small strains it is the entropic spring that determines the spring constant while near the maximum extension of the chain it is the stiffness of the bonds of the chain that matter.

To estimate the values of the spring constant and the characteristic time of bond dissociation, it is necessary to measure the work of adhesion as function of different debonding rates, and rearrange the equation of the Chaudhury's model in the following form with *n* = 1:

$$W_a = \frac{\Sigma_i}{2k_s}\left[\left(\frac{k_B T}{\lambda}\right)\ln\left(\frac{k_s V_{deb} \lambda \tau_-}{k_B T}\right)\right]^2 \quad (7)$$

$$W_a = \frac{\Sigma_i}{2k_s}\left(\frac{k_B T}{\lambda}\right)^2\left(\ln V_{deb} + \ln\left(\frac{k_s \lambda \tau_-}{k_B T}\right)\right)^2 \quad (8)$$

$$\sqrt{W_a}\left(\frac{k_B T}{\lambda}\right)^{-1} = \left(\frac{\Sigma_i}{2k_s}\right)^{1/2}\ln V_{deb} + \left[\left(\frac{\Sigma_i}{2k_s}\right)^{1/2}\ln\left(\frac{k_s \lambda \tau_-}{k_B T}\right)\right] \quad (9)$$

Therefore, when plotting $\sqrt{W_a}\left(\frac{k_B T}{\lambda}\right)^{-1}$ as function of $\ln V_{deb}$ and making a linear fit, it is possible to estimate the spring constant (k_s) from the slope and the dissociation time (τ_-) from the intercept on the y-axis.

2.2.3. GCSG model

Due to the electrostatic nature of this adhesive system, we propose the use of electrokinetic measurements (i.e. streaming potential or streaming current) to estimate the surface density of

electric charges at the surface of the hydrogel thin film. The general principle of electrokinetic measurements consists on an electrical potential (ΔU) generated by a streaming liquid (fluid with ions) along a solid phase. The force to drive the liquid stream is usually produced by a pressure difference (ΔP) in the absence of an applied electric field (**Figure 2-3**).

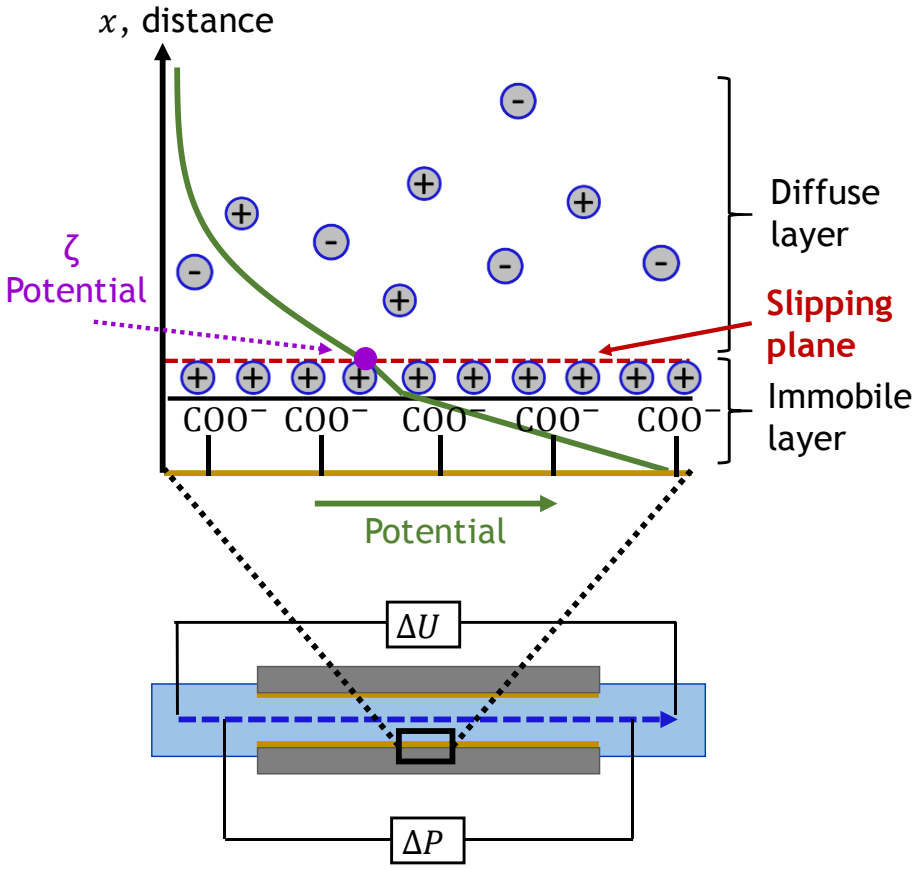

Figure 2-3. Schematic representation of the electrochemical double layer at a negatively charged interface according to the GCSG model in the frame of the general principle of streaming potential measurements. The immobile layer is the locus of specifically adsorbed ions. The potential at the slip plane is the electrokinetic or zeta-potential ζ. Moving away from the slipping plane lies the diffuse layer where the potential decays exponentially.

Descriptions of the charge distribution at the interface are based on the model developed by Gouy and Chapman and completed by Stern and Grahame (GSCG model).[28] The GSCG model describes the charging processes taking place at the solid/liquid interface by introducing two

parallel layers of charge surrounding a solid surface (**Figure 2-3**). This parallel layers (known as the electric double layer) consists of three parts: (i) Surface charge: charged ions (commonly negative) adsorbed on the particle surface. (ii) Stern layer: counterions (charged opposite to the surface charge), attracted to the particle surface and closely attached to it by the electrostatic force. And (iii) Diffuse layer: a film of the dispersion medium (solvent) adjacent to the particle. Diffuse layer contains free ions with a higher concentration of the counterions. Between these two layers lies a "slipping plane" and the potential of this plane is commonly called zeta potential (ζ).

Interpretation of electrokinetic measurements

As briefly mentioned above, electrokinetic phenomena are always related to a liquid/solid interactions. The build-up of the electrochemical double layer is the result of the properties of the two phases interacting with each other. Therefore, the ζ potential can be considered as a probe to get information about the real double layers and can be successfully used to characterize the surface properties of the solid in contact with a liquid phase. To get quantitative information of the kind of interactions between solid and liquid phase, it is possible to vary either the pH or the ionic strength.[27] The determined zeta-potential is the response on changes in the electric double layer's build-up. Therefore, for a correct interpretation of electrokinetic measurements it is necessary to measure ζ as function of either pH or ionic strength. Consequently, from this ζ(pH) value it is possible to estimate the areal charge density at the slipping plane, which is not very far from the density on the solid surface.[27,29]

Dissociation of acidic functional groups

The origin of charges at interfaces may be attributed to the dissociation of surface groups (in our case carboxyl groups). If N_v is the total number of acidic groups capable of dissociating

and present at the solid-streaming solution interface, the dissociation equilibrium may be characterized by the dissociation constant K_a as follows [28]

$$-\mathrm{COOH} \leftrightharpoons \mathrm{COO^-} + \mathrm{H^+}$$
$$K_a = \frac{[-\mathrm{COO^-}][\mathrm{H^+}]}{[-\mathrm{COOH}]} \tag{10}$$

where N_v is equal to $[-\mathrm{COO^-}] + [-\mathrm{COOH}]$ and the degree of dissociation (α) of functional groups is equal to $[-\mathrm{COO^-}]/N_v$. Moreover, the data of the zeta-potential (ζ) as function of pH can be used to estimate the degree of dissociation (α) of functional groups on the surface based on the GSCG model as follows[30]

$$\alpha = \frac{1}{1 + \exp\left(-2.3\ (\mathrm{pH}\ - pK_a) - \frac{\mathrm{F}}{\mathrm{R}}\frac{\zeta}{T}\right)} \tag{11}$$

with F the Faraday constant, R the gas constant, T the temperature, and $pK_a = f(\mathrm{pH})$ being calculated as follows

$$pK_a = \mathrm{pH} + 0.434\left\{\frac{F\zeta}{RT} + \ln\left[\frac{\sinh\left(-\frac{F\zeta_{plateau}}{2RT}\right)}{\sinh\left(-\frac{F\zeta}{2RT}\right)} - 1\right]\right\} \tag{12}$$

where $\zeta_{plateau}$ is the zeta-potential value when all dissociable groups are dissociated (α ~ 1). Furthermore, at the charged interface, the overall electro-neutrality condition must be satisfied. This means that the total charge in a volume element of the solution of unit cross section of the diffuse layer (i.e. from the slipping plane to x = ∞) must equal the charge of opposite nature that the unit area of the interface contains.[27,29] The relationship between the surface charge density and the potential at the surface in an electrolyte solution is given by the Grahame equation.[30,31] The areal density of total groups capable of dissociating per unit area (N_a) is given by

$$N_a = \frac{1}{e_0}\sqrt{8\varepsilon_r\varepsilon_0 c^{\infty} RT}\sinh\left[-\frac{F\zeta_{plateau}}{2RT}\right] \tag{13}$$

where, e_0 is the charge of an electron (1.6 $\times 10^{-19}$ C), ε_r is the dielectric constant of the measuring fluid (assume to be 80), ε_0 is the vacuum permittivity (8.85$\times 10^{-12}$ $C^2J^{-1}m^{-1}$), $\zeta_{plateau}$ is in Volts, and c^{∞} is the ions concentration of the streaming solution (in mol/m^3). Hence, the units of N_a is ions per unit area (i.e. $n\mathrm{COO}^-/\mathrm{m}^2$). For the determination of N_a, electrokinetic experiments in dependence on pH are required. Therefore, the areal density of negative charges existing at the solid/liquid interface at a specific pH (σ_a) in $n\mathrm{COO}^-/\mathrm{m}^2$ is calculated as

$$\sigma_a = \alpha N_a \tag{14}$$

2.3. Experimental

2.3.1. Chemicals

All chemicals were used as received from the supplier. For the macroscopic hydrogels, 2-(methacryloyloxy)ethyltrimethylammonium chloride 80 wt. % in H_2O (MAETAC), acrylamide for electrophoresis, ≥99% (AAm), N,N'-methylenebisacrylamide (MBA), potassium persulfate (KPS) and tetramethylethylenediamine (TEMED) were purchased from Sigma-Aldrich, France.

For the synthesis of hydrogel thin films, allylamine, 1-ethyl-3-(3-dimethylaminopropyl)carbodiimide hydrochloride (EDC), N-hydroxysuccinimide (NHS), 1,4-dithioerythritol, toluene dried (max. 0.005% H_2O), formic acid and methanol were all purchased from Sigma-Aldrich, France. Additionally, poly(acrylic acid) (PAA with M_W ~ 50 kg/mol, 25 wt% in water was obtained from Polysciences. (3-mercaptopropyl)trimethoxysilane was obtained from Alfa chemistry. Silicon wafers were purchased from ACM, France.

2.3.2. Hydrogel synthesis

A series of positively charged hydrogels was prepared by free radical copolymerization in water using a cationic monomer (MAETAC), a neutral comonomer (AAm) and a tetrafunctional crosslinker (MBA). Within this series, the total monomer concentration was

fixed at 20 wt% (80 wt% in water), using two different MAETAC/AAm molar ratios (10/90 = I10 and 20/80 = I20) and 3 different molar percentages of crosslinker (R=1, 2 and 4 mol% with respect to total monomers).

After dissolution at room temperature of the comonomers in Milli-Q water (pH 5.5), the KPS initiator was added (1 mol% relative to the total monomer) and the solution was deoxygenated under N_2 flow during 30 min. Then, as soon as the reducing agent TEMED was added (1 mol% as KPS), the solution was transferred to a PDMS mold of 0.1 cm x 2 cm x 4 cm size. The redox initiation rapidly took place and the polymerization was left to proceed overnight under nitrogen atmosphere. The mold was then opened, and the 1 mm thick gels were immersed and stored in 1 L of Milli-Q water until final use.

The poly(MAETAC-*co*-AAm) hydrogels prepared in this way will be called Ix-Ry, with x = 10 or 20 the molar percentage of ionic comonomer and y = 1, 2 or 4 mol% the molar percentage of crosslinker with respect to the monomers.

For equilibrium swelling studies, hydrogels were initially weighted in their preparation state (m_p) before immersion into a large volume of Milli-Q water. After 3 days of equilibrium with water renewal, the swollen samples were weighted again (m_s) and then dried overnight in an oven (at 60 °C) in order to get their final dry weight (m_d). These measurements allow calculating the mass swelling ratio at equilibrium ($\Lambda_e = m_s/m_d$), as well as to estimate the volume swelling ratio at preparation state according to the following equation

$$Q_0 = 1 + \frac{v_w}{v_p}\left(\frac{m_p}{m_d} - 1\right) \qquad (15)$$

where v_w=1.00 $cm^3.g^{-1}$ is the specific volume of water and v_p is the specific volume of the comonomer. v_p=0.76 $cm^3.g^{-1}$ for I10 and v_p=0.774 $cm^3.g^{-1}$ for I20.

2.3.3. Synthesis of negatively charged hydrogel thin films

Surface-attached thin hydrogel films were prepared by simultaneously crosslinking and grafting pre-functionalized poly(acrylic acid) (PAA) onto thiol-modified silicon wafers. The crosslinking and grafting took place through a thiol−ene click reaction following a previously published procedure, which will be described in the following paragraphs.[32,33]

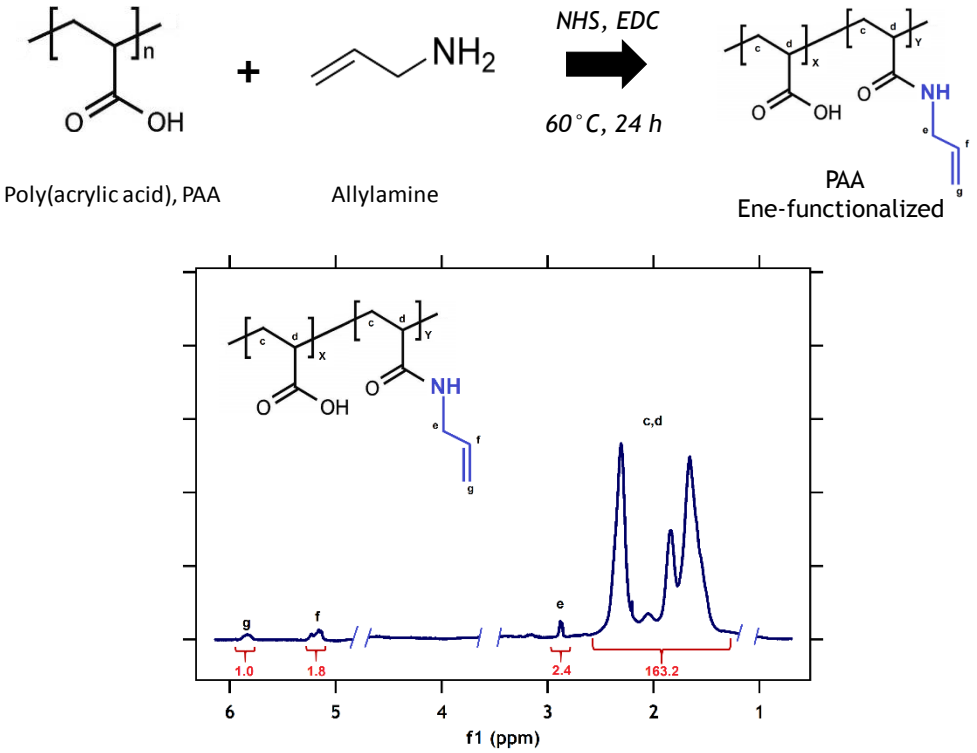

Figure 2-4. (Top) Ene-functionalization reaction of acrylic acid with allylamine by peptide bond with EDC and NHS. (Down) ^{1}H NMR spectrum of ene-functionalized PAA. Regions between 1.1 - 1.2 ppm (residual ethanol CH_2), 3.55-.3.65 ppm (residual ethanol CH_3) and 4.55-4.85 (D_2O) omitted in the interest of clarity.

Functionalization of poly(acrylic acid) with double bonds

Poly(acrylic acid) (PAA) chains were randomly functionalized with ene-groups at their carboxylic acid sites. A peptide reaction was used to graft allylamine onto polymer chains in

the presence of EDC and NHS. (**Figure 2-4, Up**).[34] Briefly, a 20 wt% solution of PAA in Milli-Q water was mixed with EDC and NHS at a pH of 4.5 for 2 h. Allylamine was then added and the pH was adjusted to 10 before the reaction was allowed to proceed for 16 h. Finally, the polymer was recovered through freeze-drying after 2 days of dialysis in 0.1 M NaCl solution and 3 days of dialysis in Milli-Q water. The ene-functionalization of PAA was confirmed by Proton Nuclear Magnetic Resonance (^{1}H NMR) spectroscopy performed in deuterated water with a 400 MHz Bruker spectrometer. (**Figure 2-4, Down**).

Thiol-modification of Substrates

Silanization of the silicon wafers with thiol functional alkoxysilane was carried out as follows. After irradiation by UV-ozone for 15 min, the wafers were transferred into a sealed reactor under N_2 atmosphere. A solution of dry toluene with 3 vol % of 3-mercaptopropyltrimethoxysilane was introduced into the reactor using a cannula. The wafers were kept immersed in the solution for 3 h inside the reactor always in N_2 (**Figure 2-5**). The samples were then rinsed and sonicated in toluene for 1 min and finally dried with nitrogen flow.

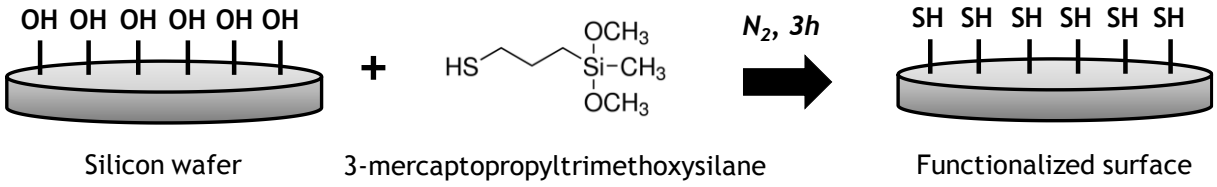

Figure 2-5. Schematic of functionalization of silicon surfaces.

Synthesis of PAA Hydrogel Thin Films

A thin layer of PAA functionalized with ene-groups was deposited on the thiol-modified wafers by spin-coating from a 2 wt% solution in methanol and formic acid (70% methanol and

30% formic acid) containing also dithioerythritol. The ratio of dithioerythritol to ene-functionalized polymer units was 15, corresponding to a molar ratio of 30 between –SH groups of the bifunctional dithioerythritol and double bonds (**Figure 2-6**). The thickness of the resultant films depends on various factors but mainly on the concentration of the polymer for spin-coating and on its molecular weight.[32] The conditions of spin-coating were fixed with a final angular velocity of 3000 rpm and a spinning time of 15 s. After spin coating, the dry films were annealed at 120°C for 24 h under vacuum to activate the thiol−ene reaction. Finally, the wafers were cleaned with water and then cleaved into pieces of 5 mm x 5 mm. Ellipsometry measurements were used to corroborate that the thiol-ene reaction effectively took place and that PAA thin films were grafted to the silicon wafer.

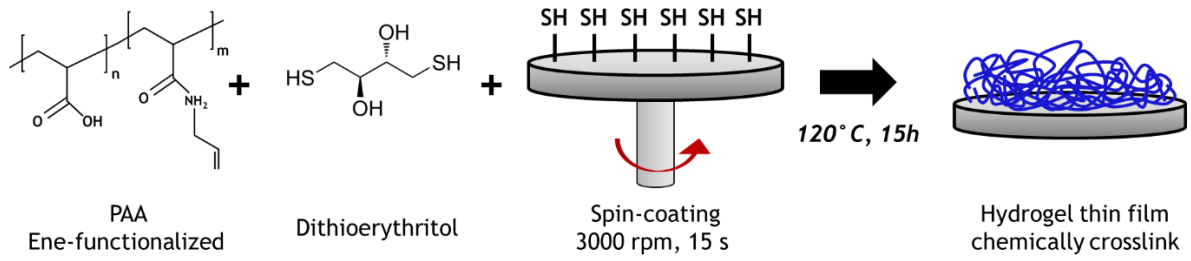

Figure 2-6. Schematic of the methodology used to prepare hydrogel thin films through thiol-ene click reaction.

2.3.4. Characterization of the elastic properties of the bulk hydrogels

Cylindrical samples (8 mm diameter, 12 mm height) were prepared in a silicone mold and tested 24 h after the polymerization, to measure the shear modulus in the preparation state (G_0), and at swelling equilibrium (G_e). Compression tests were carried out using a custom-built setup with a uniaxial testing machine (Instron, model 3343) and a 10 N load cell. Each sample was preloaded with a compression force of 50 mN followed by a compressive loading at a constant displacement rate of 50 µm/s until a maximum load of 5 N was achieved. Before the test, all

specimens were coated with paraffin oil to avoid friction forces between hydrogels and the testing plates during the uniaxial compression. The compressive modulus (E) was calculated as the slope of the linear regression line for data between 5% and 20% of strain. Assuming that hydrogels are incompressible for these relatively high rates compare to their geometry (Poisson's ratio = 0.5), the shear modulus (G) was estimated as

$$G = \frac{E}{3} \tag{16}$$

The molecular weight between crosslinks (M_C) of poly(MAETAC-*co*-AAm) hydrogels can be determined from the shear modulus of the samples in their preparation state (G_0). Here we use the phantom network model which assume that the junction points can freely move and fluctuate over time on a range which is not affected by the macroscopic deformation.[23] According to this model M_C can be determined from the following expression:

$$G_0 = \left(1 - \frac{2}{f}\right)\frac{RT}{\upsilon_p M_C}\frac{1}{Q_0} \tag{17}$$

where R is the gas constant, T the temperature, f is the functionality of the crosslinker ($f = 4$ for MBA), and Q_0 is the initial volume swelling ratio. The average number of monomers in the chain between crosslinks (N_c) is calculated as M_C divided by the average molar mass per repeat unit (M_0), which depends on the cationic monomer molar percentage (I) as follows

$$N_c = \frac{100 * M_c}{I * M_{MAETAC} + (100 - I) * M_{AAm}} \tag{18}$$

where M_{MAETAC} and M_{AAm} are the molar masses of MAETAC and AAm respectively.

2.3.5. Characterization of the hydrogel thin films

The thickness of the PAA films in air (h_a) and underwater (h_w) were measured using a spectroscopic ellipsometer (UVISEL, Horiba) with a wavelength range from 260 nm to 850 nm (in air) and from 320 to 850 nm (underwater). The refractive index (n_i) of the silicon wafer is 3.875. A model with two layers was used for measurements in air. The first layer comprises

silica and silane (n_i = 1.46) the thickness of which was determined before grafting the hydrogel film (between 2 and 3 nm). The second layer was the PAA hydrogel film (n_i = 1.50). Underwater measurements were performed with a controlled temperature liquid cell equipped with thin glass walls (fixed perpendicularly to the light path with the angle of incidence at 60°). The polymer hydrogel film was modelled as a single layer (h_w) with a constant refractive index between that of water (n_i = 1.33) and of the polymer. The swelling ratio of hydrogel films (Λ_f) was calculated as h_w/h_a, assuming that the amount of polymer is the same when immersed in water, since it is chemically grafted to the substrate.[33] The thickness was measured for samples fully immersed in Milli-Q water at pH of 2, 4, 5.5 and 8. Two replicas were performed for each test environment.

2.3.6. Streaming Potential Measurements on Charged Surfaces

Electrokinetic measurements are a versatile tool for investigating charge formation at interfaces between polymers and aqueous solutions.[35,36] By using the GSGC model described before, it is possible to relate the measured electrokinetic quantity (i.e. streaming potential or streaming current) with the degree of dissociation and the interfacial charge density of the PAA thin films. In this project, the surface potentials of the PAA hydrogel thin films were determined by streaming potential measurements using an Electrokinetic Analyzer (EKA) (Anton Paar GmbH, Austria).

For the streaming potential measurements, two pieces of silicon wafers (10 mm x 20 mm each) grafted with PAA (dry thickness: ~30 nm) were attached to the rectangular cell with adhesive tape so that they were facing each other and formed a streaming channel where the measuring fluid flows through. During the experiment, the pressure inside the fluid channel (P_0) was continuously varied and the streaming potential (ΔU) at zero net current conditions

was measured for each value of ΔP (**Figure 2-7**). The zeta potential ζ was then calculated using the expression developed by Smoluchowski[37]

$$\zeta = \frac{\Delta U}{\Delta P}\frac{\eta}{\varepsilon_r \varepsilon_0} k_c \qquad (19)$$

where ε_0 is the vacuum permittivity constant, ε_r, η and k_c are the dielectric constant, viscosity and the specific conductivity of the measuring fluid respectively. These last 3 variables are measured independently for each specific pH. The dielectric constant ε_r of the medium is highly dependent on the ionic strength and, therefore, 1 mM is used to be close to pure water. The pH-dependence of the zeta potential (ζ) for PAA thins films was determined in a KCl solution (1 mM) for a pH range from 2.5 to 10.5. Measurements started at pH ~ 6 followed by stepwise addition of HCl or KOH (0.1 M) to sweep between more acidic and more basic pH values, respectively. One pair of PAA films was used for the acidic environment and a different pair was used for the basic environment. Four measurements were conducted at each specific pH.

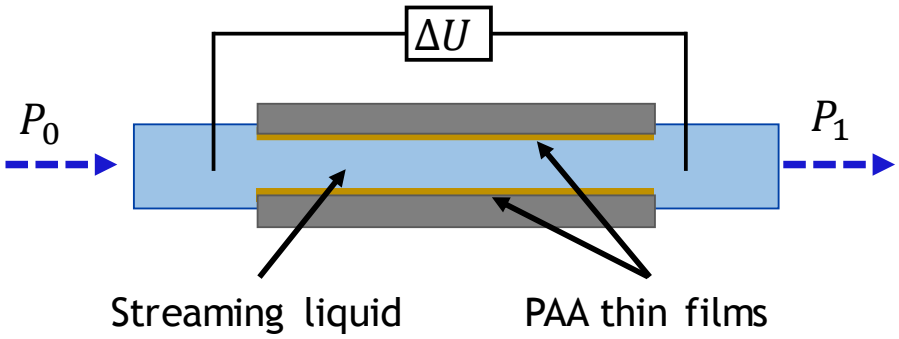

Figure 2-7. Schematic of the experimental set-up for the electrokinetic Analyzer (EKA) used in the streaming potential measurements. For these measurements a plate cell for small samples (10 x 20 mm) of the instrument equipped with Ag/AgCl-electrodes was used to measure the change in potential (ΔU). The two PAA hydrogel thin films forming the streaming channel are highlighted in yellow lines. The streaming liquid with a known ionic strength is pumped through this channel and the change in pressure is measured ($\Delta P = P_1 - P_0$).

2.3.7. Underwater Tack Test

The underwater tack test was conducted on an experimental setup designed by Sudre et al.[20] The effect of several parameters of the test have been investigated for hydrogels at equilibrium[20] and for non-swollen hydrogels.[21] In this chapter, all hydrogels were tested after reaching swelling equilibrium in Milli-Q water.

Briefly, the adhesion test consisted in forming a parallel contact and detachment between a macroscopic positively charged hydrogel (thickness ~ mm) and a negatively charged thin hydrogel film (thickness ~ nm) while both were fully immersed in an aqueous environment. The 5 mm x 5 mm wafer coated with the surface-grafted PAA hydrogel thin film was glued with a polyvinyl acetate adhesive (ref. L0196, 3M®, France) to a stainless-steel probe, which was fixed to a 10 N load cell and connected to a universal tensile machine (model 5333, Instron®, France). A sample of poly(MAETAC-*co*-AAm) hydrogel (20 mm x 20 mm x 1 mm) was glued to a glass microscope slide with a cyanoacrylate adhesive (Loctite® 495, France). The test requires a parallel contact between both surfaces to be aligned during the test. The alignment is performed in air and is considered as successful when the time to bring both surfaces into contact is less than 5 seconds for an approaching speed of 10 µm/s until a pressure of 3 kPa.[21] Additionally, the thin film is protected with a stretched layer of Parafilm® during the alignment in air. If the thin film is not protected, it is likely that the macroscopic hydrogel will break and damage the thin film surface.

After this alignment, the contact was made underwater at an approaching rate of 10 µm/s with a contact area determined by the surface of the silicon wafer functionalized by the PAA thin film. A preload of 3 kPa was applied for a given constant contact time that was varied from 1 s to 1200 s. Finally, the probe was detached at a constant debonding rate (V_{deb}) while recording the probe displacement and the force. From this experiment, the work of adhesion W_a can be calculated as follows:

$$W_a = T_0 \int_0^{\varepsilon_{max}} \sigma d\varepsilon \quad (20)$$

where ε is the nominal strain and is obtained by normalizing the displacement by the initial thickness of the thick hydrogel (T_0). σ is the average stress and is obtained by dividing the force by the contact area. Three replicates were conducted for each experiment.

Tack test recommendation

Experimental conditions are very important for this type of test and several variables drastically affect the reproducibility of W_a. The effect of some of these variables, such as contact time, contact pressure and debonding rate on the work of adhesion have been investigated by Sudre[20] and Macron[21]. However, more variables need to be taken into account to improve the reproducibility of the results. Therefore, when using this setup to measure the adhesion by electrostatic interactions between soft hydrogels and thin films, it is recommended the following:

a) The thin film needs to be well protected during the alignment in air. If the interactions are stronger than a certain level ($W_a > \approx 1\ J/m^2$), it is likely that the hydrogel will break and damage the thin film surface. One possible solution is to cover the thin film with a stretched layer of Parafilm® while performing the surface alignment in air (**Figure 2-8**).

Figure 2-8. (Left-Middel) Examples of surfaces of PAA with broken pieces of macroscopic hydrogel after an alignment process in air without the Parafilm® protection. (Right) Hydrogel thin film glued to a stainless steel cylindrical probe and covered with a stretched layer of Parafilm®.

b) Spin-coating in larger areas of thiol-modified silicon wafers makes thin film more homogeneous as seen in **Figure 2-9**.

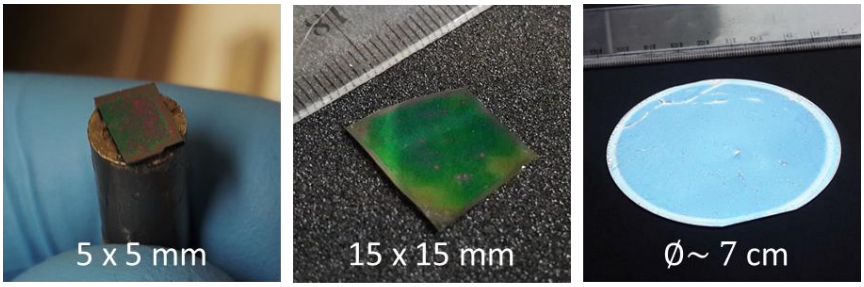

Figure 2-9. Spin coating in different size of silicon wafer with the same PAA (2wt%) solution at 3000rpm for 15s.

c) The thick hydrogel needs to be firmly attached to bottom of the setup. There are two options with the same results in W_a; gluing the thick hydrogel to a glass panel with a cyanoacrylate adhesive or clamping it between a glass slide and a Teflon-coated aluminium plate. The first option is faster but only reproducible for equilibrated hydrogels and for short tests underwater (in order to avoid diffusion of the cyanoacrylate-based adhesive into the hydrogel). In contrast, the second could be used for longer tests but requires bigger samples (longer than 4cm) and alignment will be more difficult (**Figure 2-10. Left**).

d) The surface area of the hydrogel thin film should be smaller than the probe area in order to avoid hydrodynamic and bending effects when breaking the interactions between the hydrogel and the thin film (**Figure 2-10. Right**).

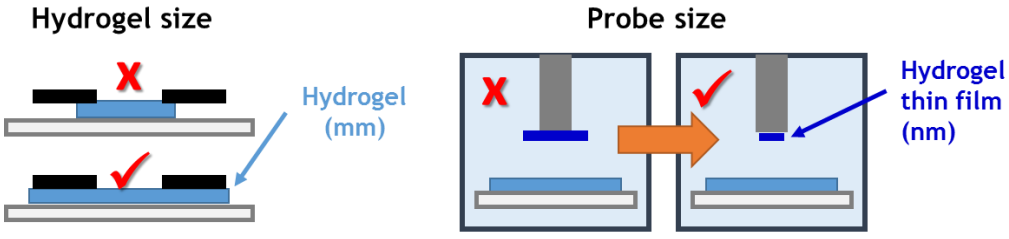

Figure 2-10. Recommendations for the hydrogel size (Left) and probe size (Right) during an underwater probe-tack test.

2.4. Results

2.4.1. Elastic moduli of the Bulk Hydrogels

A series of poly(MAETAC-co-AAm) hydrogels were synthesized to study the impact of the network architecture on the underwater adhesion properties. Swelling studies and mechanical characterization were conducted on each prepared hydrogel (**Table 2-1**). Increasing the molar ratio of crosslinker from 1 to 4 mol% caused the equilibrium degree of swelling (Λ_e) to decrease by nearly 30% and 50% for I10 and for I20, respectively.

Hydrogel	Q_0	C_e (wt%)	Λ_e	E_0 (kPa)	E_e (kPa)	M_C (kg/mol)	N_c
I10-R1	6.3	4.9	21.1	123 ± 18	99.6 ± 20.1	6.35	75
I10-R2	6.3	10.2	9.8	232 ± 8.4	207 ± 18.9	3.37	40
I10-R4	6.3	15.7	6.4	433 ± 6.9	456 ± 74.4	1.80	21
I20-R1	6.2	3.9	26.8	98.4 ± 3.9	70.8 ± 6.3	7.93	81
I20-R2	6.2	5.7	17.6	256 ± 6.0	199 ± 14.7	3.05	31
I20-R4	6.2	7.7	13	372 ± 16.8	332 ± 88.2	2.10	21

Table 2-1. Composition and characteristics of cationic hydrogels. Initial volume swelling (Q_0), total polymer concentration at swelling equilibrium (C_e), mass degree of swelling at equilibrium (Λ_e), Young's modulus in the preparation conditions (E_0) and at swelling equilibrium (E_e). Both moduli are presented as average ± standard deviation. Average molecular weight between crosslinks (M_C) obtained from the shear modulus in preparation conditions and average number of monomers between crosslinks (N_c).

The mechanical characterization of poly(MAETAC-*co*-AAm) hydrogels was carried out in compression (**Figure 2-11.a**). Representative curves, for I10-R2 and I10-R4 hydrogels at equilibrium show that the linearity of loading and unloading follows the same trajectory with a strain offset of 0.5% ± 0.05% at zero stress. This suggests that there is not much energy dissipation and that these hydrogels are very elastic at a strain lower than 20%. This property

will benefit the maximization of the sensitivity to interfacial interactions relative to bulk dissipative mechanisms. Moreover, E_0 and E_e increased linearly from approximately 100 kPa to 400 kPa for both I10 and I20 when the molar ratio of crosslinker was increased from 1 mol% to 4 mol% (**Figure 2-11.b**). Additionally, the average molecular weight (M_C) and number of monomers between crosslinks (N_c) decreased by about 50% for both I10 and I20 by doubling the crosslinking molar concentration, as expected from hydrogel network models, where M_C is inversely proportional to the degree of crosslinking of the hydrogel when elastic properties are dominated by chemical crosslinks rather than entanglements.[38]

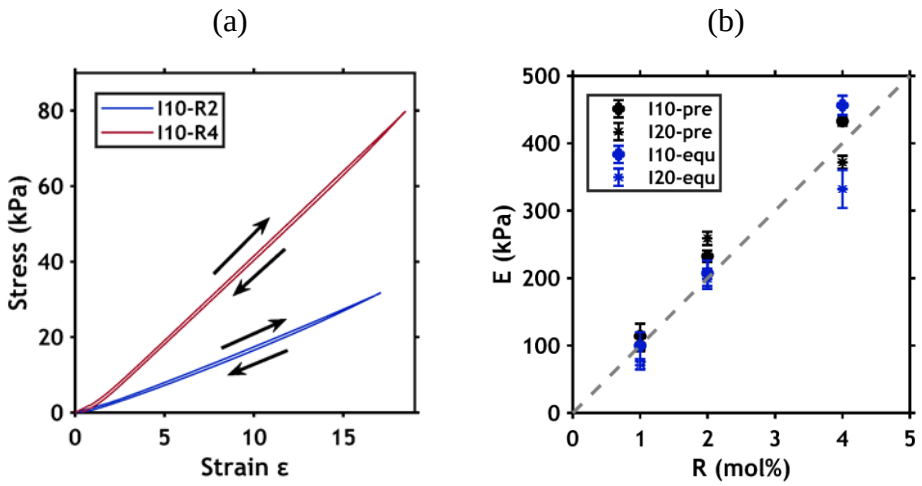

Figure 2-11. (a) Example curves of compression stress vs. strain (in %) for I10-R2 and I10-R4 hydrogels. Black arrows show loading direction. (b) I10 and I20 poly(MAETAC-*co*-AAm) hydrogel elastic modulus in the preparation state E_0 (black symbols) and at equilibrium state E_e (blue symbols) as a function of R.

2.4.2. Thickness and water content of negatively charged hydrogel thin films

We used a technique previously developed for coating polymer films with dry thicknesses ranging roughly from 20 to 600 nm.[32,33,39] These polymer films are insoluble in water as the PAA chains are covalently crosslinked and chemically grafted to the silica wafers. Ellipsometry

measurements show that their dry thickness remains constant and is therefore not damaged by underwater adhesion tests. A solution of PAA at 2 wt% leads to samples of thin films with a dry thickness of 144 nm. Only PAA solutions at this concentration were used for all the experiments in this chapter. These PAA films swell up to 200 nm at pH 2, corresponding to a swelling ratio of 1.4. By increasing the pH, the progressive ionization of COOH groups and the increasing concentration of counterions are responsible for an additional osmotic pressure within the thin gel that leads to higher swelling of the film from 1.4 at pH 2 and up to 1.8 at pH 8 (**Table 2-2**).

	$\boldsymbol{h_w}$ (nm)	Λ_e
pH 2.0	200 ± 1.4	1.39
pH 4.0	238 ± 3.8	1.65
pH 5.5	252 ± 1.2	1.75
pH 8.0	257 ± 8.5	1.78

Table 2-2. Ellipsometry measurements of the thickness of PAA films underwater (h_w) at different pH. Swelling ratio of PAA films (Λ_e). n = 2 replicas were conducted for each sample.

(a) (b)

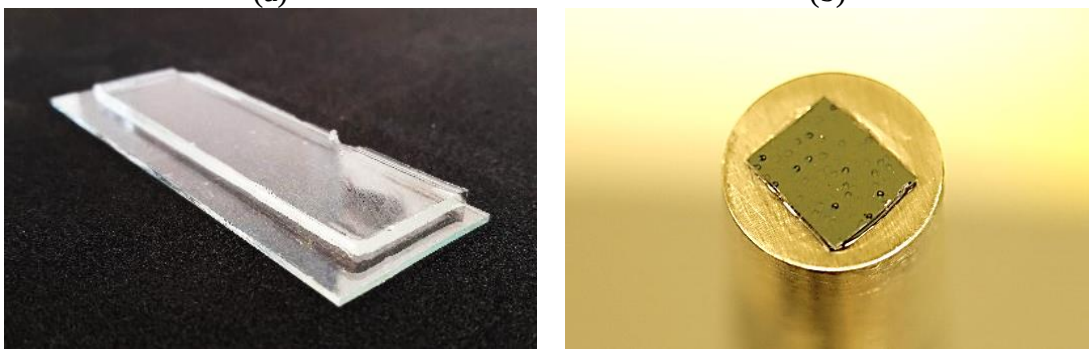

Figure 2-12. (a) Photograph of the poly(MAETAC-*co*-AAm) hydrogel I10-R2 after polymerization. Average thickness 1 mm. (b) Photograph of a PAA hydrogel thin film glued to flat cylindrical probe. Average contact area 35 mm^2.

2.4.3. Adhesive properties

Effect of experimental conditions: Contact time and debonding rate

Using the same adhesion measurement technique and geometry, previous work has shown that underwater adhesion based on H-bonds interactions depends markedly on contact time as it is necessary to maintain a contact time long enough (> 2 min) for the interactions to form at the interface and to reach values of W_a of around 100 mJ/m^2.[20] However, we observe a different behavior for electrostatic interactions. At two different debonding rates (0.1 and 0.01 mm/s), the W_a increased only by a factor of two between 1 second and 1200 seconds (**Figure 2-13.a, Figure 2-13.c and Figure 2-13.d**).

This suggests that the electrostatic interactions at the interface are formed as soon as both surfaces come into contact and the surface density of interactions remains relatively constant thereafter. A contact time of 1 second is therefore enough in this case to achieve a high adhesion energy of ~600 mJ/m^2 at V_{deb} = 0.1 mm/s and ~150 mJ/m^2 at V_{deb} = 0.01 mm/s. These values are two orders of magnitude superior to that obtained with H-bonds interactions for the same contact time and same V_{deb}.[20]

In addition to the contact time, the debonding rate may play an important role on W_a. In classical soft adhesive systems, the influence of the velocity is linked to the bulk dissipative effects that are essential for the usual viscoelastic hydrophobic adhesives,[40] while at lower velocities only the thermodynamic work of adhesion is measured. However, in the framework of our study, the hydrogels are highly elastic materials, as shown by the compression tests, and the bulk dissipative effects are therefore negligible. Nevertheless, **Figure 2-13.b.**, **Figure 2-13.e.** and **Figure 2-13.f.** show for two different contact times that W_a increases by 2 orders of magnitude (from ~10 mJ/m^2 to ~1000 mJ/m^2) as the debonding rate increases by four orders of magnitude (from 0.1 µm/s to 1 mm/s).

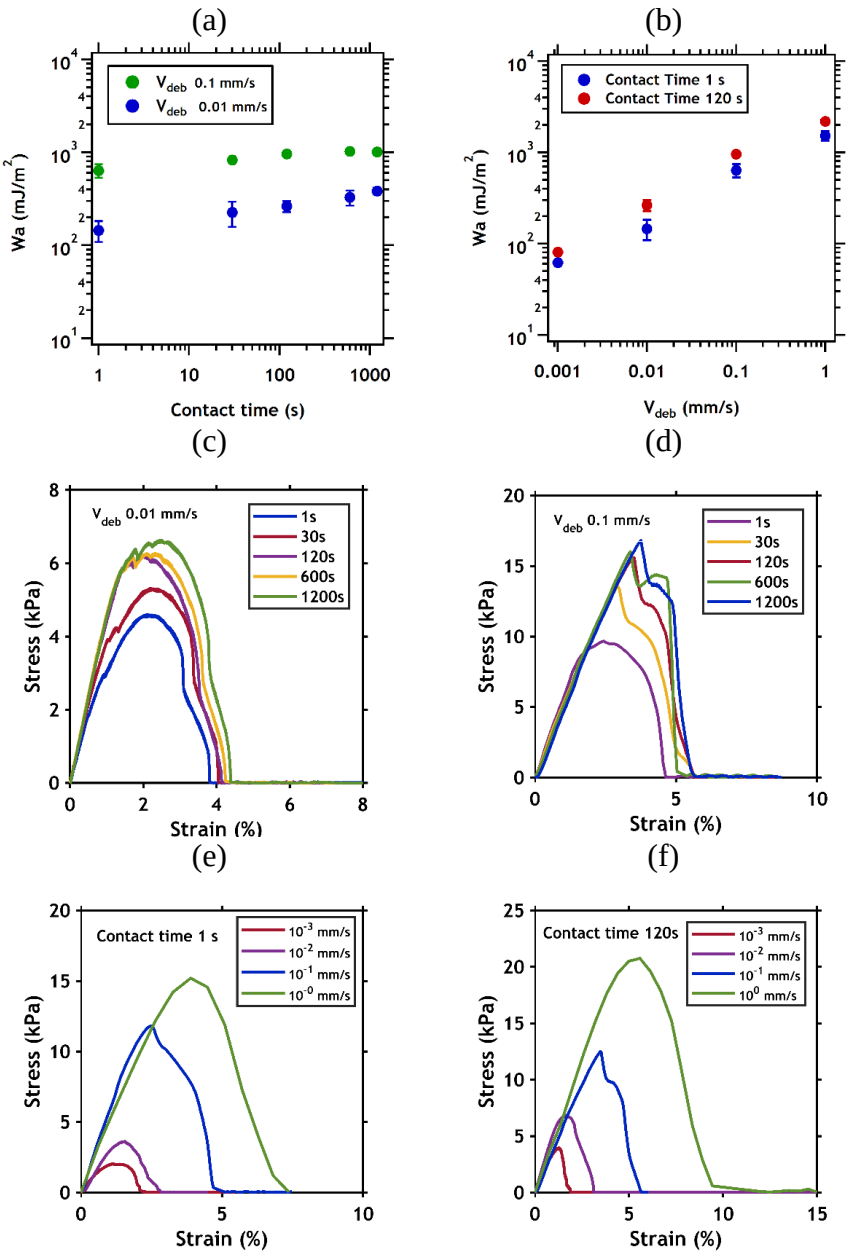

Figure 2-13. Variation of the adhesion energy measured in Milli-Q water (pH 5.5) between poly(MAETAC-*co*-AAm) hydrogel (I10-R2) and PAA hydrogel thin film (dry thickness of 150 nm) as a function of contact time (a) and V_{deb} (b). The impact of these two parameters on the adhesion energy (W_a) are detailed with stress-strain curves which have been plotted as a function of contact time at a given debonding rate, of 0.01 mm/s (c), and 0.1 mm/s (d) or as a function of debonding rate at a fixed contact time of 1 second (e) or 120 seconds (f).

Materials Effects: Effect of the Crosslinking Density R of the Hydrogel on W_a

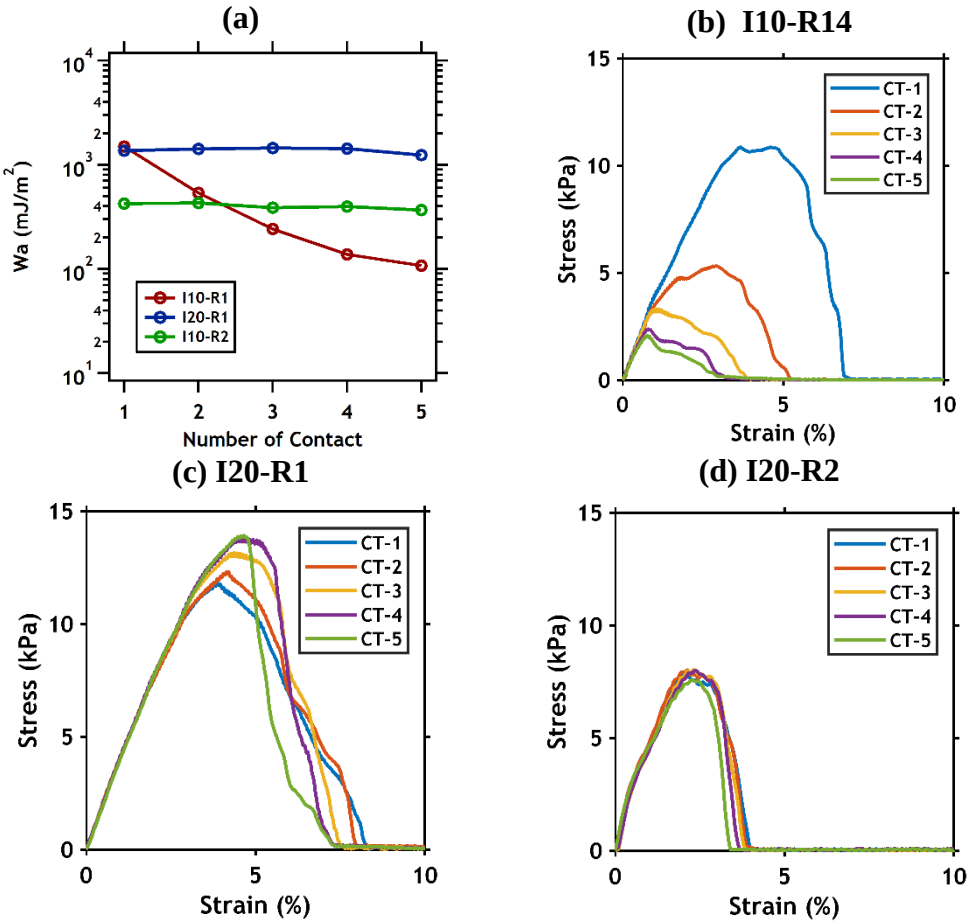

Figure 2-14. (a) Adhesion energy results of the poly(MAETAC-*co*-AAm) hydrogels and the PAA hydrogel thin film (with dry thickness of 150 nm) as function of number of contacts. (b), Examples of the stress-strain tack debonding curves for one replica of I10-R1 hydrogel with a decrease in energy, due to a cohesive failure during the test. (c), (d) Examples of the stress-strain tack debonding curves for I20-R1 and I20-R2 without any significant decrease in energy due to only adhesive failure. For (b)-(d) CT represents the number of contact.

Probe tack tests are used to measure the energy required to separate the negatively charged surface from the positively charged hydrogel without breaking any covalent bonds within either of the hydrogels. For this reason, W_a between each hydrogel and thin film was first measured as a function of different repetitions in the same spot (**Figure 2-14.a**). When W_a remained

constant for consecutive contacts in the same spot (**Figure 2-14.b** and **Figure 2-14.c**), the value of the first contact was used to compare the effect on W_a of different variables of the network architecture such as the crosslinks density and the ratio of cationic/neutral monomers in the hydrogel. In contrast, if W_a decreased with consecutive contacts (**Figure 2-14.d**), this strongly suggested that covalent bonds were broken in one of the hydrogels and the result was then not used for the study.

The impact of the hydrogel bulk mechanical properties on W_a was studied by varying the degree of crosslinking R and the molar ionic content I in the hydrogel while measuring its adhesive properties against the same PAA hydrogel thin film. The hydrogels were kept in Milli-Q water until they reached swelling equilibrium. Afterwards adhesion tests were conducted in the same environment with a contact time of 1 second and a debonding rate of 0.1 mm/s. Three replicates were done for each experiment where both the hydrogel sample and the PAA thin film were used only once.

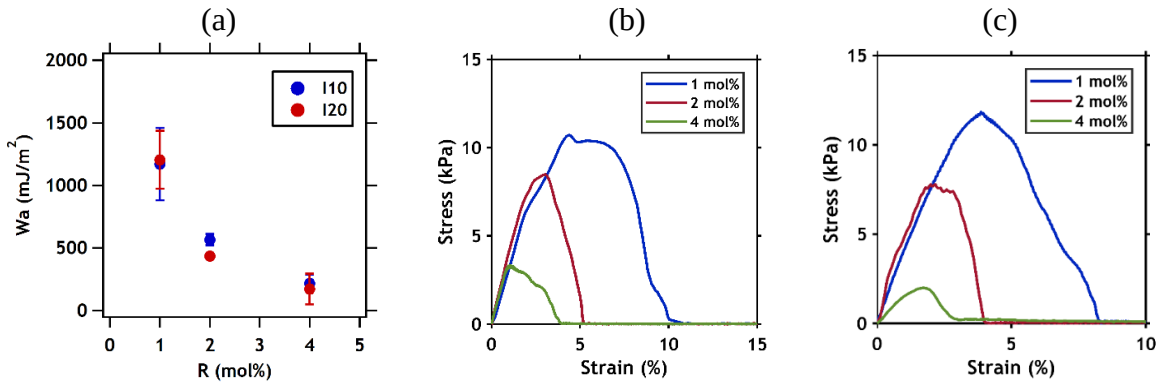

Figure 2-15. (a) Adhesion energy as a function of R for I10 and I20 hydrogels. Representative stress-strain tack debonding curves of the first contact for I10 (b) and I20 (c) hydrogels with different values of R at a contact time of 1 s and V_{deb} = 0.1 mm/s.

The adhesion energy measured as a function of R for I10 and I20 (**Figure 2-15.a**) shows that W_a decreased by a factor of 10 regardless of the amount of cationic monomer units for

increasing degree of crosslinking between 1 mol% (~1200 mJ/m^2) and 4 mol% (~ 200 mJ/m^2). The stress-strain curves (**Figure 2-15.b** and **Figure 2-15.c**) show that as R increases, the maximum debonding stress and critical strain decrease significantly. Consequently, it is clear that changing the hydrogel network architecture, such as changing the length of the chains between crosslinks, could lead to a change in the adhesion energy by almost one order of magnitude. Additionally, W_a remains nearly constant as the cationic molar concentration increases from 10% to 20%.

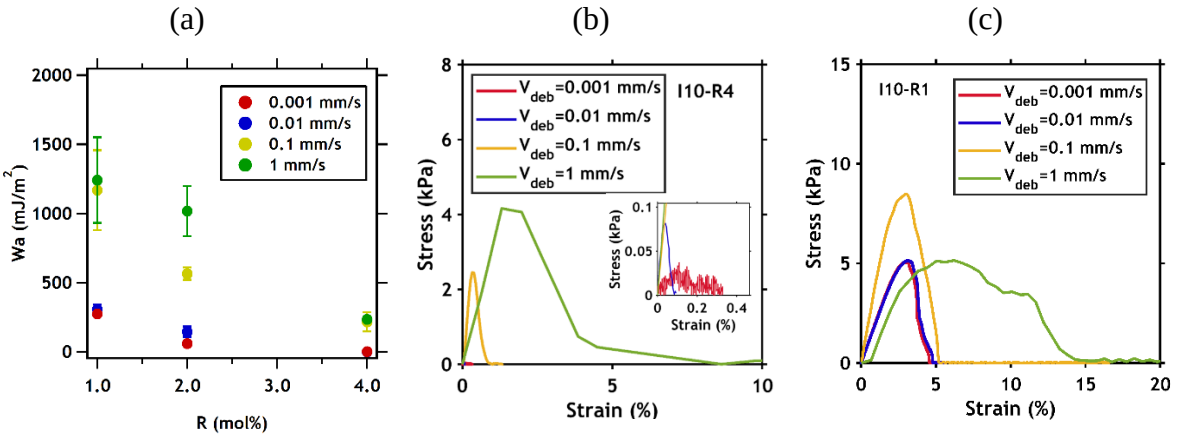

Figure 2-16. (a) Adhesion energy as a function of crosslinker concentration for I10 at different debonding rates. (b) Stress strain curves for I10-R4 at different debonding rates. A very low debonding rate (0.01 and 0.001 mm/s) almost no adhesion is measured. (c) Stress strain curve for I10-R1 at different debonding rates. Cohesive failure in the macroscopic hydrogel I10-R1 was presented at the highest debonding rate of 1 mm/s.

The effect of R on W_a was also measured at different debonding rates (**Figure 2-16.a**) and at a constant contact time of 1 s. W_a always decreased with the increasing hydrogel crosslinks density regardless of the debonding rate of the test (0.001 mm/s to 1 mm/s). Moreover, this study probed the boundaries of sensitivity of our experimental methodology. At high degree of crosslinks (R4) and low speeds (0.01 and 0.001 mm/s), the load cell just measured noise (**Figure**

2-16.b). On the contrary, a maximum adhesion energy is observed at low degree of crosslinks (R1) and high debonding rate (1 mm/s), suggesting that the test mainly measures the toughness of the gel and not W_a, since the failure mode is cohesive (within the macroscopic cationic hydrogel) and not adhesive (**Figure 2-16.c**).

Effect of the environment: pH effect on W_a

The molecular electrostatic interactions between the hydrogel and the thin film were tuned by changing the pH of the tack test medium, since the charge density of the PAA film depends on this variable while the poly(MAETAC-*co*-AAm) macroscopic hydrogel is permanently charged regardless of the pH. Therefore, the charge density at the surface of the PAA thin film will be maximum around pH 9, when all carboxylic groups are ionized, while in acidic conditions (pH < 3) there will be no charge at the surface of the film, and consequently no macroscopic adhesion by electrostatic interactions should be observed.

The bulk hydrogel I10-R2 was used for the adhesion tests at different pH values (2.0, 4.0, 5.5, 8.0 and 9.0). The hydrogels were kept in Milli-Q water until they reached swelling equilibrium. Afterwards, adhesion tests were done at each specific pH at a contact time of 1 second and a debonding rate of 0.1 mm/s. It should be noted that special care was taken when testing the samples in basic conditions (pH > 8), because when the poly(MAETAC-*co*-AAm) hydrogels are left under basic conditions for too long (>1 h), the amide group (–$CONH_2$) of acrylamide are prone to hydrolysis into carboxyl groups (-COOH). This will in turn decrease the cationicity of the hydrogel with increasing amount of negative charges,[41] and will lead to a progressive loss of adhesion energy with the negatively charged thin film as attractive electrostatic forces will decrease. Each hydrogel sample was used for only one experiment at each pH. Three replicates were done for each experiment.

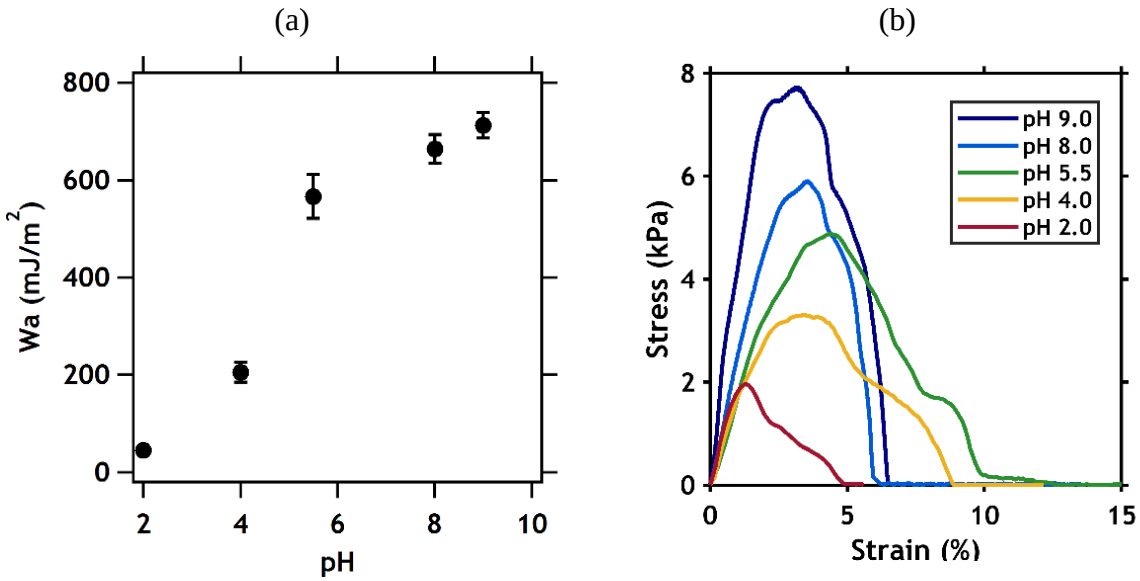

Figure 2-17. (a) Variation of the adhesion energy as a function of pH for I10-R2 on the PAA thin film (dry thickness of 150 nm) in water at different pH. Contact time = 1 s and V_{deb} = 0.1 mm/s. (b) Corresponding stress-strain tack debonding curves.

The adhesion energy and maximum debonding force between the I10-R2 hydrogel and PAA thin films was found to increase with pH (**Figure 2-17**) reaching a maximum at around pH 8 – 9. Moreover, the silica on which the PAA hydrogel thin film is grafted, is degraded in highly basic medium, typically above pH 9. By increasing the pH from 2 to 9, the maximum stress increased also by a factor of 4 (from 2 kPa to 8 kPa, respectively). This simply occurred because more force is needed to separate the two surfaces when more interactions are formed.

2.5. Discussion

2.5.1 Effect of charge distribution at the interface

In Section 3, we showed that the content of MAETAC seemed to have no effect on the adhesive properties, at least in the range investigated. These results suggest two things; 1) that the areal density of negative charges controls the adhesion energy and 2) that the positive charges on the hydrogel side, available at the interface may be in excess. Therefore, assuming

that the areal density of negative charges controls the adhesion properties between the gels, by the number of electrostatic bonds formed at the interface, the zeta potential (ζ) of PAA thin films at different pH is one of the relevant parameters to take into account. It is important to note that the ionic strength will change the interactions. However, in this chapter we considered that the ionic strength is constant.

Figure 2-18 shows a representative curve of the streaming potential measurements conducted on PAA thin films as a function of pH in a 10^{-3} M KCl solution. The non-dissociated state is achieved at pH 3 based on the pH in which ζ is zero. The increase of negative zeta potential with pH is due to the increasing dissociation of acidic surface groups. Moreover, ζ reaches a plateau at -70mV when reaching a complete dissociation of acidic functional groups at pH ≥ 8. Furthermore, the interfacial charge distribution between the poly(MAETAC-*co*-AAm) hydrogel and the PAA hydrogel thin film corresponds to the number of dissociated COOH groups at the very surface of the thin film.

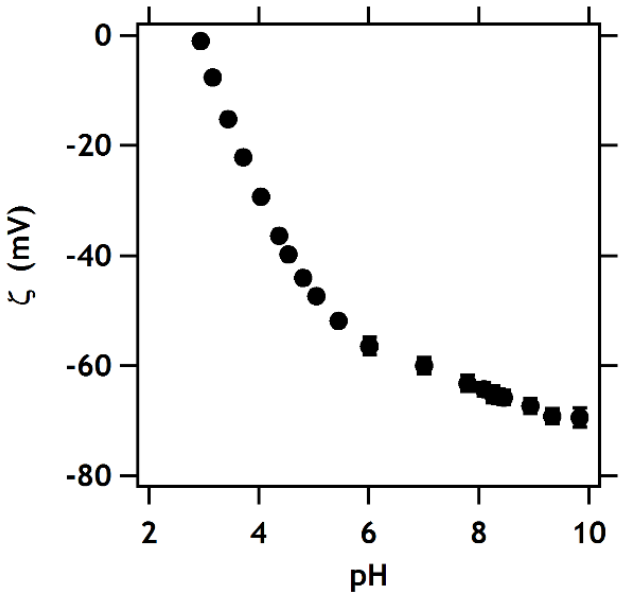

Figure 2-18. Apparent zeta potential of PAA hydrogel thin film in 10^{-3} M KCl as a function of pH.

Moreover, as introduced before in section 2.2.3, the use of streaming potential experiments as function of pH gives an estimation of the number of dissociated carboxyl groups per unit area (σ_a, in units of $n\mathrm{COO}^-/\mathrm{m}^2$). By using the Grahame equation (equation 13), which relates the surface charge density and the surface potential, it is possible to calculate the maximum number of acidic groups capable of dissociation per unit area (N_a) at the solid/liquid interface. N_a is related to the maximum potential ($\zeta_{plateau}$), which for the PAA thin films is equal to $\zeta_{plateau} = \zeta\,(\mathrm{pH} > 8)|\alpha = 1) = -70\mathrm{mV}$. Therefore, we calculate N_a equal to $6.8x10^{-3}$ C/m^2, which is equivalent to 4.23 x 10^{16} $n\mathrm{COO}^-$/m^2 = 4.23 x 10^{-2} $n\mathrm{COO}^-$/nm^2. Additionally, with equation 11 we can calculate the degree of dissociation α as function of the ζ-potential and the respective pH. Finally, **Figure 2-19.a**. shows the product of α multiplied by N_a, which is the number of dissociated groups per unit area (σ_a) as function of the pH.

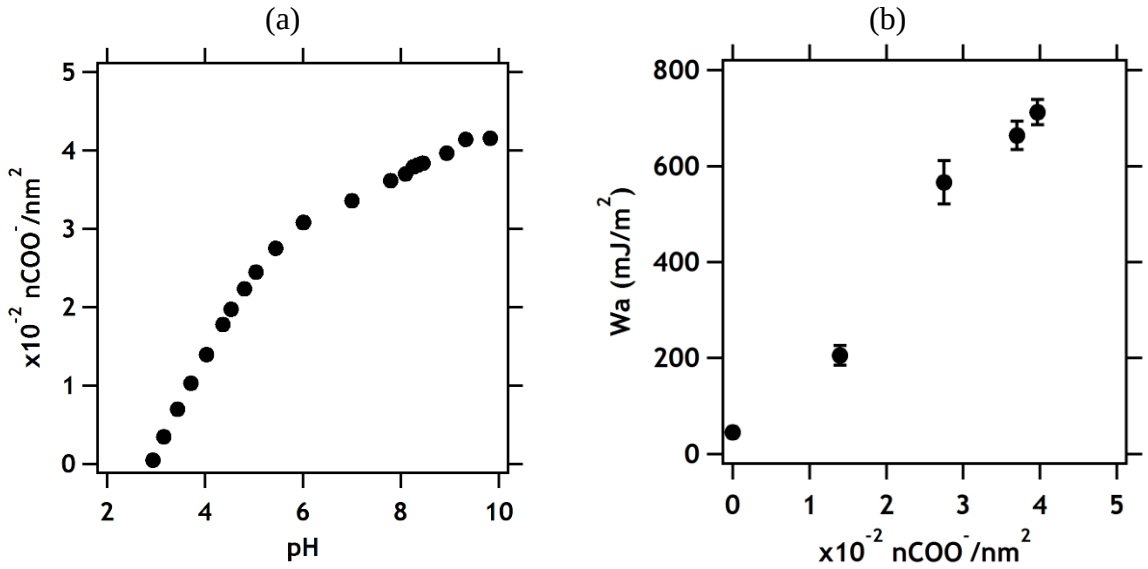

Figure 2-19. (a) Variation of the number of dissociated groups per unit area nCOO$^-$ as function of the pH estimated from streaming potential measurements; (b) Adhesion energy of I10-R2 on PAA hydrogel thin films as measured by the tack test as a function of the approximate number of dissociated groups per unit area at the interface of the hydrogel thin film. Contact time = 1 s and V_{deb} = 0.1 mm/s

We are now able to quantitatively correlate the energy of adhesion (W_a), to the pH of the medium by using the number of dissociated groups per unit area (σ_a). This correlation suggests that the charge density at the interface can indeed be modified by adjusting the pH of the medium and that W_a strongly depends on this charge density. Quantitatively, the adhesion energy increased linearly from 200 mJ/m^2 at a charge density of 1.4 x 10^{-2} $n\mathrm{COO}^-$/nm^2 to 700 mJ/m^2 with a charge density of around 4 x 10^{-2} $n\mathrm{COO}^-$/nm^2 (**Figure 2-19.b**).

2.5.2. Prediction of the effect of debonding velocity (Chaudhury's model)

According to Chaudhury's model (explained in **Section 2.2.2**), the interfacial fracture energy (W_a) for relatively fast debonding rates can be described as follows:

$$W_a = \left(\frac{\Sigma_i}{2k_s}\right)\left[\left(\frac{k_B T}{\lambda}\right)\ln\left(\frac{k_s V \lambda \tau_-}{n k_B T}\right)\right]^2 \qquad (21)$$

where Σ_i is the areal density of weak bonds. λ is the activation length of the bond, which we assume to be 0.1 nm, that is, typical of an ionic bond lengths.[27] k_s is the linear spring constant of the polymer chain which we assume inversely proportional to the number of monomers in the chain (N_c). τ_- is the characteristic time of bond dissociation, k is the Boltzmann's constant and n is the number of weak bonds in the polymer chain (one in our case).

We now adapt this model to our system (**Figure 2-20**): the adhesion is due to weak bonds attached to a flexible chain composed of strong bonds that cannot break and it takes place in immersed conditions where Van der Waals forces are small. In this model, it is possible to assume that only one weak bond is present in a polymer chain and that only the deformation of the chains of the cationic hydrogel contribute to W_a. Additionally, we assume that every polycation attached to a gel chain is able to attach to a negatively charged site so that Σ_i is already known from the streaming potential experiments (in Milli-Q water (at pH 5.5) $\Sigma_i = \sigma_a \sim 3\,x10^{-2}\,n\mathrm{COO}^-/\mathrm{nm}^2$.

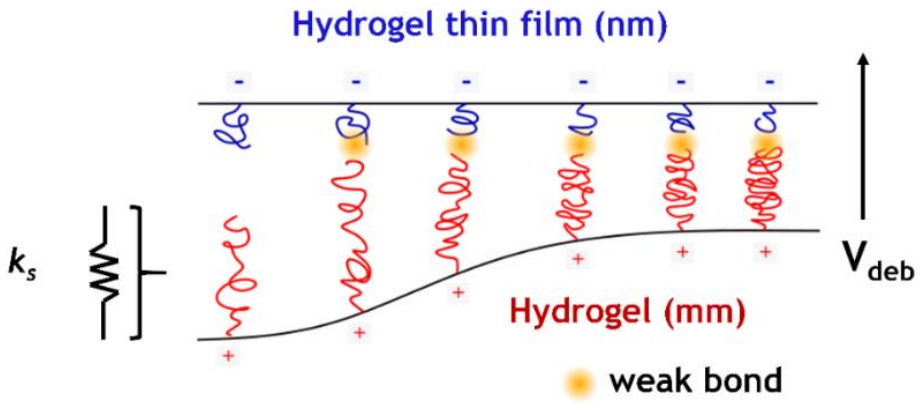

Figure 2-20. Schematic representation of the crack tip region between the positively charged hydrogel of poly(MAETAC-*co*-AAm) (in red) and the negatively charged hydrogel thin film of PAA (in blue). The yellow circles represent the weak bond (electrostatic interaction).

Based on the experimental value of the adhesion energy as a function of the detachment rate V_{deb} (which is assumed to be proportional to the rate of interfacial crack growth), it is possible to plot $W_a^{1/2}\ (k_BT/\lambda)^{-1}$ as a function of $\ln V_{deb}$ for the gel I10-R2 (**Figure 2-21**). The slope and intercept of this plot give an estimate of the spring constant k_s of the polymer chain and of the dissociation time $\tau\_$ of the electrostatic bond, respectively. With the value of Σ_i obtained in previous section, the values of k_s and $\tau\_$ are, thus, estimated to be 1.1 mN/m and 0.12 s, respectively.

As a matter of comparison, the calculated value of k_s is close to a spring constant of a polymeric chain in its enthalpic limit reflecting the fact that the electrostatic bond can stretch the polymer chain before its maximum length. Note that in the enthalpic limit the average stiffness of the polymer chain ($k_{s-enthalpic}$) is defined by

$$k_{s-enthalpic} = \frac{2N_cU_c/N_{av}}{\left(2N_c\cos\left(\frac{\theta}{2}\right)b\right)^2} \qquad (22)$$

where U_c is the bond energy of the covalent bond (400 kJ/mol), N_{av} is the Avogadro's number and b is the bond length (0.154 nm) and $\cos\left(\frac{\theta}{2}\right)$ equal to 0.81. Using the value of Table 1 for N_c (which is 40 units for I10-R2) we can calculate with equation 22 a $k_{s-enthalpic}$ = 0.5 N/m. This spring constant is very consistent with the fitted value given the nature of the approximations that we are making.

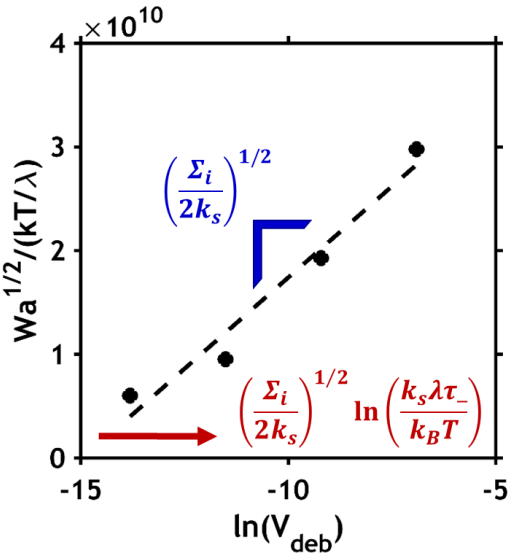

Figure 2-21. $W_a^{1/2}\,(k_BT/\lambda)^{-1}$ as function of $\ln V_{deb}$ for the I10-R2 gel against the PAA thin hydrogel film. Black symbols are the experimental data (contact time 1 s) and the dashed line is the best fit to Chaudhury's model discussed in the text.

Furthermore, according to Eyring, the natural relaxation time of a chemical bond is

$$\tau_- = \frac{h}{k_BT} exp\left(\frac{E_a}{k_BT}\right) \qquad (23)$$

where h is the Plank's constant. Therefore, the bond activation energy for an electrostatic interaction (E_a) at is calculated to be 27.3 k_BT (66.5 kJ/mol at 20 °C) which is lower than a

covalent bond and in the same magnitude of 6 k_BT as measured by Spruijt et al.[10] Moreover, according to Hui [42] if the dimensionless parameter β defined as

$$\beta = \frac{k_B T}{V_{deb} \tau\_ k_s \lambda} \tag{24}$$

is lower than 1, this means that the energy release rate for crack growth corresponds to high crack speeds or long relaxation times. At high crack speeds only chains close to the crack tip are broken as oppositely to slow crack speeds where chains are broken everywhere except those close to the crack tip. For our case β is equal to 3.22x10^{-3} at a detachment rate of 0.1 mm/s, independent on the Σ_i, meaning that regardless of the interfacial charge density, this system will always fail in the high crack speed regime.

2.5.3. Prediction of the adhesion energy from the hydrogel's degree of crosslinking.

In section 2.4.3, in addition we showed that the crosslinker concentration of positively charged hydrogels considerably affected the adhesion energy W_a when measured against the same negatively charged surface. Since Chaudhury's model assumes that polymer chains are linear springs with constant k_s, we propose to use this model to predict the adhesion energy as a function of the length of the polymer chain (N_c) since $k_s = k_3/N_c$, where k_3 is a coefficient that relates the spring constant of the polymer chain as found in the previous section for the I10-R2 hydrogel ($k_s = 1.1\ mN/m$ for a $N_c = 40$ units). Therefore, the coefficient k_3 is calculated to be 0.045. Finally, W_a will be a function of N_c as follows

$$W_a = k_1 N_c \left[\ln\left(\frac{k_2}{N_c}\right)\right]^2 \tag{25}$$

where k_1 is a coefficient which is function of the interfacial charge density Σ_i and k_2 will be a function of the velocity and both coefficients can be calculated as follows

$$k_1 = \Sigma_i \left[\frac{1}{2k_3}\left(\frac{k_B T}{\lambda}\right)^2\right] = 0.53\ \frac{mJ}{m^2}, \qquad k_2 = V_{deb}\left(\frac{k_3 \lambda \tau\_}{k_B T}\right) = 1.2x10^4 \tag{26}$$

The data of **Figure 2-15** can now be replotted in **Figure 2-22** as a function of N_c, and compared with the prediction of W_a based on Chaudhury's model. W_a was calculated for polymer chains with $0 < N_c < 200$ with k_1 and k_2 as calculated previously. N_c was directly taken from Table 1 for the experimental values of W_a. Remarkably, the model is able to predict the tendency of the experimental data, which is to increase macroscopic underwater adhesion, as does the length of the chains between crosslinks. At higher values of N_c the model predicts reasonably well the adhesion energy at this debonding rate (V_{deb} = 0.1 mm/s). In contrast, at low values of N_c, the discrepancy between the experimental data and the model could be due to the fact that the model is based on molecular aspects only and may still need to take into account variation of bulk dissipative mechanisms.

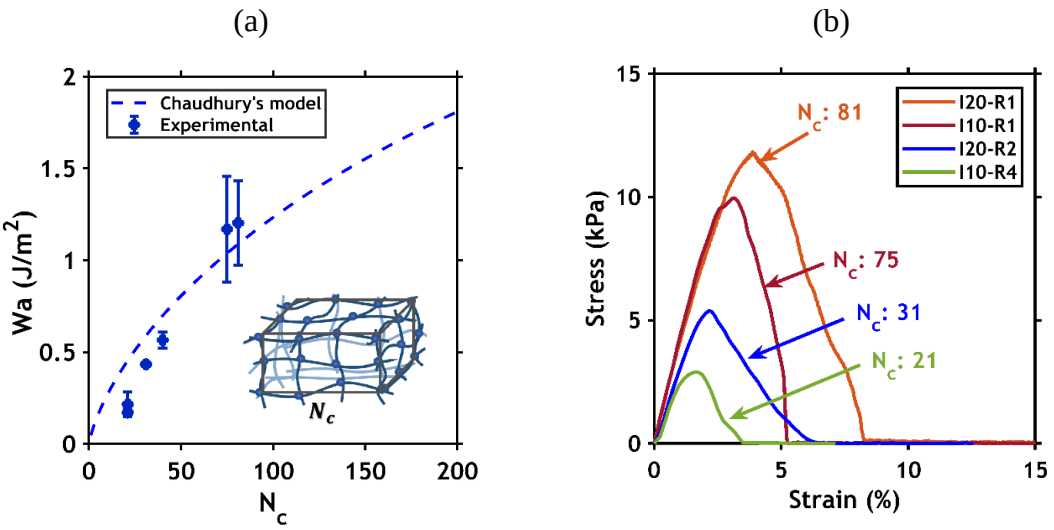

Figure 2-22. (a) Adhesion energy W_a as function of the number of monomers in the polymer chain of the poly(MAETAC-*co*-AAm) hydrogel N_c. Points are experimental data and the dashed line is the prediction of Chaudhury's model. (b) Representative stress-strain tack debonding curves of the first contact for different number of monomers between crosslinks, N_c of poly(MAETAC-*co*-AAm) hydrogels.

Moreover, it is possible to use the Chaudhury's model to calculate the work of adhesion as function of N_c at different debonding rates. The only parameter that needs to be change in the equation 25 is the coefficient k_2, which depends on $V_{deb.}$ Therefore, $k_2(V_{deb} = 0.01\ mm/s)$ is $1.2x10^3$ and $k_2(V_{deb} = 1\ mm/s)$ is $1.2x10^5$. Therefore, **Figure 2-23.a** shows the work of adhesion as function of N_c as predicted by the Chaudhury's model at 3 different debonding rates (0.01, 0.1 and 1 mm/s), and it is compare to the experimental data presented in Figure 16 for poly(MAETAC-*co*-AAm) hydrogel (I10-Rx) at different debonding rates (V_{deb}). Remarkably, the model is able to predict pretty well the tendency of the experimental data at different debonding rates ($V_{deb:}$ 0.01 mm/s and 0.1 mm/s) for the hydrogels with longer N_c (I10-R1 and I10-R2). However, this model fails to predict the adhesion for more crosslinked (I10-R4) hydrogels and for faster debonding rate ($V_{deb:}$ 1 mm/s).

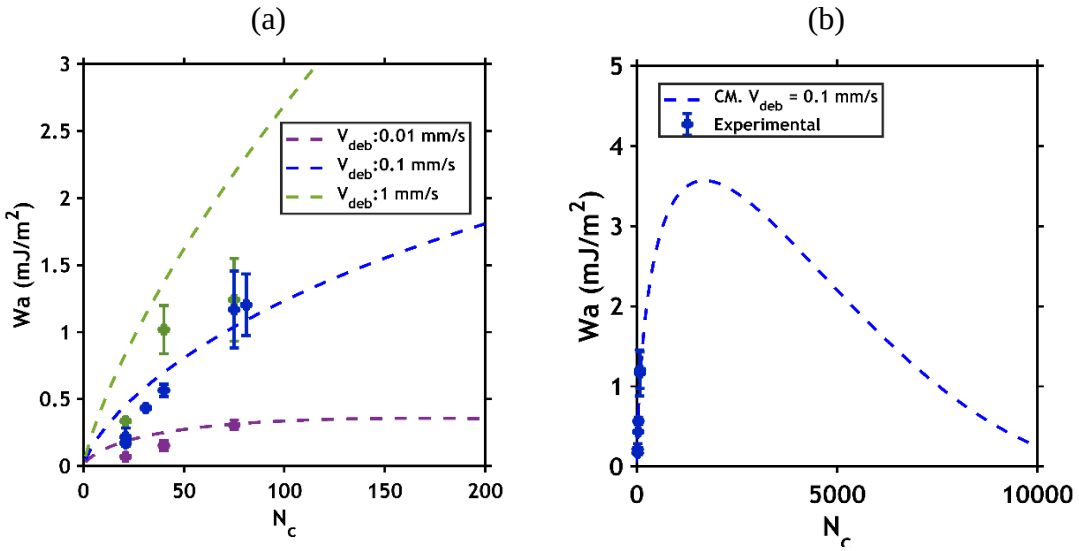

Figure 2-23. (a) Adhesion energy W_a as function of the number of monomers in the polymer chain of the poly(MAETAC-*co*-AAm) hydrogel at different debonding rates (V_{deb}). (b) Adhesion energy W_a as predicted by the Chaudhury model (V=0.1 mm/s) using higher values of N_c. Local maximum at $N_c = 1440\ units$.

It should be noted that Chaudhury's model predicts a local maximum of W_a of approximately 4 J/m^2 for $N_c \sim 1440$ (**Figure 2-23.b**). However, it is not experimentally feasible to prepare a hydrogel with this architecture since no elastic and tough hydrogel will be obtained with a 0.04 mol% of crosslinker concentration (i.e. the theoretical concentration to obtain a polymer chain of ~1440 monomer units).

2.6. Conclusions

Macroscopic underwater adhesion between oppositely charged polyelectrolytes is a complex multi-parameter problem, and the effect of some of these parameters has been highlighted in this study. The model system that we used (elastic positively charged hydrogel and negatively charged surface) emphasizes the role played by molecular interactions, specifically electrostatic interactions, on the strength of macroscopic adhesion of hydrogels underwater. We investigated the contribution of the elastic properties of the hydrogel and of the charge density at the interface and the main conclusions are the following: For a fixed gel and debonding conditions we find that the macroscopic adhesion depends linearly on the density of bonding sites at the interface. For a fixed density of binding sites and a fixed gel, the macroscopic underwater adhesion increases weakly with contact time (in stark contrast with the case of H-bonds) but strongly with debonding rate, in semi-quantitative agreement with Chaudhury's model for kinetic bond scission. Finally and importantly for fixed bonding and debonding conditions and fixed charge density, W_a increases with the inverse of the elastic modulus and can be modelled semi-quantitatively. It was found on the hydrogel side that underwater adhesion energy depends strongly on the rigidity of the hydrogels (hydrogel shear moduli). When the shear modulus increases the macroscopic adherence decreases in an analogous way to what is predicted for fracture of simple soft networks in gels or elastomers.[40]

References

(1) Stewart, R. J.; Ransom, T. C.; Hlady, V. Natural Underwater Adhesives. *J. Polym. Sci. Part B Polym. Phys.* **2011**, *49* (11), 757–771.

(2) Bhagat, V.; Becker, M. L. Degradable Adhesives for Surgery and Tissue Engineering. *Biomacromolecules* **2017**, *18* (10), 3009–3039.

(3) Mehdizadeh, M.; Yang, J. Design Strategies and Applications of Tissue Bioadhesives. *Macromol. Biosci.* **2013**, *13* (3), 271–288.

(4) Hofman, A. H.; van Hees, I. A.; Yang, J.; Kamperman, M. Bioinspired Underwater Adhesives by Using the Supramolecular Toolbox. *Adv. Mater.* **2018**, *1704640*, 1–38.

(5) Li, J.; Celiz, A. D.; Yang, J.; Yang, Q.; Wamala, I.; Whyte, W.; Seo, B. R.; Vasilyev, N. V.; Vlassak, J. J.; Suo, Z.; et al. Tough Adhesives for Diverse Wet Surfaces. *Science (80-.).* **2017**, *357* (6349), 378–381.

(6) La Spina, R. La; Tomlinson, M. R.; Ruiz-pørez, L.; Chiche, A.; Langridge, S.; Geoghegan, M. Controlling Network – Brush Interactions to Achieve Switchable Adhesion **. *Angew. Chemie Int. Ed.* **2007**, *46*, 6460–6463.

(7) Nyarko, A.; Barton, H.; Dhinojwala, A. Scaling down for a Broader Understanding of Underwater Adhesives – a Case for the Caulobacter Crescentus Holdfast. *Soft Matter* **2016**, *12* (45), 9132–9141.

(8) Alfhaid, L.; La Spina, R; Tomlinson, M. R.; Hall, A. R.; Seddon, D.; Williams, N. H.; Cousin, F.; Gorb, S.; Geoghegan, M. Adhesion between Oppositely Charged Polyelectrolytes. *J. Adhes.* **2016**, *94* (1), 58–76.

(9) Dobrynin, A. V.; Rubinstein, M. Theory of Polyelectrolytes in Solutions and at Surfaces. *Prog. Polym. Sci.* **2005**, *30* (11), 1049–1118.

(10) Spruijt, E.; Van Den Berg, S. A.; Cohen Stuart, M. A.; Van Der Gucht, J. Direct Measurement of the Strength of Single Ionic Bonds between Hydrated Charges. *ACS Nano* **2012**, *6* (6), 5297–5303.

(11) Tagliazucchi, M.; de la Cruz, M. O.; Szleifer, I. Self-Organization of Grafted Polyelectrolyte Layers via the Coupling of Chemical Equilibrium and Physical Interactions. *Proc. Natl. Acad. Sci.* **2010**, *107* (12), 5300–5305.

(12) Shull, K. R. Contact Mechanics and the Adhesion of Soft Solids. *Mater. Sci. Eng. R Reports* **2002**, *36* (1), 1–45.

(13) Kobayashi, M.; Terada, M.; Takahara, A. Reversible Adhesive-Free Nanoscale

Adhesion Utilizing Oppositely Charged Polyelectrolyte Brushes. *Soft Matter* **2011**, *7*, 5717–5722.

(14) Drechsler, A.; Synytska, A.; Uhlmann, P.; Stamm, M.; Kremer, F. Tuning the Adhesion of Silica Microparticles to a Poly (2-Vinyl Pyridine) Brush : An AFM Force Measurement Study. *Langmuir* **2012**, *28*, 15555–15565.

(15) Spruijt, E.; Stuart, M. a C.; Van Der Gucht, J. Dynamic Force Spectroscopy of Oppositely Charged Polyelectrolyte Brushes. *Macromolecules* **2010**, *43*, 1543–1550.

(16) Wei, W.; Yu, J.; Gebbie, M. A.; Tan, Y.; Martinez Rodriguez, N. R.; Israelachvili, J. N.; Waite, J. H. Bridging Adhesion of Mussel-Inspired Peptides: Role of Charge, Chain Length, and Surface Type. *Langmuir* **2015**, *31* (3), 1105–1112.

(17) Dunlop, I. E.; Briscoe, W. H.; Titmuss, S.; Jacobs, R. M. J.; Osborne, V. L.; Edmondson, S.; Huck, W. T. S.; Klein, J. Direct Measurement of Normal and Shear Forces between Surface-Grown Polyelectrolyte Layers. *J. Phys. Chem. B* **2009**, *113* (12), 3947–3956.

(18) Hayashi, S.; Abe, T.; Higashi, N.; Niwa, M.; Kurihara, K. Polyelectrolyte Brush Layers Studied by Surface Forces Measurement: Dependence on PH and Salt Concentrations and Scaling. *Langmuir* **2002**, *18* (10), 3932–3944.

(19) Rose, S.; Prevoteau, A.; Elzière, P.; Hourdet, D.; Marcellan, A.; Leibler, L. Nanoparticle Solutions as Adhesives for Gels and Biological Tissues. *Nature* **2014**, *505* (7483), 382–385.

(20) Sudre, G.; Olanier, L.; Tran, Y.; Hourdet, D.; Creton, C. Reversible Adhesion between a Hydrogel and a Polymer Brush. *Soft Matter* **2012**, *8*, 8184–8193.

(21) Macron, J.; Bresson, B.; Tran, Y.; Hourdet, D.; Creton, C. Equilibrium and Out-of-Equilibrium Adherence of Hydrogels against Polymer Brushes. *Macromolecules* **2018**, *51* (19), 7556–7566.

(22) Lake, G. J.; Thomas, A. G. The Strength of Highly Elastic Materials. *Proc. R. Soc. A Math. Phys. Eng. Sci.* **1967**, *300* (1460), 108–119.

(23) Rubinstein, M.; Colby, R. H. *Polymer Physics*, 1 edition.; Oxford University Press, 2003.

(24) Chaudhury, M. K. Rate-Dependent Fracture at Adhesive Interface. *J. Phys. Chem. B* **1999**, *103*, 6562–6566.

(25) Merkel, R.; Nassoy, P.; Leung, A.; Ritchie, K.; Evans, E. Energy Landscapes of Receptor-Ligand Bonds Explored with Dynamic Force Spectroscopy. *Nature* **1999**, *397* (6714), 50–53.

(26) Evans, E. A.; Ritchie, K. Strength of a Weak Bond Connecting Flexible Polymer Chains.

Biophys. J. **1999**, *76* (5), 2439–2447.

(27) Israelachvili, J. N. *Intermolecular and Surface Forces*, 3 edition.; Academic Press, 2011.

(28) Hunter, R. J. *Zeta Potential in Colloid Science: Principles and Applications*; 1981.

(29) Simon, F. Electrokinetic Phenomena. *COST D43 Sch. "Interfacial Eng. nanotechnology"* **2009**, 20.

(30) Jacobasch, H. J. Characterization of Solid Surfaces by Electrokinetic Measurements. *Prog. Org. Coatings* **1989**, *17* (2), 115–133.

(31) Kinraide, T. B. Use of a Gouy-Chapman-Stern Model for Membrane-Surface Electrical Potential to Interpret Some Features of Mineral Rhizotoxicity. *Plant Physiol.* **1994**, *106*, 1583–1592.

(32) Chollet, B.; D'Eramo, L.; Martwong, E.; Li, M.; Macron, J.; Mai, T. Q.; Tabeling, P.; Tran, Y. Tailoring Patterns of Surface-Attached Multiresponsive Polymer Networks. *ACS Appl. Mater. Interfaces* **2016**, *8* (37), 24870–24879.

(33) Li, M.; Bresson, B.; Cousin, F.; Fretigny, C.; Tran, Y. Submicrometric Films of Surface-Attached Polymer Network with Temperature-Responsive Properties. *Langmuir* **2015**, *31*, 11516–11524.

(34) Miquelard-Garnier, G.; Demeures, S.; Creton, C.; Hourdet, D. Synthesis and Rheological Behavior of New Hydrophobically Modified Hydrogels with Tunable Properties. *Macromolecules* **2006**, *39* (23), 8128–8139.

(35) Werner, G.; Körber, H.; Zimmermann, R.; Dukhin, S.; Jacobasch, H. J. Extended Electrokinetic Characterization of Flat Solid Surfaces. *J. Colloid Interface Sci.* **1998**, *208* (1), 329–346.

(36) Duval, J. F. L.; Küttner, D.; Nitschke, M.; Werner, C.; Zimmermann, R. Interrelations between Charging, Structure and Electrokinetics of Nanometric Polyelectrolyte Films. *J. Colloid Interface Sci.* **2011**, *362* (2), 439–449.

(37) Smoluchowski, M. *Handbuch Der Elektrizität Und Magnetismus*; Graetz, L., Ed.; Leipzig, 1921.

(38) Obukhov, S. P.; Rubinstein, M.; Colby, R. H. Network Modulus and Superelasticity. *Macromolecules* **1994**, *27* (12), 3191–3198.

(39) Chollet, B.; Li, M.; Martwong, E.; Bresson, B.; Fretigny, C. Multiscale Surface-Attached Hydrogel Thin Films with Tailored Architecture. *ACS Appl. Mater. Interfaces* **2016**, *8*, 11729–11738.

(40) Ciccotti, M.; Creton, C. Fracture and Adhesion of Soft Materials : A Review. *Reports*

Prog. Phys. **2016**, *79*, 046601.

(41) Tanaka, T.; Sun, S. T.; Nishio, I.; Swislow, G.; Shah, A. Phase Transitions In Ionic Gels. *Phys. Rev. Lett.* **1980**, *45* (20), 1636–1639.

(42) Hui, C. Y.; Tang, T.; Lin, Y. Y.; Chaudhury, M. K. Failure of Elastomeric Polymers Due to Rate Dependent Bond Rupture. *Langmuir* **2004**, *20* (14), 6052–6064.

Chapter 3

3. Underwater adherence screened by salt. A probe-tack test and AFM colloidal probe study.

In this chapter we present a comparison of work of adhesion (W_a) between a macroscopic scale measurements using the underwater probe-tack test and a microscopic underwater adhesion test using the AFM colloidal probe technique (AFM-CP). We focus the comparison on the effect of salt concentration in the testing medium at both scales (macro and micro) on the work of adhesion. Additionally, we use the AFM-CP to systematically study the effect of the main experimental parameters that affect macroscopically the work of adhesion as shown in Chapter 2 (i.e. Debonding rate, contact time, pH and hydrogel elastic moduli). The W_a measured in both systems (Probe-tack and AFM-CP) were normalized by the interfacial charge density (Σ_i), which was estimated using streaming potential measurements on the hydrogel thin film and on the colloidal probe. Remarkably, we found that at both scales the strength of the electrostatic interaction is kinetically dependent since the measured macroscopic rupture energy is rate dependent, and this behavior can be explained semi-quantitatively by using the Evans model of kinetic bond breakage between polymeric chains. We also found that the mechanical properties of the macroscopic hydrogel affect considerably the adhesion underwater as W_a increases with the inverse of the elastic modulus at both macro and micro scales. Additionally, Σ_i is an important parameter to control and predict the underwater adhesion energy, since it can be modified and screened by changing the pH or by increasing the salt concentration of the medium, respectively.

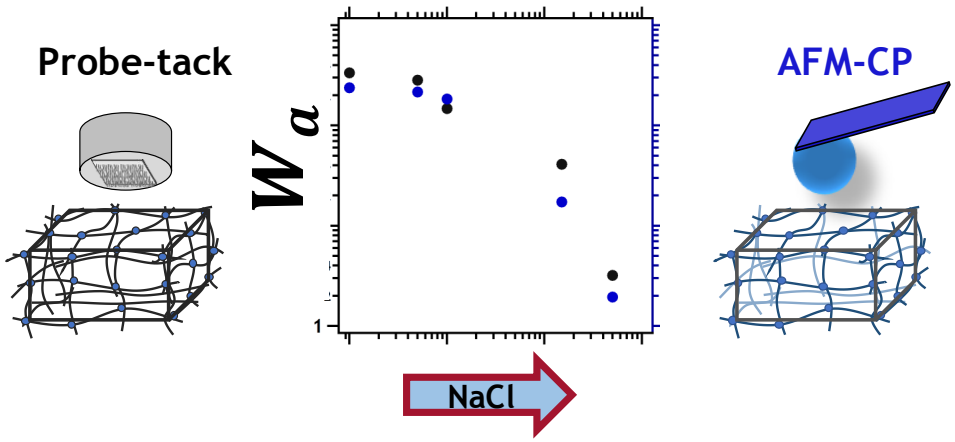

The content of this chapter is the result of a collaboration with Ugo Sidoli and Dr. Alla Synytska at the Leibniz Institute of Polymer Research, Dresden, Germany.

Contents

3.1. Introduction

Underwater adhesion (W_a) between oppositely charged polyelectrolytes is a complex multi-parameter problem, and the effect of some of these parameters has been highlighted in the previous chapter. We investigated the adhesive properties of a model system composed of a macroscopic positively charged gel and an oppositely charged polyelectrolyte thin film. The macroscopic adhesion energy W_a was successfully linked to the bulk mechanical properties of the soft hydrogel material and to the surface density of electrostatic interactions formed at the interface with a hydrogel thin film. Briefly, it was found that W_a is clearly rate-dependent as it increases when increasing the pulling rate. Additionally, by adjusting the pH in the medium, W_a increases linearly with the interfacial charge density (Σ_i), and finally, we found that W_a increases with the inverse of the elastic modulus of the macroscopic hydrogels. However, the two main parameters that contribute to the prediction and control of macroscopic adhesion are the Σ_i, which is controlled by the pH and the ionic strength of the medium and the elastic modulus of the macroscopic hydrogel, which varies with the average number of monomer units between crosslinks (N_c). The control and prediction of W_a from these parameters were highlighted in the previous chapter.

In this chapter, we investigate two additional questions concerning the adhesion and contact phenomena of this system. First, the effect of the same parameters (rate-dependence, interfacial charge density, elastic modulus) for a more microscopic contact area is still unknown for the same positively charged soft hydrogel against a hard negatively charge surface. Second, if the adhesion energy shown in the previous chapter indeed corresponds to the breaking of electrostatic interactions at the interface between oppositely charged polyelectrolytes, then its magnitude (at a macroscopic and microscopic level) should be highly sensitive to the ionic strength of the medium, i.e the concentration of added salt.

Developments of different adhesion measurement methods allowed the study of macro- and micro- scale-contact phenomena: macro-scale contacts are in general characterized using tack, peel and shear tests.[1,2] The advantage of macro-scale methods is the well-defined contact area. However, these methods are limited to smooth and chemically homogenous samples over a few hundred μm^2.[3] On the micro-scale side, the main advantage is the knowledge of the interaction forces between colloidal particles (micron-sized particle), single molecules and surfaces. Direct measurement of intermolecular forces has benefited greatly since the introduction of the atomic force microscopy (AFM)[4] and the surface force apparatus (SFA).[5] These techniques have made possible the direct measurement of different type of interaction forces between several types of surfaces and molecular structures ranging from hydrophobic colloids,[6] charged colloids,[7,8] covalent bonds[9] and to complete strands of DNA.[10] Moreover, there are several advantages of the AFM over the SFA, In addition to its versatility and ability to perform force measurements with both high normal and lateral resolution,[8] the AFM can work under any aqueous environment as it allows a precise control of several parameters such as temperature, pH, solvent, humidity.[4] Therefore, we focus our underwater adhesion experiments at a micro-scale using the AFM technique.

Ionic strength is a key variable in the underwater adhesion tests between oppositely charged polyelectrolyte hydrogels. It is well known that the screening process of an electrostatic interaction can be described quantitatively as a salt-enhanced activated process. In general, at low salt concentration, the attraction of oppositely charges is strong enough to keep two colloidal particles together. However, with increasing salt concentration, the electrostatic attraction is progressively screened and the colloidal particles will separate. For ions in vacuum, Coulomb's Law gives a precise value of the force, but the presence of a medium such as water containing monovalent salt ions leads to hydration, dielectric effects, and screening of the charges. How the combination of these effects modifies the short-range attractive force of ions

connected to soft polymeric materials is still poorly understood. As a result, the strength of ionic bonds between two soft surfaces carrying opposite charges as function of different salt concentrations and its contribution to macroscopic and microscopic underwater adhesion is not yet fully understood.

This chapter aims to present a comparison between macroscopic scale measurements using an underwater tack tester and microscopic underwater adhesion experiments using the AFM colloidal probe technique (AFM-CP). We focus the study on the effect of salt concentration in the testing medium at both scales (macro and micro) on the work of adhesion. Additionally, we use the AFM-CP to study systematically the effect of the main experimental parameters that affect macroscopically the work of adhesion.

3.1.1. Atomic force microscopy

One of the methods available for direct measurement of surface forces is the atomic force microscope (AFM) introduced in 1986 by Binnig, Quate and Gerber.[11] The surprising simplicity of the microscope, capability of measuring in air and practically in any gas and liquid environment, makes it indispensable both in scientific research and in industry. The AFM was inspired by the scanning tunneling microscope (STM), which was able to scan substrates with an atomic resolution. Yet, it was limited to conductive materials due to the dependence on the tunnelling current, as interaction between sample and microscope tip. In contrast, the AFM, measures the force when the tested sample and a cantilever (probe) interact, and therefore, it can be used on conductive as well as insulating materials.[4]

A rigid cantilever is mounted on one end that is connected to a piezoelectric element, which can move it in three dimensions. A laser is reflected of the back of the unfixed end of the cantilever, and is detected by a photo-diode with multiple segments. Deflecting the cantilever causes deflection of the optical lever, which is registered on the photo-diode (**Figure 3-1**). The

original use of AFM is to study topography of surfaces. The cantilever is in contact with the sample and the deflection of the cantilever from short range repulsive forces is held constant with a feedback loop between photodiode and piezo. The cantilever is moved over the surface and how much the piezo has to move up and down to keep the deflection constant depends on the interactions with the sample and the topography of the sample. This way line by line an image is created.[4] The cantilever is therefore, the interpreter from the surface topography and interaction to the image and force values. A proper cantilever's calibration in therefore vital for a correct measurement.

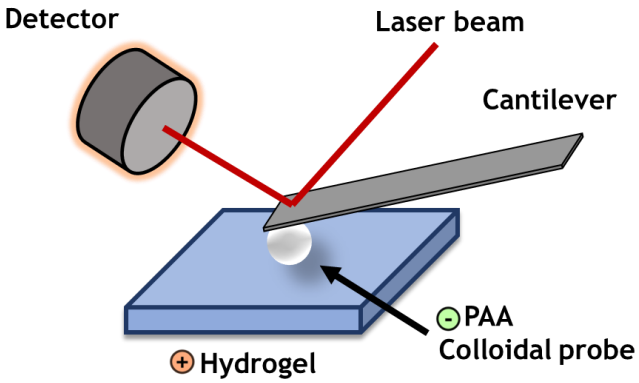

Figure 3-1. Schematic draw of a simplified setup and essential parts of an AFM-Colloidal probe.

There are several procedures and strong background in spring constant calibration methods available in literature.[12] In this chapter, a theoretical and a commonly used experimental approach are introduced. For small deflection, a rigid beam like a cantilever for AFM acts as a linear spring. In this case, the force F is given as

$$F = k_c d \qquad (1)$$

with a cantilever's spring constant k_c (N/m) and deflection d (m). The deflection is measured by the AFM, however, the spring constant of the cantilever needs to be determined.

Theoretical cantilever spring constant calculation

In principle, the spring constant can be calculated for a cantilever with constant rectangular cross-section. The cantilever is assumed to be a rigid beam of length l, width w and thickness t fixed on one end, under the conditions that the deflection of the free end is small, and for an idealized point load, the spring constant can be calculated from its dimensions and its materials properties (Young's modulus E) as[13]

$$k_c = \frac{Ewt^3}{4l^3} \tag{2}$$

It would be ideal if calculation of the spring constant for all cantilevers manufactured in the same dimensions could be done only once, however this purely theoretical calculation can lead to significant errors. Practical concerns are structural variation or defects of the material and variation in dimensions,[14] notably variation in thickness due to the t^3 dependecy of the spring constant. The absolute error margin of spring constant for cantilevers manufactured in expectation of the same properties can reach variation around the expected value of over 300%. Clearly using the average value would introduce unjustifiably large error, and another way to determine the spring constant must be used.

Thermal oscillations method for cantilever spring constant calculation

A method to determine spring constants of cantilevers directly using the AFM was introduced by Hutter and Bechhoefer in 1993.[14] It uses the average deflection of the cantilever caused by thermal vibrations. For small deformations cantilevers are described in good approximation as harmonic oscillator with one degree of freedom. The corresponding Hamiltonian for the system is

$$H = \frac{p^2}{2m} + \frac{1}{2}m\omega_0^2 q^2 \tag{3}$$

with p as momentum, m as oscillating mass, ω_0 as resonance frequency and Mean-square fluctuations in amplitude q. The equipartition theorem gives the relation

$$\frac{1}{2}m\omega_0^2 q^2 = \frac{1}{2}k_b T \quad (4)$$

with k_b Boltzmann's constant and temperature T. Using the relation $\omega_0 = \left(\frac{k_c}{m}\right)^{1/2}$ the spring constant can be determined by the mean squared displacement q, which is directly measured by the AFM at the resonance frequency. Therefore, we obtained the following expression

$$k_c = \frac{k_b T}{q^2} \quad (5)$$

This method is highly recommended for its simplicity of use and broad applicability. Hence, this method was used to determine spring constants of all cantilevers in this chapter.

3.1.2. AFM colloidal probe technique

The colloidal probe technique was introduced independently in 1991 by Ducker et al. attaching silica spheres onto cantilevers [15] and by Butt[16] gluing glass spheres onto cantilevers (**Figure 3-2.a**). The main feature of this method is the interaction of the tested sample with a small spherical particle (typical diameter: 1-50µm) instead of a sharp silicon tip. The spherical particle, also called colloidal probe (CP), is glued to the end of the cantilever after the estimation of the cantilevers spring constant. Cantilevers manufactured with a sharp tip are useful for creating images of substrates with high resolution. Moreover, the shape of AFM tips cannot be accurately controlled in the manufacturing process or even during measurements (**Figure 3-2.b**).[15,17] This leads to two significant problems. Firstly, that the geometry is not exactly known due to variation in the manufacturing process and the risk of wear during use.[3] The second problem is that the interaction surface area with the sample is small, which might limit the resolution of the force measurement and not reveal how more averaged regions on the tested sample behaves similar. In contrast, a main advantage of using a spherical body as a probe is

that alignment of sample and probe are avoided and the contact geometry is well defined.[1,7] The colloid can consist of different materials, or the surface can be modified prior or after attachment of the probe to the cantilever.

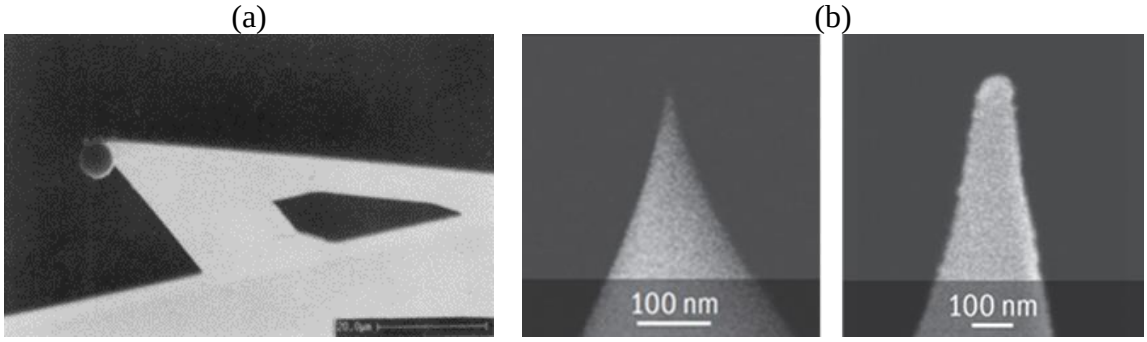

Figure 3-2. (a) SEM image of one of the first published colloidal probse glued to an AFM cantilever by Ducker et al., scale bar 20 μm.[15] (b) SEM images of the regular silicon tips. MikroMasch-Product-Catalogue, (Left, Regular Tip. Right, DPE tip).[18]

Force measurement with the AFM-CP

The measuring principle of the colloidal probe technique is identical to that of a standard AFM and is outlined in **Figure 3-3**. Initially the cantilever is far from the sample and as a good approximation no force is acting on it. As the piezo approaches, the cantilever moves towards the sample's surface (point 1). At point 2, is it possible to measure steric or Pauli repulsive forces when the probe comes closer in contact with the sample. The cantilever continuous to make contact with the sample and at point 3, a maximum applied force is reached. After a certain constant contact time, the drive direction of the piezo is inverted, and the cantilever starts retracting away from the sample. Finally, the highest magnitude of attractive force is reached at point 4. This force is linked to the forces of adhesion acting between the probe and the surface. During the pull-off and depending on several parameters (e.g. type of interactions, roughness, contact time) two behaviors can take place. (i) A single detachment event (the so-

called vertical jump off contact) where all interacting points are broken at the same time, or a continuous event where not all interacting points are broken at the same time (frequently observed for soft polymeric surfaces).[19] Once the cantilever is fully detached from the sample, the force drops to zero.

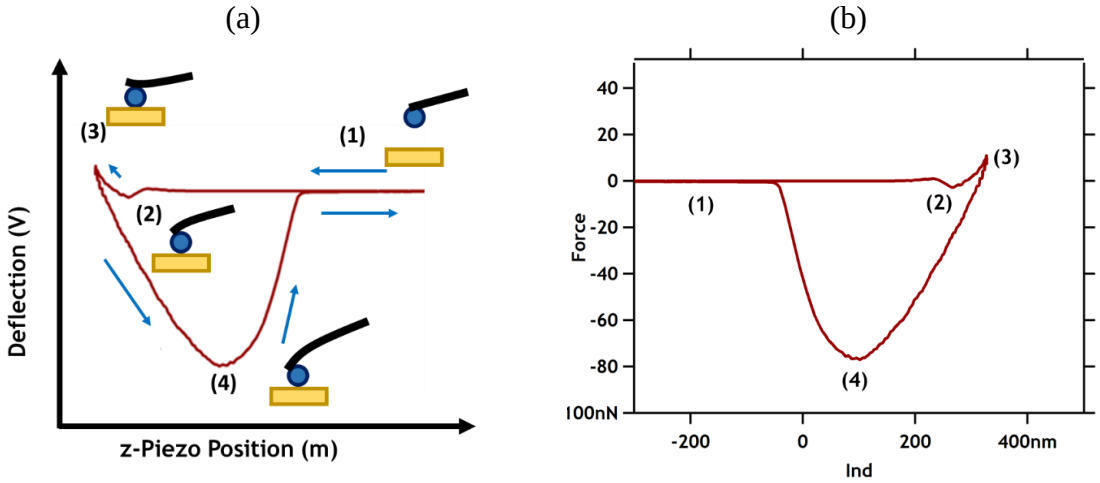

Figure 3-3. (a) Schematic of a deflection signal versus piezo position curve. Raw data of a typical force measurement with the AFM on a soft substrate (b) Corresponding force versus distance curve after multiplying the deflection with the calibration coefficient obtained from a linear fit of the constant compliance region and the spring constant of the cantilever, and adding the cantilever deflection to the piezo position.

AFM-CP Data processing

Some further processing of the raw data is needed to get a force-distance plot that allows to study the adhesion energy from the AFM raw data of the deflection of the laser on the photo-diode (V) and the position of the piezo (m). First, it is necessary to convert the deflection in volts to a force in Newtons. How the signal of the photo-diode (U_{pd}) translates to a cantilever deflection (d) is known by measuring the force as the cantilever deflects against a hard substrate. When the cantilever (with the colloidal probe) and a hard substrate are in contact, the deflection of the cantilever is precisely known because it is exactly as much as the piezo extends

and the voltage of the photo-diode is measured. The relation between U_{pd} and d is linear, and the slope is called the optical lever sensitivity (OLS) in units of V/m. Hence, the OLS is estimated as follows

$$OLS = \frac{\Delta U_{pd}}{\Delta z_p} \tag{6}$$

where ΔU_{pd} is the change in signal of the photo-diode and Δz_p is the piezo vertical displacement. Once the OLS is determined, the deflection of the cantilever is calculated as

$$d = \frac{1}{OLS} U_{pd} \tag{7}$$

Therefore, the deflection of the cantilever is converted to force by using equation (1).

$$F = k_c \frac{1}{OLS} U_{pd} \tag{8}$$

In the next step the contact point is determined. As the distance between cantilever and sample can not be directly measured, it has to be deduced from the force. When approaching the cantilever to the samples it is possible to find steric or Pauli repulsion interactions which start acting from a certain distance and the cantilever is bent backwards, or there is an attractive potential at first causing the probe to "jump-in" at a certain distance and the cantilever tends to bend downwards before repulsion starts acting. In case of a jump in, which is most common in our experiments, the contact point is exactly where the jump in starts, but where the curve is still at zero force.

From the piezo position shown on the *x*-axis in **Figure 3-3.a**, the deflection of the cantilever has to be subtracted. It can be done by using the known force, and equation (1). Typically, at this point the *x*-axis is inverted, so the value of indentation (how far the probe travels into the sample after contact) is shown to the right of the graph (**Figure 3-3.b**). The indentation is related to both the mechanical behavior of the hydrogel sample and to the thickness of the polymer brush on the colloidal probe.

3.2. Theory

3.2.1. Introduction to contact mechanics

From the force–displacement curves, it is possible to draw information about the elastoplastic behavior of materials. In fact, the first force curves taken with the AFM were aimed at analyzing the nanomechanical properties of solid materials.[4] Contact mechanics models have the advantage that from the force of adhesion and the knowledge of geometry of the bodies in contact, the energy of adhesion can be easily calculated.[20] In the case of the colloidal probe technique, these criteria are met. The adhesion force F_{ad} of two rigid and incompressible macroscopic spheres of radius R_1 and R_2, is simply related to their work of adhesion by the Derjaguin approximation

$$F_{ad} = 2\pi\bar{R}W_a \tag{9}$$

where $\bar{R} = {R_1R_2}/{R_1 + R_2}$ and $W_a = W_{132}$ for the general case of two different bodies 1 and 2 interacting in a third medium 3. Heinrich Hertz in 1881 developed the first contact model describing contact surfaces and deformations.[21] The model leads to the contact radius a for the circle shaped contact area of two elastic deformable spherical bodies.

$$a = \sqrt[3]{\frac{3p(\vartheta_1 + \vartheta_2)}{16(\varsigma_1 + \varsigma_2)}} \tag{10}$$

with average pressure p over the contact area, ϑ_i as constant depending on the material mechanical properties of body i and ς_i as reciprocal radius of the body i. If no external forces are acting on the bodies p is zero and thus the contact radius vanishes. However, real particles, deform elastically under the influence of any externally applied load as well as the attractive intersurface forces that pull the two surfaces together, which gives rise to a finite contact area even under zero external load.[20] This means that the Hertz model actually neglects adhesion forces. It nevertheless lays the groundwork for development of other contact models and can

be applied in the case of non adhesive contact surfaces or in the limit of large external forces, to determine the mechanical properties.

Johnson-Kendall-Roberts model

A modification of the Hertz model including adhesion forces is known as the JKR model.[22] It includes the effects of adhesion by considering the surface energy U_s that is needed to separate the surfaces in contact

$$U_s = \pi a^2 \gamma \tag{11}$$

with a as radius of a spherical contact area and γ as energy per surface area. At mechanical equilibrium their contact area will have a radius a given by

$$a^3 = \frac{\bar{R}}{K}\left(P + 3W\pi\bar{R} + \sqrt{6W\pi\bar{R}P + (3W\pi\bar{R})^2}\right)$$
$$\frac{1}{K} = \frac{1-\upsilon_{p1}^2}{E_1} + \frac{1-\upsilon_{p2}^2}{E_2} \tag{12}$$

with K as constant of the material elastic properties, E_i and υ_{pi} are the Young's moduli and Poisson's ratios of the two bodies in contact. $\bar{R}$ is the effective radius of the spheres in contact and P as external force acting on the bodies. For a sphere of radius R on a flat surface of the same material, we may add $R_2 = \infty, R_1 = R$ and $W = 2\gamma$ in the above equation, so that under zero load the contact radius is finite and given by

$$a_0^3 = \frac{12\pi R^2 \gamma}{K} \tag{13}$$

Removing the external force P leads to a finite contact radius and the spheres are only separated when an external force of

$$P = -\frac{3}{2}\gamma\pi R \tag{14}$$

is pulling the two bodies apart. The absolute value of P is referred to as the adhesion force F_{adh}. And the separation will occur abruptly at a contact radius of $a_s = 0.63a_0$. For measurements

of adhesion with the colloidal probe technique, the JKR model can be applied to calculate the work of adhesion γ_{jkr} from the force of adhesion F_{adh} and the radius of the colloidal probe (R_{cp}) as

$$\gamma_{jkr} = \frac{2}{3\pi R_{cp}} F_{adh} \tag{15}$$

We must take into account that the forces acting outside of the immediate contact area are neglected. This approximation makes the model most suitable when the surface forces are short range in comparison with the range of elastic deformations, (i.e. in cases of soft materials, strong adhesion force and large colloid radii).[23]

Derjaguin-Muller-Toporov model

The Derjaguin Muller Toporov (DMT) model was developed for the case of a plane sample in contact with a colloid.[24] In contrast to the JKR model that only considers adhesion acting in the contact area, the DMT model assumes that the contact profile remains the same as in Hertz model but includes an additional attractive interactions outside the contact area. Therefore, this contact area is slightly larger than the one derived by JKR

$$a^3 = \frac{R}{K}(P + 2\gamma\pi R) \tag{16}$$

When the pull-off force is achieved, the contact area becomes zero and there is no singularity in the contact stresses at the edge of the contact area. Therefore, the energy of adhesion calculated by this model is lower when compared to the JKR model and is calculated as follows

$$\gamma_{DMT} = \frac{1}{2\pi R_{cp}} F_{adh} \tag{17}$$

The DMT model is especially applicable in cases of stiff materials, weak adhesion forces and small colloidal radii.[23]

Daniel Maugis later formed a theory, according to which the JKR and DMT models are part of a single unified theory,[25] defining a transition parameter between them, allowing to apply an

intermediary model for cases where both contributions to adhesion, inside and outside the contact area, have to be considered. All models were developed for macroscopic bodies, and are only approximations for a detachment process of a small probe on a real substrate. Nevertheless, both JKR and DMT models have shown good agreement with experimental data.[17,26] However, to determine which model is better to apply to treat the force of adhesion data of a measurement, it is convenient to use a nondimensional physical parameter to quantify these limits and cases in between. This parameter is known as Tabor's parameter (μ_T),[27] and it is estimated as follows

$$\mu_T = \left(\frac{R_{cp}\gamma^2}{K_T^2 z_0^3}\right)^{\frac{1}{3}} \qquad \frac{1}{K_T} = \frac{3}{4}\left(\frac{1-\upsilon_1^2}{E_1} + \frac{1-\upsilon_2^2}{E_2}\right) \tag{18}$$

with z_0 the equilibrium separation of the surfaces. The value of μ_T is in fact equal to the ratio of the elastic deformation just before the surfaces separate to z_0. According to Fery and coworkers,[3,26] for μ_T < 5 the DMT theory is valid and for μ_T > 5 the JKR theory becomes appropriate.[3,28]

3.2.2. Electrostatic forces in aqueous medium

Electrostatic double-layer force and DLVO theory

It was well known that many colloids carrying the same charges in an aqueous medium coagulate after the addition of salt. The explanation for this behavior was given with the introduction of the DLVO theory, named after Derjaguin, Landau, Verwey, and Overbeek.[4,20] In the DLVO theory the interaction between two particles is assumed to consist of two contributions: the van der Waals attraction and an electrostatic double-layer repulsion (explained in the previous chapter, section 2.2.3.). If the colloidal particles have the same sign of charge, at low salt concentration the double-layer repulsion is strong enough to keep the

colloidal particles apart. When the salt concentration rises, the electrostatic interactions are screened and at a certain concentration, the van der Waals attraction overcomes the repulsive electrostatic barrier and coagulation sets in.[4]

Effect of ionic strength on the interaction forces

For the understanding of the effect of salt on the mean rupture energy of a single ionic bond, it is necessary to introduce the energy landscape of the disruption of this molecular interaction. Spruijt and coworkers,[7,29] presented a molecular rupture model for ionic bonds that quantitatively estimates the mean rupture force of a single ionic bond as a function of salt concentration in the medium and loading rate of the test. In this model, the activation energy barrier (E_a) has to be overcome by a pulling force, which is a rate-dependent phenomenon before an electrostatic bond ruptures. This model was inspired mainly by the model developed by Evans and Ritchie[30,31] of mean rupture force of single molecules as a function of temperature and loading rate, and by the Debye-Hückel theory of electrostatic double-layer forces.[20]

Without any external force, $E_a(0)$ can be estimated as the difference between the Coulombic energy of an ion pair in contact (E_C) and the electrical free energy of the separated ions at a distance equal to the screening length (E_S). According to Coulomb's Law, the energy of the electrostatic attraction (E_S) between two charged particles is proportional to the magnitude of the charges ($z_i e_0$) and inversely proportional to the internuclear distance between the particles (r):

$$\frac{E_S}{k_B T} = -\frac{z_i^2 e_0^2}{4\pi\varepsilon_0\varepsilon_r k_B T r} = -\frac{z_i^2 \lambda_B}{r} \tag{19}$$

where z_i is the charge number of ion species, e_0 is the elementary charge, ε_r is the dielectric constant of the medium, ε_0 the vacuum permittivity and λ_B the Bjerrum length

$$\lambda_B = \frac{e_0^2}{4\pi\varepsilon_0\varepsilon_r k_B T} \tag{20}$$

corresponding to the distance at which the electrostatic interaction between two elementary charges is comparable in magnitude to the thermal energy k_BT. For two monovalent charges, located at a distance equal to the Debye-length (λ_D), which correspond to the thickness of the electric double layer, the free energy can be written as

$$\frac{E_S}{k_BT} = -\frac{\lambda_B}{\lambda_D}$$

where the Debye-length can be calculated as follows

$$\lambda_D = \sqrt{\frac{\varepsilon_0 \varepsilon_r k_B T}{2N_{av} c_\infty e_0^2}} = \frac{1}{\sqrt{8x10^3 \pi \lambda_B N_{av} c_\infty}} \tag{21}$$

where c_∞ is the salt concentration in mol/L. For instance, water (ε_r = 80) at room temperature (T=300K), λ_B is 7.1 x 10^{-10} m. On the other hand, the Coulombic energy of an ion pair in close contact, separated by an internuclear distance (r_0) which is around 0.3 nm, can be written as

$$\frac{E_C}{k_BT} = -\frac{\lambda_B}{r_0} \tag{22}$$

Therefore, combining the expressions for E_C and E_S the activation energy barrier E_a as function of salt can be expresses as:

$$E_a(0) = E_S - E_C = -\left(\frac{\lambda_B}{\lambda_D} + \frac{\lambda_B}{r_0}\right) k_BT = \left(-\sqrt{8x10^3 \pi \lambda_B^3 c_\infty N_{av}} + \frac{\lambda_B}{r_0}\right) k_BT \tag{23}$$

where, $E_a(0)$ is therefore, the activation energy barrier before applying any external force in Joules. On the other side, when a constant force $f(t)$ is applied, a change in the activation energy barrier occurs as function of this force with a dissociation rate (k_{off}). Evans and Ritchie describe the rate of escape from the bound state (dP/dt) as a first-order process[32–34]

$$\left(\frac{dP}{dt}\right) = k_{off} P(t) \tag{24}$$

k_{off} is function of the constant force and tends to lower the activation energy as follows

$$k_{off}(f) = \frac{1}{\tau_D}\exp\left(\frac{E_a(0) - f^* x_\beta}{k_B T}\right) \tag{25}$$

where τ_D is the characteristic diffusion time of motion in the system and x_β is the distance between the bound state and the transition state (**Figure 3-4**), which can be surprisingly small since $k_B T$~4x10^{-21} J at room temperature and x_β can reach ~ 0.1 nm.[33] The solution for equation 23 derived by Evans[30,34] is the force *f** with maximum probability of bond failure in the case of constant force loading rate ($r_f = V_{deb} k_s$):

$$f^* = \frac{k_B T}{x_\beta}\ln\left(\frac{x_\beta \tau_D r_f}{k_B T}\mathrm{e}^{(E_a(0)/k_B T)}\right)$$
$$f^* = \frac{k_B T}{x_\beta}\ln\left[\frac{x_\beta \tau_D}{k_B T}\mathrm{e}^{(E_a(0)/k_B T)}\right] + \frac{k_B T}{x_\beta}\ln r_f \tag{26}$$

Equation 26 predicts a logarithmic dependence of the bond breakage force of a single electrostatic interaction with the force loading rate with the slope equal to $f_\beta = k_B T/x_\beta$. Thus, providing a way to extract the value of x_β from the experimental data. Finally, a combination of equations 23 and 26 provides a prediction for the effect of ionic strength and the force loading rate on the mean rupture force (f^*) on a single ionic bond

$$f^* = f_\beta\left[\ln\left(\frac{\tau_D r_f}{f_\beta}\right) - \sqrt{8x10^3 \pi \lambda_B^3 c_\infty N_{av}} + \frac{\lambda_B}{r_0}\right] \tag{27}$$

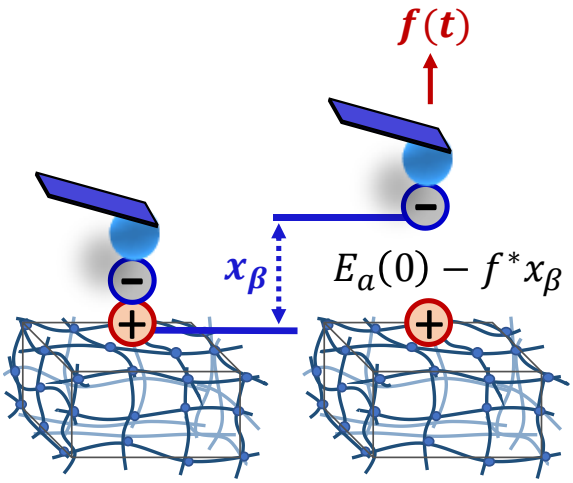

Figure 3-4. Schematic energy process when breaking an ionic bond with a constant force.

3.3. Experimental

3.3.1. Chemicals

All chemicals were used as received from the supplier. For the macroscopic hydrogels, 2-(methacryloyloxy)ethyltrimethylammonium chloride 80 wt. % in H_2O (MAETAC), acrylamide for electrophoresis, ≥99% (AAm), N,N'-methylenebisacrylamide (MBA), potassium persulfate (KPS) and tetramethylethylenediamine (TEMED) were purchased from Sigma-Aldrich, France.

For the synthesis of hydrogel thin films, allylamine, 1-ethyl-3-(3-dimethylaminopropyl)carbodiimide hydrochloride (EDC), N-hydroxysuccinimide (NHS), 1,4-dithioerythritol, toluene dried (max. 0.005% H_2O), formic acid and methanol were all purchased from Sigma-Aldrich, France. Additionally, poly(acrylic acid) (PAA with M_W ~ 50 kg/mol, 25 wt% in water was obtained from Polysciences. (3-Mercaptopropyl)trimethoxysilane was obtained from Alfa chemistry. Silicon wafers were purchased from ACM, France.

For the colloidal probes, Silica particles were purchased from Micro Particles GmbH, Germany. Ethanol abs. (EtOH, 99.9%) was purchased from VWR, Germany. Additionally, 3-aminopropyl-triethoxysilane (APTES, ABCR, 97%), anhydrous dichloromethane (99.8%), chloroform (99%), triethylamine were purchased from Fluka, Germany. Finally, a-bromoisobutyryl bromide (BrIn, 98%), tert-butyl acrylate, copper(II) bromide (CuBr2, 99.999%), N,N,N´,N´´,N´´-pentamethyldiethylenetriamine (PMDTA, 99%), Sn(II) 2-ethylhexanoate (99%), ethyl α-bromoisobutyrate (EBiB, 98%), toluene and methanesulfonic acid were purchased from Sigma Aldrich, Germany.

3.3.2. Hydrogel synthesis

A series of positively charged hydrogels was prepared by free radical copolymerization in water using a cationic monomer (MAETAC), a neutral comonomer (AAm) and a

tetrafunctional crosslinker (MBA). Within this series, the total monomer concentration was fixed at 20 wt% (80 wt% in water), the MAETAC/AAm molar ratios at 10/90 (10% MAETAC and 90% AAm), and 3 different molar percentages of crosslinker (R=1, 2 and 4 mol% with respect to total monomers).

After dissolution at room temperature of the comonomers in Milli-Q water (pH 5.5), the KPS initiator was added (1 mol% relative to the total monomer) and the solution was deoxygenated under N_2 flow during 30 min. Then, as soon as the reducing agent TEMED was added (1 mol% as KPS), the solution was transferred to a PDMS mold of 0.1 cm x 2 cm x 4 cm size. The redox initiation rapidly took place and the polymerization was left to proceed overnight under nitrogen atmosphere. The mold was then opened, and the 1 mm thick gels were immersed and stored in 1 L of Milli-Q water until final use. The poly(MAETAC-*co*-AAm) hydrogels prepared in this way were called Ry, with y = 1, 2 or 4 mol% the molar percentage of crosslinker with respect to the monomers (**Table 3-1**).

Hydrogel	Q_0	C_e (wt%)	Λ_e	E_0 (kPa)	E_e (kPa)
R1	6.3	4.9	21.1	123 ± 18	99.6 ± 20.1
R2	6.3	10.2	9.8	232 ± 8.4	207 ± 18.9
R4	6.3	15.7	6.4	433 ± 6.9	456 ± 74.4

Table 3-1. Composition and characteristics of cationic hydrogels as measured in Chapter 2. Initial volume swelling (Q_0), total polymer concentration at swelling equilibrium (C_e), mass degree of swelling at equilibrium (Λ_e), Young's modulus in the preparation conditions (E_0) and at swelling equilibrium (E_e). Both moduli are presented as average ± standard deviation.

3.3.3. Synthesis of negatively charged hydrogel thin films

Surface-attached thin hydrogel films were spin coated by simultaneously crosslinking and grafting pre-functionalized poly(acrylic acid) (PAA) onto thiol-modified silicon wafers. The

crosslinking and grafting took place through a thiol−ene click reaction following the procedure already presented in Chapter 2, section 2.3.3, which will be briefly described in the following paragraph.

A thin layer of PAA functionalized with ene-groups (see NMR spectrum of chapter 2. Figure 4.) was deposited on the thiol-modified wafers by spin-coating from a 2 wt% solution in methanol and formic acid (70% methanol and 30% formic acid) containing also dithioerythritol. The conditions of spin-coating were fixed with a final angular velocity of 3000 rpm and a spinning time of 15 s. After spin coating, the dry films were annealed at 120°C for 24 h under vacuum to activate the thiol−ene reaction. Finally, the wafers were cleaned with water and then cleaved into pieces of 5 mm x 5 mm. Ellipsometry measurements were used to corroborate that the thiol-ene reaction effectively took place and that PAA thin films were grafted to the silicon wafer.

3.3.4. Underwater Tack Test

Briefly, the adhesion test consisted in forming a parallel contact and detachment between a macroscopic positively charged hydrogel (thickness ~ mm) and a negatively charged thin hydrogel film (thickness ~ nm) while both are fully immersed in an aqueous environment. The 5 mm x 5 mm wafer coated with the surface-grafted PAA hydrogel thin film was glued with a polyvinyl acetate adhesive (ref. L0196, 3M®, France) to a stainless-steel probe, which was fixed to a 10 N load cell and connected to a universal tensile machine (model 5333, Instron®, France). A sample of poly(MAETAC-*co*-AAm) hydrogel (20 mm x 20 mm x 1 mm) was glued to a glass microscope slide with a cyanoacrylate adhesive (Loctite® 495, France). Additionally, the thin film is protected with a stretched layer of Parafilm® during the alignment in air. After this alignment, the contact was made underwater at an approaching rate of 10 µm/s with a contact area determined by the surface of the silicon wafer functionalized by the PAA thin film.

A preload of 3 kPa was applied for a given constant contact time that was varied from 1 s to 1200 s. Finally, the probe was detached at a constant debonding rate (V_{deb}) while recording the probe displacement and the force. From this experiment, the work of adhesion W_a can be calculated as follows:

$$W_a = T_0 \int_0^{\varepsilon_{max}} \sigma d\varepsilon \quad (28)$$

where ε is the nominal strain and is obtained by normalizing the displacement by the initial thickness of the thick hydrogel (T_0). σ is the average stress and is obtained by dividing the force by the contact area. Three replicates were conducted for each experiment.

3.3.5. Colloidal probe synthesis

Initiator-modified colloidal particles

Silica particles (diameter: 19.59 µm) were stirred for 24 hours in a 5% APTES solution in ethanol to introduce amino groups onto the surface. The APTES-modified particles were purified by several washing and centrifugation cycles in ethanol and were dried at 60°C. The dried APTES-modified particles were suspended in dry dichloro-methane (35 ml) and α-Bromoisobutyryl bromide was added. Then, triethylamine was added to the suspension. The reaction mixture was stirred at room temperature for two hours. The BrIn-functionalized particles were collected by centrifugation, washed in dichloromethane and ethanol, and were dried under reduced pressure.

Colloidal probes covered with Poly acrylic acid (PAA) brushes

50.2 g of initiator-modified particles were dispersed in 5 mL of tert-butyl acrylate. 70 µL of CuBr2 (catalyst) and 70 µL of PMDTA (ligand for copper ions) were added, along with 0.15 µL of EBIB as initiator in the bulk solution. The mixture was purged with Ar for 10 minutes, then 150 µL of Sn(II) 2-ethylhexanoate (reducing agent) were added and the polymerization

was carried out for 5 h at 115°C. Afterwards, the particles were washed multiple times with chloroform, toluene and ethanol abs., and then were dried in a vacuum oven at 40°C.

The PAA functionalities were obtained by deprotection of the tert-butyl units: the particles were dispersed in 5 mL of chloroform and 2 mL of methanesulfonic acid for 4 h. Afterwards they were washed multiple times with chloroform and ethanol abs. and were dried in the vacuum oven at 40°C.

(a) (b) (c)

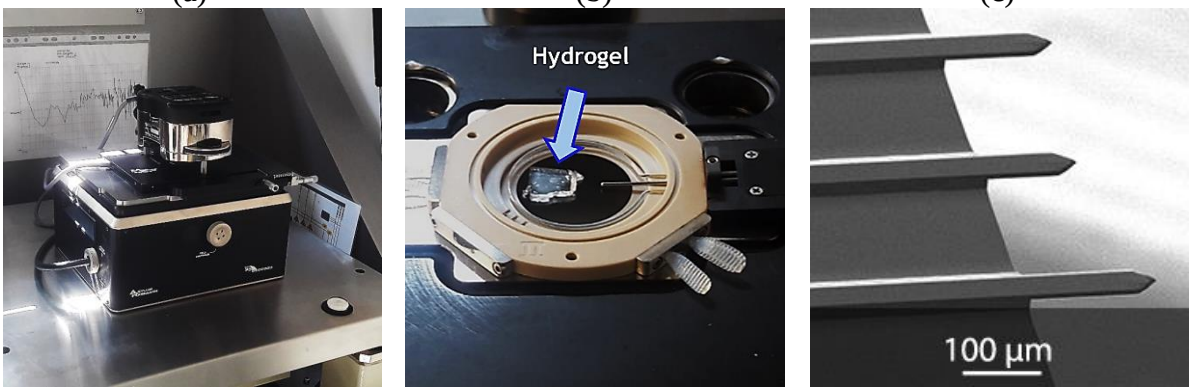

Figure 3-5. (a) AFM (MFP-3D, Asylum Research Inc., USA). (b). AFM BioHeater fluid cell with a poly(MAETAC-*co*-AAm) hydrogel sample of approximately 1 cm x 1 cm size. (c) Cantilever series of NSC36. Mikromash, USA.

3.3.6. Underwater AFM Colloidal probe test (AFM-CP)

An AFM (MFP-3D, Asylum Research Inc., USA), equipped with a BioHeater fluid cell with heating element (Asylum Research Inc. USA) was used for cantilever calibration and force measurements (**Figure 3-5**). Cantilever series of NSC36, tipless and without aluminum coating cantilevers (Mikromash, USA) were used for all experiments.

Cantilever calibration and samples preparation

For determination of the spring constant, the OLS was determined by performing at least nine force measurements against a cleaned microscopy glass slide, then the thermal oscillation method (as described in section 3.1.1.) was used to determine spring constant.

Using a micromanipulator (MP-285, Shutter Instrument, USA) on an optical microscope and glass capillary (modified to have a sharp edge of a few micrometers), a small droplet of a two component epoxy resin (UHU plus endfest 300, UHU GmbH, Germany) was applied on the pre-calibrated AFM cantilever (0.7-1.5 N/m). Right after, a colloidal probe was placed on top of the glue using a second modified glass capillary (**Figure 3-6**). Special care was taken when leaving the colloidal probe covered with the epoxy adhesive. After hardening of the adhesive, cantilevers with probes were briefly submerged in DI-water and ethanol, to clean the colloid surfaces and confirm sufficiently strong attachment. After 24 h of drying, the sample was ready for an adhesion test.

(a) (b) (c)

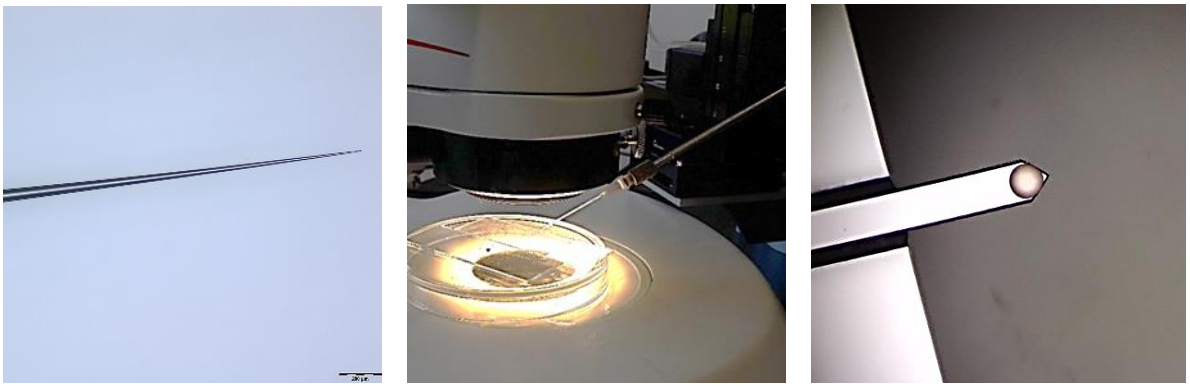

Figure 3-6. (a) Microscope image of the edge of a the modified glass capillary used in the micromanupulator. Scale bar of 200 µm. (b) Setup, micromanipulator, glass capillary. (c) Microscope image of a colloidal probe (20 µm diameter) glued to a cantilever. 40x magnification.

A 5 x 5 mm piece of Poly(MAETAC-AAm) hydrogel is cut and placed on a glass slides. Electrolyte solutions were prepared at different NaCl concentration (5mM, 10mM, 150mM and 500mM). Sample and cantilever were given at least 30 minutes time to equilibrate in the solution used for the measurement. OLS was determined by performing at least nine measurements in a zone of a glass slide without hydrogel (a hard surface is necessary to have a linearity and estimate the OLS). The maximum compressive force applied to the probe upon approach was set constant to 10 nN. The piezo movement speed for bonding the colloidal probe to the hydrogel was set to 5µm/s, and the detachment movement was varied between 50 nm/s, 100 nm/s, 500 nm/s and 5000 nm/s. Three force maps (20µm x 20µm), each consisting of 16 single force measurements, were made in a box pattern around a random spot on the hydrogel surface.

3.4. Results

3.4.1. Macroscopic hydrogels, PAA hydrogel thin films and PAA colloidal probes

The macroscopic hydrogels used in this chapter were characterized by swelling and compression tests as described in Chapter 2. Section 2.3.4. Moreover, the R2 hydrogel was immersed in mediums with different salt concentrations and its equilibrium swelling behaviour was studied. For equilibrium swelling studies, hydrogels were initially weighted in their preparation state before immersion into a large volume of Milli-Q water at different NaCl concentration (5mM, 10mM, 150mM and 500mM). After 3 days of equilibrium, the swollen samples were weighted again (m_s) and then dried overnight in an oven (at 60 °C) in order to get their final dry weight (m_d). These measurements can be used to calculate the mass swelling ratio at equilibrium ($\Lambda_e = m_s \,/\, m_d$). Λ_e of the poly(MAETAC-co-AAm) hydrogels was found to decrease with increasing concentration of aqueous NaCl solution as expected (**Table 3-2**).

NaCl (mM)	Q_0	Λ_e	C_e (wt%)
0	6.3	9.8	10.2
5	6.3	8.8	11.4
10	6.3	6.5	15.6
150	6.2	6.4	15.4
500	6.2	6.0	16.7

Table 3-2. Equilibrium swelling behaviour of hydrogel R2 at different NaCl concentrations. Initial volume swelling (Q_0), total polymer concentration at swelling equilibrium (C_e), mass degree of swelling at equilibrium (Λ_e).

PAA hydrogel thin films were chemically stable underwater and presented a dry thickness of 144.1±1 nm. As presented in the previous chapter, the swelling ratio for these films increases from 1.39 ± 0.1 at pH 2 to 1.75 at pH 8, while the water volume fraction increases from 0.28 at pH 2 to 0.44 at pH 8. Finally, according to the GSGC model, at pH 5.5 the interfacial charge density is Σ_i ~3 x10^{-2} $n\mathrm{COO}^-$/nm^2.

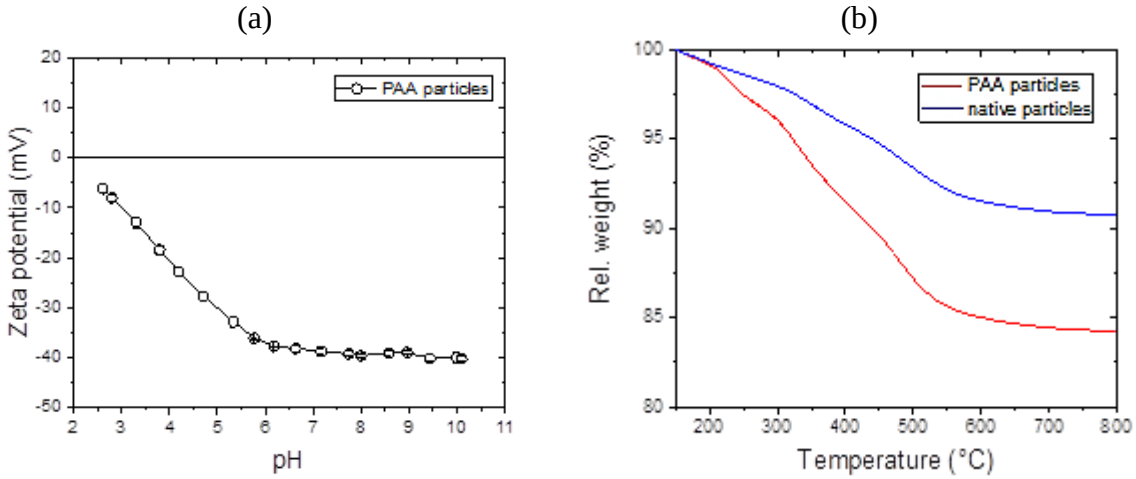

Figure 3-7. (a) Streaming potential of PAA colloidal particles in KCl at 1 mM. (b) TGA on native silica particles and on PAA-modified particles.[35]

Furthermore, PAA colloidal probes were produced via "grafting from" approach. Confirmation of the presence of the PAA functionalities after deprotection was confirmed via electrokinetic measurement of streaming potential as shown in **Figure 3-7.a**. The modified particles have the point of zero charge at pH 2.5, which is consistent with several electrokinetic measurements reported in literature. After pH 7, the zeta potential reaches a plateau ($\zeta_{plateau} = -40\ mV$) that corresponds to the complete ionization of the carboxylic functionalities. By using the GSGC model, (Chapter 2, equation 13 and 14) the number of acidic groups capable of dissociating per unit area is calculated to be around ~ 2 x10^{-2} $n\mathrm{COO}^-$/nm^2. Therefore, at pH 5.5 the total surface charge density is around ~ 1 x10^{-2} $n\mathrm{COO}^-$/nm^2.

Additionally, the presence of polymer chains on the particles has been further confirmed by performing TGA measurements as shown in **Figure 3-7.b**. From TGA measurements and by knowing the molecular weight of the polymer chains, the grafting density of PAA brushes on the colloidal particles (σ_{i-c}) can be estimated by applying the following equation[35]

$$\sigma_{i-c} = \frac{R_s \rho_s \phi_{p-w} N_{av}}{3M_n(1-\phi_{p-w})} \qquad (29)$$

where $R_s = 10$ μm is the radius of silica particle, $\rho_s = 2.65$ g/cm^3 is the mass density of silica, ϕ_{p-w} is the mass fraction of the polymer (obtained using TGA measurements); $M_n = 50$ kg/mol is the average molar mass of polymer chains, and N_{av} is the Avogadro's number. Therefore, by using equation 29, the PAA grafting density on the colloidal probe is $\sigma_{i-c} = 0.2\ chains$/nm^2.

3.4.2. Underwater tack test. Salt effect on W_a

Probe-tack tests are used to measure the energy required to separate the negatively charged surface from the positively charged hydrogel without breaking any covalent bonds within either of the hydrogels. For this reason, W_a between each hydrogel and thin film was first measured as a function of different repetitions in the same spot as shown in the previous chapter (Section

2.4.3. Figure 14). When W_a remained constant for consecutive contacts in the same spot, the value of the first contact was used to compare the effect of salt concentration on W_a and the maximum stress (σ_{max}) measured in the stress-strain curves.

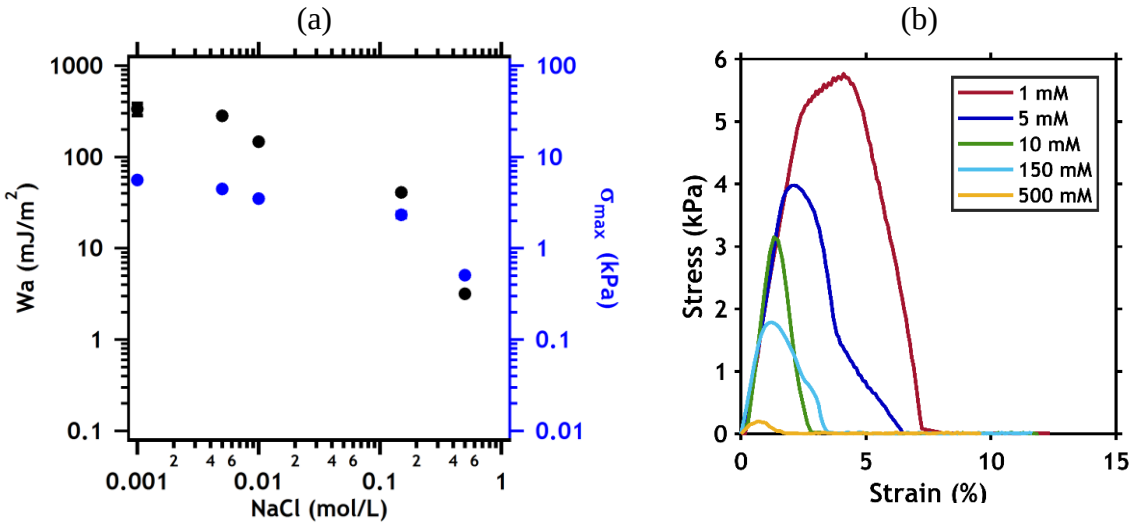

Figure 3-8. (a) Adhesion energy in solutions containing different salt concentrations (NaCl concentration is in M). Phosphate buffer solution (PBS) was used for the experiment at 0.138 M. (b) Stress-strain debonding curves for Poly(MAETAC-co-AAm) hydrogel R2 and a PAA thin film (dry thickness of 150 nm) in different salt concentrations.

The adhesive interactions between molecules are screened when running the experiments in water with salt. The effect of screening by salt (using NaCl) of charge-charge interactions on macroscopic underwater adhesion was studied by characterizing the macroscopic adhesion between the R2 hydrogel and a PAA thin film (dry thickness ~150 nm). The adhesion energy was measured as a function of salt concentration in the medium (**Figure 3-8.a**). W_a decreased slightly between 1mM and 10 mM (>100 mJ/m^2) but significantly decreased by two orders of magnitude from around 300 mJ/m^2 in 1 mM of NaCl to around 2 mJ/m^2 at 500 mM of NaCl. Additionally, the maximum stress decreased also slightly between 1mM and 10 mM (between 3-5 kPa) but significantly decreased by one order of magnitude from around 5 kPa in 1 mM of

NaCl to around 0.3 kPa at 500 mM of NaCl (**Figure 3-8.b**). This simply occurred because less force is needed to separate the two surfaces when more interactions are screened. Moreover, it was not possible to conduct a probe-tack test with a salt concentration above 0.5 M since the maximum force was in the same values (~1 mN) of the load cell noise.

3.4.3. Underwater AFM-CP test

Force maps

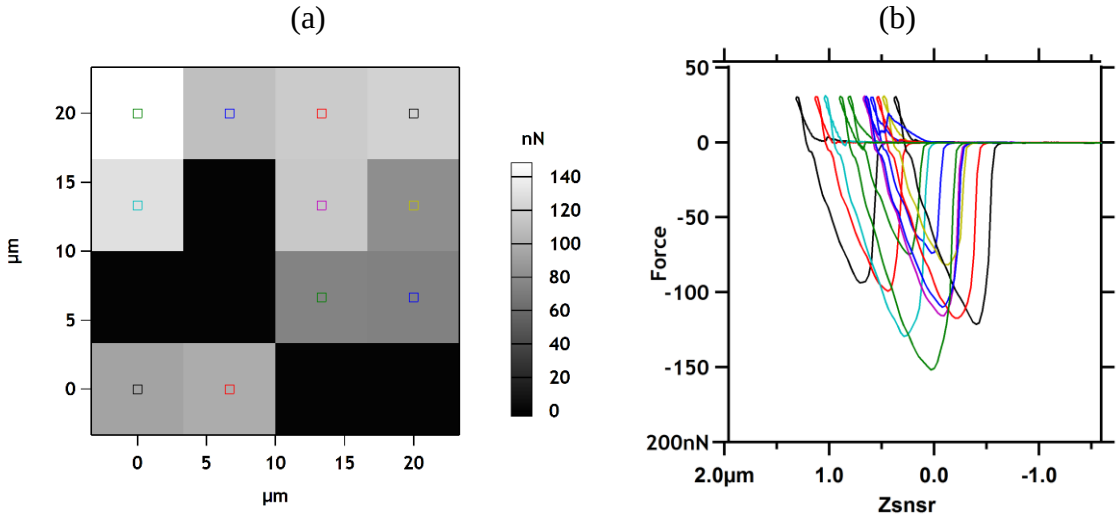

Figure 3-9. (a) Example of a 20µm x 20µm force map containing 16 single force measurements. Grey scale represent the peak force of each force measurement. Squares in black are tests without a peak of adhesion force. (b) Raw data of the force map with the respective curves of force vs. piezo displacement ($\boldsymbol{Z_{snsr}}$).

Three to four force maps of deflection (V) over z-piezo position (Z_{snsr}) were conducted for each variable in the present study. Each force map consists on 16 individual force measurements given a total of 64 force-displacement measurements (**Figure 3-9**). Each individual force measurement was processed according to the procedure described in section 3.1.2. Only the average adhesion force ± 2 x the standard deviation is reported from entire measurements of

the force maps. Measurements outside this range were considered outliers due to an irregular variation of the substrate, and were removed from the analysis. Moreover, the reproducibility of our data was checked by comparing the post-processed data of force-displacement curves with different samples of PAA colloidal probes and different samples of the same hydrogel. (**Figure 3-10**).

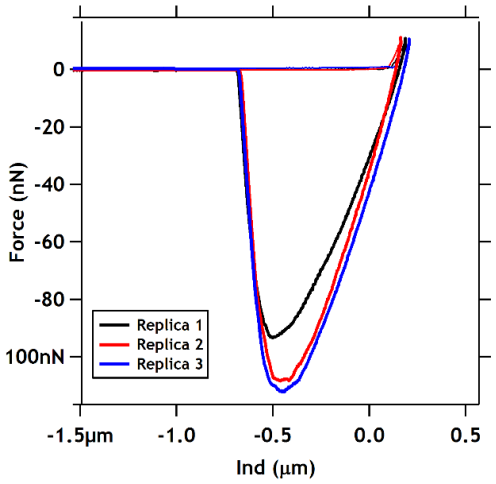

Figure 3-10. Force distance (Ind) curves of raw data from AFM-CP measurements between R2 hydrogel and a PAA colloidal probe. Three replicas with different CP and different macroscopic R2 hydrogel.

Using the measured force of adhesion and using the contact models given in section 2.1.2 the energy of adhesion was calculated. However, to analyze our data we have to decide which theory of contacts mechanics is suitable to describe our system. For the macroscopic hydrogel surface ($R_1 \sim \infty, E_1 = 0.1 - 0.5\ MPa, \nu_1 = 0.5$) touching a hard colloidal probe covered with a polymer brush ($R_2 = 20\mu m, E_2 = 2 - 4GPa, \nu_2 = 0.1 - 0.5$),[36] the effective radius of curvature R reduces to R_2 and the effective modulus of the system K lies between 0.11 MPa and 0.44 MPa. Assuming z_0 is 0.5 nm, and typical thermodynamic work of adhesion of w= 10 mJ/m^2 the Tabor parameter (equation 17) lies in the range of $\mu_T > 6.5$. Therefore, our system

is in the JKR regime and the work of adhesion is estimated using equation 14 where $\gamma_{jkr} = W_a$ and F_{adh} is the peak force in a AFM-CP test.

Kinetics of bond formation and disruption, V_{deb} and contact time effect on W_a

The previous chapter has shown that the macroscopic underwater adhesion from electrostatic interactions increased weakly with contact time (in stark contrast with the case of H-bonds) but strongly with debonding rate. These two parameters were studied at a smaller scale by using the AFM-CP between R2 hydrogel and the PAA colloidal probe underwater at 1 mM NaCl concentration. If one of the materials shows viscoelastic deformation, the contact area and adhesion force increase with contact time. However, since the macroscopic hydrogel is purely elastic, no dependence of the adhesion force on contact time is expected. **Figure 3-11.a** shows the work of adhesion as function of the contact time applied between the PAA colloidal probe and the R2 hydrogel at a V_{deb} of 5µm/s. The contact time was varied between 0-10 seconds. For a zero contact time, the colloidal probe is detached from the hydrogel as soon as it reaches the maximum compression force of 10 nN. The contact time dependence was compared for the macroscopic hydrogels R1 and R2. When the contact time was varied, adhesion forces increased with contact times up to 1 s and remained fairly constant if the contact time was further prolonged to 10 s for both macroscopic hydrogels. This suggests that the electrostatic interactions at the interface are formed as soon as both surfaces come into contact for more than 1 s and the surface density of interactions remains relatively constant thereafter. Additionally, R1 showed a higher adhesion energy compared to R2 as expected from the effect of the degree of crosslinking as discussed in the previous chapter, however, a more systematic effect of degree of crosslinking on W_a at a microscopic scale will be discussed in the following section.

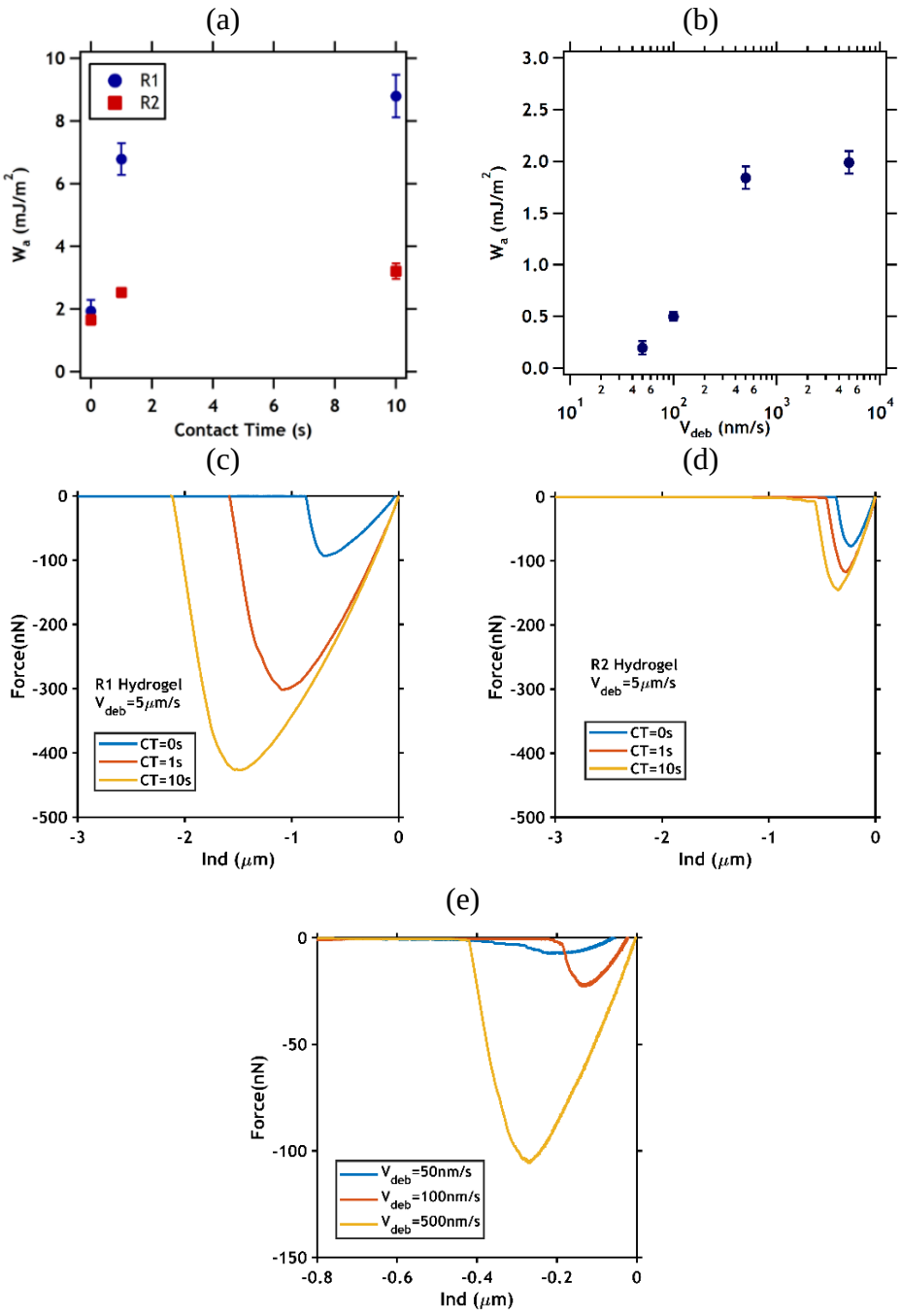

Figure 3-11. Variation of the adhesion energy measured in Milli-Q water (pH 5.5, NaCl 1mM) between poly(MAETAC-*co*-AAm) hydrogel (R1 and R2) and a PAA colloidal probe as a function of contact time (a) and V_{deb} (b). The impact of these two parameters on the adhesion energy ($\boldsymbol{W_a}$) are detailed with force-displacement curves which have been plotted as a function of contact time at a given debonding rate of 5 µm/s for (c) R1 and (d) R2. Or as a function of debonding rate at a fixed contact time of 1 second for R2 hydrogel.

The kinetic processes are studied by changing the loading rate (V_{deb}) of the disruption process.[7] If the separation process is dominated by the kinetics of ion pair disruption (weak interaction) the rupture force is expected to scale logarithmically with the debonding rate.[30,32] **Figure 3-11.b** shows the adhesion energy increasing linearly as function of debonding rate until a V_{deb} of 500 nm/s. Values higher than 5000 nm/s where not considered as hydrodynamic forces mislead the peak force results.

Effect of the degree of crosslinking on W_a

The impact of the hydrogel bulk mechanical properties on the microscopic W_a was studied by varying the degree of crosslinking *R* in the hydrogel while measuring its adhesive properties against the same PAA colloidal probe. The hydrogels were kept in Milli-Q water until they reached a swelling equilibrium. Afterwards, adhesion tests were conducted underwater (1 mM NaCl) with a contact time of 1 second and a debonding rate of 5 µm/s. Three force maps (16 force measurements per map) were done for each hydrogel.

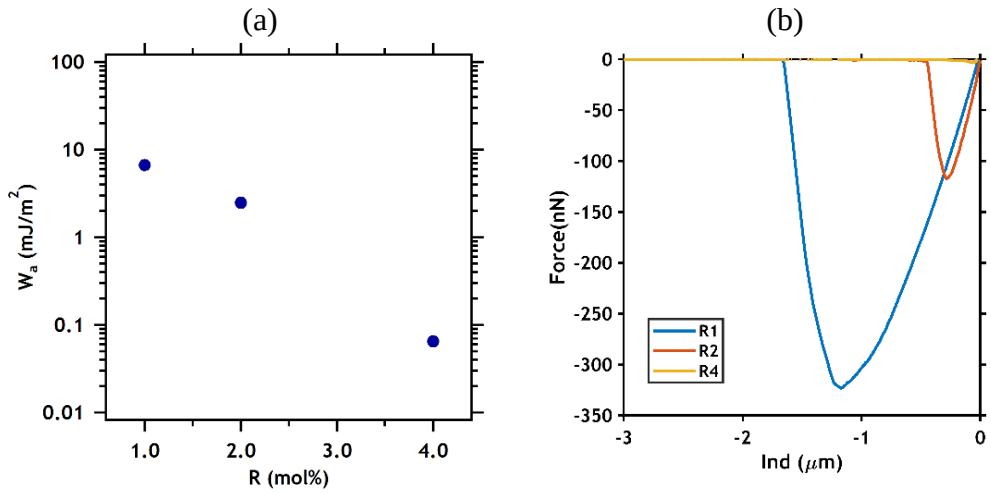

Figure 3-12. (a) Adhesion energy as a function of degree of crosslinking. (b) Representative force-displacement curves for hydrogels with different values of R at a contact time of 1 s and V_{deb} = 5µm/s.

The adhesion energy measured as a function of R (**Figure 3-12**) shows that W_a decreased by a factor of 3 between 1 mol% (~7 mJ/m^2) and 2 mol% (~2.5 mJ/m^2), however, between R1 and R4 the adhesion energy decreased by two orders of magnitude reaching an adhesion energy of ~0.06 mJ/m^2 for the most crosslinked gel. The force-displacement curves (Figure 12.b) show that as R increases, the maximum peak force and critical displacement decrease significantly. Consequently, at a microscopic scale, it is clear that changing the hydrogel network architecture, such as changing the length of the chains between crosslinks, could lead to a change in the adhesion energy by almost two order of magnitude.

Furthermore, it is possible to calculate the contact area with the JKR model (equation 13) and with the elastic moduli of the hydrogels as found in the compression tests (Chapter 2. Section 2.4.1. **Figure 2-11**). In **Table 3-3** are summarized the average contact width (a) and its corresponding contact area (A_c) as calculated using equation 13, assuming an elastic modulus of 4 GPa for the colloidal particle[36] and a poisson ratio of 0.5 for both the hydrogel and the colloidal particle.

Hydrogel	$\boldsymbol{a}$ **(μm)**	$\boldsymbol{A_c}$ **(μm^2)**
R1	5.75	104
R2	3.24	32.9
R4	0.74	1.71

Table 3-3. Contact width and contact area as calculated by the JKR model for the three different macroscopic hydrogels.

pH effect on W_a

The molecular electrostatic interactions between the macroscopic hydrogel and the PAA colloidal probe were tuned by changing the pH of the AFM chamber, since the charge density of the PAA brushes on the colloidal probe depends on this variable. Therefore, the charge

density at the surface of the PAA colloidal probe will be maximum around pH 9, when all carboxylic groups are ionized, while in acidic conditions (pH < 3) there will be no charges and no adhesion by electrostatic interactions should be observed, as shown in the previous chapter.

The macroscopic hydrogel R2 was used for the adhesion tests at different pH values (2.0, 5.5, and 9.0). The hydrogels were kept in Milli-Q water until they reached their swelling equilibrium. Afterwards, adhesion tests were done at each specific pH and at a contact time of 1 second and V_{deb} = 5 µm/s. The adhesion energy between the R2 hydrogel and PAA colloidal probe was found to increase with pH (**Figure 3-13**) as expected from the macroscopic adhesion experiments made with the cylindrical probe.

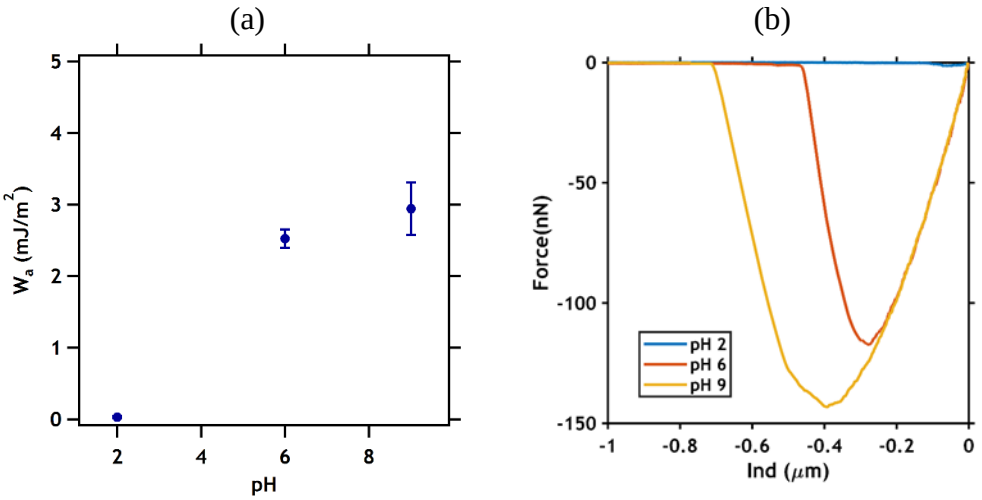

Figure 3-13. (a) Variation of the adhesion energy as a function of pH for R2 on the PAA colloidal probe in water at 1 mM of NaCl and at different pH. Contact time = 1 s and V_{deb} = 5 µm/s. (b) Corresponding AFM force displacement curves of the retraction process.

Salt concentration effect on W_a

Qualitatively, we showed in the previous section that salt has a strong effect on the interaction between oppositely charged polyelectrolyte hydrogels at a macroscopic level. Here we determine the value of the interaction force, as a function of salt concentration at the

microscopic level. **Figure 3-14** shows the adhesion energy as function of NaCl concentration and the corresponding force-displacement separation curves for a fixed V_{deb} of 5 µm/s. It was found that the rupture forces at the microscopic level indeed decrease with increasing salt concentration. The critical point is reflected by a sudden jump to a lower mean rupture force between 0.01 and 0.1 M. The nonzero residual rupture force beyond 0.1M salt is attributed to the very few electrostatic interactions that are left available.

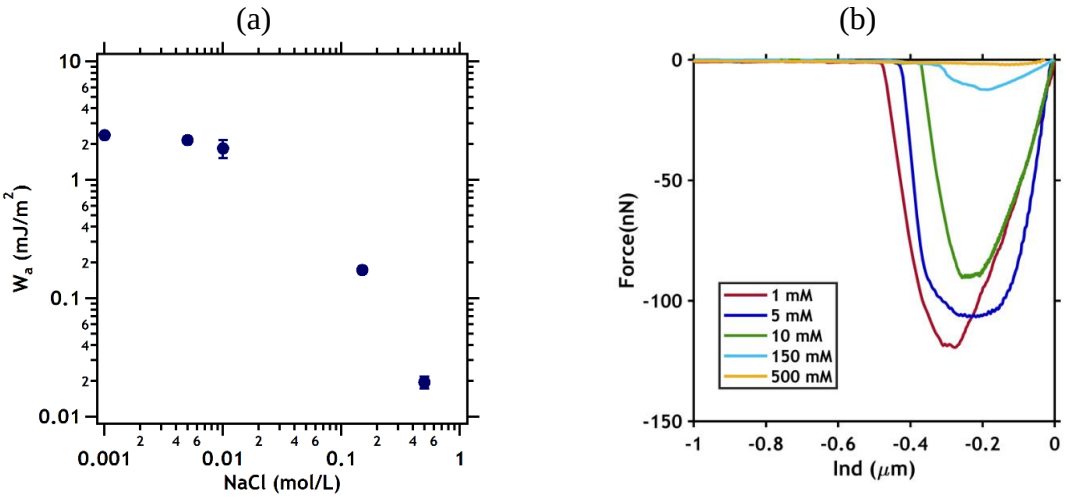

Figure 3-14. (a) Variation of the adhesion energy as a function of NaCl concentration for R2 on the PAA colloidal probe. Contact time = 1 s and V_{deb} = 5 µm/s. (b) Corresponding AFM force displacement curves of the retraction process.

3.5. Discussion

3.5.1. Scaling and predicting the salt effect on the work of adhesion

In our experiments, we found the same effect and tendency of salt concentration on the adhesion energy at both macroscopic and microscopic scales. However, the main difference is that the adhesion energy (per unit area) measured at the macroscopic level with the underwater probe-tack test is two orders of magnitude higher than at the microscopic scale as measured by

the AFM colloidal probe technique (**Figure 3-15**). Interestingly, the adhesion energy at both scales remain fairly constant between 1 mM and 10 mM but significantly decreased when tested at a salt concentration higher than 0.1 M. Additionally, a critical salt concentration of 0.5 M was found at both scales, since at higher salt concentration, no adhesion energy was measured due to the limitation of the measurement instruments. We explain this high critical salt concentration by a competition between monovalent salt ions and ionic groups on the polymer chains for the formation of ion pairs. When monovalent ions are in excess, the attractive interaction between oppositely charged polymer chains disappears.[29] For monovalent ions to dominate in the ion pair formation at the interface level, the bulk salt concentration needs to be higher than the interfacial charge density. This interfacial charge density can be estimated from streaming potential measurements as explained in detail in the previous chapter.

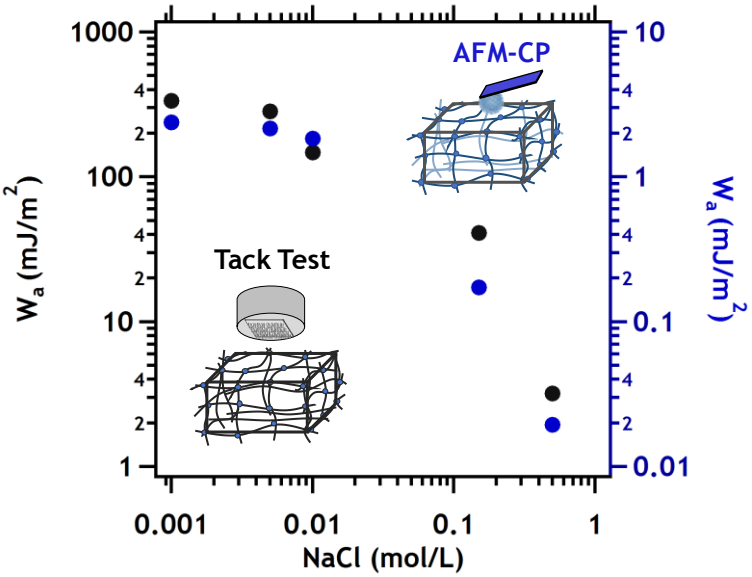

Figure 3-15. Comparison of the NaCl concentration effect on $\boldsymbol{W_a}$ at the macroscopic and microscopic scale between the same positively charged macroscopic poly(MAETAC-*co*-AAm) hydrogel (R2) and a PAA hydrogel thin film for the tack test (left *y* axis) and PAA brushes on the colloidal probe for the AFM-CP (right *y* axis).

It is possible to normalize the experimental values of adhesion energy measured at the macro and micro scale levels, when dividing the maximum force of adhesion by the number of charges at the interface. This amount of charges is calculated by multiplying the contact area (A_c) by the areal charge density as estimated from streaming potential measurements (Σ_I) Using the GCSG model, at pH 5.5 and 1 mM KCl concentration, the PAA colloidal probe has around $\Sigma_i \sim 1\ x\ 10^{-2}\ nCOO^-/nm^2$, while for the PAA hydrogel thin film is $\Sigma_i \sim 3\ x\ 10^{-2}\ nCOO^-/nm^2$. The average contact area for the probe-tack test is ~30 mm^2 and for the colloidal probe is ~30 μm^2 as shown in **Table 3-3** from the JKR model for the hydrogel R2 (**Figure 3-16**). Therefore, in the interface of the probe-tack test, there are on average $\sim 10^{12}$ ionic bonds and in the interface of the AFM-CP there are on average $\sim 10^5$ ionic bonds. Therefore, this normalization results in the estimation of a mean force to break one single bond (f^*). **Figure 3-17.a** shows f^* as function of NaCl concentration, and remarkably, both the probe-tack test and AFM-CP measurements show the same tendency and same order of magnitude of the mean force of a single ionic bond.

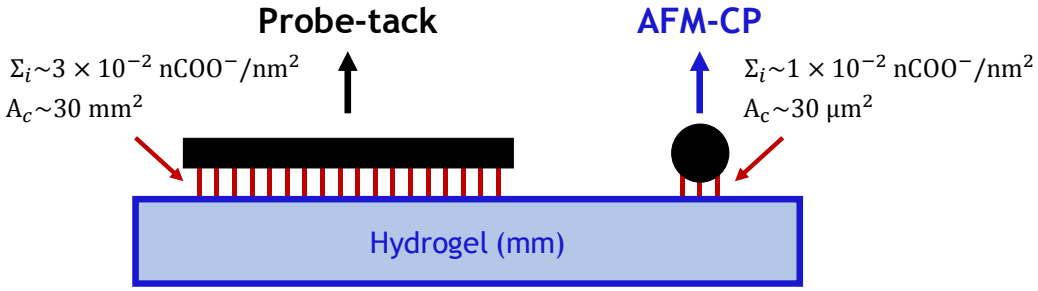

Figure 3-16. Schematic of the macroscopic hydrogel interacting with either the colloidal probe in the AFM-CP experiment or the hydrogel thin film in the Probe-tack test. Red lines represent the electrostatic bond at the interface.

By doing this normalization, several assumptions are taken into account; (i) every polycation attached to a gel chain is able to attach to a negatively charged site (on the hydrogel thin film

or on the colloidal probe). (ii) All the formed interactions between the colloidal probe and the hydrogel are broken by a parallel configuration, which is commonly reported even for single ionic force measurements.[29] For the parallel configuration, we assume that each bond rupture event is far from equilibrium with no chance of rebinding, and that the force is shared equally by all the interactions at the interface.[33] (iii) It is assumed that Σ_I will not vary significantly, as NaCl is increased in the medium. (iv) There is no cooperative effect between ionic bonds and (v) there is no coupling with bulk dissipation mechanisms.

Furthermore, it is possible to predict the mean force of a single ionic bond as function of the force pulling rate and the salt concentration in the medium by using the model presented by Spruijt and coworkers,[29] which was described in detail in section 3.2.3, equation 27.

$$f^* = f_\beta \left[\ln\left(\frac{\tau_D r_f}{f_\beta}\right) - \sqrt{8x10^3 \pi \lambda_B^3 c_\infty N_{av}} + \frac{\lambda_B}{r_0} \right] \qquad (27)$$

This model estimates f^* as function of salt concentration (c_∞ in mol/L) and the force pulling rate ($r_f = V_{deb} k_s$ in N/s), where V_{deb} is 5µm/s and k_s is the spring constant of the polymer chain (Chapter 2. **Section 2.5.2**. Equation 21. k_s= 1.1 nN/m). Additionally, τ_D was also used as in the previous chapter (Chapter 2. **Section 2.5.2.** Equation 21. τ_D= 0.11 s) and r_0 is assumed to be 0.3 nm which is a typical internuclear distance of an ionic bond.[37] Additionally, x_β was calculated to be 30.7 nm as extracted from a linear fit of f^* vs $\ln(r_f)$ as measured in the AFM-CP experiments (**Figure 3-17**).

Remarkably, the model is able to predict with the same order of magnitude the tendency of the experimental data, which is to decrease the average rupture force per ionic bond as function of salt concentration in the medium. At low salt concentration, the model predict with the same order of magnitude the experimental data, however, at salt concentration above 0.1 M a significant difference in the predicted values is observed. There are several ways to improve the prediction of the model, for instance, it is necessary to normalized the data by σ_c at each

specific salt concentration. For this information, is necessary to have streaming potential measurements of PAA samples at different ionic strength and then use the GSCG model to estimate Σ_i as function of pH and the ionic strength of the medium.

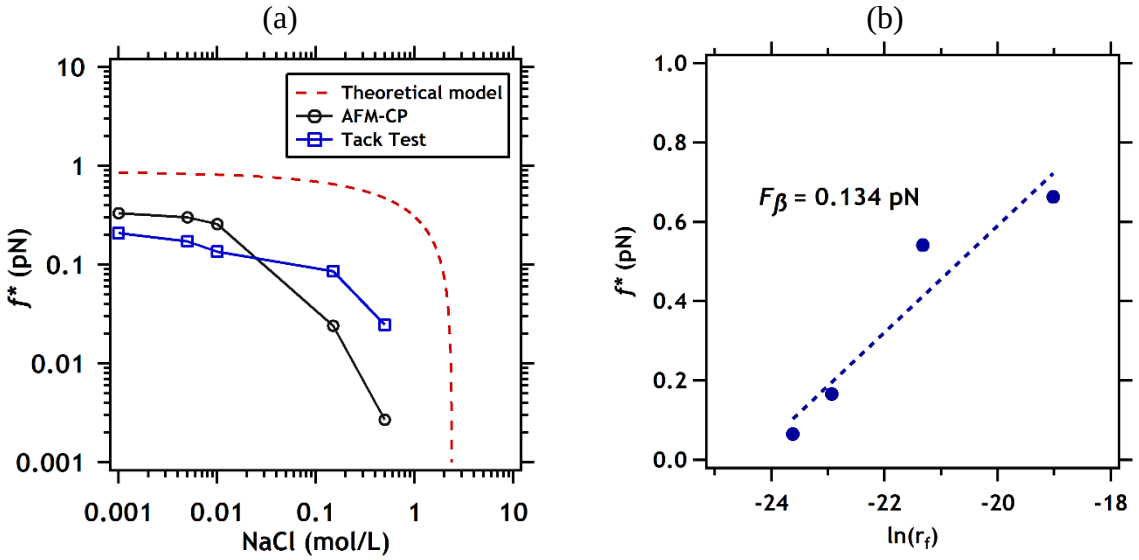

Figure 3-17. (a) The average normalized force of a single electrostatic interaction as function of NaCl concentration as measured at the macroscopic and microscopic scale between the same positive charged macroscopic poly(MAETAC-*co*-AAm) hydrogel (R2) and a PAA hydrogel thin film for the tack test and PAA brushes on the colloidal probe for the AFM-CP. The red dash line is the model from equation 27. (b) $f^* = F_{adh}/A_c\Sigma_i$ as function of $\ln(r_f)$ using the AFM-CP between the positive charged macroscopic poly(MAETAC-*co*-AAm) hydrogel (R2) and the colloidal probe.

3.6. Conclusions

The model system that we used (elastic positively charged hydrogel and negatively charged surface) leads to several conclusions at the macro and micro scales when linking molecular electrostatic interactions to underwater adhesion energy. First, the mechanical properties of the macroscopic positively charged hydrogel affect considerably the adhesion underwater as W_a

increases up to two orders of magnitude as the elastic modulus of the gel varies from 400 kPa to 100 kPa at both micro and macro scales. Second, the interfacial charge density (Σ_i) is an important parameter for the control and prediction of the adhesion energy underwater. Σ_i can be modified and/or be screened by changing the pH or the ionic strength of the medium, respectively. Third, the adhesion energy is dependent on the retraction velocity of the CP or of the macroscopic probe. This result strongly suggests that the electrostatic interactions break at forces that are dependent on the loading rate and this behavior can be explained semi-quantitatively by using the Evans model of rupture of single bonds. This model, coupled with the Debye-Hückel theory of electrostatic double-layer forces, bring us to a description of the debonding process controlled by the kinetic rupture of ionic bonds as a function of debonding rate and the ionic strength of the medium. Remarkably, the magnitude and tendency of the predictions of this model follow our experimental data at both scales (Tack test and AFM-CP), when they are normalized by the amount of charges presented at the interface.

References

(1) Ciccotti, M.; Creton, C. Fracture and Adhesion of Soft Materials : A Review. *Reports Prog. Phys.* **2016**, *79*, 046601.

(2) Shull, K. R. Contact Mechanics and the Adhesion of Soft Solids. *Mater. Sci. Eng. R Reports* **2002**, *36* (1), 1–45.

(3) Erath, J.; Schmidt, S.; Fery, A. Characterization of Adhesion Phenomena and Contact of Surfaces by Soft Colloidal Probe AFM. *Soft Matter* **2010**, *6* (7), 1432–1437.

(4) Butt, H. J.; Cappella, B.; Kappl, M. Force Measurements with the Atomic Force Microscope: Technique, Interpretation and Applications. *Surf. Sci. Rep.* **2005**, *59* (1–6), 1–152.

(5) Israelachvili, J.; Adams, G. Measurement of Forces between Two Mica Surfaces in Aqueous Electrolyte Solution. *J. Chem. Soc. Fard. Trans. I* **1978**, *74*, 975–1001.

(6) Rabinovich, Y. I.; Yoon, R. H. Use of Atomic Force Microscope for the Measurements of Hydrophobic Forces between Silanated Silica Plate and Glass Sphere. *Langmuir* **1994**, *10* (6), 1903–1909.

(7) Spruijt, E.; Stuart, M. a C.; Van Der Gucht, J. Dynamic Force Spectroscopy of Oppositely Charged Polyelectrolyte Brushes. *Macromolecules* **2010**, *43*, 1543–1550.

(8) Hu, K.; Fan, F.-R. F.; Bard, A. J.; Hillier, A. C. Direct Measurement of Diffuse Double-Layer Forces at the Semiconductor/Electrolyte Interface Using an Atomic Force Microscope. *J. Phys. Chem. B* **1997**, *101* (41), 8298–8303.

(9) Grandbois, M.; Beyer, M.; Rief, M.; Clausen-schaumann, H.; Gaub, H. E. How Strong Is a Covalent Bond ? *Science (80-.).* **1999**, *283* (3), 1727–1731.

(10) Boland, T.; Ratner, B. D. Direct Measurement of Hydrogen Bonding in DNA Nucleotide Bases by Atomic Force Microscopy. *Proc. Natl. Acad. Sci.* **1995**, *92* (12), 5297–5301.

(11) Binning, G.; Quate, C. F.; Gerber, C. Atomic Force Microscope. *Phys. Rev. Lett.* **1986**, *56* (9), 930–934.

(12) Burnham, N. A.; Chen, X.; Hodges, C. S.; Matei, G. A.; Thoreson, E. J.; Roberts, C. J.; Davies, M. C.; Tendler, S. J. B. Comparison of Calibration Methods for Atomic-Force Microscopy Cantilevers. *Nanotechnology* **2003**, *14* (1), 1–6.

(13) Li, R.; Ye, H.; Zhang, W.; Ma, G.; Su, Y. An Analytic Model for Accurate Spring Constant Calibration of Rectangular Atomic Force Microscope Cantilevers. *Sci. Rep.* **2015**, *5* (October), 1–8.

(14) Hutter, J. L.; Bechhoefer, J. Calibration of Atomic-Force Microscope Tips. *Rev. Sci. Instrum.* **1993**, *64* (7), 1868–1873.

(15) Ducker, W. A.; Senden, T. J.; Pashley, R. M. Direct Measurement of Colloidal Forces Using an Atomic Force Microscope. *Lett. to Nat.* **1991**, *353*, 239–241.

(16) Butt, H. J. Measuring Electrostatic, van Der Waals, and Hydration Forces in Electrolyte Solutions with an Atomic Force Microscope. *Biophys. J.* **1991**, *60* (6), 1438–1444.

(17) Kappl, M.; Butt, H. J. The Colloidal Probe Technique and Its Application to Adhesion Force Measurements. *Part. Part. Syst. Charact.* **2002**, *19* (3), 129–143.

(18) MikroMasch. MikroMasch SPM Probes & Test Structures https://www.spmtips.com/pdf_downloads/MikroMasch-Product-Catalogue.pdf.

(19) Kessel, S.; Schmidt, S.; Müller, R.; Wischerhoff, E.; Laschewsky, A.; Lutz, J. F.; Uhlig, K.; Lankenau, A.; Duschl, C.; Fery, A. Thermoresponsive PEG-Based Polymer Layers: Surface Characterization with AFM Force Measurements. *Langmuir* **2010**, *26* (5), 3462–3467.

(20) Israelachvili, J. N. *Intermolecular and Surface Forces*, 3 edition.; Academic Press, 2011.

(21) Hertz, H. Ueber Die Beruehrung Elastischer Koerper (On Contact Between Elastic

Bodies). *J. für die reine und Angew. Math.* **1881**, *171* (92), 156–171.

(22) Johnson, K. L.; Kendall, K.; Roberts, A. D. Surface Energy and the Contact of Elastic Solids. *Proc. R. Soc. A Math. Phys. Eng. Sci.* **1971**, *324* (1558), 301–313.

(23) Carpick, R. W.; Ogletree, D. F.; Salmeron, M. A General Equation for Fitting Contact Area and Friction vs Load Measurements. *J. Colloid Interface Sci.* **1999**, *211*, 395–400.

(24) Derjaguin, B. V.; Muller, V. M.; Toporov, Y. P. Effect of Contact Deformations on the Adhesion of Particles. *Eff. Contact Deform. Adhes. Part.* **1975**, *53*, 314–326.

(25) Maugis, D. Adhesion of Spheres: The JKR-DMT Transition Using a Dugdale Model. *J. Colloid Interface Sci.* **1992**, *150* (1), 243–269.

(26) Seuss, M.; Schmolke, W.; Drechsler, A.; Fery, A.; Seiffert, S. Core-Shell Microgels with Switchable Elasticity at Constant Interfacial Interaction. *ACS Appl. Mater. Interfaces* **2016**, *8* (25), 16317–16327.

(27) Tabor, D. *Surface Forces and Surface Interactions*; Academic Press, INC., 1977; Vol. 58.

(28) Johnson, K. L.; Greenwood, J. A. An Adhesion Map for the Contact of Elastic Spheres. *J. Colloid Interface Sci.* **1997**, *192*, 326–333.

(29) Spruijt, E.; Van Den Berg, S. A.; Cohen Stuart, M. A.; Van Der Gucht, J. Direct Measurement of the Strength of Single Ionic Bonds between Hydrated Charges. *ACS Nano* **2012**, *6* (6), 5297–5303.

(30) Evans, E. A.; Ritchie, K. Strength of a Weak Bond Connecting Flexible Polymer Chains. *Biophys. J.* **1999**, *76* (5), 2439–2447.

(31) Merkel, R.; Nassoy, P.; Leung, A.; Ritchie, K.; Evans, E. Energy Landscapes of Receptor-Ligand Bonds Explored with Dynamic Force Spectroscopy. *Nature* **1999**, *397* (6714), 50–53.

(32) Evans, E.; Ritchie, K. Dynamic Strength of Molecular Adhesion Bonds. *Biophys. J.* **1997**, *72* (4), 1541–1555.

(33) Evans, E. Probing the Relation Between Force-Lifetime-and Chemistry in Single Molecular Bonds. *Annu. Rev. Biophys. Biomol. Struct.* **2001**, *30*, 105–128.

(34) Zepeda, S.; Yeh, Y.; Noy, A. Determination of Energy Barriers for Intermolecular Interactions by Variable Temperature Dynamic Force Spectroscopy. *Langmuir* **2003**, *19* (5), 1457–1461.

(35) Marschelke, C.; Raguzin, I.; Matura, A.; Fery, A.; Synytska, A. Controlled and Tunable Design of Polymer Interface for Immobilization of Enzymes: Does Curvature Matter?

Soft Matter **2017**, *13* (5), 1074–1084.

(36) Choi, J.; Hui, C. M.; Pietrasik, J.; Dong, H.; Matyjaszewski, K.; Bockstaller, M. R. Toughening Fragile Matter: Mechanical Properties of Particle Solids Assembled from Polymer-Grafted Hybrid Particles Synthesized by ATRP. *Soft Matter* **2012**, *8* (15), 4072–4082.

(37) Kumar, S.; Nussinov, R. Relationship between Ion Pair Geometries and Electrostatic Strengths in Proteins. *Biophys. J.* **2002**, *83* (3), 1595–1612.

PART II

Bio-based system

Chapter 4

4. Underwater adhesion between oppositely charged gelatin-based hydrogels.

In the two previous chapters, we developed a detailed analytical procedure to investigate the adhesion properties between synthetic gels of opposite charges. In this chapter we propose to expand this study to bio-based hydrogels derived from gelatins. A macroscopic cationic hydrogel was prepared with gelatin type A (Gel_A; pI = 5) where pI is the isoelectric point, and an anionic hydrogel thin film was prepared with gelatin type B (Gel_B; pI= 9). Gel_A hydrogels were chemically crosslinked through amidification reaction (peptide) by using EDC/NHS as coupling agent (EDC is N,N-(3-(dimethylamino)propyl)-N'-ethylcarbodiimide and NHS is N-hydroxysuccinimide). Gel_B hydrogel thin films were crosslinked and grafted to amino-modified silica wafers by using the same chemistry. Gel_A hydrogels were characterized by differential scanning calorimetry (DSC), compression tests, swelling behavior and linear rheology. The interfacial charge density was quantified as a function of pH using streaming potential measurements on the Gel_B films, as in the previous chapters. Adhesion tests were conducted on a custom-built probe-tack setup that measures W_a when both the hydrogel and the thin film are fully immersed in an aqueous environment. According to rheological and probe-tack tests, chemically crosslinked Gel_A hydrogels at swelling equilibrium presented stable elastic properties and superior W_a against Gel_B films when compared to non-chemically crosslinked Gel_A hydrogels.

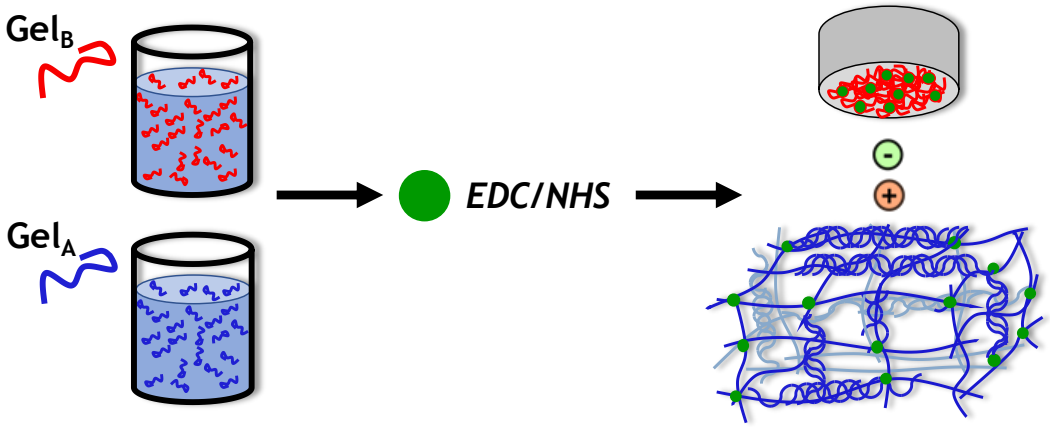

Contents

4.1. Introduction

In the previous chapter, we reported a synthetic experimental model system where the underwater adherence energy (W_a) at a macroscopic and microscopic scale, was directly related to molecular electrostatic interactions.[1] The model system that we used leads to several conclusions. First, the elastic modulus of the macroscopic positively charged hydrogel affects considerably the adhesion underwater, since the adhesion a both scales increased by making the hydrogels softer. In addition, the interfacial charge density (Σ_i) is an important parameter for the control and prediction of adhesion energy underwater. Σ_i can be modified and/or be screened by changing the pH or by increasing the salt of the medium. Secondly, the electrostatic interaction is kinetically dependent since its rupture energy at the macro and micro scales were found to be rate dependent. This behavior was explained semi-quantitatively at the micro scale level by using the Evans model of kinetic rupture of single polymer chains and at the macro scale level by using the Chaudhury's model for the kinetic bond scission of polymeric materials. Remarkably, this model is able to fit almost quantitatively our experimental data of work of adhesion as function of ionic strength and the length of the chains between crosslinks of the macroscopic hydrogel.

We now propose to extend this approach to a bio-based system using hydrogels prepared from gelatin. Gelatin is derived from the hydrolysis of collagen, and when it is produced from an acid-treated precursor, it is known as type-A (Gel_A), while gelatin derived from an alkali-treated process is known as type-B (Gel_B). Gel_A has a net positive charge below its isoelectric point pI ≅ 8 and Gel_B is negatively charged above its pI ≅ 5.[2–4] Therefore, both are oppositely charged in a pH range between 5 and 8. Moreover, the formation of thermoreversible physical gels in water is one of gelatin's most important properties. Yet, these physically crosslinked gels are neither thermally nor mechanically stable. Therefore, a method to chemically crosslink

gelatin is needed to improve its stability, necessary for soft tissue adhesion.[5] In this project, gelatin hydrogels are chemically crosslinked through the amidification reaction (or peptide coupling) using EDC/NHS coupling agent (for the carbodiimide reaction of N,N-(3-(dimethylamine)propyl)-N'-ethylcarbodiimide (EDC) and N-hydroxysuccinimide (NHS)). This amide bond formation enables to prepare macroscopic gelatin hydrogels and gelatin hydrogel films on silicon wafers. However, several questions arise from using this reaction on the formation of gelatin networks. Since the amidification reaction uses the amino groups of the gelatin polymer chains, it is not clear whether the free ionic amino groups left after crosslinking are sufficient to achieve measurable macroscopic adhesion. Another question is the chemical stability of crosslinked gelatins underwater for both macroscopic hydrogels and thin films.

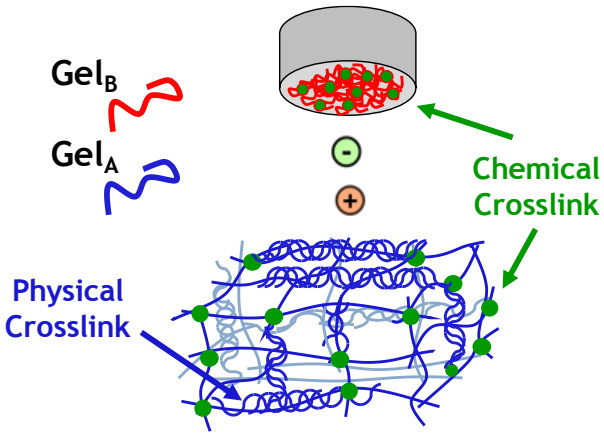

Figure 4-1. Simplified scheme of a bio-based probe-tack test underwater between a gelatin type A hydrogel (Gel_A) (thickness < 2 mm) and a gelatin type B hydrogel thin film (Gel_B) (thickness < 0.5 µm).

The main objective of this project is to study the W_a between Gel_A hydrogels and Gel_B hydrogel thin films (**Figure 4-1**). Adhesion properties are expected to be improved for chemically crosslinked gels and to decrease as the degree of crosslinking increases.

Additionally, the W_a is expected to be pH-dependent, since the interfacial charge density is pH-dependent. Gel_A and Gel_B should be oppositely charged in a pH range between 5 and 8. Outside this range, no macroscopic adhesion through electrostatic interactions is expected between Gel_A and Gel_B.

4.1.1. Gelatin physical and chemical properties

Gelatin is a high molecular weight polypeptide derived from collagen, the primary protein component of animal connective tissues, which include bone, skin and tendon.[6] The simplest way to transform collagen into gelatin is to denature soluble collagen. Thermal denaturation can take place by heating the collagen in neutral or slightly acidic conditions to about 40°C. Gelatin is nearly tasteless and odorless. It is a glassy, brittle solid faintly yellow in color. It contains 8-13% moisture and has a relative density of 1.3-1.4.[7] When gelatin granules are soaked in cold water, they hydrate absorbing 5 to 10 times their own volume of water. As soon as temperature rises, these swollen particles dissolve to form a homogeneous solution. The physicochemical properties of gelatin solutions are influenced by temperature, pH, ash content, type of gelatin, thermal history and concentration. Gelatin is also soluble in aqueous solutions of polyhydric alcohols such as glycerol and propylene glycol. Examples of highly polar, hydrogen-bonding, organic solvents in which gelatin will dissolve are acetic acid, trifluoroethanol, and formamide. Gelatin is insoluble in less polar organic solvents such as benzene, acetone, primary alcohols and dimethylformamide.

When a solution of gelatin is cooled, it is widely known that it forms a physical network (**Figure 4-2**). The basic mechanics of gelation is the random coil-helix reversion proposed by Djabourov and Papon.[8] The imino acid-rich regions of the different polypeptide chains adopt a helical conformation on cooling and these helices are stabilized by hydrogen bonding, which

gives the three-dimensional physically crosslinked hydrogel. The formation of gelatin is a partial formation of collagen and these reformed parts act as crosslink points of the hydrogel.[5,8]

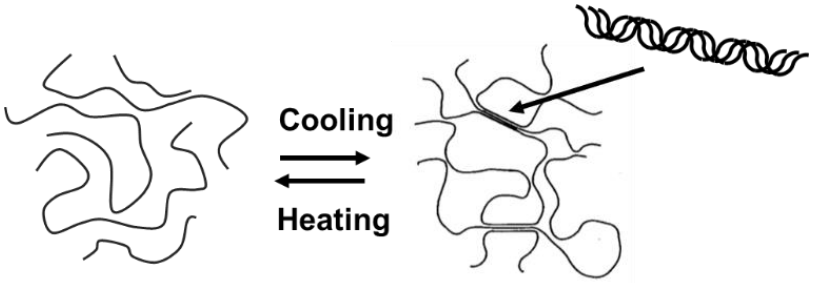

Figure 4-2. Schematic of the reversible thermal properties of gelatin, from solution to a physical gelatin network.

Bloom Number	Average Molar Mass (kg/mol)
50-125 (Low Bloom)	15 -25
175-225 (Medium Bloom)	40 -50
225-325 (High Bloom)	50 -300

Table 4-1. Approximate relation between bloom number and gelatin average molecular mass.

Gelatin is a mixture of fractions composed entirely of amino acids joined by peptide linkages to form polymers varying in molar mass from 15 to 300 kg/mol. The strength of a physically crosslinked gelatin network formed from a solution of known concentration is characterized by its Bloom number, as determined by the Bloom gelometer.[7,9] The Bloom unit is a measure of the minimum force (weight) required to lower a specified plunger (normally with a diameter of 0.5 inch) into a sample gel volume by a distance of 4 mm. The bloom number is proportional to the molar mass, the higher the Bloom number, the stronger the gel (**Table 4-1**).

In native collagen, the two acidic amino acids, glutamic and aspartic acids, are present to the extent of about 35% in the amidated form of glutamine and asparagine respectively. In the case of gelatin type B, both asparagine and glutamine amino acids are almost completely converted to aspartic and glutamic acids respectively, therefore, type A has a lower concentration of these amino acids (**Table 4-2**).[10] The rest of amino acids that are present in collagen, Gel_A and Gel_B

hardly differ between them. Hence, the main difference between type A and type B lies in the composition of the amino acids with negatively charged side chains present in gelatin, which are highlighted in **Table 4-2** with their respective pKa. On the contrary, the amino groups in both gelatins hardly differ between each other and come from the amino acids of arginine (Guanidine group, pKa ≅ 14)[11], histidine (imidazole group, pKa ≅ 6) and lysine (ε-amino group, pKa ≅ 10).

Amino acid	Structure	Type A (Pork skin)	Type B (Calf skin)
Polar basic			
Arginine	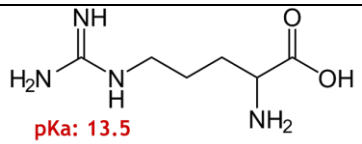	0.49-0.55	0.49-0.55
Histidine	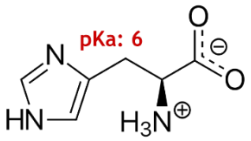	0.04 – 0.07	0.04-0.05
Lysine	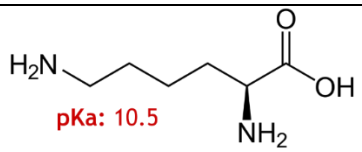	0.27-0.32	0.28-0.32
Polar acid			
Aspartic Acid	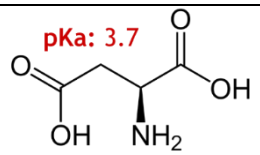	0.29 - 0.40	0.50 – 0.52
Glutamic Acid	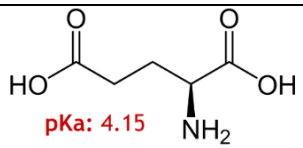	0.48 - 0.57	0.72 - 0.78
Polar uncharged side chains			
Asparagine	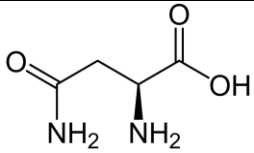	0.16	-
Glutamine	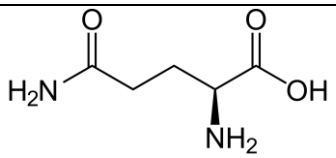	0.25	-

Table 4-2. Polar-amino acid composition of gelatin in mmol/grams of dry gelatin.[7,10,12]

Consequently, gelatin is capable of acting either as an acid or as a base. In an acid solution, the gelatin is positively charged and migrates as a cation in an electric field. In an alkaline solution, gelatin is negatively charged and migrates as an anion. The pH of the intermediate point, where the net charge is zero and no movement occurs, is known as the Isoelectric Point (pI). Type A gelatin has a broad isoelectric range between pH 8 and 9. Type B has a narrower isoelectric range between pH 4.7 and 5.4 and contains approximately 0.3 10^{-3} moles of ε-amino groups per gram of protein on the lysine residues, and approximately 1.26 10^{-3} moles of carboxylic acid groups on aspartic and glutamic acid residues.[4]

4.1.2. Gelatin-based adhesive systems

Gelatins have been used for centuries as adhesives for several technical applications[13] and were among the first polymeric components to be adapted for medical adhesives.[10,14–19] Gelatin-based tissue adhesives have been already proposed in several *in vivo* medical applications, such as gluing blood vessels, [20] skin lacerations in pig animal models[21] and even recently in humans by sealing pulmonary tissues.[22] In spite of its promising qualities, the mechanical strength of physically crosslinked gelatin adhesives is not sufficient as an adhering substance on its own.[19] These hydrogels are relatively unstable in aqueous solutions (they swell and typically dissolve above 35ºC). Various chemical crosslinking methods have been used to confer stability under biological conditions to meet bio-adhesive properties.[18,23] The primary purpose of the chemical modification of gelatin with a crosslinker is to increase its adhesion strength and control its degradation rate; crosslinking can be achieved through chemical and enzymatic approaches, as described in the following sections.

Gelatin-resorcinol-formaldehyde, GRF glue.

One of the well-known gelatin tissue adhesives is gelatin-resorcinol-formaldehyde (GRF) or gelatin-resorcinol-formaldehyde–glutaraldehyde (GRFG) adhesive. GRF was introduced in the

60s in the medical scenario as an adhesive system for gastro-internal surgery showing great advantages compared to industrial adhesives such as cyanoacrylates, but facing challenges of cytotoxicity associated with its components.[24] In these formulations, gelatin chains are crosslinked by aldehydes through a polycondensation reaction between amino groups. Simultaneously, gelatin amine groups can also react with amine groups present on tissue proteins forming covalent bonds at the interface between the gelatin network and the tissue; in addition, resorcinol molecules are crosslinked with formaldehyde to yield a three-dimensional network (**Figure 4-3**).

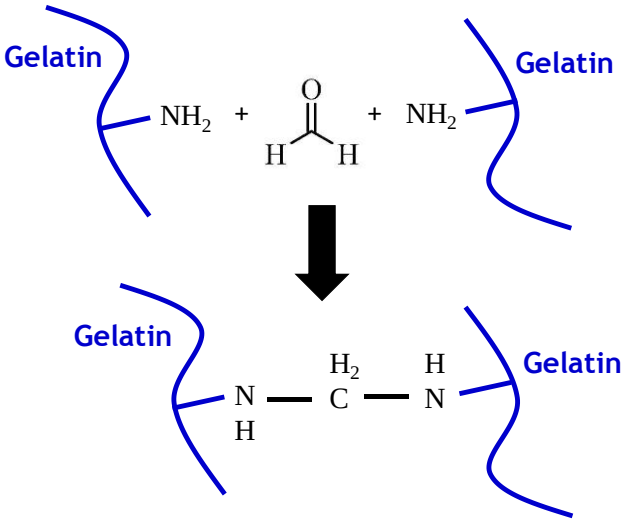

Figure 4-3. Cross-linking reaction of formaldehyde and gelatin under basic conditions.

GRF have been used widely for medical applications; for example, for preventing and sealing pulmonary air leakage,[22] and to reinforce tissues in type A acute aortic dissection surgery.[25,26] Although the bonding strength of the GRF glue to tissue is acceptable,[27] the most important concern regarding this glue comes from the toxicity of both formaldehyde and glutaraldehyde, which limits its applicability.[14,28] However, a surgical application of GRF glues is recommended in cases where tissue integrity is poor, hemostasis is challenging, and high bonding strength is absolutely imperative. In these cases, there was a commercial product called

GRF Biological Glue produced by Microval in France. However, in 2015 its fabrication and distribution were suspended.[29]

Enzymatically crosslinked gelatin (gelatin-mTG adhesive)

Gelatin can be used as a sealant in combination with a microbial transglutaminase (mTG) as the crosslinking catalyst. mTG catalyzes the formation of a covalent bond between a free amine group of a peptide-bound Lys and the acyl group at the end of the side chain of a peptide-bound Gln (**Figure 4-4**). The gelatin-mTG adhesive sticks the opposing tissues together with ultimate adhesive strengths of 12-23 kPa, which are significantly higher than the strength observed for fibrin sealants under wet condition.[30] The gelatin–mTG adhesive was tested recently in an animal model showing promising application in retinal attachment under wet conditions.[31] The safety of mTG for medical applications has not been extensively tested, but it is worthwhile to note that this enzyme is approved for food uses. However, additional long-term studies are required to ensure the biocompatibility and biodegradability of this adhesive and to assess the potential of the gelatin-mTG adhesives in order to promote wound healing process.

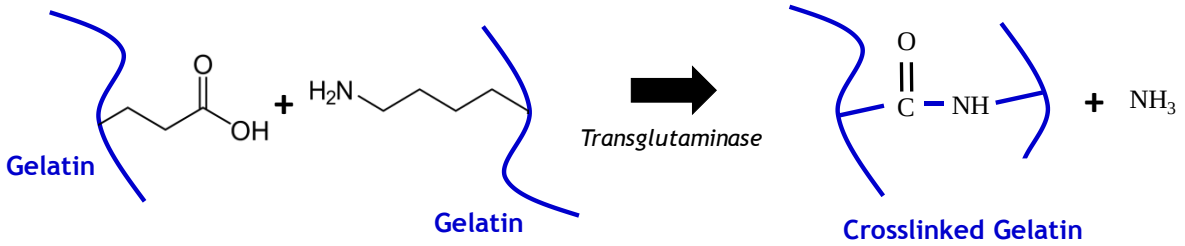

Figure 4-4. Gelatin-mTG crosslinking reaction.

Gelatin chemically crosslinked using EDC/ NHS coupling agent

A carbodiimide molecule such as EDC is a zero-length cross-linking agent that activates the carboxylic acid groups to react with free amine groups, resulting in the formation of an amide bond without incorporation of additional structures into the network. The chemistry behind

crosslinking proteins containing carboxylic acid with carbodiimide functional groups has been proposed in the late 70s.[32,33] The water-based carbodiimide crosslinking agents are reported to be significantly less cytotoxic than formaldehyde and glutaraldehyde.[26,34] Additionally, since lacerated tissues contain exposed amino and carboxylic groups which can participate in the crosslinking reaction, this protein-carbodiimide bioadhesives have the potential to be especially attractive for tissue adherence. Remarkably, Zilberman and co workers[21,23,35–37] have made great efforts toward the development of bioadhesives based on a combination of gelatin with alginate as a polymeric additive and crosslinked with carbodiimide (EDC) in order to combine high mechanical strength with biocompatibility and other desired properties (suitable viscosity, curing time, etc).

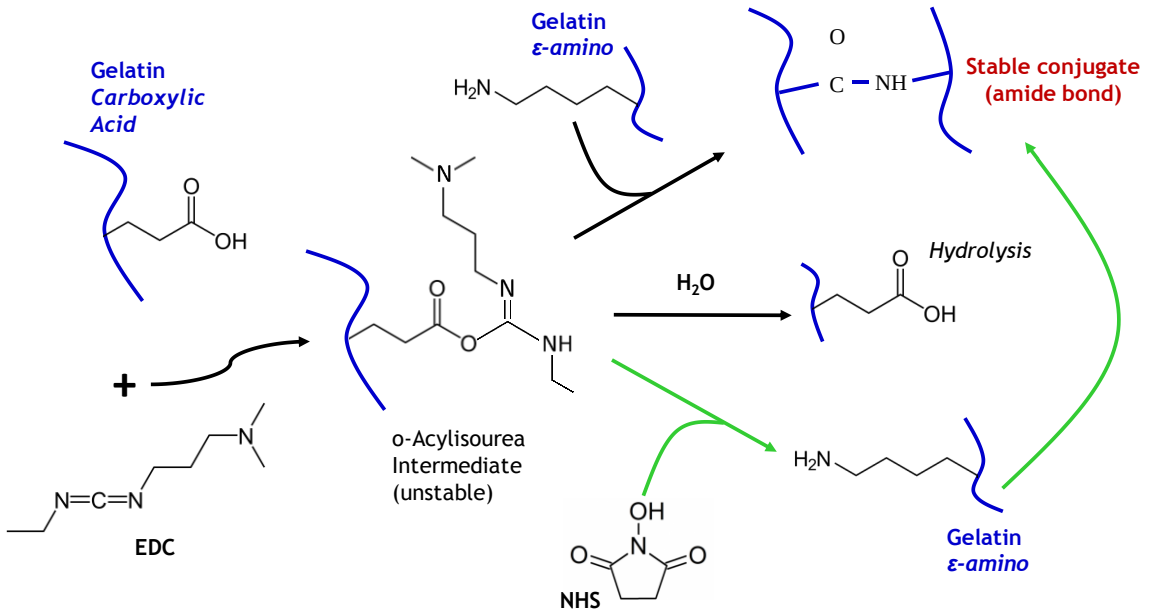

Figure 4-5. Schematic of the amidification reaction with EDC/NHS coupling agent. Carboxyl-to-amine (amide bond) crosslinking using the carbodiimide EDC and NHS. Addition of NHS to EDC reactions (green pathway) increases efficiency.

In the crosslinking reaction (**Figure 4-5**), EDC activates carboxylic acid groups in the gelatin to form *O*-acylisourea groups. Then there is a nucleophilic attack on the activated carboxylic acid residues by the free amine residues (ε-amino groups of lysine), resulting in the formation of amide bonds and the release of urea. This gelatin-EDC reaction is optimum at pH 5.[38] Possible side reactions are the hydrolysis of the *O*-acylisourea group and the formation of carboxylic acid and N-acylurea group.[32] The incorporation of NHS in the crosslinking reaction yields NHS activated carboxylic acid groups, which are less susceptible to hydrolysis, prevents rearrangements, and shifts the reaction toward the creation of peptide bonds while reducing the side reaction.[39]

4.1.3. Gelatin films as model for human living tissues

Gelatin is known to function as a skin model for many applications.[40] Physical properties of gelatin, such as density, stiffness, sound speed, energy dissipation, coincide with those of human skin. [41] Derail and coworkers, [41–43] have extensively worked on the viscoelastic and adherence properties of pressure-sensitive adhesive (PSA) formulations dedicated to medical applications. However, when testing medical adhesion on living skin, many variables from the biological tissue itself induce variability in the results. To overcome this, they developed a specific viscoelastic substrate to measure the adherence properties, which mimics the mechanical properties of an "average" human skin. This viscoelastic substrate (thickness ∼1 mm) is based on gelatin from pig skin (∼10 wt%) which is crosslinked with formaldehyde. The main properties that they aim to mimic are the surface energy, rheological behavior and roughness (**Figure 4-6.a**).[41] Moreover, a simplified version of using gelatin as a model substrate for adhesion tests is now widely used as spreading a highly concentrated solution of gelatin (>∼20 wt%) uniformly on the glass slides, letting them dry and then use them for lap shear or tack tests in air (**Figure 4-6.b**).[44–46] Nevertheless, as all these techniques neither crosslink nor

attach chemically the gelatin film to a surface, they cannot be applied in underwater adhesion measurements.

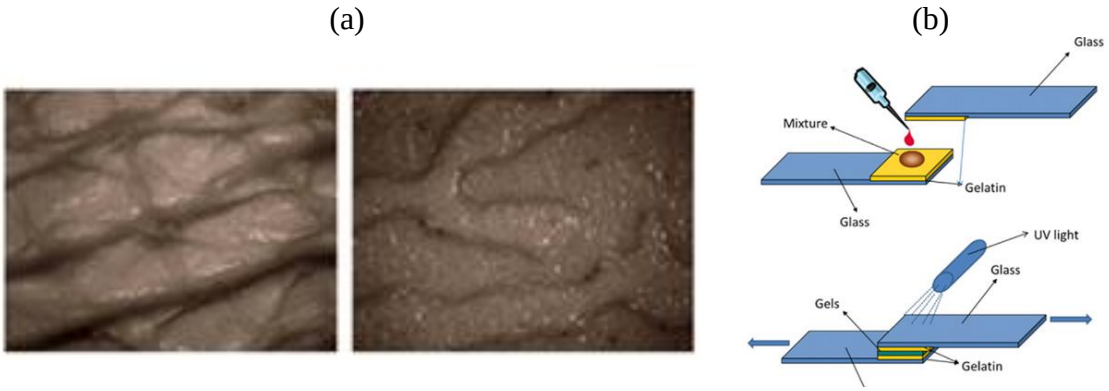

Figure 4-6. (a) Similar topographies between human skin (left) and the gelatin-based artificial substrate (right) as reported from Renvoise et al.[41,43] (b) Schematic of preparation of lap-shear sample using a dry coating of gelatin to mimic the living tissue as reported by Wang et al,[44] Li et al[45] and Nie et al.[46]

4.2. Theory

4.2.1. Structural analysis of a gelatin network

An important characteristic of a polymer network is the degree of cross-linking, i.e., the number density of junctions or crosslinks connecting the chains in a network structure. In general, the number of moles of elastic junctions per unit volume of the network (μ) and the number of moles of elastic network chains per unit volume of the network (ν) are used to describe the density of crosslinks and chains of the polymer network. Consequently, ν and μ determine the average molecular weight between the junctions (M_c). The functionality of the junctions (f), being the number of chains leaving from one crosslink point, determines the relation between ν and μ by the following equation:

$$\mu = \frac{2\nu}{f} \qquad (1)$$

In the physically crosslinked gelatin gel, the crosslink functionality (f_{ph}) is 6, while the functionality of a chemical peptide bond (f_{ch}) is 4. Generally, the shear modulus at preparation state of a polymer network (G_0) is used to estimate μ, ν, and M_c. In this study, G_0 was used to obtain information on the network structure, based on the phantom network model where G_o is calculated as[47]

$$G_0 = \left(1 - \frac{2}{f}\right) \nu RT \tag{2}$$

where R is the gas constant and T is the absolute temperature. This model assumed that the crosslink points fluctuate over time. However, we consider our gelatin as a bimodal network structure,[5] where G_0, the shear modulus in the preparation state, results from the additive contributions of the chemical crosslinking (G_{ch}), introduced during the chemical reaction, and the physical gelation (G_{ph}) induced at low temperature .

$$G_0 = \left(1 - \frac{2}{f_{ch}}\right) \nu_{ch} RT + \left(1 - \frac{2}{f_{ph}}\right) \nu_{ph} RT \tag{3}$$

where ν_{ph} is the number of moles of elastic network chains physically crosslink per unit volume of the network and ν_{ch} is number of moles of elastic network chains per unit volume of the network which are additionally created by chemical crosslinking with EDC/NHS coupling agent.

4.3. Experimental

4.3.1. Chemicals

Gelatin type A (Gel_A, G1890, porcine skin, 300 bloom, derived from acid-cured tissue, Lot#SLBL7508V) and Gelatin type B (Gel_B, G9382, calf skin, 225 bloom, derived from lime-cured tissue, Lot#SLBN8199V), 1-ethyl-3-(3-dimethylaminopropyl)carbodiimide hydrochloride (EDC) and N-hydroxysuccinimide (NHS) were purchased from Sigma-Aldrich,

France. For the synthesis of hydrogel thin films, allylamine, 1,4-dithioerythritol, dry toluene (max. 0.005% H_2O), formic acid and methanol were all purchased from Sigma-Aldrich, France. Additionally, poly(acrylic acid) (PAA with M_W ~ 50 kg/mol, 25 wt% in water) was obtained from Polysciences. (3-Mercaptopropyl)trimethoxysilane was obtained from Alfa chemistry. Silicon wafers were purchased from Applications Couches Minces ACM, France.

4.3.2. Characterization techniques of the gelatin

Size exclusion chromatography

The molecular weight and dispersity of polymers were determined by size exclusion chromatography (SEC). SEC equipped with OHpak SB-806M HQ columns and triple detection was performed to measure the molecular weight distribution of gelatin type A and type B. The measure for a 0.2 M solution of gelatin in $NaNO_3$ was conducted at a flow rate of 0.7mL/min at 45ºC.

Potentiometric titration of amino groups of gelatin A and B

The acid-base titration of gelatin was carried out to determine the concentration of amine and carboxylic acid groups in order to quantify the negative and positive charges present in gelatin A and B. The titration was performed at T=40 °C with a gelatin solution of 8 wt% in 30 mL of Milli-Q water. In a gelatin type B solution at 8wt% concentration, the theoretical concentration of amino groups is 0.03 M, and that of carboxyl groups is 0.1 M.[48] Therefore, NaOH at 1 M was used for titration to avoid a high dilution of gelatin since by adding a small amount of titrant solution, it is possible to measure the real concentration of functional groups. The solution was heated and was stirred at 40°C overnight. The starting pH of the solution was 5.5 and then HCl 1 M was added (2.5 mL) to decrease the pH at 1.6. At this stage the titration started and the pH was measured after each addition of 0.1 mL of NaOH using a micropipette until reaching a stable pH around 12.

Moisture content of gelatin A and B

Thermogravimetric Analysis (TGA) using a SDT Q600 from TA instruments was used to investigate the water content in both gelatin type A and type B before any immersion in water. The gelatin powder coming from the bottle, (≈ 5 mg) was directly loaded into the sample holder, a platinum pan, at room temperature. The samples were submitted to a temperature ramp from room temperature to 150 °C. After that, samples were kept at this temperature for 30 min. The final weight was recorded and the difference in weight was attributed to the water content in the original gelatin sample.

4.3.3. Synthesis and characterization of gelatin macroscopic hydrogels

Gel_A (20 wt%) was chemically crosslinked using the amidification reaction with EDC/NHS coupling agent (**Figure 4-7**). EDC and NHS concentrations were equal and varied from 10 mM (R01) to 20 mM (R02). At 20 wt% of Gel_A, the concentration of free ε-amino groups is expected to be 70 mM. Therefore, the molar ratio between EDC and ε-amino that we used is 1:7 for R01 and 2:7 for R02 with the intention not to involve all the amino groups in the gelatin crosslinked hydrogel and to allow free amino groups for electrostatic interactions.

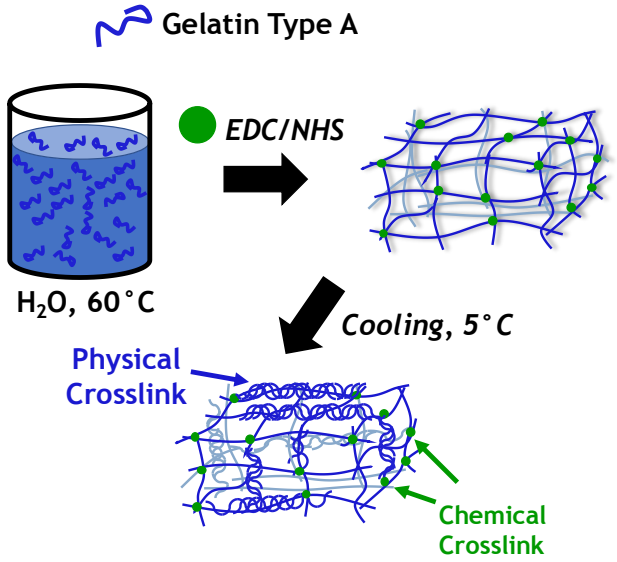

Figure 4-7. Synthesis dual-crosslinked Gelatin A hydrogel.

Briefly, Gel_A was dissolved in 8 mL of MilliQ water at 60 °C overnight. Afterwards, a 2 mL solution of EDC and NHS freshly prepared was added, and was transferred to a glass mold and the carbodiimide reaction was left to proceed for 3 h. Finally, the mold was kept at 4°C during 3 h to form the physical crosslinks. As explained previously, the EDC/NHS coupling enables to form covalent peptide bond between free carboxylic and amino groups on the gelatin polymer chains.[38]

Swelling measurements

The physical and chemical gelatin gels were dried and weighted. The gels were swollen in MilliQ water for 3 days and during this time, 4 or 5 measurements of their weight were taken. Experiments were carried out in triplicates. The volume degree of swelling (Q) was calculated as the ratio between the volume of water taken up by the hydrogel (V_{gel}) and the dry volume of the gelatin in its dry state (V_{dry}). The volumes were calculated from the dry weight and swollen weight of the hydrogel. Hence, the density of gelatin was taken equal to 1.3 g/mL.

Compression tests

Cylindrical samples (8 mm diameter, 12 mm height) were prepared in a silicone mold and tested 24 h after the polymerization to estimate the elastic modulus in the preparation state (E_0), and after swelling equilibrium in the equilibrated state (E_e). Compression tests were conducted using a custom-built setup with a uniaxial testing machine (Instron, model 3343) with a 10 N load cell. Each sample was preloaded with a compression force of 50 mN followed by a compressive loading and unloading at a constant displacement rate of 50 µm/s until a maximum load of 5 N was achieved. Before the test, all specimens were coated with paraffin oil to avoid friction forces between hydrogels and the testing plates during the uniaxial compression. The compressive modulus (E) was calculated as the slope of the linear regression line for data between 5% and 20% of strain.

Chemical determination of free amine groups in gelatin gels using the TNBS-assay

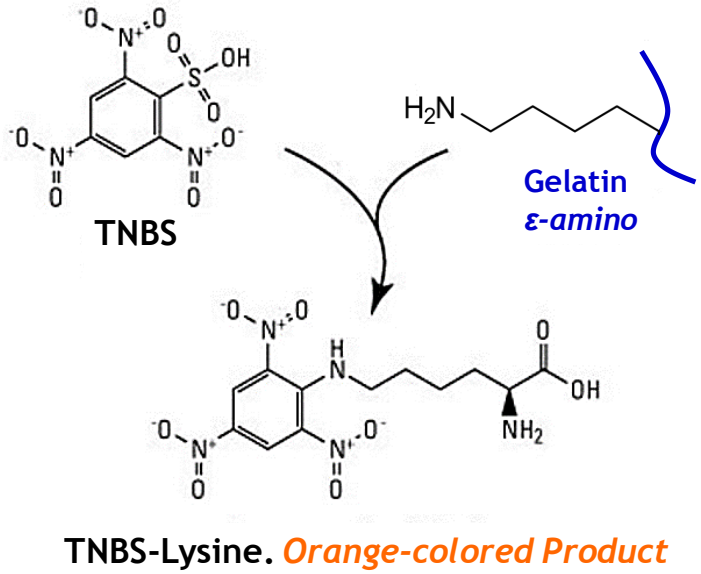

Figure 4-8. Reaction of TNBS with the ε-amino group of lysine to produce a chromogenic derivative.[49]

A previously reported assay was used to determine the number of un-crosslinked ε-amino groups in the non-crosslinked and crosslinked gelatin hydrogels (**Figure 4-8**).[4,5,50,51] Briefly, either gelatin type A or type B (10-15 mg) was incubated in 2 mL of a solution of 2,4,6,-trinitrobenzenelsulfonic acid (TNBS) at 0.5 wt% in sodium bicarbonate ($NaHCO_3$) (pH 8.2, 4 w/v %) for 3h at 40 °C. Then hydrochloric acid (6 M, 3 mL) was added to the solution to hydrolyze the gelatin gels in 1.5 h at 60 °C. After cooling to room temperature, deionized water (5 mL) was added to the solution. Measurement of absorbance was conducted on a Spectrophotometer (UV-visible HP8453, France) at λ=345 nm against a TNBS solution without gelatin, which had been treated in exactly the same way as the cross-linked gelatin samples. The amount of amino groups/g gelatin was calculated as follows

$$\frac{moles\ of\ amino\ groups}{g\ gelatin} = \frac{(Absorbance)V_s}{\left(1{,}46 \times 10^4 \frac{L}{mol\ cm}\right) bx} \qquad (4)$$

where $1{,}46 \times 10^4 \frac{L}{mol\ cm}$ is the molar absorptivity of TNBS-lysine, b is the cell path length which is 1 cm, V_s is the sample volume 0.02 L and x is the gelatin weight in grams.

Differential Scanning Calorimetry (DSC)

The temperature transition of gelatin was determined by DSC measurements using a Q200 from TA instruments. Gel_A hydrogels (~40 mg) were loaded into a Tzero Pan at room temperature. The samples, together with a reference filled with the same quantity of solvent (Milli-Q water), were at first equilibrated for 10 minutes at 70 °C. After that, they were submitted to a cooling temperature ramp from 60 °C to 2 °C and a heating temperature ramp from 2 °C to 60 °C. Between cooling and heating ramps, samples were kept at 2 °C for 30 minutes. The heating rate was equal to 2 °C/min for both ramps.

Monitoring of chemical and physical crosslinking by rheology

Linear rheology was performed on a stress-controlled rheometer (HAAKE RheoStress 600, Thermo Scientfic) using a cone-plate geometry to follow the crosslinking reaction of EDC/NHS with the gelatin solution at high temperature. GelA (20 wt%) was dissolved in 8 mL of MilliQ water at 60 °C overnight. Then a 2 mL solution of EDC and NHS freshly prepared was added to the gelatin solution and the reactive medium was rapidly transferred to the rheometer plate thermostated at 60 °C. The crosslinking reaction is then monitored with a time sweep for the first 200 seconds at 60 °C at a fixed frequency of 1 rad/s and at a fixed maximum stress of 1 Pa. This time was selected because it is enough to observe the sol/gel transition between the liquid state of the initial solution and the solid state of the crosslinked gelatin hydrogel at high temperature. Furthermore, the reversible physical crosslinking process was monitored in the rheometer by cooling down the gelatin solution from 60°C to 10°C and heating up again to 60°C while following the elastic and dissipative moduli. Two freshly prepared solutions of gelatin with and without EDC/NHS (R0, R01 and R02) were kept during 3 hours at 60 °C.

Then, a temperature sweep was performed from 60 °C to 10 °C at a fixed frequency of 1 rad/s and at a fixed maximum stress of 1 Pa. The gelatin hydrogel was kept at 10°C for 1 hour. Then the temperature was increased from 10°C to 60°C. The temperature rate during heating and cooling was constant at 2 °C/min taking two data points per 1°C. Two replicas were conducted for each sample.

Linear rheology of hydrogels at swelling equilibrium

Linear rheology was conducted as well on chemically crosslinked Gel_A at swelling equilibrium using a plate-plate corrugated geometry and disk shape samples (2-3 mm thickness and 8 mm diameter). The geometry of the rheometer was adapted by gluing sandpaper on the bottom plate to avoid slippage of the gels during the test. Samples of Gel_A were used with a disc shape of 2-3 mm thickness and 8 mm diameter. Samples were placed between the geometries during 15 min at 5°C until a normal force of 0.5 N was reached. Temperature sweeps were performed at a fixed frequency of 1 rad/s and at a fixed stress of 1 Pa as the temperature was increased from 5°C to 60 °C at a rate of 2 °C/min, while taking 2 data points per 1 °C. Two replicas were conducted for each sample.

4.3.4. Synthesis and characterization of hydrogel thin films

Synthesis of gelatin type B thin Films

Gel_B thin films were synthesized by simultaneously crosslinking and grafting gelatin chains to the amino-modified silica wafers with peptide covalent bond as shown in **Figure 4-9**. An amino self-assembled monolayer was prepared by immersing silicon wafers in a solution of 3-aminopropyl triethoxysilane in dry toluene (5% v/v) for 3 hours under N_2. Gel_B at different concentration (2.5 wt%, 5.0 wt% or 7.0 wt%) in 8 mL of MilliQ water was stirred at 60°C overnight to dissolve the gelatin. Then, a 2 mL solution of EDC and NHS in MilliQ water was added to the gelatin solution. The molar ratio of ε-amino groups/EDC was set to 1.5 when using

a concentration of ε-amino equal to 0.3 mM. The detailed quantities in mass of EDC and NHS added are presented in **Table 4-3**. After stirring for 1 min, the mixture was deposited on the amine-modified wafers by spin-coating at 5000 rpm during 30 s. After spin-coating, the gelatin film was left for 3 hours in an oven at 60 °C. At this temperature, the gelatin film is in the (mobile) melt state and not in the gel state. After this, the samples were washed and sonicated in Milli-Q hot water (> 40°C) in order to remove all unreacted polymer chains. After this, it was kept overnight at 5°C. Finally, samples were washed and sonicated in Milli-Q water at room temperature.

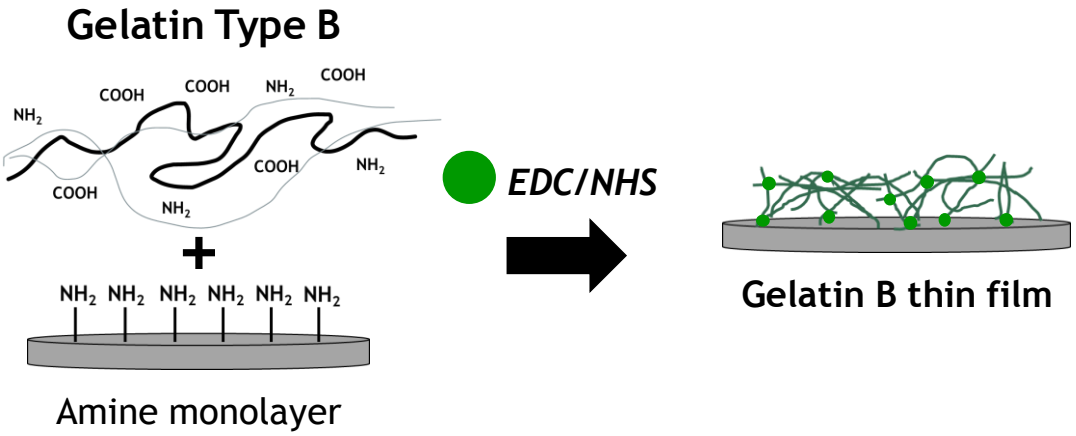

Figure 4-9. Synthesis of surface-Attached Gel_B thin films

Gel_B (sol wt%)	EDC (mg)	NHS (mg)	EDC & NHS [mM]	ε-amino/EDC
2.5	9.6	5.75	5.0	1.5
5.0	19.2	11.51	10.0	1.5
7.0	26.8	16.11	14.0	1.5

Table 4-3. Composition of solutions containing gelatin type B and EDC/NHS coupling agent for the synthesis of hydrogel thin films

Characterization of gelatin hydrogel thin films

The thickness of the Gel_A films in air (h_a) and underwater (h_w) were measured using a spectroscopic ellipsometer (UVISEL, Horiba) with a wavelength range from 260 nm to 850 nm (in air) and from 320 to 850 nm (underwater). The refractive index (n_i) of the silicon wafer is 3.875. A model with two layers was used for measurements in air. The first layer comprises natural silica and amino-silane (n_i = 1.46) the thickness of which was determined before grafting the hydrogel film (between 2 and 3 nm). The second layer was the Gel_B hydrogel film (n_i = 1.50). Underwater measurements were performed with a controlled temperature liquid cell equipped with thin glass walls (fixed perpendicularly to the light path with the angle of incidence at 60°). The polymer hydrogel film was modelled as a single layer (h_w) with a constant refractive index between that of water (n_i = 1.33) and of the gelatin polymer. The swelling ratio of hydrogel films (Λ_f) was calculated as h_w/h_a, assuming that the amount of polymer is the same when immersed in water, since it is (stable) chemically grafted to the substrate.[52] The thickness of gelatin hydrogel film in water was measured for samples fully immersed in Milli-Q water at pH of 2, 4, 5.5 and 8. pH was adjusted with HCl (0.1 M) and NaOH (0.1 M). Two replicas were performed for each test environment.

The surface potential (ζ) of the Gel_B thin films was determined by streaming potential measurements using the SurPASS 3 (Anton Paar GmbH, Austria). Two pieces of silicon wafers (10 mm x 20 mm each) grafted with homogeneous Gel_B film were attached to the rectangular cell with adhesive tape so that they were facing each other and formed a streaming channel where the measuring fluid flows through. During the experiment, the pressure inside the fluid channel (p) was continuously varied and the streaming potential at zero net current conditions (U) was measured for each value of p. The zeta potential ζ was then calculated using the expression developed by Smoluchowski[53]

$$\zeta = \frac{dU}{dp}\frac{\eta}{\varepsilon_r \varepsilon_0} k \quad (5)$$

where ε_0 is the vacuum permittivity constant (8,85x10^{-12} F/m). ε_r, η and k are the dielectric constant, viscosity and the specific conductivity of the measuring fluid respectively. These last three variables were measured independently for each specific pH. The pH-dependence of the zeta potential (ζ) for Gel_B thin films was determined in a KCl solution (1 mM) for a pH range from 2.5 to 10.5. Measurements started at pH ~ 6 followed by stepwise addition of HCl or KOH (0.1 M) to sweep between more acidic and more basic pH values, respectively. One pair of films was used for the acidic environment and a different pair was used for the basic environment. Four measurements were conducted at each specific pH.

4.3.5. Underwater Tack Test

Briefly, the adhesion test consisted in forming a parallel contact and detachment between a macroscopic positively charged Gel_A hydrogel (thickness ~ mm) at swelling equilibrium and a negatively charged Gel_B hydrogel thin film (thickness ~ nm) while both are fully immersed in an aqueous environment. The 5 mm x 5 mm silicon wafer coated with Gel_B hydrogel thin film was glued with a polyvinyl acetate adhesive (ref. L0196, 3M®, France) to a stainless-steel probe, which was fixed to a 10 N load cell and connected to a universal tensile machine (model 5333, Instron®, France). A sample of gelatin type A hydrogel (20 mm x 20 mm x 1 mm) was glued to a glass microscope slide with a cyanoacrylate adhesive (Loctite® 495, France). The contact between the macroscopic Gel_A material and the Gel_B hydrogel thin film was made underwater at an approaching rate of 10 µm/s. A preload of 1 kPa was applied for a given constant contact time that was varied from 1 s to 600 s. Finally, the probe was detached at a constant debonding rate (V_{deb}) while recording the probe displacement and the force. From this experiment, the work of adhesion W_a can be calculated as follows:

$$W_a = T_0 \int_0^{\varepsilon_{max}} \sigma d\varepsilon \quad (8)$$

where ε is the nominal strain which is obtained by normalizing the displacement by the initial thickness of the thick hydrogel (T_0). σ is the average stress obtained by dividing the force by the contact area. Three replicates were conducted for each experiment.

4.4. Results

4.4.1. Characterization of gelatin type A and B

SEC and TGA

Gelatin type A and type B were characterized by SEC chromatography at 45°C. The different molecular weights and the dispersity indices are reported in **Table 4-4**. At high temperature, the chains have a random coil conformation and the distribution of molecular mass on both gelatins is quite narrow since Mw/Mn is below 1.5. The molecular weight data measured by SEC are in the normal range of values for gelatin type A and Type B extracted from porcine and bovine skin, with bloom number 225 and 300, respectively.

The moisture content according to TGA measurements was estimated after keeping the gelatin type A and type B samples for 30 min at 150°C. During this time, the samples weight decreased to 88.9% for Gel_A and 88.4% for Gel_B (i.e. with the initial weight of gelatin as 100%). Therefore, the moisture content of gelatin was calculated to be 11.1% for Gel_A and 11.6% for Gel_B.

	Mn (kg/mol)	Mw (kg/mol)	Mw/Mn (Đ)
Gelatin A	140	160	1.2
Gelatin B	110	148	1.3

Table 4-4. Average molecular weight and dispersity index of gelatin A and B.

Titration curve of gelatin

A gelatin solution (either Gel_A of Gel_B) at 8 wt% (this weight includes moisture content) on 30 mL of Milli-Q water was used to determine the concentration of carboxylic acids and amino groups (imidazole and ε-amino groups) with a titrant solution of NaOH at 1 M. After dissolving the gelatin solution overnight, 2.5 mL of 1 M HCl were added. The starting pH of the gelatin solution was around ~1.5. The resultant titration curves for either gelatin made by the alkaline or the acid treatment are given in **Figure 4-10.a**. Additionally, **Figure 4-10.b** shows m as the slope of the change in pH over the added NaOH volume as $m = \Delta pH/\Delta V_{NaOH}$, as NaOH volume increases, it shows three characteristic peaks for both gelatins. The first peak characterizes the titration of HCl and the initial state of titration of carboxyl groups until the volume of NaOH reach the second peak. The difference in volume between these two peaks represents the concentration of NaOH ions needed to titrate all the carboxyl groups that are present in the gelatin solution.

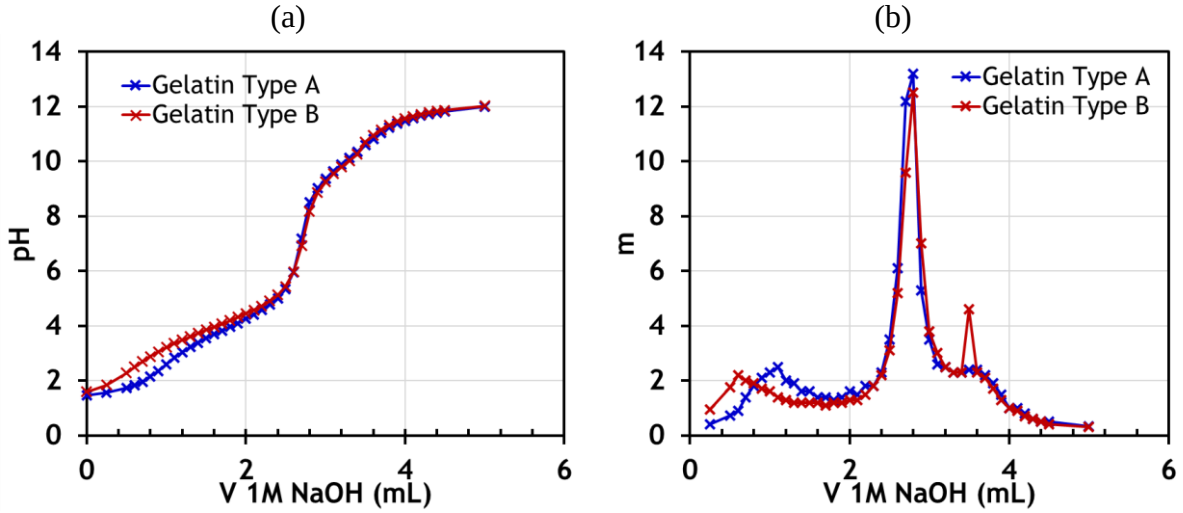

Figure 4-10. (a) Titration curves of gelatin type A and gelatin type B. (b) Change of pH as function of added solution of NaOH (1 M):

Therefore, and taking into account the moisture percentage in the gelatin (~ 11%), the carboxyl groups in the case of gelatin type A are calculated to be 0.77 mmol/g and type B are 1.01 mmol/g. Moreover, the third peak characterizes the titration of amino groups, hence, the difference in volume between the third and second peak, is the concentration of NaOH ions needed to titrate the amino groups present in the gelatin. We found for gelatin type A, an amount of amino groups of 0.39 mmol/g and for gelatin Type B of 0.37 mmol/g. This values are very similar to the ones reported in literature as shown in Table 2 from the residues of histidine and lysine amino acids.[12] Moreover, the total positive charges must include the guanidine groups (pKa 12.1) in the residues of the amino acid arginine. The concentration of arginine in Gel_A and Gel_B is estimated not far from 0.5 mmol/g,[10] therefore the total positive charges in type A is around 0.89 mmol/g and in type B is around 0.87 mmol/g. Furthermore, **Figure 4-11** shows the total amount of carboxyl and amino groups as function of pH for Gel_A and Gel_B. This figure shows the isoelectric point for both gelatins when the curve of $[NH_x^+]$ (which is the same for both gelatins) crosses the curve of $[COO^-]$ for both gelatins. Therefore, the pI for Gel_A is calculated to be at pH~9 and for Gel_B is calculated to be at a pH of ~5.

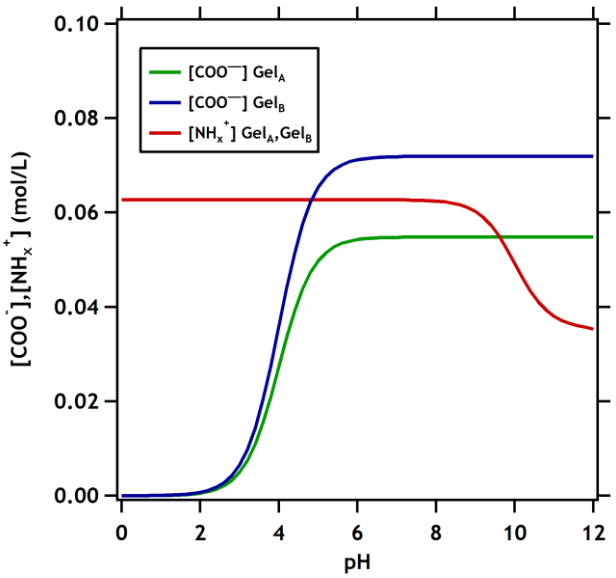

Figure 4-11. Concentration of total carboxyl and amino groups for gelatin type A and type B.

4.4.2. Gelatin macroscopic hydrogel

Gel_A hydrogels swelling behavior and free amino groups left after crosslinking

The reaction of activated carboxylic acid residues with the free ε-amino groups residues of lysine and on (other) gelatin macromolecules results in the creation of a peptide bond without becoming part of the actual linkage. **Figure 4-12** shows the volume swelling behavior of gelatin hydrogels thus obtained and the amount of free amine groups still present after crosslinking. At an EDC concentration 0 mM, physical gelatin gels were formed. When the amount of EDC crosslinker was increased, less free ε-amine groups were present after cross-linking; thus the crosslinks density increased, and the hydrogels showed a lower degree of swelling at equilibrium.

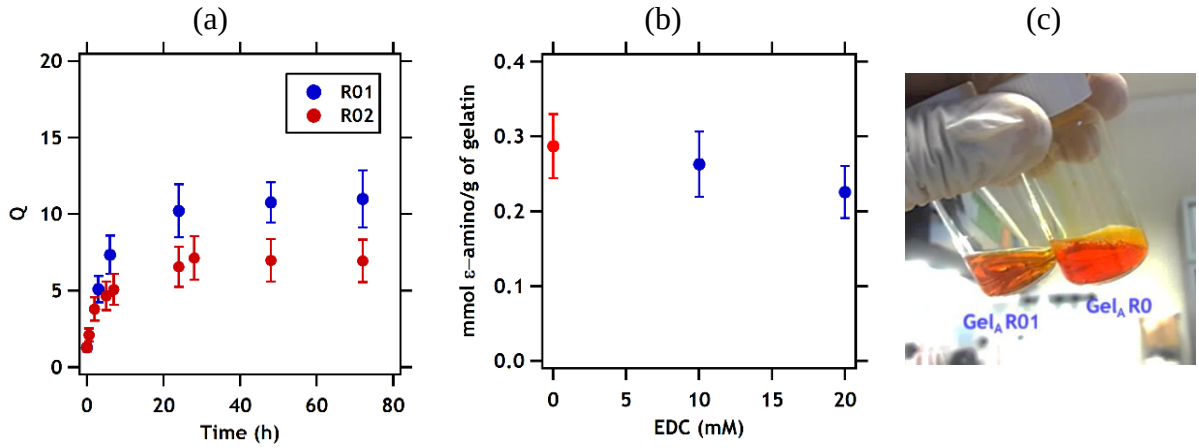

Figure 4-12. (a) Volume swelling as a function of time for R01 and R02 hydrogels**.** (b) **N**umber of free ε-amine groups per gram of gelatin as a function of EDC concentration. In red is R0 and in blue are represented R01 and R02. (c) Samples of gelatin R0 and R01 after reacting with TNBS. The more orange, the more free ε-amino groups of lysine in the sample.

The reaction of TNBS with primary amino groups of un-crosslinked gelatin leads to values in the order of 0.3 mmol/g of gelatin, which is similar to the value of amino groups found in the potentiometric titration method for gelatin type A and several reported values in literature.[12,49]

Moreover, from the estimate of amino groups before and after crosslinking (**Table 4-5**), it is possible to calculate the yield of the carbodiimide reaction. The free amino groups before crosslinking is 64 mM. Then, after crosslinking with 10 mM of EDC for R01, only 6 mM are indeed crosslinked (0.29 mmol ε-amino/g of gelatin = 58 mM) leaving to a yield of 60%. Moreover, in the case of R02 the yield is of 70% where only 14 mM of free amino groups are crosslinked.

Hydrogel nomenclature	**R0**	**R01**	**R02**
EDC concentration (mM)	0	10	20
mmol ε-amino/g of gelatin	0.32 ± 0.04	0.29 ± 0.04	0.25 ± 0.03
Q	-	10.5 ± 1.8	8.6 ± 2.4
E_0 (kPa)	113 ± 28	38.5 ± 4.4	48.9 ± 10.3
E_e (kPa)	--	2.10 ± 0.05	4.2 ± 0.7

Table 4-5. Nomenclature, composition and characteristics of Gel_A hydrogels. The volume swelling at equilibrium (Q) and the ratio of amino groups (mmol ε-amino groups/g of gelatin) were measured from the TNBS-assay. Young's moduli in the preparation conditions (E_0) and at swelling equilibrium (E_e) are presented as average ± standard deviation.

Compression tests

The first step of the adhesion test consists in a light compression of the hydrogel. For this reason, its mechanical response to compression is important. Compression tests were carried out to estimate the elastic modulus of Gel_A hydrogels in cylindrical samples (**Figure 4-13.a**). Representative curves, for R01 and R02 at preparation state, show that the linearity of loading and unloading do not follow the same trajectory. However, after unloading, there is a strain offset of 1% ± 0.05%. This suggests that there is not much energy dissipation and that these hydrogels are elastic at a strain less than 20%, which is lower than a normal compression in the tack test.

The elastic modulus at swelling equilibrium was not measured for un-crosslinked gelatin since no stable physical gel was obtained after reaching its equilibrium. Moreover, for chemically crosslinked gels, E_e increased linearly from approximately 2 kPa to 4 kPa when the molar crosslinker concentration was increased from 10 mM to 20 mM (**Figure 4-13.b**). Finally, E_0 decreased by a factor of two when crosslinking chemically the gelatin network. This result suggests that by chemical crosslinking the gelatin chains, less physical crosslink points are created decreasing therefore the rigidity of the network.

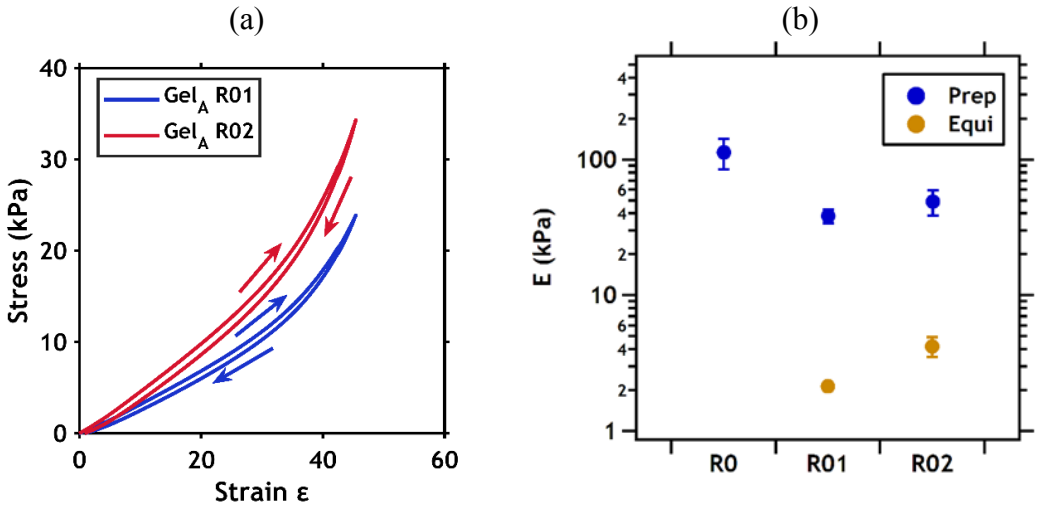

Figure 4-13. (a) Example of compression stress-strain curves for Gel_A R01 and R02 hydrogels at preparation state, arrows showing loading direction (b) R0, R01 and R02 hydrogel elastic modulus in the preparation state E_0 (blue symbols) and at equilibrium state E_e (yellow symbols).

Differential scanning calorimetry measurements

The first important step for understanding the gelation of the different gelatin samples is the melting or the helix-coil transition of soluble collagens.[8,54] **Figure 4-14** displays a typical thermogram recorded from chemically un-crosslinked and crosslinked gelatin samples. When cooling, un-crosslinked gelatin exhibits an endothermic peak centered at about 21 °C, associated to the helix-coil transition of the gelatin, with a denaturation enthalpy of ~15 J/g.

The denaturation enthalpy decreased by a factor of 3 for R02 compared to un-crosslinked gelatin reaching a value of ~5 J/g. This result confirms that in the chemical gel the physical gelation does not take place similarly and that the amount of triple-helix formed are less than in the R0 gel. In the thermogram recorded from the crosslinked gelatin hydrogel R01, the endothermic peak is centered at about 19 °C, and the associated denaturation enthalpy is 10.5 J/g. The values of denaturation temperature and denaturation enthalpy are reported in **Table 4-6**. When heating the gelatin samples, calorimetric curves presented similar values and trends in temperature transition and change in enthalpy. The three hydrogels showed a similar denaturalization temperature of around ~ 25 °C. However, crosslinking with EDC-NHS decreases the physically crosslinked chains since the denaturation enthalpy decreased reaching 8 J/g with the highly crosslinked hydrogel (R02).

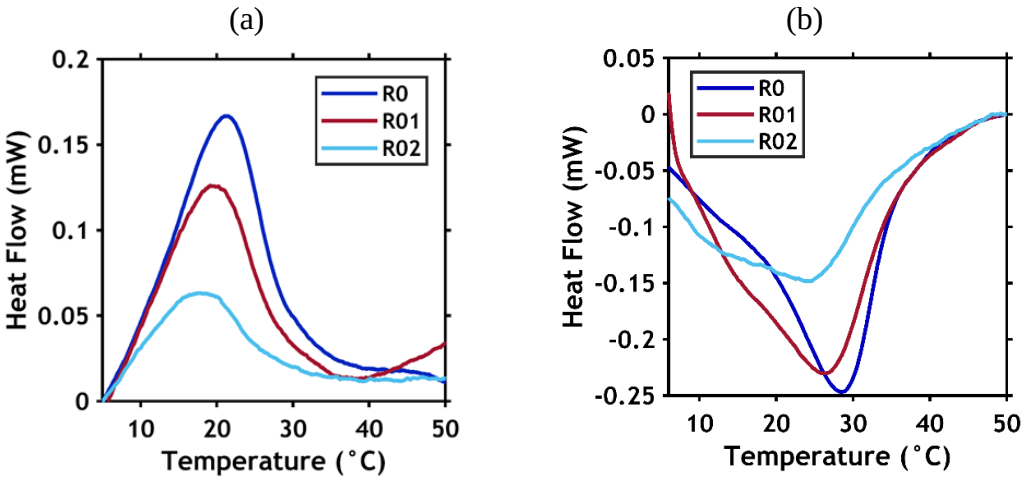

Figure 4-14. Differential Scanning Calorimetry analysis of chemically un-crosslinked and crosslinked Gel_A hydrogels when cooling (a) and heating (b) between 5 °C and 50 °C at a scanning rate of 2°C/min**.**

It is generally accepted that the endothermic process present in the DSC thermogram of collagenous material, such as gelatin, involves rupture of hydrogen bonds and a rearrangement

of the triple helix into a random configuration.[55] The decrease in thermal stability of collagen with aging has been related to the reduction of hydrogen bonds.[56] Thus, the observed decrease of enthalpy values of gelatin on increasing crosslinker concentration can be attributed to a decrease of hydrogen bonds, which break endothermically.

	Cooling		Heating	
Hydrogel	Enthalpy (J/g)	Td (°C)	Enthalpy (J/g)	Td (°C)
R0	15.1	21.1	21.9	28.5
R01	10.5	19.2	20.2	26.3
R02	5.89	16.4	8.45	24.6

Table 4-6. Transition temperatures (Td) and enthalpy energy per gram of gelatin for un-crosslinked and crosslynked Gel_A hydrogels determined by DSC.

Linear rheology

Figure 4-15 shows the follow up by linear rheology of the chemical crosslinking reaction between gelatins using EDC/NHS coupling agent for the hydrogel Gel_A (R01) at 60 °C. The first 30 seconds are missing since it is the time that is left to mix EDC and NHS in the magnetic stirrer. At 45 seconds, the initial material is liquid-like since G' is below G''. The transition time from liquid to solid occurs at around 60 seconds. After this, keeping the sample at high temperature, a solid-like behavior was found in the hydrogel since G' becomes higher that G''.

Temperature sweeps were performed to monitor the reversible physical crosslinking process for gelatin solutions with and without any chemical crosslinking. **Figure 4-16.a** shows the cooling and heating temperature sweep for the R01 hydrogel. In the whole studied range of temperatures, the dual-crosslinked gelatin hydrogel presents a typical solid-like behavior with G' over G''. At high temperature, the elastic modulus is of the order of ~1 kPa and is attributed to only chemical crosslinks. When cooled down, after passing the temperature transition, it is

possible to evaluate the contribution of the physical crosslinks since G' increased by 1 order of magnitude reaching values in the order of ~10 kPa. Moreover, when the temperature is kept at 10 °C for 1 hour, more physical crosslinks are generated resulting in an increase by a factor of 2 of G' reaching ~20 kPa. As soon as the temperature increases again to a value higher than the transition temperature, G' decreases and reaches the same starting value of ~1 kPa, proving the thermoreversible properties of this dual-crosslinked gelatin hydrogel.

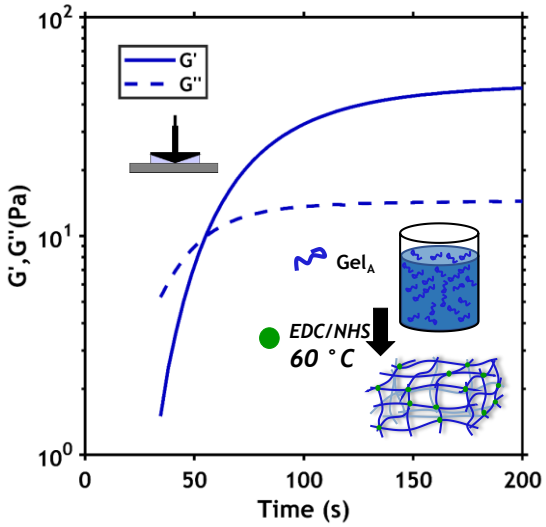

Figure 4-15. Time sweep at 1 Hz and at 1 Pa of the chemical crosslinking reaction between gelatin chains using EDC/NHS coupling agent for the hydrogel Gel$_A$ (R01) at 60 °C.

Figure 4-16.b shows the comparison of the thermoresponsive elastic and dissipative properties of non-chemically crosslinked Gel$_A$ hydrogel (R0) and the chemically crosslinked hydrogels R01 and R02. R0 at high temperature is a liquid-like material with G' lower than G'', however as soon as it reaches temperatures lower than 30 °C, it becomes a solid-like gel reaching a maximum G' value of ~40 kPa. R01 and R02 showed solid-like properties over the whole range of temperatures. However, R02 was stiffer than R01 in the whole range of temperatures. Remarkably, at low temperature, both R01 and R02 reached lower G' values than

the non-chemically crosslinked gelatin hydrogel. This confirms the DSC measurements and the behavior and values of elastic moduli found previously by compression tests.

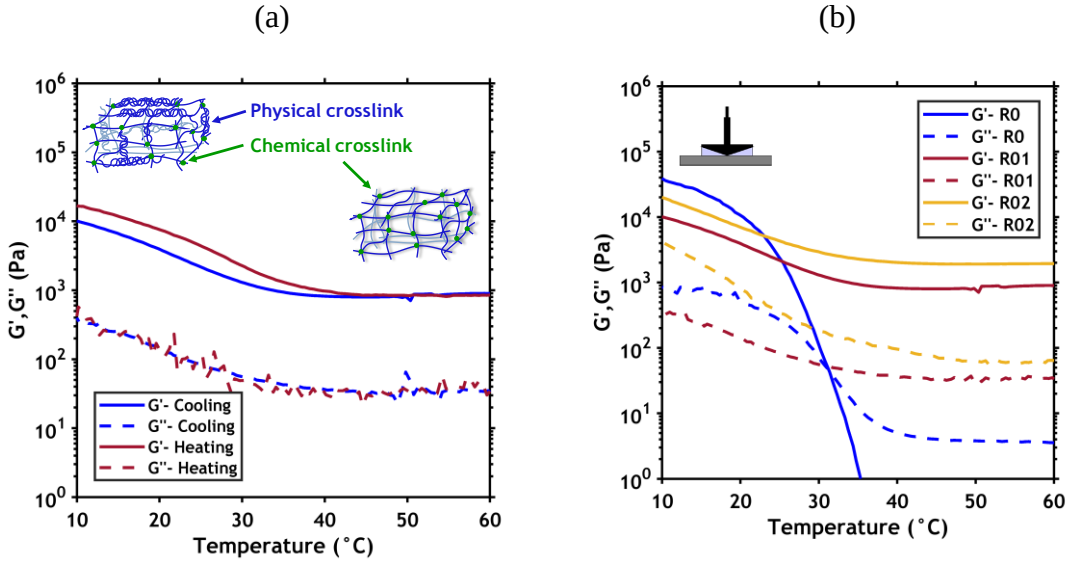

Figure 4-16. (a) Cooling and heating temperature sweep of dual-crosslinked Gelatin A hydrogel R01. (b) Linear rheology of a **c**ooling temperature sweep from 60°C to 10°C of no-chemically crosslinked (R0) and chemically crosslinked Gelatin A hydrogels (R01 and R02) at preparation state (Gel_A concentration: 20 wt%). Cone-plate geometry.

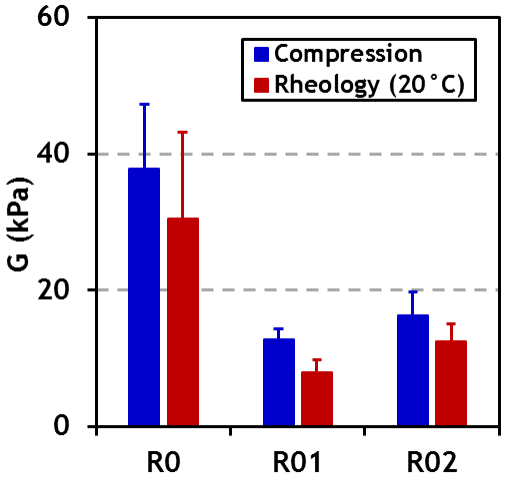

Figure 4-17. Comparison of the shear moduli of the GelA hydrogels at preparation state and the values of G' from the temperature sweep at 20°C.

Moreover, in **Figure 4-17** are shown the values of G' at 20°C (as presented by the temperature sweep) for the Gel_A hydrogels. These values are very similar to the E values obtained from the compression tests presented in **Figure 4-13**. The shear moduli is calculated from the Young's modulus as shown in Chapter 2. Section 2.3.4. Equation 16).

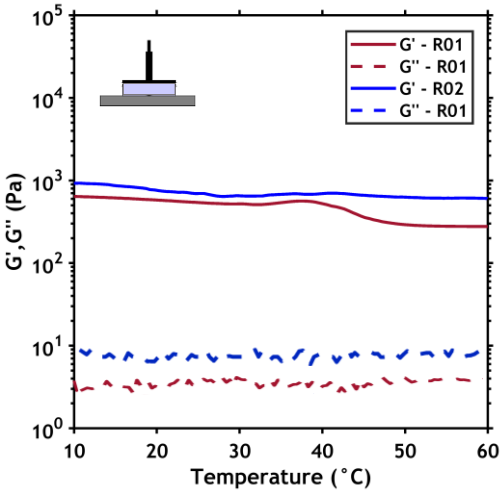

Figure 4-18. Temperature sweep of dual-crosslinked Gelatin A hydrogel for different degree of chemically crosslinking at the equilibrium state.

Finally, the linear rheological properties of chemically crosslinked gelatin hydrogels at swelling equilibrium showed that these gels are elastic in the whole range of temperature since the loss moduli are roughly two orders of magnitude lower that G' (< 1 kPa) and roughly constant during the temperature sweep for both R01 and R02 hydrogels (**Figure 4-18**). Thus, as expected by introducing chemical crosslinks, gelatin gels become stable over the whole temperature range; additional physical crosslinks formed at room temperature strongly reinforce the network and dominate the elastic behavior. However, at swelling equilibrium, gelatin chains are more diluted and stretched and consequently the formation of physical crosslinks through chains intertwining at low temperature becomes weaker.

4.4.3. Gelatin hydrogel thin films

Swelling and stability of Gel_B hydrogel thin films

Swelling properties of Gel_B thin films spin-coated at different gelatin concentration (2.5 wt%. 5.0 wt% and 7.0 wt%) were studied after 30 minutes of equilibrium in the specific environment. The swelling equilibrium (Λ_f) increased from 2.8 to 3.5 when increasing the initial gelatin concentration in the solution used to prepare the film from 2.5 wt% to 7.0 wt%, respectively. Additionally, Gel_B thin films made from solutions of 5.0 wt% and 7.0 wt% were chemically stable in different pH environments (**Table 4-7**). For Gel_B at 7.0 wt%, the underwater thin film thicknesses were found to be slightly higher at pH 8 (473 ± 1 nm) than at pH 4 (437 ± 2 nm) The average swelling ratio, which is around 3.5, corresponds to a water volume fraction of 71%. It is not significantly sensitive to the pH environment since the charges of amine groups do not vary highly between pH 4 and pH 8.

Gelatin B	Thickness (nm)					
	Air	pH 4	pH 5.5*	pH 7.4**	pH 8	Λ_f*
2.5 wt%	32.5	-	91.2	-	-	2.8
5.0 wt%	145.6	437.4	462.1	461.1	473.0	3.2
7.0 wt%	250.2	892.6	863.8	882.6	860.2	3.5

Table 4-7. Thickness of Gel_B hydrogel thin films prepared from solutions at different gelatin initial concentrations and different pH. The molar ratio of EDC/ε-amino was kept at 1.5 for all three groups. Air corresponds to the dry thickness. *In MilliQ water. **In Phosphate Buffer Solution (PBS).

The Gel_B hydrogel film obtained from spin-coating of gelatin solution at 5 wt% showed a a dry thickness of 145.6 ± 1.1 nm and a stable behavior when being immersed in water. The swollen thickness increased to 462.1 ± 1.5 nm in water at 20°C and was 450.2 ± 3.8 nm at 60°C.

Gel_B hydrogel thin films obtained from gelatin solutions of 7.0 wt% had a dry thickness of 239.4 ± 12.2 nm. Moreover, we showed that they were chemically stable when keeping them underwater at 50°C since they showed no significant decrease in dry thickness. The dry thickness was 227.2 ± 12.7 nm after 15 hours at high temperature (**Figure 4-19**).

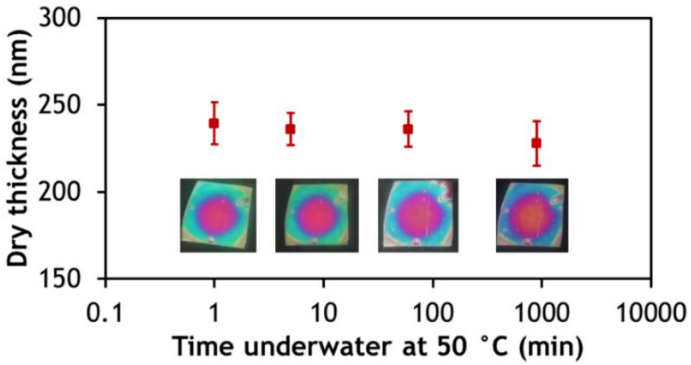

Figure 4-19. Dry thickness of Gel_B hydrogel thin films (obtained from spin-coating of gelatin solutions at 7.0 wt% and EDC/NHS concentration of 30mM) as function of immersion time in water at 50 °C. Each measured time has a respective photography of the state of the gelatin surface.

Streaming potential measurements of Gel_B hydrogel thin films

Very homogeneous Gel_B samples (**Figure 4-20.a**) obtained with solutions at 2.5 wt% (dry thickness ~30 nm) and 5.0 wt% (dry thickness ~150 nm) were prepared on silicon wafers for streaming potential measurements following the procedure explained in section 4.3.3. The pH-dependence of the zeta potential was determined in the presence of KCl solution at 1 mM. We started at pH 6 and decreased/increased the pH value by stepwise adding HCl at 50 mM or KOH at 25 mM.

The isoelectric point (pI=pH|ζ=0) of both samples was found to be around pH 5 (**Figure 4-20.b**) in good agreement with the potentiometric titration. This reflects the gelatin protein structure with a mixture of acidic and basic functional groups. The plateau ζ values are determined by the number of functional groups and by the swelling degree. The absolute plateau

value of the zeta potential for Gel_B at 2.5 wt% was found to be around -25 mV and slightly lower than for Gel_B at 5.0 wt% of -20 mV. This suggests that the composition of the electrical double layer is influenced by the absorbed amount of water, since we found a lower $\zeta_{plateau}$ values for films with a higher swelling ratio.

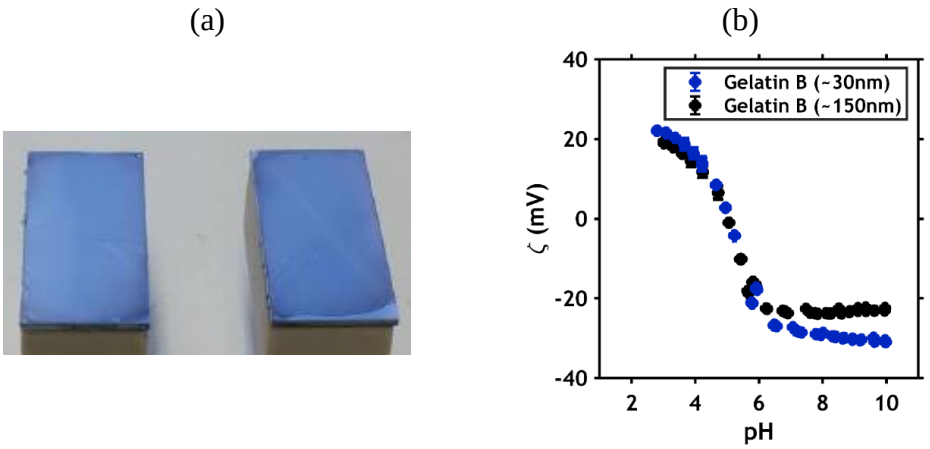

Figure 4-20. (a) Pictures of homogeneous gelatin hydrogel thin films used for the streaming potential measurements, the dry thickness being ~30 nm. (b) Zeta potential vs. pH of the gelatin B hydrogel film with different dry thickness.

4.4.4. Underwater adhesion

Effect of experimental conditions: V_{deb}, contact time and thickness of Gel_B films

Previous chapters showed that W_a increased logarithmically with V_{deb} at both the macro and micro scale for synthetic gels. This increase was attributed to the rate dependence of bond fracture. We also found a linear dependence of W_a with the logarithm of the V_{deb} when measuring the adhesion between the chemically crosslinked gelatin hydrogel R01 and a Gel_B hydrogel thin film (**Figure 4-21.a** and **Figure 4-21.d**). W_a increased around 1 order of magnitude (from ~ 20 mJ/m^2 to ~ 250 mJ/m^2) when the debonding rate increased from 1 µm/s to 1 mm/s.

Moreover, **Figure 4-21.b** and **Figure 4-21.e** show the work of adhesion as a function of contact time for the contact between Gel_B hydrogel thin films (dry thickness of 30 nm) and the R01 hydrogel at a V_{deb} of 0.1 mm/s and pH 6. When the contact time was varied, the adhesion energy slightly increased with contact times up to 120 s. However, W_a significantly increased if the contact time was further prolonged to 600 s.

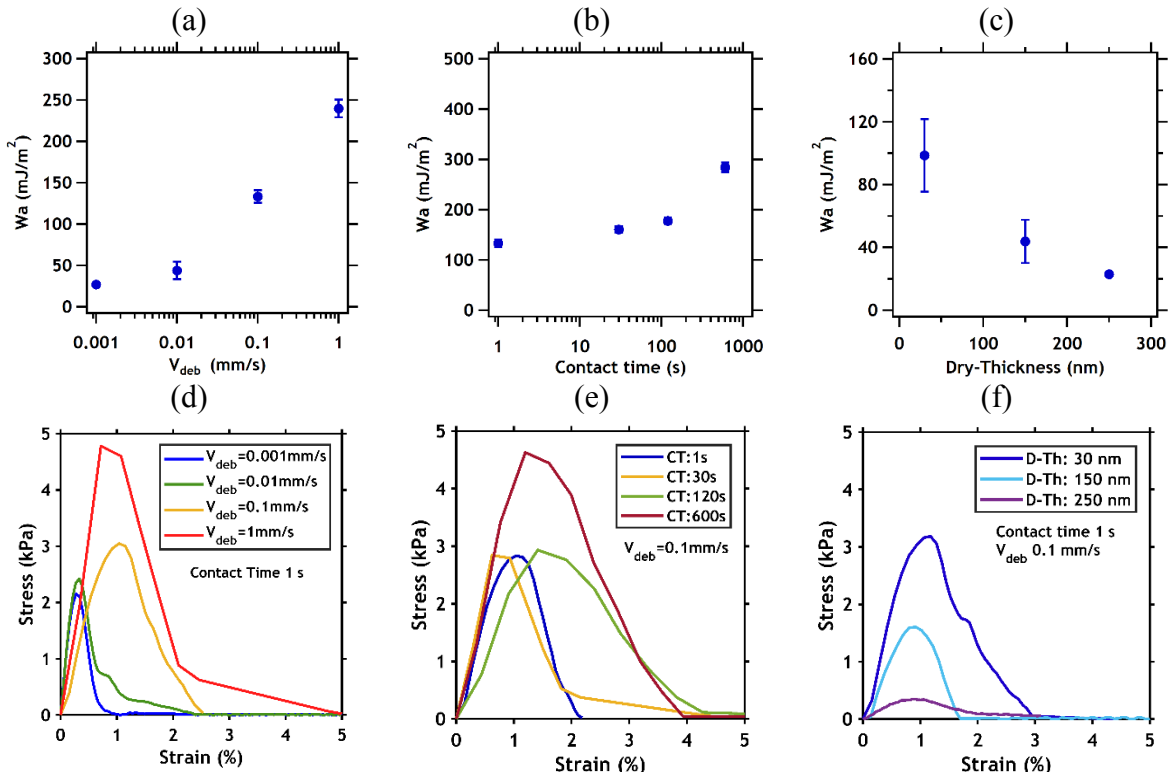

Figure 4-21. Variation of the adhesion energy measured in Milli-Q water (pH 6.0 and temperature 20 °C) between Gel_A-R01 macroscopic hydrogel and Gel_B thin film (2.5 wt%, dry thickness ~30 nm) as a function of debonding rate (a) and contact time (b). Corresponding stress-strain detachment curves as function of debonding rate (d) and contact time. Variation of the adhesion energy measured in Milli-Q water between Gel_A-R01 macroscopic hydrogel and Gel_B thin films obtained from spin-coating of gelatin solutions at different concentrations, at a contact time of 1 s and debonding rate of 0.1 mm/s (c). Corresponding stress-strain detachment curves (f).

Finally, the adhesion energy is shown to depend upon the thickness of the Gel_B hydrogel thin film (**Figure 4-21.c** and **Figure 4-21.f**), since thinner films showed a higher adhesion energy. This is consistent with higher charge concentrations for thinner films (or also with higher swelling ratio and lower absolute zeta potential).

Effect of the aqueous environment: pH and Phosphate Buffer Saline solution

Since the level of charges of both Gel_A and Gel_B is pH-dependent, the adhesion properties between the chemically crosslinked Gel_A hydrogel and the Gel_B hydrogel thin films of 30 nm was investigated for different pH values (**Figure 4-22.a** and **Figure 4-22.b**). The macroscopic hydrogel Gel_A-R01 was used for the adhesion tests at different pH values (3.0, 6.0, 7.0 and 9.0). pH was adjusted by adding either only HCl (for pH 3.0) or only NaOH (for pH > 5.5). The hydrogels were kept before the test underwater at each specific pH and tack tests were conducted at a contact time of 1 second and a debonding rate of 0.1 mm/s. As expected, the measured W_a went through a maximum value at pH 6, while in both acidic and basic conditions (pH < 4 and pH > 8) a lower but non zero adhesion was measured suggesting a more complex picture than simply the effect of repulsive electrostatic forces.

Finally, W_a was measured between macroscopic Gel_A hydrogel and Gel_B thin film in a medium containing a phosphate buffer solution (PBS) which has a pH of 7.4 and a salt concentration of 0.138 M of NaCl (**Figure 4-22.c**). The adhesion energy in PBS for a debonding rate of 0.1 mm/s and a contact time of 1 s and 120 s was found to be significantly lower compared to the same test conditions at pH 7 without NaCl. This suggest that the salt contained in the PBS is enough to screen the few charges that contribute to the macroscopic adhesion.

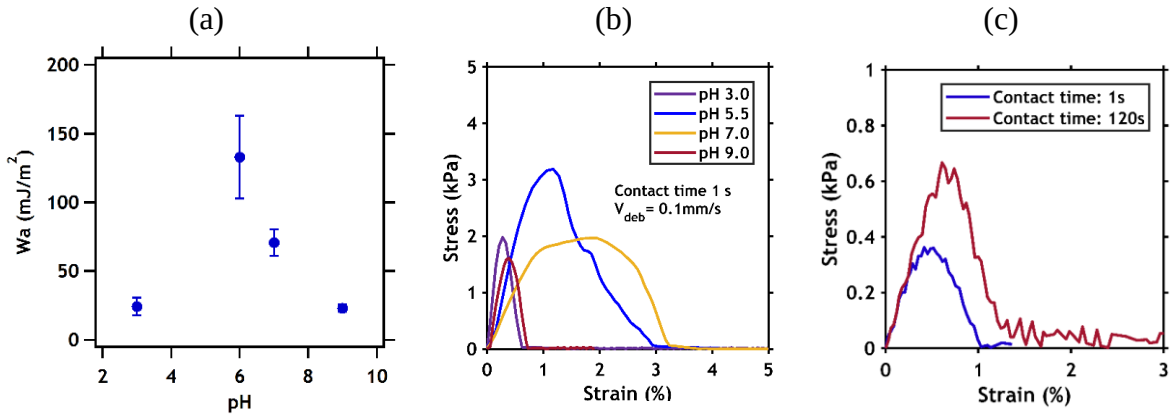

Figure 4-22. (a) Adhesion energy between Gel_A-R01 macroscopic hydrogels and Gel_B hydrogel thin films (2.5 wt%, dry thickness ~30 nm) as a function of pH. (b) Corresponding stress-strain detachment curves. (c) Stress-strain detachment curves for Gel_A-R01 against Gel_B hydrogel thin films in a Phosphate Buffer Saline (PBS) solution at two different contact times.

Effect of the crosslinks density of the Gel_A hydrogel

Interestingly underwater tack tests between macroscopic Gel_A hydrogels (R0, R01 and R02) and Gel_B hydrogel thin films (2.5 wt%, dry thickness ~30 nm) at pH 6 showed a clear optimum in adhesion with varying crosslinks density (**Figure 4-23**). A significant increase in W_a of the first contact was obtained with the moderately chemically crosslinked Gel_A hydrogel R01 when compared to hydrogel R0. Additionally, the crosslinks density of chemically crosslinked Gel_A hydrogels considerably affected the W_a against the same negatively charged surface, since W_a decreased by a factor of 10 after increasing EDC concentration between 10 mM and 20 mM.

Moreover, the interfaces of R0 and R01 against the same Gel_B thin film failed cohesively after the first contact since the adhesive energy measured for the following contacts decrease significantly. This suggest that the adhesion energy is indeed higher than the cohesive strength of these hydrogels. Moreover, only the hydrogel R02 showed an adhesive failure the interface since the work of adhesion was constant for at least five different repetitions.

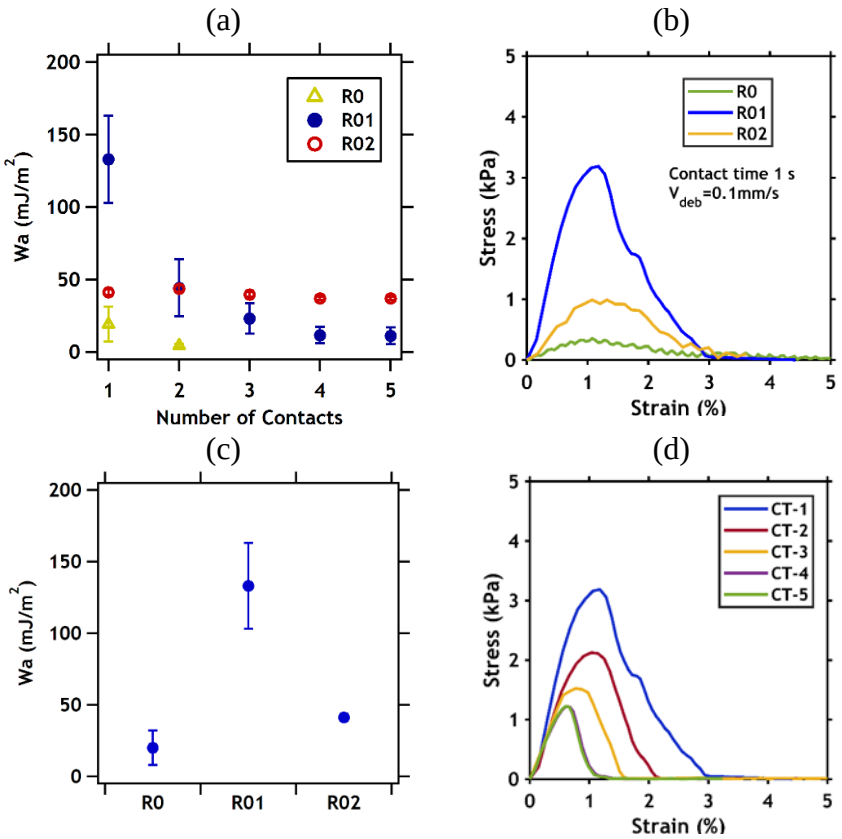

Figure 4-23. (a) Adhesion energy between macroscopic Gel_A hydrogel (R0, R01 and R02) and Gel_B hydrogel thin film (2.5 wt%, dry thickness ~30 nm) at pH 6 as a function number of contacts (b) Corresponding stress-strain detachment curves for the first contact between the Gel_A hydrogel against Gel_B thin film. (c) Work of adhesion of the first contact between macroscopic Gel_A hydrogel and Gel_B hydrogel thin films as a function of EDC concentration on the macroscopic hydrogel. (d) Examples of the stress-strain tack debonding curves for one replica of R01 hydrogel with a decrease in energy, due to a cohesive failure during the test. CT is the number of contact.

4.5. Discussion

4.5.1. Comparison of ζ and W_a between PAA and Gel$_B$ hydrogel thin films

In chapter 2, we presented the swelling and streaming potential properties of PAA hydrogel thin films. Briefly, these films presented a dry thickness of 144.1±1 nm. The swelling ratio for these films increases from 1.39 ± 0.1 at pH 2 to 1.75 at pH 8, corresponding to the water volume fraction of 0.28 at pH 2 and 0.44 at pH 8. **Figure 4-24.a** shows the comparison of streaming potential measurements between PAA and Gel$_B$ thin films as function of pH and shows an isoelectric point (pI=pH$|_{\zeta=0}$) at pH 5.5 for Gel$_B$ and at pH 3 for PAA. Remarkably, the ζ plateau value ($\zeta_{plateau}$), which above the pI is related to the density of functional groups, was found to be significantly different for both samples. The PAA film has more negative charges than the Gel$_B$ film, since $\zeta_{plateau}$ is -70 mV for PAA and -30 mV for Gel$_B$.

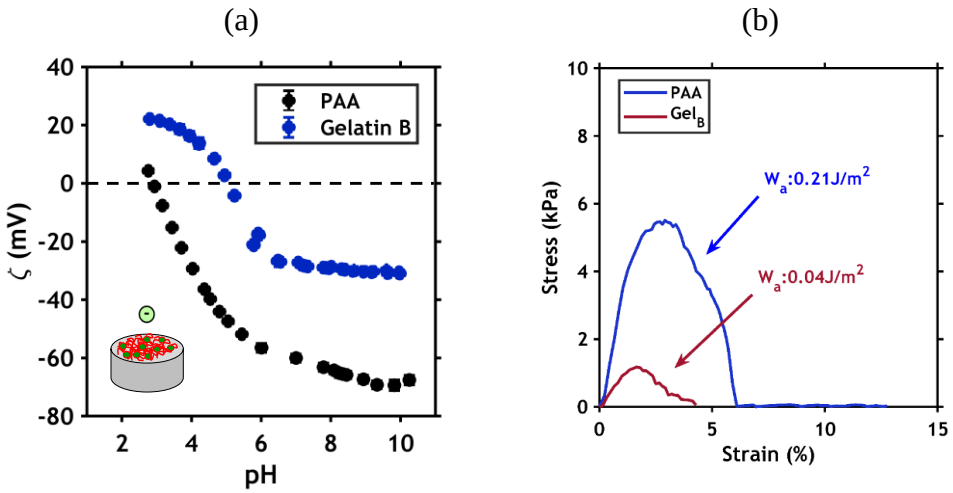

Figure 4-24. (a) Zeta potential of PAA and Gel$_B$ thin film in 10^{-3} M KCl as a function of pH. (b) Comparison between PAA and GelB hydrogel thin films on Stress-Strain tack debonding curves against the same macroscopic GelA crosslinked hydrogel.

Furthermore, we measured an average work of adhesion underwater of 209 ± 10 mJ/m^2 between a PAA hydrogel thin film (dry thickness of 144.1±1 nm) and the macroscopic Gel$_A$ R02 hydrogel in Milli-Q water (pH 6) at a contact time of 1 second and a debonding rate of 0.1 mm/s (**Figure 4-24.b**). Consequently, the measured adhesion energy using the PAA films is higher by one order of magnitude compared to Gel$_B$ hydrogel thin film at the same conditions. Both the PAA and the Gel$_B$ showed adhesive failure at the interface since the stress-strain curves for different repetitions sowed the same behavior, and therefore the same work of adhesion (**Figure 4-25**).

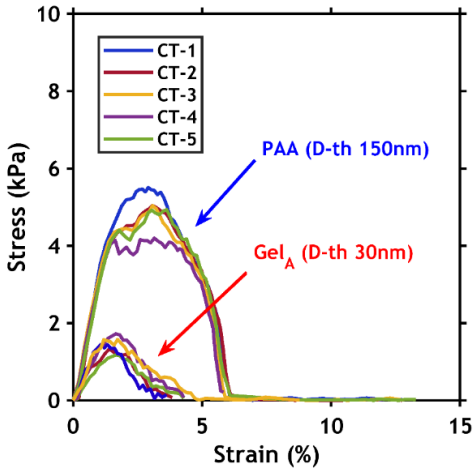

Figure 4-25. Stress-strain curves for different repetitions between PAA and GelB hydrogel thin films on against the same macroscopic GelA R02 crosslinked hydrogel showing same curves meaning an adhesive failure.

Based on the GCSG model[57,58] and the streaming potential measurements, the number of dissociated carboxyl groups per unit area ($n\mathrm{COO}^-/\mathrm{nm}^2$) was calculated as a function of the number of acidic groups capable of dissociating (N_a) and the degree of dissociation of functional groups (Chapter 2. Section 2.2.3). Using this model, N_a is calculated to be 1.4 x10^{-2} $n\mathrm{COO}^-/\mathrm{nm}^2$ and at pH 6 the degree of dissociation is 0.55, therefore for Gel$_B$ the areal density

of negative charges is calculated to be ~0.82 x10^{-2} $n\mathrm{COO}^{-}$/nm^2, while for PAA it is ~3 x10^{-2} $n\mathrm{COO}^{-}$/nm^2. This estimate suggests that at this pH, the difference in W_a between the PAA and $\mathrm{Gel_B}$ films comes from the density of negative charges, since the PAA films have around three times more interfacial interactions than using the $\mathrm{Gel_B}$ film. Therefore, the measured W_a is higher since more force is needed to separate the two surfaces when more interactions are formed.

4.5.2. Effect of macroscopic hydrogel architecture on the adhesion energy

The systematic study of the effect of the crosslinks density showed that the W_a decreases not by losing its free ε-amino groups, but by increasing the crosslinks density of the gels, as shown in previous chapters where the adhesion energy decreased by increasing the rigidity of the elastic hydrogels. We also saw the same behavior for the chemically crosslinked gelatin hydrogels. **Figure 4-26** shows the decrease in adhesion energy as function of the elastic modulus at equilibrium as measured in compression test at room temperature. This suggest the same behavior as previous reported with the Lake and Thomas model, were adhesion scales with the inverse square root of the elastic moduli. However, there are only two data points to make a strong conclusion and both points have different failure mechanism.

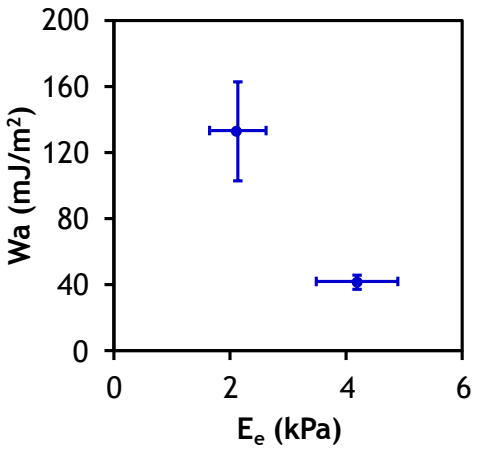

Figure 4-26. Adhesion energy as a function of the shear moduli of $\mathrm{Gel_A}$ hydrogels at their preparation state.

4.6. Perspectives of bio-based systems for underwater adhesion

Gelatin chemically crosslinked with EDC/NHS coupling agent is an interesting bio-based model system to modulate underwater adhesion by controlling different molecular architectures and the areal density of electrostatic interactions. The values of adhesion energy are however at least one order of magnitude inferior than the macroscopic W_a measured in synthetic system. For this reason, in this section we report briefly a possible candidate that can be used to replace this gelatin-EDC as a bio-based system to obtain a higher underwater adhesion strength.

It is well known that adhesion strength can be improved by increasing the dissipation in the bulk and the concept of double networks gels developed by J.P. Gong and coworkers[59] and Z. Suo and coworkers[60] could be an interesting way to explore when linking electrostatic interactions to macroscopic underwater adhesion. Therefore, we present results obtained with a gel based on gelatin type A interpenetrated with a loosely chemically crosslinked polyacrylamide (Gel_A–AAm) as a new system (IPN) to measure underwater adhesion.

4.6.1. Gel_A–AAm hydrogel

Interpenetrated networks of acrylamide and gelatin have been widely studied in the 90s by Chatterji and coworkers[61,62] and more recently by Yan et al.[63] who prepared in a one single reaction step, a gelatin/polyacrylamide IPN gel by combining a physically crosslinked gelatin as the first network and a loosely crosslinked polyacrylamide as the second network. These gels presented superior properties which were largely attributed to effective energy dissipation via the rupture of the gelatin first network.[63] Inspired by these previous works, we use IPN gels based on gelatin type A and acrylamide chemically crosslinked with methylenebisacrylamide (MBA) to test the idea that is possible to improve the adhesion energy by increasing the hydrogel toughness. We describe briefly how these gels are prepared, then we present their equilibrium swelling and mechanical properties in uniaxial tensile configuration and finally, we

report the adhesion properties using the underwater probe-tack test against a PAA hydrogel thin film.

Synthesis of Gel_A–AAm hydrogel

IPN gels were prepared by interpenetrating a highly concentrated and loosely chemically crosslinked polyacrylamide network into a low concentrated Gel_A physical network (**Figure 4-27**). The total polymer concentration was kept constant at 40 wt% and the weight ratio between AAm and Gel_A was fixed at 7:1 (AAm: 35 wt% and Gel_A: 5 wt%). MBA concentration was kept constant at 0.05 mol% with respect to the acrylamide concentration. Ammonium persulfate (APS) was used as red-ox initiator at 0.1 mol% respect to acrylamide concentration.

Briefly, IPN hydrogels were prepared by dissolving Gel_A, acrylamide and MBA in Milli-Q water at 60°C for 15 h. After bubbling N_2 for 30 min, APS was added and the solution was transferred to a glass mold. The initiation rapidly took place and the polymerization was left to proceed during 3 h at 60°C. After this, the mold was cooled down for 3 h at 5°C to form the gelatin network. Finally, the mold was opened, and the 1 mm thick gels were immersed and stored in Milli-Q water (pH 5.5) until final use.

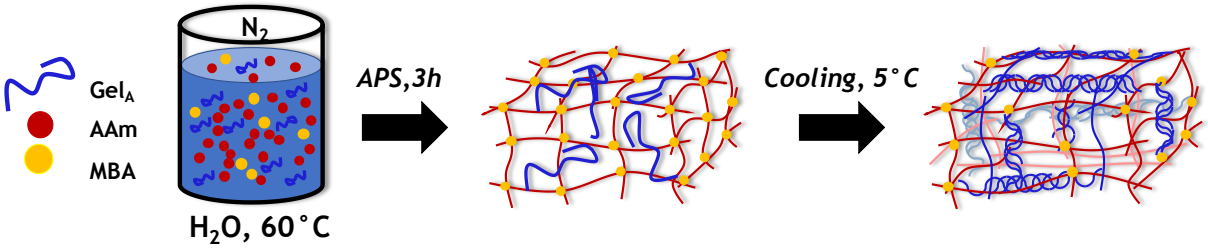

Figure 4-27. Schematic of the synthesis of interpenetrated network based on Gelatin A and acrylamide (AAm) chemically crosslinked with methylenebisacrylamide (MBA) under nitrogen atmosphere at 60°C.

Swelling and tensile properties of Gel$_A$–AAm hydrogel

For equilibrium swelling studies after 3 days of equilibrium with water renewal, the swollen gel samples were weighted (m_s) and then dried overnight in an oven (at 60 °C) in order to get their final dry weight (m_d). These measurements are used to calculate the mass swelling ratio at equilibrium ($\Lambda_e = m_s/m_d$). It was found an equilibrium swelling for this gel of Λ_e = 6.15; i.e. an equivalent polymer concentration at equilibrium of 16 wt% were Gel$_A$ is only 2 wt%.

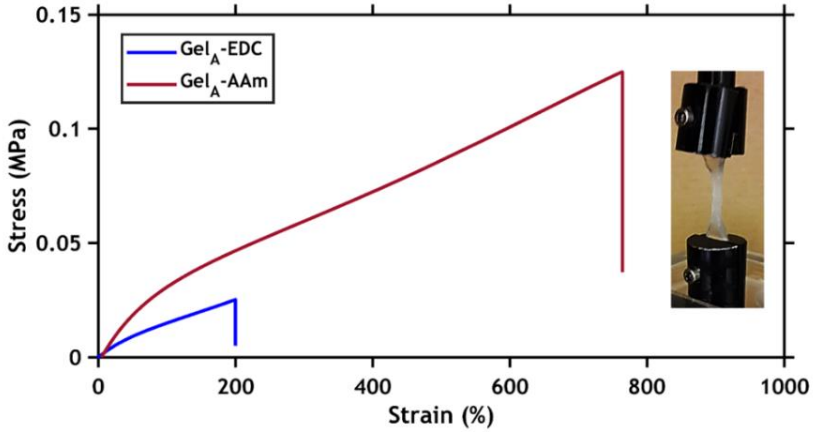

Figure 4-28. Nominal stress vs strain showing the tensile properties of interpenetrated networks based on Gel$_A$ and acrylamide, in comparison with Gel$_A$ chemically crosslinked using EDC/NHS coupling agent both at preparation state (non-swelling equilibrium).

The large deformation behavior of the gels at preparation state was studied by uniaxial loading and unloading tensile tests on an Instron 5565 tensile tester with a 10 N load cell. Samples had dog-bone shape with 4 mm width, 3 mm thickness, and 18 mm length (length between clamps). Tensile curves at a pulling rate of 0.5 mm/s are shown in **Figure 4-28** for the GelA–AAm and are compared to the R02 hydrogel (Gel$_A$–EDC). The maximum extensibility of the IPN gel (ε_{max} ~700%) remarkably improves when compared to a gelatin network (ε_{max} is less than 40%). After four loading and unloading cycles at different extensibility, the gels

showed almost no dissipation energy (**Figure 4-29**). The remarkable extensibility of the IPN hydrogel is presumably due to the loosely crosslinked network structure of the chemical acrylamide combined with the energy dissipation brought by the physical crosslinks of the gelatin.[64,65] This results are encouraging, however, they are preliminary without replicas and no strong conclusions can be made.

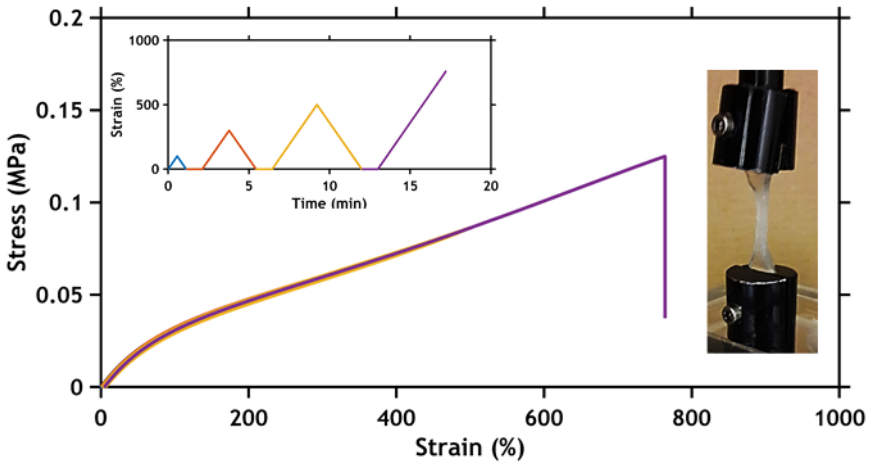

Figure 4-29. Nominal stress vs strain showing the loading and unloading tensile properties of interpenetrated hydrogel networks based on Gel_A and acrylamide.

Underwater adhesion of Gel_A–AAm hydrogel and PAA hydrogel thin film

Underwater probe-tack tests between Gel_A–AAm hydrogel and PAA thin films showed that W_a was remarkably higher (~4 J/m^2) by one order of magnitude when compared to the chemically crosslinked gelatin R01 (~0.2 J/m^2) with the same test parameters (pH 6, V_{deb} = 0.1 mm/s and contact time of 1 second) (**Figure 4-30**). However, both presented cohesive failure after the first detachment meaning that adhesion energy is indeed higher than the toughness of these hydrogels. This suggest that both can form enough interfacial charge densities to pull the polymer chains at the interface of the PAA film and the gel. Since the Gel_A-AAm gel is able to

reach higher extensibility than the Gel_A-EDC, therefore, it is able to reach a larger maximum strain in the stress-strain tack debonding curves resulting in a higher work of adhesion.

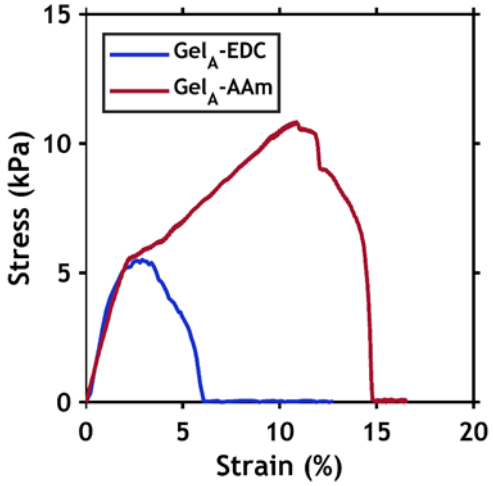

Figure 4-30. Comparison of stress-strain underwater probe-tack debonding curves between either Gel_A–AAm hydrogel or the chemically crosslinked gelatin R02 (Gel_A-EDC) and a PAA hydrogel thin film (dry thickness: 150 nm). pH 6, V_{deb} = 0.1 mm/s and contact time of 1 second.

4.7. Conclusions

We succeed in preparing dual crosslink macroscopic hydrogels and thin films based on gelatin. Additionally, we were able to measure macroscopic underwater adhesion between oppositely charged gelatin gels without any contribution of the natural thermoreversible properties of gelatin. Additionally, the new developed gelatin hydrogel thin films serves as a good surface model for mimicking human tissues when testing adhesive systems for medical applications under aqueous environments.

When adhesive failure occurred, the W_a of Gel_A hydrogels against PAA films was significantly higher than against Gel_B films showing that W_a strongly depends on the interfacial charge density since PAA has a higher density of negative charges than Gel_B, as shown by streaming potential measurements. Finally, for adhesion experiments between Gel_A and Gel_B,

it was possible to tune W_a by changing the pH of the tested medium since the charge level of both Gel_A and Gel_B is pH-dependent.

We showed with this bio-based system, that interfacial charge density and mechanical properties of macroscopic hydrogels are important parameters that permit to control underwater macroscopic adhesion between oppositely charged hydrogels. Moreover, the connection of molecular architecture and macroscopic adhesion underwater of this gelatin system is not fully understood, since is still harder to predict the W_a when more molecular interactions are occurring at the interface between two gelatin gels. Finally, we have presented very briefly a new model system to study the work of adhesion underwater between a gelatin-acrylamide double network hydrogel. Yet, a systematic study of the molecular architecture of this system is necessary to fully understand its connection with the macroscopic underwater adhesion strength.

References

(1) Cedano, F.; Tran, Y.; Hourdet, D.; Creton, C. From Electrostatic Interactions to Macroscopic Underwater Adhesion. In *41st Adhesion society meeting*; San Diego, CA, 2017.

(2) Solorio, L.; Zwolinski, C.; Lund, A. W.; Farrell, M. J.; Jan, P. Gelatin Microspheres Crosslinked with Genipin for Local Delivery of Growth Factors. *J Tissue Eng Regen Med.* **2011**, *4* (7), 514–523.

(3) Aramwit, P.; Jaichawa, N.; Ratanavaraporn, J.; Srichana, T. A Comparative Study of Type A and Type B Gelatin Nanoparticles as the Controlled Release Carriers for Different Model Compounds. *Mater. Express* **2015**, *5* (3), 241–248.

(4) Ofner, C. M.; Bubnis, W. A. Chemical and Swelling Evaluations of Amino Group Crosslinking in Gelatin and Modified Gelatin Matrices. *Pharmaceutical Research*. 1996, pp 1821–1827.

(5) Kuijpers, A. J.; Engbers, G. H. M.; Feijen, J.; De Smedt, S. C.; Meyvis, T. K. L.; Demeester, J.; Krijgsveld, J.; Zaat, S. A. J.; Dankert, J. Characterization of the Network Structure of Carbodiimide Cross-Linked Gelatin Gels. *Macromolecules* **1999**, *32* (10),

3325–3333.

(6) Imeson, A. *Thickening and Gelling Agents for Food*; Springer Science+Business Media Dordrecht, 1997.

(7) GIMA. Gelatin Handbook. *Gelatin Manuf. Inst. Am.* **2012**, 25.

(8) Djabourov, M.; Papon, P. Influence of Thermal Treatments on the Structure and Stability of Gelatin Gels. *Polymer (Guildf).* **1983**, *24*, 537–542.

(9) Gelatin Manufacturers Institute of America. Standard Testing Methods for Edible Gelatin. **2013**, No. July, 28.

(10) Schrieber, R.; Gareis, H. *From Collagen to Gelatine*; 2007.

(11) Fitch, C. A.; Okon, M.; Platzer, G.; Garcia-Moreno E., B.; McIntosh, L. P. Arginine: Its PKa Value Revisited. *Protein Sci.* **2015**, *24* (5), 752–761.

(12) Eastoe, J. E.; . The Amino Acid Composition of Mammalian Collagen and Gelatin. *Biochem. J.* **1955**, *61* (above 400), 589–602.

(13) Israelachvili, J.; Ruths, M. Brief History of Intermolecular and Intersurface Forces in Complex Fluid Systems. *Langmuir* **2013**, *29* (31), 9605–9619.

(14) Bouten, P. J. M.; Zonjee, M.; Bender, J.; Yauw, S. T. K.; Van Goor, H.; Van Hest, J. C. M.; Hoogenboom, R. The Chemistry of Tissue Adhesive Materials. *Prog. Polym. Sci.* **2014**, *39* (7), 1375–1405.

(15) Ghobril, C.; Grinstaff, M. W. The Chemistry and Engineering of Polymeric Hydrogel Adhesives for Wound Closure: A Tutorial. *Chem. Soc. Rev.* **2015**, *44* (7), 1820–1835.

(16) Duarte, A. P.; Coelho, J. F.; Bordado, J. C.; Cidade, M. T.; Gil, M. H. Surgical Adhesives: Systematic Review of the Main Types and Development Forecast. *Prog. Polym. Sci.* **2012**, *37* (8), 1031–1050.

(17) Mehdizadeh, M.; Yang, J. Design Strategies and Applications of Tissue Bioadhesives. *Macromol. Biosci.* **2013**, *13* (3), 271–288.

(18) Scognamiglio, F.; Travan, A.; Rustighi, I.; Tarchi, P.; Palmisano, S.; Marsich, E.; Borgogna, M.; Donati, I.; De Manzini, N.; Paoletti, S. Adhesive and Sealant Interfaces for General Surgery Applications. *J. Biomed. Mater. Res. - Part B Appl. Biomater.* **2016**, *104* (3), 626–639.

(19) Bhagat, V.; Becker, M. L. Degradable Adhesives for Surgery and Tissue Engineering. *Biomacromolecules* **2017**, *18* (10), 3009–3039.

(20) Matsuda, M.; Ueno, M.; Endo, Y.; Inoue, M.; Sasaki, M.; Taguchi, T. Enhanced Tissue Penetration-Induced High Bonding Strength of a Novel Tissue Adhesive Composed of

Cholesteryl Group-Modified Gelatin and Disuccinimidyl Tartarate. *Colloids Surfaces B Biointerfaces* **2012**, *91* (1), 48–56.

(21) Foox, M.; Keren, A.; Pinkas, O.; Cohen, E.; Goldstein, N.; Gilhar, A.; Zilberman, M.; Ullmann, Y. In Vivo Efficacy of Novel Bioadhesives for Closure of Surgical Incisions : Evaluation in a Porcine Model. *Adv. Biomater. Devices Med.* **2015**, *2*, 70–78.

(22) Nomori, H.; Horio, H.; Suemasu, K. The Efficacy and Side Effects of Gelatin-Resorcinol Formaldehyde- Glutaraldehyde (GRFG) Glue for Preventing and Sealing Pulmonary Air Leakage. *Surg. Today* **2000**, *30* (3), 244–248.

(23) Cohen, B.; Shefy-Peleg, A.; Zilberman, M. Novel Gelatin/Alginate Soft Tissue Adhesives Loaded with Drugs for Pain Management: Structure and Properties. *J. Biomater. Sci. Polym. Ed.* **2014**, *25* (3), 224–240.

(24) Bonchek, L. I.; Braunwald, N. S. Experimental Evaluation of a Cross-Linked Gelatin Adhesive in Gastrointestinal Surgery. *Ann. Surg.* **1967**, *165* (3), 420–424.

(25) Fukunaga, S.; Karck, M.; Harringer, W.; Cremer, J.; Rhein, C.; Haverich, A. The Use of Gelatin-Resorcin-Formalin Glue in Acute Aortic Dissection Type A. *Eur. J. Cardio-thoracic Surg.* **1999**, *15* (5), 564–570.

(26) Sung, H. W.; Huang, D. M.; Chang, W. H.; Huang, R. N.; Hsu, J. C. Evaluation of Gelatin Hydrogel Crosslinked with Various Crosslinking Agents as Bioadhesives: In Vitro Study. *J. Biomed. Mater. Res.* **1999**, *46* (4), 520–530.

(27) Basu, S.; Marini, C. P.; Bauman, F. G.; Shirazian, D.; Damiani, P.; Robertazzi, R.; Jacobowitz, I. J.; Acinapura, A.; Cunningham, J. N. Comparative Study of Biological Glues: Cryoprecipitate Glue, Two-Component Fibrin Sealant, and "French" Glue. *Ann. Thorac. Surg.* **1995**, *60* (5), 1255–1262.

(28) Chen, H.; Yao, J.; Wang, F.; Zhou, Y.; Chen, K.; Zhuang, R.; Choi, M. M. F.; Zaray, G. Toxicity of Three Phenolic Compounds and Their Mixtures on the Gram-Positive Bacteria Bacillus Subtilis in the Aquatic Environment. *Sci. Total Environ.* **2010**, *408* (5), 1043–1049.

(29) ANSM. Décision du suspension de fabrication de la cholle chirurgicale stérile GRF. https://www.ansm.sante.fr/S-informer/Informations-de-securite-Retraits-de-lots-et-de-produits/Colle-chirurgicale-GRF-Microval-Rappel (accessed Jan 31, 2019).

(30) McDermott, M. K.; Chen, T.; Williams, C. M.; Markley, K. M.; Payne, G. F. Mechanical Properties of Biomimetic Tissue Adhesive Based on the Microbial Transglutaminase-Catalyzed Crosslinking of Gelatin. *Biomacromolecules* **2004**, *5* (4), 1270–1279.

(31) Chen, T.; Janjua, R.; McDermott, M. K.; Bernstein, S. L.; Steidl, S. M.; Payne, G. F. Gelatin-Based Biomimetic Tissue Adhesive. Potential for Retinal Reattachment. *J. Biomed. Mater. Res. - Part B Appl. Biomater.* **2006**, *77* (2), 416–422.

(32) Lloyd, D. R.; Burns, C. M. Coupling of Acrylic Polymers and Collagen by Use of a Water-Soluble Carbodiimide. II. Investigations of the Coupling Mechanism. *J. Polym. Sci. Polym. Chem. Ed.* **1979**, *17* (11), 3473–3483.

(33) Timkovich, R. Detection of the Stable Addition of Carbodiimide to Proteins. *Anal. Biochem.* **1977**, *79* (1–2), 135–143.

(34) Liang, H. C.; Chang, W. H.; Liang, H. F.; Lee, M. H.; Sung, H. W. Crosslinking Structures of Gelatin Hydrogels Crosslinked with Genipin or a Water-Soluble Carbodiimide. *J. Appl. Polym. Sci.* **2004**, *91* (August), 4017–4026.

(35) Foox, M.; Raz-Pasteur, A.; Berdicevsky, I.; Krivoy, N.; Zilberman, M. In Vitro Microbial Inhibition, Bonding Strength, and Cellular Response to Novel Gelatin-Alginate Antibiotic-Releasing Soft Tissue Adhesives. *Polym. Adv. Technol.* **2014**, *25* (5), 516–524.

(36) Cohen, B.; Pinkas, O.; Foox, M.; Zilberman, M. Gelatin-Alginate Novel Tissue Adhesives and Their Formulation-Strength Effects. *Acta Biomater.* **2013**, *9* (11), 9004–9011.

(37) Pinkas, O.; Goder, D.; Noyvirt, R.; Peleg, S.; Kahlon, M.; Zilberman, M. Structuring of Composite Hydrogel Bioadhesives and Its Effect on Properties and Bonding Mechanism 3 Rd Revised Version. *Acta Biomater.* **2017**, *51* (15 March 2017), 125–137.

(38) Friess, W. Collagen - Biomaterial for Drug Delivery. *Eur. J. Pharm. Biopharm.* **1998**, *45* (2), 113–136.

(39) Grabarek, Z.; Gergely, J. Zero-Lenght Crosslinking Procedure with the Use of Acetyl Esters. *Anal. Biochem.* **1990**, *185*, 131–135.

(40) Dąbrowska, A.; Rotaru, G. M.; Spano, F.; Affolter, C.; Fortunato, G.; Lehmann, S.; Derler, S.; Spencer, N. D.; Rossi, R. M. A Water-Responsive, Gelatine-Based Human Skin Model. *Tribol. Int.* **2017**, *113* (January), 316–322.

(41) Renvoise, J.; Burlot, D.; Marin, G.; Derail, C. Adherence Performances of Pressure Sensitive Adhesives on a Model Viscoelastic Synthetic Film: A Tool for the Understanding of Adhesion on the Human Skin. *Int. J. Pharm.* **2009**, *368* (1–2), 83–88.

(42) Baït, N.; Grassl, B.; Derail, C.; Benaboura, A. Hydrogel Nanocomposites as Pressure-Sensitive Adhesives for Skin-Contact Applications. *Soft Matter* **2011**, *7* (5), 2025–2032.

(43) Renvoise, J.; Burlot, D.; Marin, G.; Derail, C. Peeling of PSAs on Viscoelastic Substrates: A Failure Criterion. *J. Adhes.* **2007**, *83* (4), 403–416.

(44) Wang, T.; Nie, J.; Yang, D. Dextran and Gelatin Based Photocrosslinkable Tissue Adhesive. *Carbohydr. Polym.* **2012**, *90* (4), 1428–1436.

(45) Li, H.; Niu, R.; Yang, J.; Nie, J.; Yang, D. Photocrosslinkable Tissue Adhesive Based on Dextran. *Carbohydr. Polym.* **2011**, *86* (4), 1578–1585.

(46) Nie, W.; Yuan, X.; Zhao, J.; Zhou, Y.; Bao, H. Rapidly in Situ Forming Chitosan/ε-Polylysine Hydrogels for Adhesive Sealants and Hemostatic Materials. *Carbohydr. Polym.* **2013**, *96* (1), 342–348.

(47) Obukhov, S. P.; Rubinstein, M.; Colby, R. H. Network Modulus and Superelasticity. *Macromolecules* **1994**, *27* (12), 3191–3198.

(48) Ofner, C. M.; Budnis, W. A. Chemical and Swelling Evaluations of Amino Group Crosslinking in Gelatin and Modified Gelatin Matrices. 1996, pp 1821–1827.

(49) Ofner III, C. M.; Bubnis, W. A. The Determination of Epsilon-Amino Groups in Soluble and Poorly Soluble Proteinaceous Materials by a Spectrophotometric Method Using Trinitrobenzenesulfonic Acid. *Anal. Biochem.* **1992**, *207*, 129–133.

(50) Bubnis, W. A.; Ofner, C. M. The Determination of ??{lunate}-Amino Groups in Soluble and Poorly Soluble Proteinaceous Materials by a Spectrophotometrie Method Using Trinitrobenzenesulfonic Acid. *Anal. Biochem.* **1992**, *207* (1), 129–133.

(51) Habeeb, A. F. S. A. Determination of Free Amino Groups in Proteins by Trinitrobenzenesulfonic Acid. *Anal. Biochem.* **1966**, *14* (3), 328–336.

(52) Chollet, B.; Li, M.; Martwong, E.; Bresson, B.; Fretigny, C. Multiscale Surface-Attached Hydrogel Thin Films with Tailored Architecture. *ACS Appl. Mater. Interfaces* **2016**, *8*, 11729–11738.

(53) Smoluchowski, M. *Handbuch Der Elektrizität Und Magnetismus*; Graetz, L., Ed.; Leipzig, 1921.

(54) Joly-Duhamel, C.; Hellio, D.; Djabourov, M. All Gelatin Networks: 1. Biodiversity and Physical Chemistry. *Langmuir* **2002**, *18* (19), 7208–7217.

(55) Bigi, A.; Panzavolta, S.; Rubini, K. Relationship between Triple-Helix Content and Mechanical Properties of Gelatin Films. *Biomaterials* **2004**, *25* (25), 5675–5680.

(56) Bigi, A.; Cojazzi, G.; Panzavolta, S.; Rubini, K.; Roveri, N. Mechanical and Thermal Properties of Gelatin Films at Different Degree of Crosslinking. **2001**, *22*, 3–8.

(57) Hunter, R. J. *Zeta Potential in Colloid Science: Principles and Applications*; 1981.

(58) Grahame, D. C. Diffuse Double Layer Theory for Electrolytes of Unsymmetrical Valence Types. *J. Chem. Phys.* **1953**, *21* (6), 1054–1060.

(59) Gong, J. P.; Katsuyama, Y.; Kurokawa, T.; Osada, Y. Double-Network Hydrogels with Extremely High Mechanical Strength. *Adv. Mater.* **2003**, *15* (14), 1155–1158.

(60) Sun, J.-Y.; Illeperuma, W. R. K.; Zhao, X.; Mooney, D. J.; Vlassak, J. J.; Chaudhuri, O.; Suo, Z.; Oh, K. H. Highly Stretchable and Tough Hydrogels. *Nature* **2012**, *489* (7414), 133–136.

(61) Chatterji, P. R. Interpenetrating Hydrogel Networks. I. The Gelatin–polyacrylamide System. *J. Appl. Polym. Sci.* **1990**, *40* (3–4), 401–410.

(62) Kaur, H.; Chatterji, P. R. Interpenetrating Hydrogel Networks. 2. Swelling and Mechanical Properties of the Gelatin-Polyacrylamide Interpenetrating Networks. *Macromolecules* **1990**, *23* (22), 4868–4871.

(63) Yang, J.; Yan, X.; Chen, F.; Wei, D.; Chen, Q.; Zheng, J.; Zhu, L.; Chen, H.; Tang, Z. High Strength and Self-Healable Gelatin/Polyacrylamide Double Network Hydrogels. *J. Mater. Chem. B* **2017**, *5* (37), 7683–7691.

(64) Zhao, X. Multi-Scale Multi-Mechanism Design of Tough Hydrogels: Building Dissipation into Stretchy Networks. *Soft Matter* **2014**, *10* (5), 672–687.

(65) Creton, C. 50th Anniversary Perspective: Networks and Gels: Soft but Dynamic and Tough. *Macromolecules* **2017**, *50* (21), 8297–8316.

PART III

Underwater adhesion of complex coacervates

Chapter 5

5. Underwater adhesion of complex coacervates.

Sandcastle worms have developed protein-based adhesives, which they use to construct protective tubes from sand grains and shell bits. A key element in the adhesive delivery is the formation of a fluidic complex coacervate phase. After delivery, the adhesive transforms into a solid upon an external trigger. In this work, a fully synthetic in-situ setting adhesive based on complex coacervation is reported by mimicking the main features of the sandcastle worm's glue. The adhesive consists of oppositely charged polyelectrolytes grafted with thermoresponsive poly(*N*-isopropylacrylamide) (PNIPAM) chains mixed at a high salt concentration and starts out as a fluidic complex coacervate, that can be injected at room temperature. Upon increasing the temperature above the lower critical solution temperature (LCST) of PNIPAM (*temperature switch*) or decreasing the salt concentration in the environment (*salt switch*), the complex coacervate changes into a non-flowing viscoelastic hydrogel while preserving its volume – the water content in the material stays constant. The setting of the adhesive can be precisely controlled by the balance between the components and shows an even higher adhesion energy (W_a) when a combined temperature-salt switch is applied, making it a potential candidate for tissue adhesion in biological environments, where similar conditions are present.

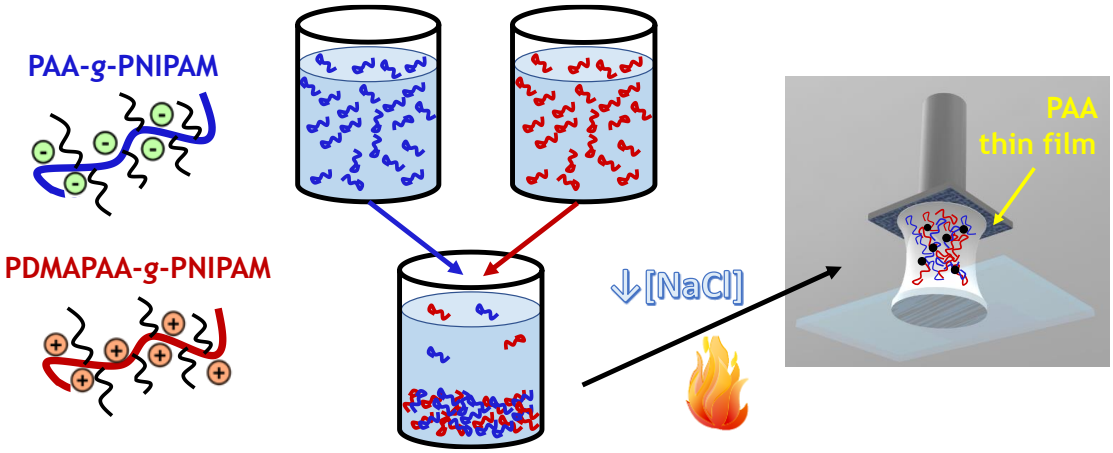

The content of this chapter is the result of a collaboration with Marco Dompé and Prof. Dr. M. Kamperman at the Laboratory of Physical Chemistry and Soft Matter, Wageningen University, The Netherlands. Part of the content is already accepted for publication. This chapter focuses on the underwater tack test developed during this collaboration. Nevertheless, it is necessary to briefly introduce and present the synthesis and characterization of the tested materials.

Contents

5.1. Introduction

Underwater adhesion is technically challenging, because the performance of most adhesives is compromised by the presence of water, which eventually leads to bond failure.[1] The challenge of developing a fully functional underwater adhesive has been successfully overcome by several aquatic organisms, such as mussels, sandcastle worms and barnacles, which are able to bond dissimilar materials together underwater using protein-based adhesives.[1–4] A phenomenon, which is believed to play a fundamental role in the adhesive delivery, is complex coacervation, which is an associative liquid-liquid phase separation of oppositely charged polyelectrolyte solutions.[5,6] Complex coacervates are particularly suitable for underwater adhesion, because of their fluid-like, yet water immiscible properties[7,8] and good wettability.[9] In natural systems, after establishing molecular contact upon delivery, the complex coacervate liquid transforms into a solid-like material by the introduction of covalent or strong non-covalent interactions activated by a change in environmental conditions (e.g. higher pH in seawater, exposure to oxygen).[10] This principle has been mimicked in synthetic systems by designing polyelectrolyte material systems either responsive to a particular trigger (pH,[11–13] ionic strength,[14,15] solvent[16]) or toughened via a crosslinking reaction.[11,17,18] In this work, a new temperature-triggered setting mechanism is introduced in a fully synthetic adhesive by grafting thermoresponsive poly(N-isopropylacrylamide) (PNIPAM) chains on oppositely charged polyelectrolyte backbones.

The use of complex coacervation and thermoresponsive (LCST) domains to solidify the physical network results in a material system that has not yet been explored with key advantages for underwater adhesion: (1) Low viscosity at ambient temperature to ensure precise and controlled delivery (e.g. via a syringe with needle).[15] (2) Easy manipulation in wet environments due to immiscibility of complex coacervates with water,[8] ensuring that the adhesive remains at the application site during setting. (3) Adhesion to diverse surfaces, because of the self-adjustable nature of the system. That means that, depending on the target surface,

different features (cationic, anionic or hydrophobic) will be exposed to the surface.[19] (4) Effective in the presence of water, as no chemical reaction with water or functional groups at the tissue surface is required, and thus can be injected through a fluid without being compromised. (5) In-situ setting in the order of seconds or minutes with limited swelling. The liquid-to-solid transition is activated by a temperature gradient,[20] without the introduction of any chemical cross-linker, and can be tuned further by pH and salt concentration of the surrounding medium. (6) Controlled cohesive properties: the final material is held together by non-covalent ionic and hydrophobic interactions with a variety of bond strengths. Strong bonds may act as permanent crosslinks, imparting elasticity, whereas weak bonds can reversibly break and re-form, and thereby dissipating energy.

In this chapter we are going to briefly introduce and present the synthesis and characterization of the tested materials. The detailed protocol for the complex coacervates grafted with PNIPAM is presented in the annexes. However, we will compare the physicochemical characterization by differential scanning calorimetry, the water content and the rheological properties for complex coacervates prepared with grafting PNIPAM on the backbone polymer chains (Graft) and without grafting PNIPAM (Homo). Additionally, we focus this chapter on the underwater adhesion properties of these complex coacervates, therefore, all underwater probe tests.

5.1.1. Synthesis of negative and positive charged polymers grafted with PNIPAM

The adhesive starts out as a fluid complex coacervate, obtained by mixing two oppositely charged graft copolymers solutions, namely poly(acrylic acid)-grafted-poly(N-isopropylacrylamide) (PAA-g-PNIPAM) and poly(dimethylaminopropyl acrylamide)-grafted-poly(N-isopropylacrylamide) (PDMAPAA-g-PNIPAM) (**Figure 5-1.a**). The anionic polymer, PAA-g-PNIPAM (Mn: 400 kDa), was synthesized using a “grafting to” reaction, i.e. attaching

PNIPAM side chains (Mn: 5.5 kDa) onto a PAA backbone (Mn: 200 kDa) using a coupling reaction.[21] The cationic polymer, PDMAPAA-g-PNIPAM (Mn: 250 kDa), was obtained by copolymerizing DMAPAA monomers with PNIPAM macromonomers (Mn: 5.5 kDa), i.e. PNIPAM chain with a polymerizable end-group, using a "grafting through" polymerization process.[22] The synthesis procedures and the characterization for both polymers are described in more detailed in the annexes. In both polyelectrolytes, the molar ratio of the charged backbone and the PNIPAM side chains is around 70:30 (**Table 5-1**).

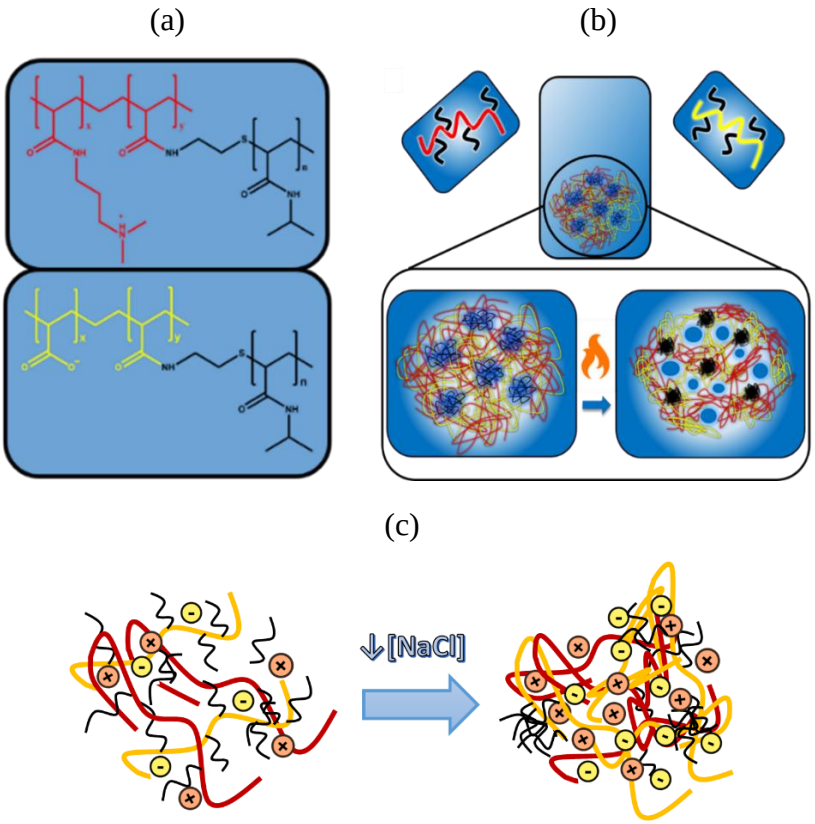

Figure 5-1. (a) Molecular structure of PAA-*g*-PNIPAM (yellow and black) and PDMAPAA-*g*-PNIPAM (red and black). (b) Composition and temperature responsiveness of the complex coacervate phase and the schematics of the phase separation and of the structure below and above the LCST. (c) Schematic representation of the graft copolymer complex coacervate phase before (left) and after (right) the salt switch.

Polymer	M_n NMR (kg/mol)	M_n SEC (kg/mol)	Molar (weight) ratio *monomer backbone/PNIPAM side chains* (%)
PAA	-	239	-
PAA-*g*-PNIPAM	467	403	***71:29 (61:39)***
PDMAPAA	-	139	-
PDMAPAA-*g*-PNIPAM	-	248	***65:35 (72:28)***

Table 5-1. Characteristics of polymers used in this study.

5.1.2. Complex coacervation

Complex coacervation strongly depends on mixing parameters, such as pH, mixing ratio and salt concentration. It is known that, in general, complexation is most effective when both polyelectrolytes carry the same number of charges.[8] To establish the point of charge neutrality and optimal complexation conditions, pH titrations and zeta potential experiments were performed (Annexes). Based on the results of these experiments, the polyelectrolytes were mixed at pH 7.0 and at 1:1 stoichiometric ratio of chargeable units, to reach a total charged monomer concentration of 0.05 M. Additionally, salt concentration affects the strength and the relaxation dynamics of the ionic bonds and thereby the viscosity of the complex coarcervate.[9] In order to obtain a material that can easily flow, providing good contact with the surface of interest, the polyelectrolytes should be mixed at a salt concentration close to the critical salt concentration (CSC, concentration at which complexation is suppressed),[7,8] which is detected slightly above 0.8 M NaCl. For this reason, a salt concentration of 0.75 M NaCl has been chosen in this study.

The solidification of the material, required to resist detachment forces, will be provided by a temperature or by a salt triggered mechanism, also defined as *temperature switch* or *salt switch,* respectively. For the temperature switch at a fixed ionic strength, the complex coacervate phase shows a liquid-to-solid transition when the temperature is raised above the

PNIPAM lower critical solution temperature (LCST, 23 °C in this system) forming physical crosslinks between PNIPAM chains (**Figure 5-1.b**). The salt switch consists on forming stronger electrostatic interactions by immersing the material in a lower ionic strength medium. The salt ions diffuse out of the complex coacervate phase, allowing the formation of stronger electrostatic interactions between oppositely charged polyelectrolyte chains (**Figure 5-1.c**). Consequently, the material, initially a viscoelastic liquid, turns into a soft polyelectrolyte gel. This transition macroscopically resembles the temperature-triggered one described before, but it is intrinsically different since the thermoresponsive domains are inactive because the temperature of the surrounding environment is kept below the LCST and the reinforcement of the material is only ascribed to the formation of stronger electrostatic interactions.

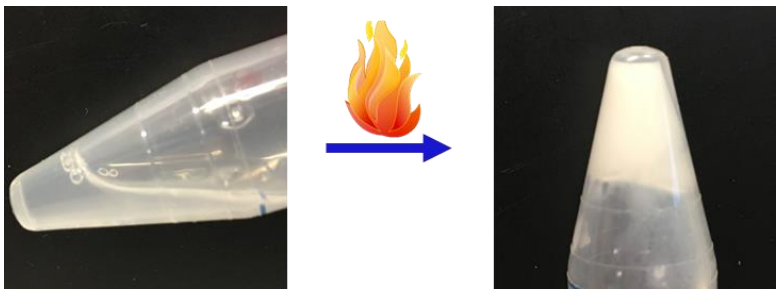

Figure 5-2. Solidification triggered by increasing the temperature above PNIPAM LCST.

5.2. Characterization of complex coarcervates

5.2.1. Physical and chemical properties of complex coacervates

To study the influence of the thermoresponsive PNIPAM grafts, complex coacervates were prepared at room temperature at 0.75 M by mixing graft copolymer solutions (PAA-g-PNIPAM and PDMAPAA-g-PNIPAM) and homopolymer solutions (PAA and PDAMAPAA). When heated at high temperature, the complex coacervates prepared from graft copolymer solutions become white and solid-like (**Figure 5-2**), unlike samples prepared from homopolymer

solutions which remain transparent and liquid. This transition is attributed to the aggregation of PNIPAM side-chains into microdomains, which densify when the temperature is raised above the transition temperature (T_c),[23] leading to the formation of physical crosslinks in the material.

Differential scanning calorimetry

The LCST phase transition of PNIPAM aqueous solutions is a well-studied process: while at low temperature the PNIPAM chains assume a coil conformation in order to maximize hydrogen bonding with the water molecules, above the LCST a transition to the globular state is observed, leading to phase separation.[20] Since energy is required to break the interactions between water molecules and amide groups, Differential Scanning Calorimetry (DSC) can be used to monitor the endothermic process. A typical thermogram is shown in **Figure 5-3**.

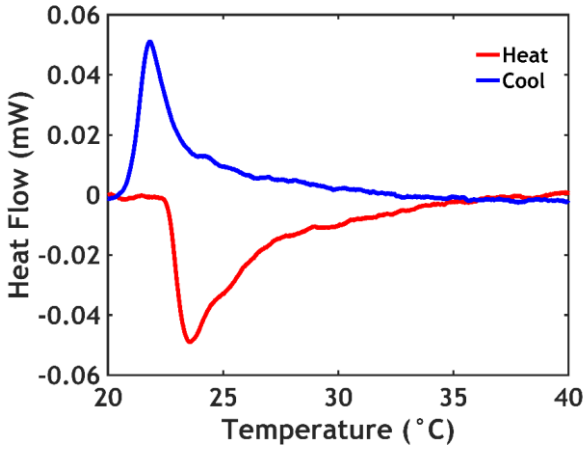

Figure 5-3. Example of a DSC thermogram performed on graft copolymer complex coacervate prepared at 0.75 M NaCl and a ratio of 40 PNIPAM / total polymer molar ratio (mol/mol%).

The endothermic peak in the thermogram is related to the phase transition upon heating. By integrating the area of the peak, it is possible to calculate the enthalpy of the transition (ΔH). In this case, the peak temperature (T_{heat}) is observed at 23.5 °C and ΔH_{heat} equal to 1.8 kJ/mol of NIPAM. This T_c is much lower than the usual value reported for PNIPAM (≈32 °C). This is

due to the high salt concentration of the sample (0.75 M NaCl). Sodium chloride is known to drastically decrease the T_c of PNIPAM and the values observed in this work are in agreement with the data reported in the literature for PNIPAM solutions.[24] When cooling down, an exothermic peak appears at a slightly lower temperature (T_{cool} = 21.8 °C) and with a slightly lower enthalpy (ΔH_{cool} = 1.3 kJ/mol): this hysteresis effect might be due to the different kinetics in the association and dissociation process of the PNIPAM chains, which is a rate-dependent phenomenon.[25]

Small angle X-ray scattering (SAXS)

Small angle X-ray scattering (SAXS) analysis was performed to investigate structural differences below and above the LCST. The detailed protocol used to perform SAXS analysis on the complex coacervates samples is presented in the annexes. At high wave vector q (0.3 – 3 nm^{-1}, length scales at which the conformation of single polymer chains is detected), the curves for both homopolymer (**Figure 5-4.a**) and graft copolymer (**Figure 5-4.b**) complex coacervates show a similar slope ($I \approx q^{-1.7}$) regardless of temperature. This suggests that the conformation of the individual chains is similar in both graft and homopolymer systems and does not change much as a function of temperature. More specifically, this q-dependence indicates that the polymer chains attain a self-avoiding random walk conformation, behaving nearly as in a semidilute polyelectrolyte solutions.[26]

At larger length scales (q-range 0.06 – 0.3 nm^{-1}) an upturn is detected, whose intensity increases as a function of temperature and which is not visible in complex coacervates prepared from homopolymers. This upturn is attributed to the formation of segregated PNIPAM domains (with dimensions of tens of nanometers, according to the observed q-range) and the decreased compatibility between PNIPAM and the complex phase. The absence of a well-defined peak might indicate that the generated PNIPAM domains are polydisperse or too far from each other

to be observed in the q window. The upturn is already observed at temperatures below the LCST indicating that some heterogeneity in PNIPAM chains distribution already exists at room temperature.

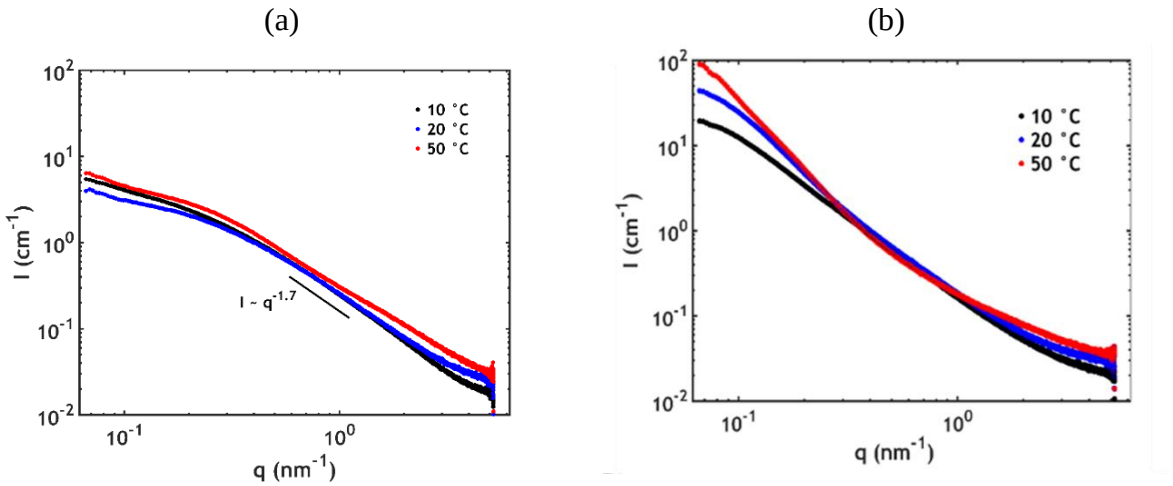

Figure 5-4. SAXS pattern for samples at 0.75 M NaCl solution of (a) homopolymer complex coacervates and for (b) graft copolymer complex coacervates obtained at different temperatures.

Water content in complex coacervates before and after the temperature switch

The water content of the complex coacervate phase below and above the LCST was calculated as follows. Below the T_c, the dilute phase was removed from the tubes containing the samples. After that, a small amount of complex coacervate phase was loaded into an Eppendorf Tube® and weighed on a Mettler Toledo XS205DU analytical balance. The samples were freeze-dried for four days. To study the water content above the T_c, the Falcon™ tubes containing both the dilute phase and the complex coacervate phase were left in a water bath at 40 °C for four days. After removing the dilute phase, the same weighing and freeze-drying procedures were performed. The water content was determined by the weight difference before and after the freeze-drying process. Three replicas were conducted to ensure data

reproducibility. In **Table 5-2**, the details of the complex coacervates prepared from homopolymer and from graft copolymer solutions are shown.

Upon collapse of the PNIPAM chains the domains are expected to shrink and to expel water, as observed in PNIPAM hydrogels.[27] However, no significant change in water content (~91%) and volume is detected upon the liquid-to-solid transition. We speculate that the water expelled by PNIPAM is retained in pockets inside the complex coacervate phase, leading to the formation of a porous structure (**Figure 5-1.b**).[5,28] The isochoric nature of this transition might be beneficial to the overall adhesive performance, since it will prevent the lubrication of the sample-probe interface from the release of water.[1] Moreover, keeping a relatively high level of water within the coacervate will allow to maintain the flexibility and stretchability of the material.[29]

Parameters	**Homopolymer complex coacervates**	**Graft copolymer complex coacervates**
Water Content below LCST (w/w %)	83.1	91.0
Water Content above LCST (w/w %)	-	90.7
PNIPAM Content (mol/mol of total charged monomer %)	0	33

Table 5-2. Preparation details of the complex coacervates analyzed in this work.

Water content in complex coacervates before and after the salt switch

When performing a *salt switch*, it is important to monitor the evolution of the water content and of the total volume of the sample, because both swelling and shrinking might be detrimental for the adhesive performance.[29,30] Thermogravimetric Analysis (TGA) using a SDT Q600 from TA instruments was used to investigate the water content in both homopolymer and graft copolymer complex coacervates before and after the salt switch. After removing the dilute

phase from the Falcon™ tube, in order to determine the water content before the setting reaction, the complex coacervate phase (≈50 mg) was directly loaded into the sample holder, a platinum pan, at room temperature. After the setting reaction, the complex coacervate phase was immersed in a lower ionic strength (0.1 M NaCl) water medium before loading it into the sample holder. The samples were at first equilibrated for 15 minutes at 110 °C. After that, they were submitted to a temperature ramp from 110 °C to 1200 °C at a heating rate equal to 20 °C/min. A typical thermogram is shown in **Figure 5-5**.

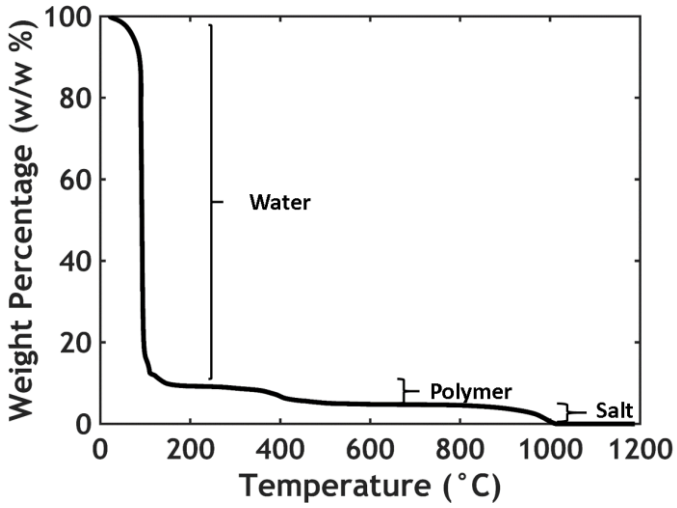

Figure 5-5. Thermogram of a graft copolymer complex coacervate before the salt switch.

From the thermogram, it is possible to determine the weight percentage of the single components of the complex coacervate phase (namely water, polymer and salt), which all have a different degradation temperature. Water is completely removed before reaching 200 °C, the polymeric chains are degraded between 200 °C and 600 °C, while the inorganic salt can be completely eliminated when reaching 1000 °C. By knowing the initial mass of the sample, it is then possible to determine the weight percentage of the single components, which are reported in **Table 5-3**. After the setting reaction, the salt content drastically decreases, as expected. The salt ions diffuse out of the complex coacervate phase and, as a consequence, the water and the

polymer content increase. The total amount of water anyway is not the same, meaning that some water might leave the coacervate phase together with the salt ions. In addition to that, a lot of water is trapped in pores, which are responsible for the opacity of the material after the salt switch.

Sample	Water Content (w/w %)	Polymer Content (w/w %)	Salt Content (w/w %)
Homopolymer Complex Coacervate (Before Setting Reaction)	83.1	9.5	6.4
Homopolymer Complex Coacervate (After Setting Reaction)	85.4	12.4	2.2
Graft Copolymer Complex Coacervate (Before Setting Reaction)	90.7	4.5	4.8
Graft Copolymer Complex Coacervate (After Setting Reaction)	92.9	5.6	1.4

Table 5-3. Weight percentage of single components of complex coacervates obtained from TGA

At high salt concentration (0.75 M NaCl), the homopolymer complex coacervates have a lower water content (83.1%) than the graft copolymer complex coacervates (91%). The presence of the hydrophilic PNIPAM chains reduces the driving force for phase separation, allowing therefore a higher water retention. In both cases, no variation in water content (85% in homopolymer complex coacervates, 93% in graft copolymer complex coacervate) and volume is observed. However, the water content of the complex coacervate phase is generally known to decrease when reducing the salt concentration.[8] On the other hand, when performing a salt switch, the thermodynamic equilibrium between the dilute and the complex coacervate phase cannot be reached because of a kinetic barrier, with most of the water being trapped in pores inside the material. Furthermore, in PNIPAM-reinforced complex coacervates, the presence of hydrophilic chains might favor water retention.[20]

5.2.2. Rheological properties of complex coacervates

Methodology

Rheological measurements were performed on an Anton Paar MCR301 stress-controlled rheometer using a cone-plate geometry (cone diameter 25 mm, cone angle 1°, measurement position 0.05 mm, glass plate). A Peltier element was used to regulate the temperature. The sample loading was performed as follows. The supernatant was taken off from the FalconTM tube using a Pasteur pipette, ending up with the complex coacervate phase only. This phase was then applied on the rheometer using a Pasteur pipette and contact with the cone was performed at the measurement position. When performing a salt switch, the lower ionic strength water (0.1 M NaCl) medium was applied around the sample at 20 °C, with one hour contact time before performing any rheological experiment. When performing a temperature switch, tetradecane was added around the sample and a solvent trap with a metal lid was installed to prevent water evaporation. The temperature was then raised to 50 °C and a waiting time of 15 minutes was applied before any measurement.

When performing a combined switch, the procedure changed depending on the order of the switch performed. If the salt switch was performed first, the 0.1 M NaCl solution was applied at 20 °C, with one hour contact time before raising the temperature to 50 °C, followed by 15 minutes of waiting time before measurement. If the temperature switch was applied first, a 0.75 M NaCl solution was applied and the temperature was raised to 50 °C in a solvent trap, followed by 15 minutes of contact time at the selected temperature before removing the water medium. The 0.1 M NaCl solution was then added around the sample at 50 °C and a contact time of one hour was applied before measurement. Before loading a new sample, the complex coacervate phase together with the dilute phase was centrifuged at 4000 g for 15 minutes.

Linear rheology after the temperature switch

Rheological measurements were performed as a function of frequency and temperature in the linear regime. At 20 °C both complex coacervates prepared from homopolymer and graft copolymer solutions possess a fluid character with the storage modulus (G') crossing the loss modulus (G'') only at high frequencies (**Figure 5-6.a**). In both systems, at room temperature the chains slide along each other with transient electrostatic interactions, giving rise to sticky Rouse dynamics.[31] The crossover frequency (ω_c) is higher (~70 rad/s) in graft copolymer coacervates as compared to homopolymer complex coacervates (~45 rad/s), while both moduli are lower over the whole frequency range. We attribute these differences to the higher water content in the graft copolymer systems, leading to a lower level of polymer entanglement as well as a lower concentration of charged units (sticky points), which lead together to shorter relaxation times τ ($\tau = 1/\omega_c$).

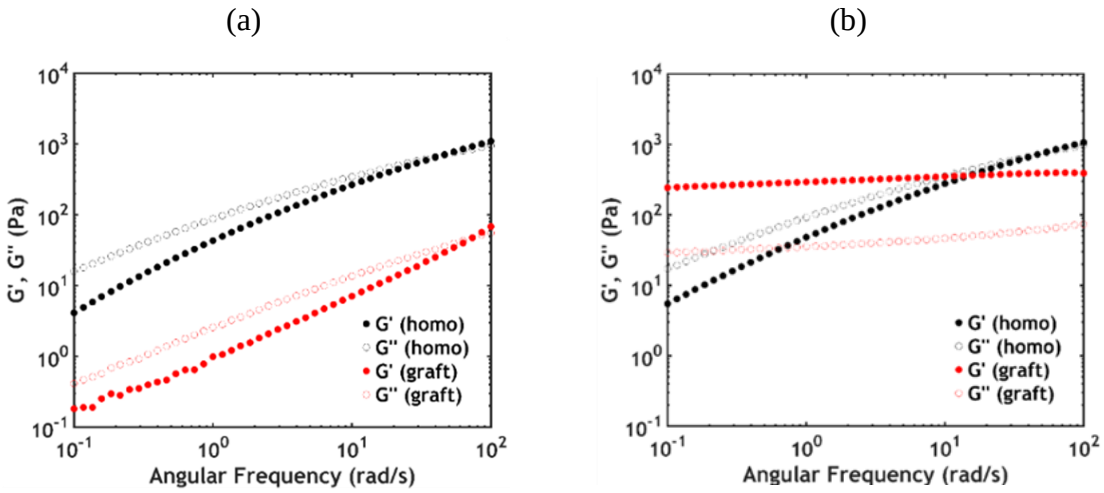

Figure 5-6. Frequency sweeps performed at 20 °C (a) and (b) at 50°C for samples at 0.75 M NaCl solution of homopolymer complex coarcervates and for graft copolymer complex coacervates.

When rising the temperature, the rheological data obtained at 50 °C show that graft copolymers complex coacervates behaves differently from homopolymer complex coacervates. I graft copolymers, both moduli increase and become nearly frequency independent, with G' overcoming G'' (**Figure 5-6.b**). This indicates that the complex coacervate, upon the increase in temperature, turns into a soft elastic solid gel because of the slowing down of the PNIPAM chain dynamics in the phase separated domains, leading to the formation of physical crosslinks which stiffen the material.[32] The G' and G'' values are comparable, in order of magnitude, to those obtained for water solutions of graft copolymers with a neutral backbone (poly(N,N-dimethylacrylamide)) and PNIPAM side chains.[20] It is not surprising to detect similarities since at such a high salt concentration, the charged units are almost completely screened and the few remaining ones are complexed with each other, so that the polyelectrolyte complex backbone is overall neutral.

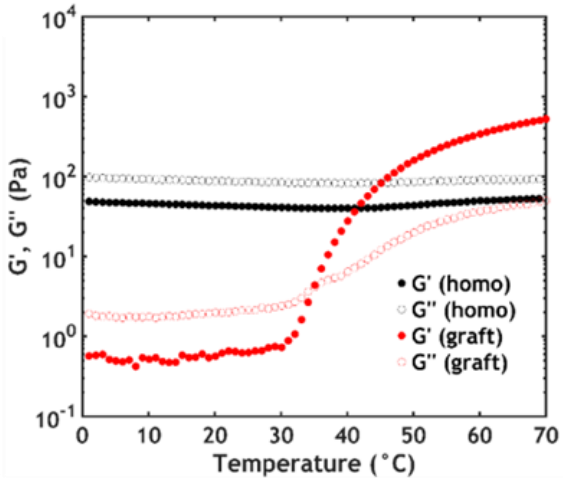

Figure 5-7. Temperature sweeps performed at 1 rad/s for homopolymer and graft copolymer complex coacervates at 0.75 M salt. The value of both G' and G'' in graft copolymer coacervates starts increasing above 26 °C, with the transition occurring at 34 °C, where the crossover of the moduli is detected.

This phase transition is desirable for injectable underwater adhesives, which need to properly wet the surface upon application, yet sustain stress to prevent debonding.[33] At low temperatures, PNIPAM allows higher water retention, making the material more liquid-like and providing good contact with the surface. After that, the temperature increase reinforces the material. Additionally, temperature sweeps were performed on the complex coacervates, heating the sample from 0 °C to 70 °C (**Figure 5-7**) to accurately detect the liquid-to-solid transition. While the moduli of homopolymer complex coacervates are temperature independent, both G' and G'' in graft copolymer coacervates start increasing above 26 °C, with the sol/gel transition occurring at 34 °C, where the moduli crossover is detected.

Linear rheology after a salt switch

The evolution of the storage (*G'*) and of the loss (*G''*) moduli after the salt switch was monitored by a time sweep using linear rheology (**Figure 5-8.a**). The material, initially possessing a fluid character (*G' < G''*), turns immediately into a solid gel (*G' > G''*) when immersed into a lower ionic strength medium. It should be note however that the salt needs to diffuse out and presumably during this transition stage, the structure of the coacervate is heterogeneous since there will be a gradient in new physical crosslinks decreasing when reaching the center. Therefore, therefore its mechanical properties are presumably heterogeneous as well. Moreover, an increase of almost two orders of magnitude in *G'* is observed in the first 20 minutes: afterwards, the moduli head towards a plateau, indicating that the ion diffusion process is over by the end of the experiment.

At high salt concentration and low temperature, both homopolymer and graft copolymer complex coacervates show typical features of a viscous liquid as showed previously (**Figure 5-6.a**). After the setting reaction (*salt switch*), both moduli become almost frequency independent, with *G'* exceeding *G''* (**Figure 5-8.a**). The formation of stronger electrostatic

interactions slows down the chain dynamics, stiffening considerably the material.[32] Before and after the transition, the moduli are higher in the homopolymer complex coacervates than for the graft because of the lower water content and therefore of a higher concentration of crosslink points (**Table 5-3**).

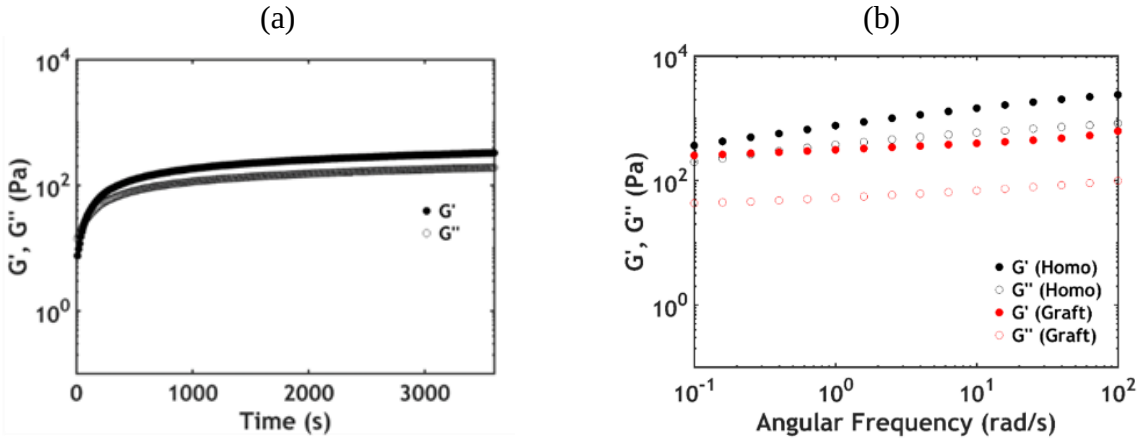

Figure 5-8. (a) Evolution of *G'* and *G''* in homopolymer complex coacervates during the setting reaction (from 0.75 M of NaCl to 0.1 M of NaCl) at a fixed frequency of 0.1 rad/s. (b) Frequency sweeps performed on both material systems after the salt switch (at 0.1 M of NaCl) and at 20°C.

With regard to the graft copolymer complex coacervates, it is interesting to compare the material properties after a setting reaction obtained in response to different environmental triggers, namely temperature and salt. In addition to the different activated interactions, it is important to stress the difference in the kinetics of the transition. When the target temperature is reached, the collapse of the thermoresponsive chains is immediate.[34] On the other hand, the ion diffusion process taking place during a salt switch requires more time.[35] Despite these differences and probably by chance, the moduli measured at the end of the transition have the same value (**Figure 5-9**). *G'* exceeds *G''* over the whole range of frequencies, indicating in both cases the formation of a soft elastic gel with the same amount of crosslink points per unit

volume. After either the temperature switch (**Table 5-2**) or salt switch (**Table 5-3**), the water content in the coacervate is similar around 90%. Therefore, there are still chances that the nonlinear properties are not the same.

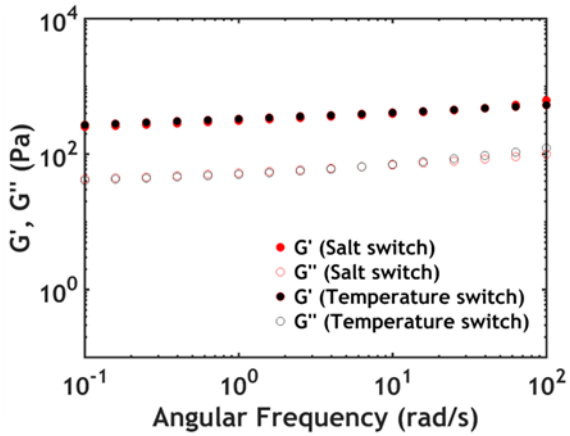

Figure 5-9. Mechanical behavior of the graft copolymer complex coacervate phase in response to different triggers. The tested medium for salt switch was 0.1 M at 20°C and for temperature switch was 0.75 M at 50°C.

Linear rheology after a combined temperature and salt switch

Since the material combines polyelectrolyte components and thermoresponsive units, it makes sense to investigate the setting reaction obtained in response to a combined temperature-salt trigger (**Figure 5-10**). It turns out that the order in which the switch is performed considerably affects the material properties. If the salt switch is performed before the temperature switch, the moduli obtained reach the same values as the ones measured after a single trigger. Vice versa, if the temperature is raised above the LCST before activating the electrostatic interactions, the final moduli increase by one order of magnitude, with *G'* reaching values around 1 kPa. Once more, the polymer architecture affects considerably the final properties. If the long polyelectrolyte chains self-associate first, the short PNIPAM units do not

have the required mobility to form well-entangled nodes. It is not surprising, therefore, that higher moduli are obtained by performing a temperature switch first, which stimulates the collapse of the shorter PNIPAM chains, followed by the salt switch, that activates electrostatic interactions between the longer polyelectrolyte backbones, leading to an overall increase of the number of cross-linking points per unit volume. This type of switch is more likely to occur in applications of injection inside the body where the temperature switch may be immediate and the reinforcement by the salt switch more progressive.

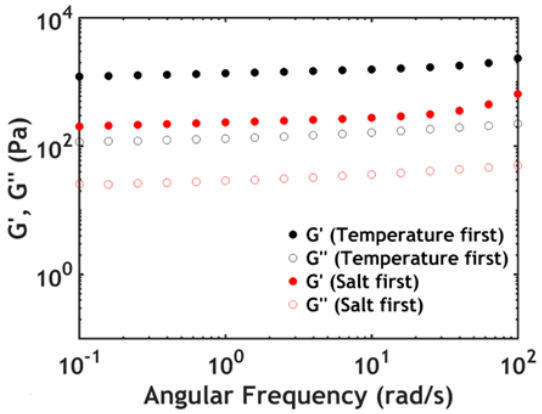

Figure 5-10. Effect of the history of the setting process on the rheological properties when performing a combined temperature and salt-triggered setting reaction for samples at 0.75 M NaCl solution.

5.3. Underwater adhesion

5.3.1. Surfaces synthesis used for the underwater tack test

Poly(acrylic acid) hydrogel thin films

The PAA hydrogel thin films were used as in previous chapters. These samples were synthesized by simultaneously crosslinking and grafting pre-functionalized poly(acrylic acid) (PAA) onto thiol-modified wafers through a thiol−ene click reaction according to the protocol

developed by Chollet.[36] The dry thickness (h_a) for this set of experiments is 144.1 ± 0.2 nm, while the underwater thickness (h_w) is 256.9 ± 0.3 nm. The films swelling ratio (SR), calculated as h_w/h_a, is 1.78.

Positively charged PDMAEMA brushes

Positively charged brush surfaces were synthesized according to the protocol developed by Synytska and coworkers.[37] Briefly, polymer brushes were synthesized using a grafting-from approach of poly(2-dimethylaminoethyl methacrylate) (PDMAEMA) on planar silicon oxide substrates. Silicon wafers with native oxide layer were first modified by aminosilane (3-aminopropyltriethoxysilane) to introduce amino groups on the surface. These amino groups were used for the further immobilization of initiator (α-bromoisobutyryl bromide, BrIn) for ATRP. Thus, polymer grew only over the areas modified with ATRP initiator. Polymerization of DMAEMA on initiator-modified substrates was performed using ARGET-ATRP resulting in a growth of polymer brushes with varied grafting density. In this chapter, we used only PDMAEMA surfaces with 50 nm dry thickness and 0.6 grafting density (nm^{-2}). The films swelling ratio was around 3.5.

5.3.2. Experimental methodology to measure W_a with complex coacervates

The methodology to measure underwater adhesion properties for a temperature and a salt switch was based on the underwater tack test setup developed by Sudre et al.[38] and highly presented during the first chapters of this thesis. However, the test had to be modified since we are testing a liquid-like material that turns into a viscoelastic solid-like gel. The test consists of establishing first a parallel contact and detachment underwater between a homogeneous layer of the complex coacervate (thickness between 0.25 and 0.75 mm) and a Poly(acrylic acid) (PAA) hydrogel thin film (dry thickness: 150 nm). (**Figure 5-11**).

The 10 × 10 mm wafer coated with the PAA hydrogel thin film was glued with a polyvinyl acetate adhesive to a mobile stainless steel probe, which was fixed to the load cell and connected to the Instron machine. The complex coacervate sample was deposited onto a glass. The glass slide was fastened to the bottom of the chamber using plastic screws. Contact between the clean PAA thin film and the complex coacervate was performed in air at 20 °C until a fixed thickness was reached (**Figure 5-12**). A NaCl solution at 20 °C was poured in the internal chamber with a pH of the medium matching the one of the coacervate sample (pH 7.0). The setup was covered at the top with a rubber layer that could provide heat insulation and temperature control. Afterwards, a temperature switch was conducted when the whole chamber was heated to 50 °C using an external temperature control equipment. In contrast, a salt switch was conducted in the following way: After the contact was made between the coacervate sample and the hydrogel thin film, water at 20 °C was poured in the chamber with a pH of the medium matching the one of the coacervate sample (pH 7.0) and a salt concentration of 0.1M.

(a) (b)

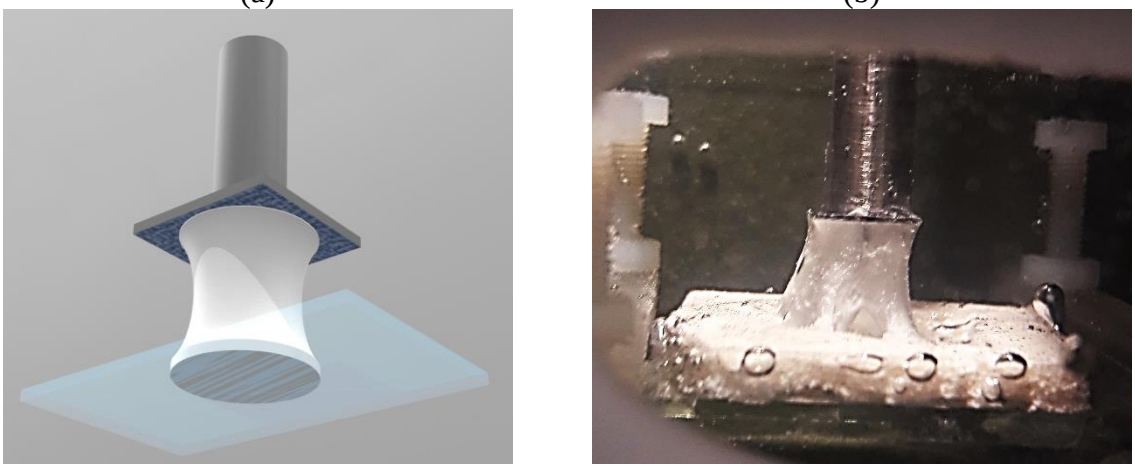

Figure 5-11. Underwater adhesion experiments. (a) Schematics and (b) Picture of the probe tack test performed underwater on a graft copolymer sample after a temperature switch at 50°C in a medium at 0.75 M NaCl.

During either temperature or salt switch the probe was kept motionless at a constant thickness for a certain contact time. Detachment was then performed at a fixed displacement rate of the probe. Raw data of force and displacement were converted into stress and nominal strain values to obtain the work of adhesion (W_a). The strain ε was obtained by normalizing the displacement by the initial thickness of the sample (T_0). The normalized stress σ was calculated by dividing the force by the thin film contact area. The work of adhesion W_a was then calculated as follows

$$W_a = T_0 \int \sigma d\varepsilon \quad (1)$$

Three replicates were conducted for every experiment to ensure data reproducibility.

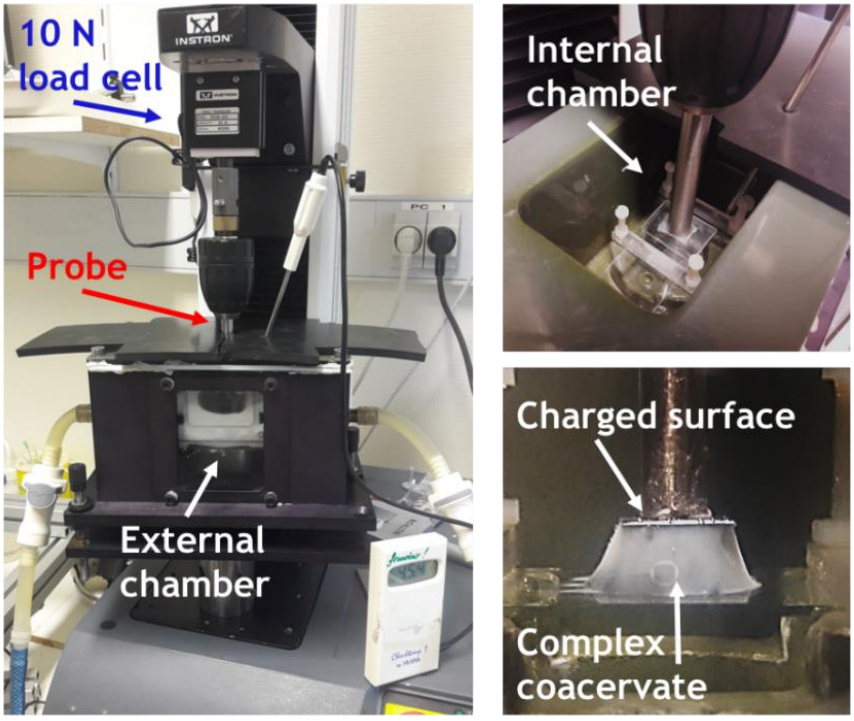

Figure 5-12. (Left) Complete set up of the underwater tack test. (Right-top) Top view of the internal chamber where the complex coacervate sample makes contact with the charged surface, which is glued to the stainless steel probe. (Right-down) Picture of the probe tack test performed underwater after a salt switch.

Initially, the complex coacervate was glued with a cyanoacrylate adhesive onto the glass slide to prevent adhesive failure at the glass surface. However, as shown in **Figure 5-13.a**, no difference in adhesion performance was detected when comparing a test done using cyanoacrylate as additional fixing agent with a test in which the sample was directly loaded onto the glass slide. In order to decrease the number of preparation steps, it was decided not to use the cyanoacrylate adhesive. Additionally, the same adhesion performance is obtained when making contact underwater or in air, meaning that good contact with the PAA hydrogel surface can always be achieved, also through water (**Figure 5-13.b**). This would not be feasible with glues that cure upon reaction with water, like conventional cyanoacrylates, or with water solutions of thermoresponsive graft copolymers bearing neutral backbones[20] since they would disperse in the environment.

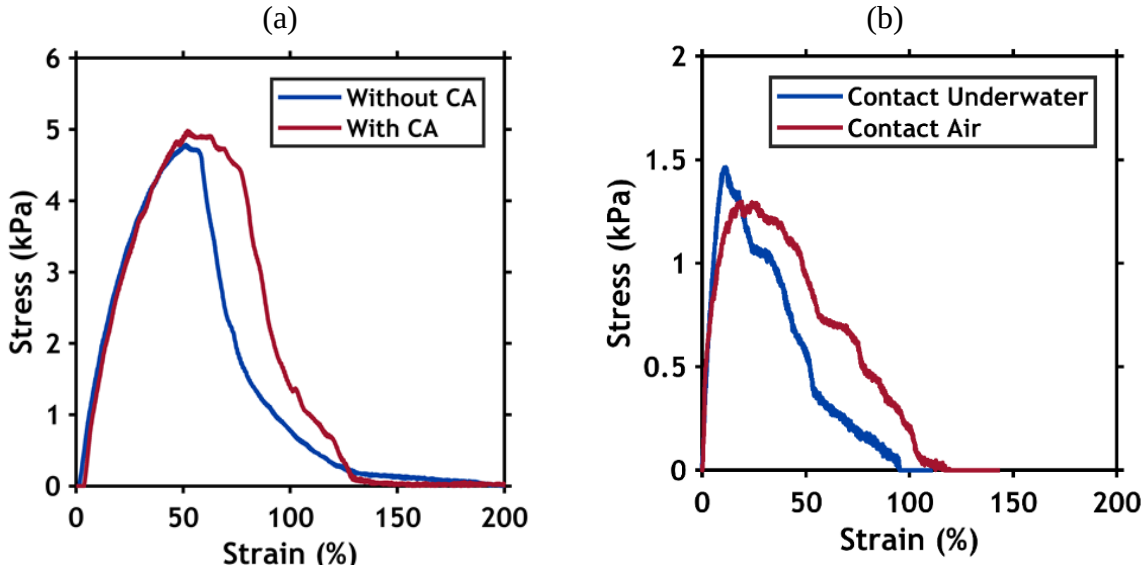

Figure 5-13. (a) Effect of the presence of an additional layer of cyanoacrylate (CA) on the adhesive performance in a probe-tack test. The detachment was performed at 50 °C, in a medium at 0.75 M NaCl at a fixed complex coacervate film thickness (0.5 mm) and at a fixed stretch rate (0.2 s^{-1}). (b) Effect of making the contact either underwater or in air on the adhesive performance. The detachment was performed at 50 °C, at a fixed complex coacervate film thickness (0.5 mm) and at a fixed stretch rate (0.1 s^{-1}).

5.3.3. Underwater adhesion triggered by a temperature switch

As presented before, the water solution in the measurement chamber was prepared at the same pH and salt concentration as that of the analyzed coacervate sample, so that the setting mechanism observed could only be attributed to a temperature difference. At first, contact with a negatively charged poly(acrylic acid) (PAA) hydrogel thin film, forming the probe surface, was made at 20 °C while detachment was performed at 50 °C at a fixed stretch rate (0.1 s^{-1}) and at a fixed initial thickness (h_0 = 0.5 mm). Complex coacervates prepared from homopolymer solutions at 0.75 M NaCl can reach high strain values but cannot sustain any stress, both at 20 °C and at 50 °C, due to their viscous fluid character. A similar trend is observed when probing, at 20 °C, the performance of complex coacervates prepared from graft copolymer solutions at the same salt concentrations, providing low values of work of adhesion (W_a~20 mJ/m^2). When detachment is performed at 50 °C and at 0.2s^{-1}, the formation of PNIPAM physical cross-links strengthens the adhesive, resulting in an increase in work of adhesion of two orders of magnitude in (W_a = 1.6 J/m^2) (**Figure 5-14**).

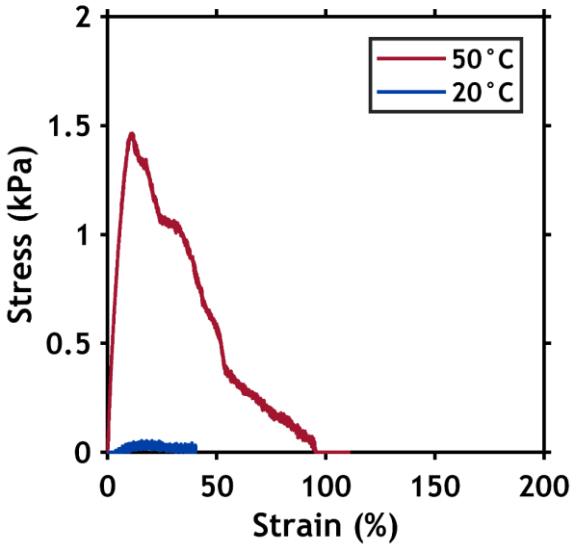

Figure 5-14. The complex coacervate is loaded on a glass slide and contact with a charged probe surface is made underwater at 20 °C. The detachment is then performed either at 20 °C or at 50 °C in a medium at 0.75 M NaCl. Stretch rate: 0.1 s^{-1}.

When performing the temperature switch at different stretch rates, a trend similar to what was observed in other adhesion studies on viscoelastic materials was detected.[39] The stress peak and the work of adhesion increase as a function of detaching speed, indicating that at higher rates the system has insufficient time to relax the stress when probed, so that more energy is dissipated upon detachment (**Figure 5-15.a** and **Figure 5-15.b**). The mode of failure is most often cohesive: at the end of the test, residues of material can always be found on the probe surface.

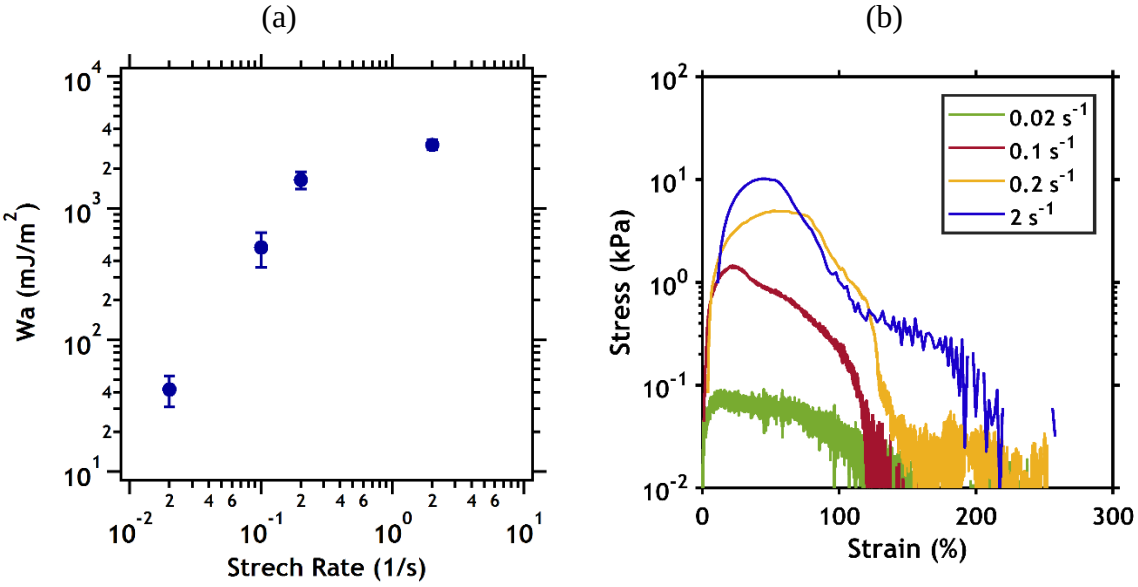

Figure 5-15. (a) Shows the values of the work of adhesion obtained when the detachment was performed at 50 °C, in a medium at 0.75 M NaCl and at a fixed grafted complex coacervate film thickness (0.5 mm), in a stretch rate range from 0.02 s^{-1} to 2 s^{-1}. (b) Corresponding stress-strain curves showing the effect of stretch rate on the adhesion energy.

Additionally, in these experiments, the bulk mechanical properties of the adhesive are tested since this system fails cohesively. Therefore, the work of adhesion increases linearly as a function of the adhesive film thickness, meaning that the loading of more material, results in a higher energy dissipation (**Figure 5-16.a** and **Figure 5-16.b**). However, after a critical thickness

(0.5 mm), the adhesive performance drastically drops, probably because of the introduction of more defects in the sample.

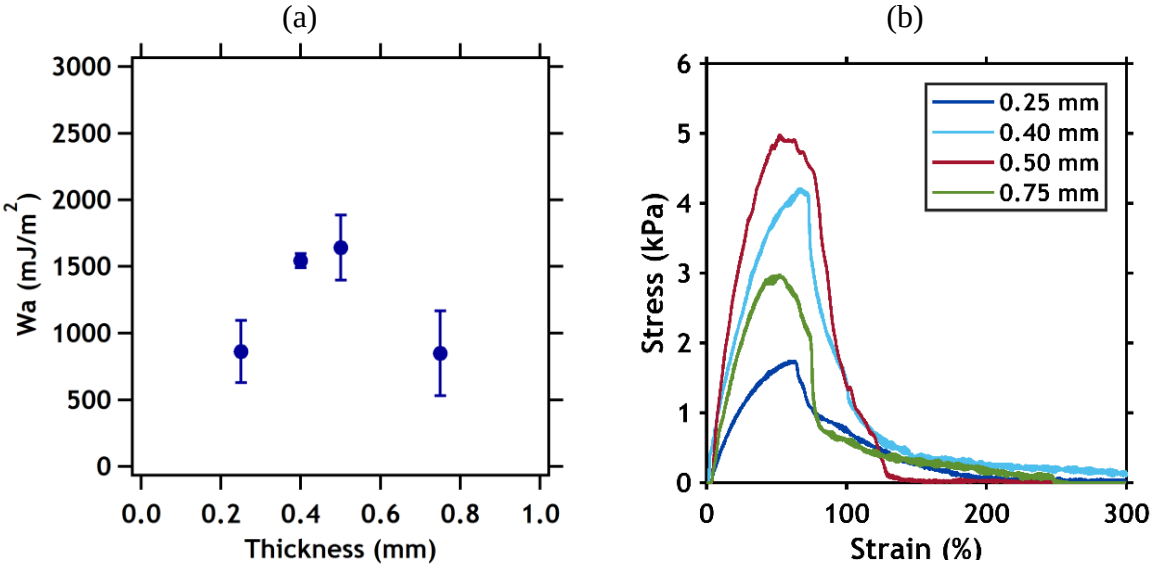

Figure 5-16. (a) Values of work of adhesion obtained when the detachment was performed at 50 °C and at a fixed stretch rate (0.2 s^{-1}), in a graft complex coacervate film thickness range from 0.25 mm to 0.75 mm. (b) Corresponding stress-strain curves showing the effect of thickness on the adhesion energy.

Another parameter that may play a key role in the adhesion performance is the interaction between the coacervate sample and the probe surface. The same probe-tack experiments were performed by using a positively charged probe surface,[37] and the same adhesion strength as with the negatively charged probe surface was obtained (**Figure 5-17**). The complex coacervate contains an equal amount of positive and negative charges, possessing similar characteristics to the polyampholyte gels synthesized by Roy.[19] These materials are found to form ionic bonds with any charged surface, either positive or negative, because of a local polarization of the hydrogel at the interface when a charged countersurface is approached. It is plausible that a similar phenomenon occurs in our system. Electrostatic interactions may form between the

probe surface and the complex coacervate, contributing, together to the strengthening mechanism introduced by thermoresponsive PNIPAM chains, to the overall adhesion performance.

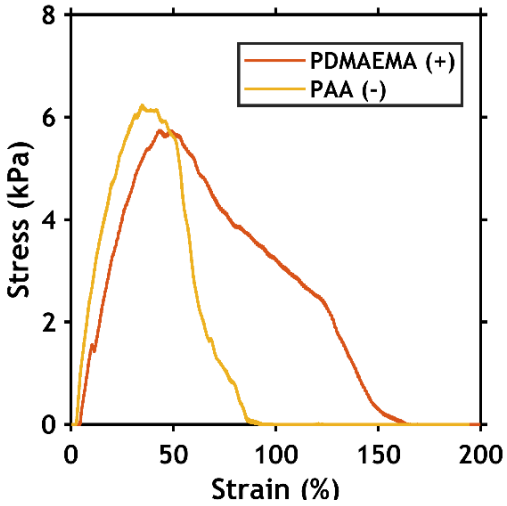

Figure 5-17. Effect of the type of surface on the work of adhesion when the detachment was performed at 50 °C, in a medium at 0.75 M NaCl and at a fixed complex coacervate film thickness (0.5 mm), in a stretch rate range of 0.2 s^{-1}. The calculated work of adhesion for both surfaces is in the same order of ~2 J/m^2.

5.3.4. Underwater adhesion triggered by a salt switch at 20°C

Contact was made between the fluid complex coacervate phase and a negatively charged poly(acrylic acid) (PAA) hydrogel thin film, until a fixed thickness of 0.5 mm was reached. A 0.1 M NaCl water solution at 20 °C was then added in the interior chamber of the underwater tack test setup. Afterwards, the probe was pulled off at a fixed debonding velocity of 100 µm/s (corresponding to a stretch rate of 0.2 s^{-1}) after a certain contact time. Moreover, it is important to determine if this contact time between the sample and the probe is enough to allow complete ion diffusion out of the coacervate phase and reach the equilibrium. **Figure 5-18** shows the

adhesion performance after a salt switch where the contact time was either one hour or 15 hours (overnight). Since only a moderate enhancement of work of adhesion was observed after one night of contact time, it was decided to use one hour of contact time for all the reported experiments.

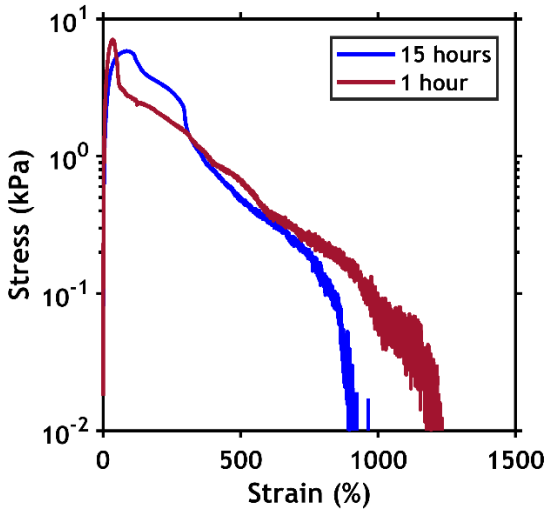

Figure 5-18. Effect of contact time on adhesive performance after a salt switch (from 0.75 M to 0.1 M) when the detachment was performed at 20 °C and at a fixed complex coacervate film thickness (0.5 mm) and a stretch rate of 0.2 s^{-1}. The calculated work of adhesion for both contact times is in the same order of ~7 J/m^2.

A proper adhesive performance is obtained with a good balance between cohesive properties and viscoelastic dissipation.[40] **Figure 5-19.a** presents the adhesion behavior at T=20 °C of homopolymer and graft copolymer complex coacervates, when tested at the same stretch rate of 0.2 s^{-1}. If the bulk elastic energy is high enough to overcome the adhesion energy, as it is observed in homopolymer complex coacervates (W_a = 3.2 J/m^2), the detachment occurs at a low strain (~500%) and the material fails adhesively, without leaving any residues on the probe (**Figure 5-19.b, top**). On the other hand, in graft copolymer complex coacervates, a higher work of adhesion (W_a = 6.5 J/m^2) can be reached because of the formation of filaments (**Figure**

5-19.b, bottom). These filaments can hold stress up to high strain (~1000%) and break by leaving residues of material on the detaching surface (cohesive failure). The presence of the PNIPAM chains apparently induces an energy dissipation mechanism by softening the material and allowing the relaxation of polymer chains during extension.

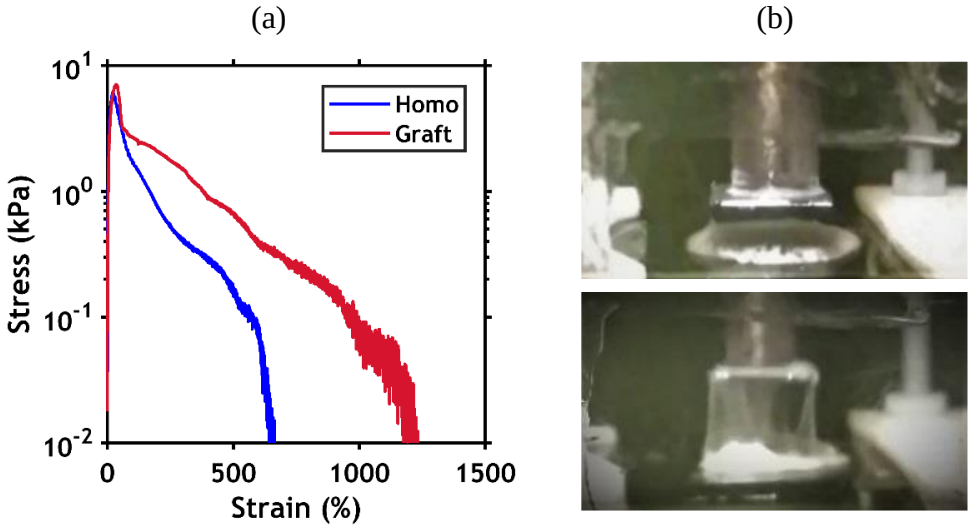

Figure 5-19. (a) Comparison of underwater adhesive performance of both material systems after a salt switch (from 0.75 M to 0.1 M) and a detachment stretch rate of $0.2s^{-1}$ at 20°C. (b) Modes of failure in underwater probe-tack test: Typical observations upon (top) adhesive failure in homopolymer complex coacervates, (bottom) cohesive failure in graft copolymer complex coacervates.

The effect of stretch rate on the work of adhesion was studied by varying the stretch rate in the probe-tack experiments. The work of adhesion increases as a function of the stretch rate applied, being higher in graft copolymer than homopolymer complex coacervates at a stretch rate of 0.02 s^{-1} and 0.2 s^{-1} and being fairly similar at the highest stretch rate of 2 s^{-1} (**Figure 5-20.a**). Adhesion energy increases at higher debonding speeds since the adhesive is not able to relax the stress applied, so that energy needs to be dissipated upon detachment.[39] Remarkably, in graft complex coacervates the mode of failure is cohesive and not change with

the stretch rate applied and can be seen in the stress-strain curves that the strain at failure is very similar at around 1000% (**Figure 5-20.b**). In contrast, for homopolymer complex coacervates it is possible to observe a transition from an adhesive to a cohesive mode of failure when increasing the stretch rate. At a stretch rate of 0.02 s^{-1} the homopolymer complex coacervate failed adhesively reaching a very low strain at failure of around 100%, however, by increasing the stretch rate, this strain a failure increase at around 500% meaning that the coacervate was able to stretch before breaking cohesively (**Figure 5-20.c**).

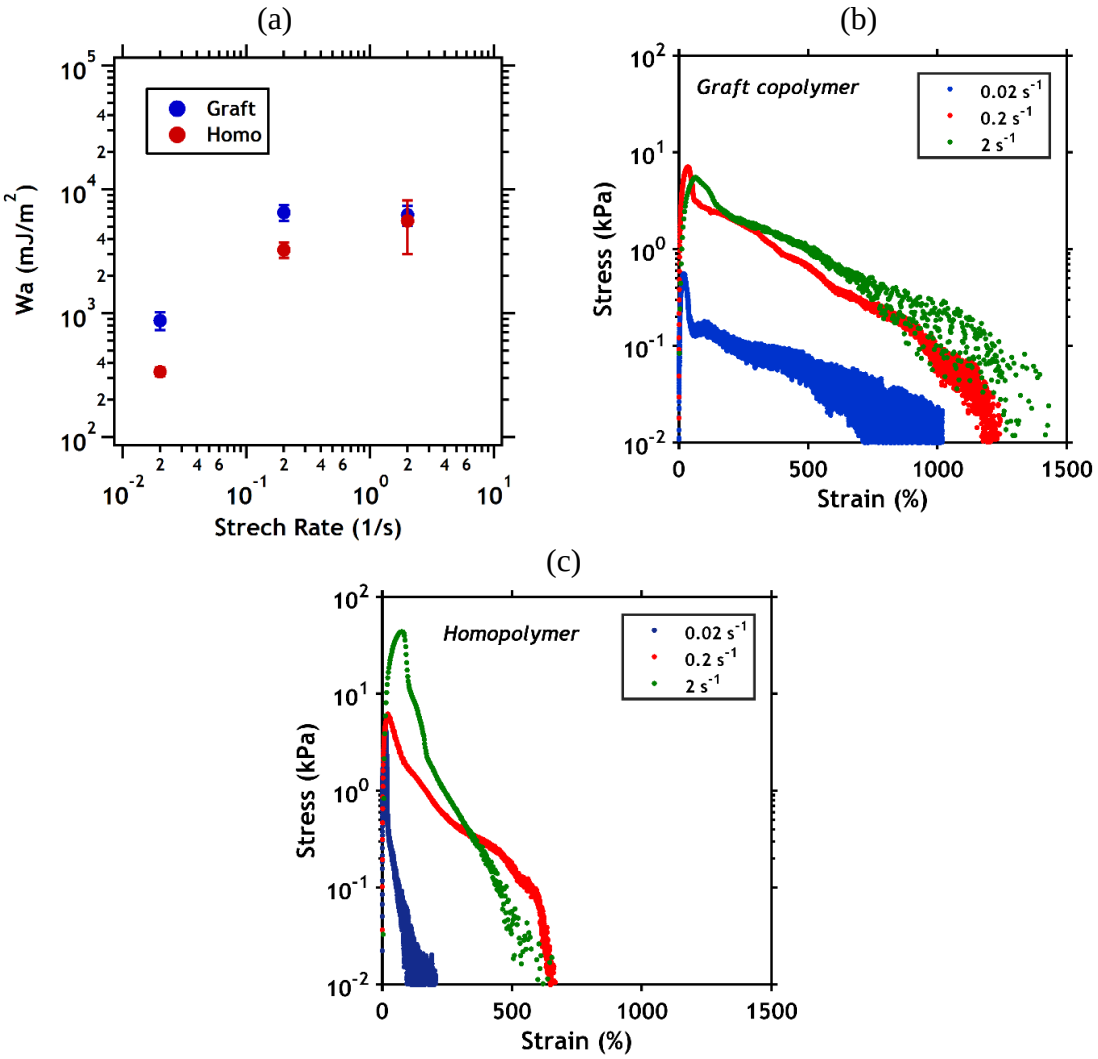

Figure 5-20. (a) Adhesion energy as function of stretch rate after a salt switch for homopolymer and graft copolymer complex coacervates (from 0.75 M to 0.1 M) at 20°C. (b) Effect of stretch rate on the adhesive performance in the graft copolymer complex coacervate. (c) Effect of stretch rate on the adhesive performance in the homopolymer complex coacervate.

5.3.5. Underwater adhesion triggered by a temperature and a salt switch

As described above, the work of adhesion for the graft copolymer complex coacervate obtained after performing a temperature switch at a stretch rate of 0.2 s^{-1} (~1.8 J/m^2. **Figure 5-15**) is almost four times lower than the one reached after a salt switch at the same stretch rate of 0.2 s^{-1} (~7 J/m^2. **Figure 5-18**). Despite the same cohesive mode of failure, in the salt switch case the adhesive can be stretched to a maximum strain (~1000%), which is almost one order of magnitude higher than in the temperature switch (~150%). The architecture of the polymers used and size of the formed domains might play a key role here: the graft copolymers have long polyelectrolyte backbones (M_n ≈ 200 kg/mol) bearing short PNIPAM side chains (M_n ≈ 5.5 kg/mol). When performing a temperature switch, the short PNIPAM units, with restricted mobility because of anchoring onto the main chain, are collapsed forming relatively small domains. Consequently, the maximum strain at failure will be much lower than when performing a salt switch, which promotes stronger electrostatic interactions between the polyelectrolyte backbones, having a much higher mobility and molecular weight than the PNIPAM chains.

The order in which the switch is performed considerably affects the material properties as shown previously in the linear rheology of both setting mechanism as different order (**Figure 5-10**). These rheology experiments presented that if the temperature is raised above the LCST and afterwards the electrostatic interactions are activated by the salt switch, the final elastic moduli increased one order of magnitude compared to the salt switch and the temperature switch alone. By performing a temperature switch first, which stimulates the collapse of the shorter PNIPAM chains, followed by the salt switch that activates electrostatic interactions between the longer polyelectrolyte backbones, leading to an overall increase of the number of cross-linking points per unit volume. In contrast, if the salt switch is performed before the

temperature switch, the long polyelectrolyte chains will collapsed first and the short PNIPAM units will not have the required mobility to form well-entangled nodes.

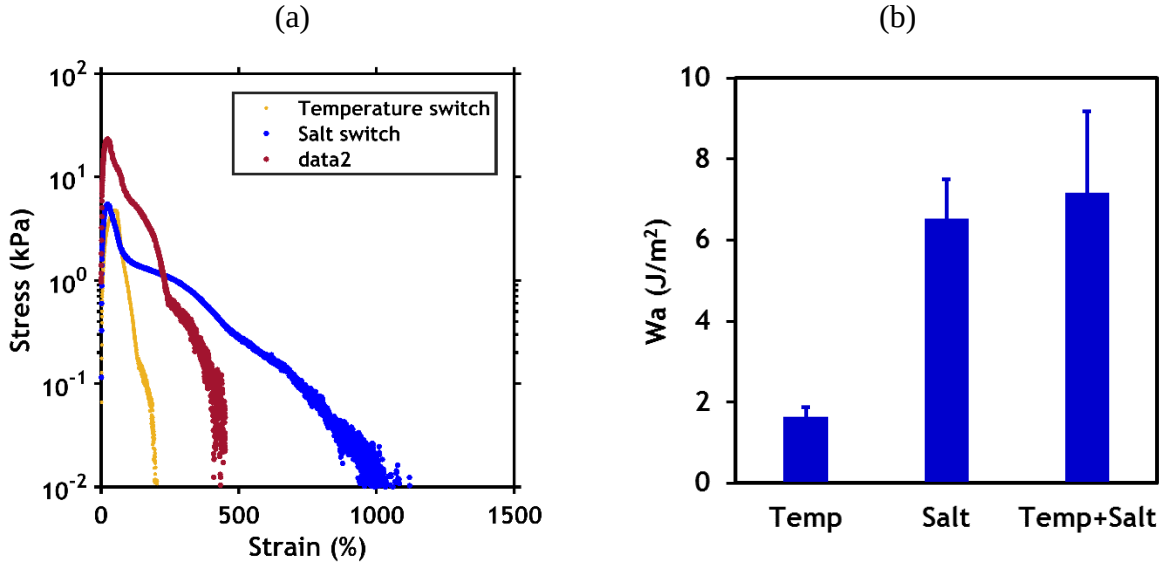

Figure 5-21. Work of adhesion of the graft copolymer complex coacervate measured after different environmentally triggered setting reactions at a stretch rate of 0.2 s^{-1}.

In this context, the adhesive performance of graft copolymer complex coacervate was tested after performing a combined temperature and salt activated setting reaction, where the temperature switch was the first setting mechanism. After loading the adhesive, a 0.1 M NaCl water solution, pre-heated at 50 °C, was added and, after 1 hour contact time, the probe was retracted. The adhesive fails again in a cohesive fashion, leaving residues on the probe. Moreover, by doing the dual setting mechanism in the graft copolymer, it is possible to achieve a higher maximum stress (~20 kPa) compared to either the temperature or the salt switch (~5 kPa). Therefore, since all three setting mechanisms failed cohesively, it is plausible that the average number of cross-linking points per unit volume are higher by doing the double setting mechanism with the temperature switch first (**Figure 5-21.a**). Furthermore, the final work of adhesion is slightly higher (~8 J/m^2) than the one obtained after either a salt switch or a

temperature switch (**Figure 5-21.b**). Therefore, by doing both setting mechanisms, which have different time scales, the underwater adhesive performance is not only maintained but also improved. This means that it is not only the higher value of work of adhesion that matters, but also the kinetics of the transition: the time required for ion diffusion is much longer than the one required for the collapse of the PNIPAM domains. This means that the presence of PNIPAM allows an immediate setting, which would not be possible in homopolymer complex coacervates, followed by a further reinforcement of the material over time due to the formation of stronger electrostatic interactions.

5.4. Conclusions

A new technology for underwater adhesion has been developed in this work. The results show that a complex coacervate with the combination of electrostatic interactions and thermoresponsive domains results in a material system with promising properties as delivery vehicle for underwater adhesives. We have shown that PNIPAM-reinforced complex coacervates provide an outstanding underwater adhesion performance, in response to different triggers, compared to the unmodified counterpart (homopolymer coacervate). Particularly, when tested with the dual combination of an increase in temperature and a decreased in the salt concentration of the environment. Moreover, the graft copolymer complex coacervate failed cohesively and reached only a work of adhesion of 10 J/m^2, which means that the adhesion can indeed be improved by increasing its toughness. For instance, it can be improved by changing the architecture of the polyelectrolyte backbones, the length and amount of PNIPAM chains grafted on the backbones or by introducing local reinforcement in the complex coacervate phase, such as incorporating silica nanoparticles.

The applications of this novel technology are very large since avoids many of the problems of current underwater adhesives. For instance, in biological environments, such as inside the

human body (temperature above the LCST and low salt concentration), the proposed technology is an ideal candidate to bond biological tissues. Outside the human body, the complex coacervate prepared at a high salt concentration is a liquid-like material and when injected inside the body, it can turns into a viscoelastic and sticky material. Therefore, this system will be interested for the unmet surgical adhesives market.

References

(1) Waite, J. H. Nature's Underwater Adhesive Specialist. *Int. J. Adhes. Adhes.* **1987**, *7* (1), 9–14.

(2) Walker, G. The Histology, Histochemistry and Ultrastructure of the Cement Apparatus of Three Adult Sessile Barnacles, Elminius Modestus, Balanus Balanoides and Balanus Hameri. *Mar. Biol.* **1970**, *7* (3), 239–248.

(3) Stewart, R. J.; Weaver, J. C.; Morse, D. E.; Waite, J. H. The Tube Cement of Phragmatopoma Californica: A Solid Foam. *J. Exp. Biol.* **2004**, *207* (26), 4727–4734.

(4) Waite, J. H.; Andersen, N. H.; Jewhurst, S.; Sun, C. Mussel Adhesion: Finding the Tricks Worth Mimicking. *J. Adhes.* **2005**, *81* (3–4), 297–317.

(5) Stewart, R. J.; Wang, C. S.; Song, I. T.; Jones, J. P. The Role of Coacervation and Phase Transitions in the Sandcastle Worm Adhesive System. *Adv. Colloid Interface Sci.* **2017**, *239*, 88–96.

(6) Stewart, R. J.; Wang, C. S.; Shao, H. Complex Coacervates as a Foundation for Synthetic Underwater Adhesives. *Adv. Colloid Interface Sci.* **2011**, *167*, 85–93.

(7) Gucht, J. van der; Spruijt, E.; Lemmers, M.; Cohen Stuart, M. A. Polyelectrolyte Complexes: Bulk Phases and Colloidal Systems. *J. Colloid Interface Sci.* **2011**, *361* (2), 407–422.

(8) Spruijt, E.; Westphal, A. H.; Borst, J. W.; Cohen Stuart, M. A.; Van Der Gucht, J. Binodal Compositions of Polyelectrolyte Complexes. *Macromolecules* **2010**, *43* (15), 6476–6484.

(9) Spruijt, E.; Sprakel, J.; Lemmers, M.; Stuart, M. A. C.; Van Der Gucht, J. Relaxation Dynamics at Different Time Scales in Electrostatic Complexes: Time-Salt Superposition. *Phys. Rev. Lett.* **2010**, *105* (20), 1–4.

(10) Hofman, A. H.; van Hees, I. A.; Yang, J.; Kamperman, M. Bioinspired Underwater

Adhesives by Using the Supramolecular Toolbox. *Adv. Mater.* **2018**, *1704640*, 1–38.

(11) Shao, H.; Stewart, R. J. Biomimetic Underwater Adhesives with Environmentally Triggered Setting Mechanisms. *Adv. Mater.* **2010**, *22* (6), 729–733.

(12) Lawrence, P. G.; Lapitsky, Y. Ionically Cross-Linked Poly(Allylamine) as a Stimulus-Responsive Underwater Adhesive: Ionic Strength and PH Effects. *Langmuir* **2015**, *31* (4), 1564–1574.

(13) Seo, S.; Das, S.; Zalicki, P. J.; Mirshafian, R.; Eisenbach, C. D.; Israelachvili, J. N.; Waite, J. H.; Ahn, B. K. Microphase Behavior and Enhanced Wet-Cohesion of Synthetic Copolyampholytes Inspired by a Mussel Foot Protein. *J. Am. Chem. Soc.* **2015**, *137* (29), 9214–9217.

(14) Wang, Q.; Schlenoff, J. B. The Polyelectrolyte Complex/Coacervate Continuum. *Macromolecules* **2014**, *47* (9), 3108–3116.

(15) Jones, J. P.; Sima, M.; O'Hara, R. G.; Stewart, R. J. Water-Borne Endovascular Embolics Inspired by the Undersea Adhesive of Marine Sandcastle Worms. *Adv. Healthc. Mater.* **2016**, *5* (7), 795–801.

(16) Zhao, Q.; Lee, D. W.; Ahn, B. K.; Seo, S.; Kaufman, Y.; Israelachvili, J.; Waite, J. H. Underwater Contact Adhesion and Microarchitecture in Polyelectrolyte Complexes Actuated by Solvent Exchange. *Nat. Mater.* **2016**, *15* (4), 407–412.

(17) Ahn, B. K.; Das, S.; Linstadt, R.; Kaufman, Y.; Martinez-Rodriguez, N. R.; Mirshafian, R.; Kesselman, E.; Talmon, Y.; Lipshutz, B. H.; Israelachvili, J. N.; et al. High-Performance Mussel-Inspired Adhesives of Reduced Complexity. *Nat. Commun.* **2015**, *6*, 1–7.

(18) Kaur, S.; Weerasekare, G. M.; Stewart, R. J. Multiphase Adhesive Coacervates Inspired by the Sandcastle Worm. *ACS Appl. Mater. Interfaces* **2011**, *3* (4), 941–944.

(19) Roy, C. K.; Guo, H. L.; Sun, T. L.; Ihsan, A. Bin; Kurokawa, T.; Takahata, M.; Nonoyama, T.; Nakajima, T.; Gong, J. P. Self-Adjustable Adhesion of Polyampholyte Hydrogels. *Adv. Mater.* **2015**, *27* (45), 7344–7348.

(20) Guo, H.; Brûlet, A.; Rajamohanan, P. R.; Marcellan, A.; Sanson, N.; Hourdet, D. Influence of Topology of LCST-Based Graft Copolymers on Responsive Assembling in Aqueous Media. *Polymer (Guildf).* **2015**, *60*, 164–175.

(21) Durand, A.; Hourdet, D. Synthesis and Thermoassociative Properties in Aqueous Solution of Graft Copolymers Containing Poly(N-Isopropylacrylamide) Side Chains. *Polymer (Guildf).* **1999**, *40* (17), 4941–4951.

(22) Petit, L.; Karakasyan, C.; Pantoustier, N.; Hourdet, D. Synthesis of Graft Polyacrylamide with Responsive Self-Assembling Properties in Aqueous Media. *Polymer (Guildf).* **2007**, *48* (24), 7098–7112.

(23) Heskins, M.; Guillet, J. E. Solution Properties of Poly(N-Isopropylacrylamide). *J. Macromol. Sci. Part A - Chem.* **1968**, *2* (8), 1441–1455.

(24) Van Durme, K.; Rahier, H.; Van Mele, B. Influence of Additives on the Thermoresponsive Behavior of Polymers in Aqueous Solution. *Macromolecules* **2005**, *38* (24), 10155–10163.

(25) Hourdet, D.; L'Alloret, F.; Audebert, R. Synthesis of Thermoassociative Copolymers. *Polymer (Guildf).* **1997**, *38* (10), 2535–2547.

(26) Marciel, A. B.; Srivastava, S.; Tirrell, M. V. Structure and Rheology of Polyelectrolyte Complex Coacervates. *Soft Matter* **2018**, *14* (13), 2454–2464.

(27) Kaneko, Y.; Yoshida, R.; Sakai, K.; Sakurai, Y.; Okano, T. Temperature-Responsive Shrinking Kinetics of Poly (N-Isopropylacrylamide) Copolymer Gels with Hydrophilic and Hydrophobic Comonomers. *J. Memb. Sci.* **1995**, *101* (1–2), 13–22.

(28) Porcel, C. H.; Schlenoff, J. B. Compact Polyelectrolyte Complexes: "Saloplastic" Candidates for Biomaterials. *Biomacromolecules* **2009**, *10* (11), 2968–2975.

(29) Han, L.; Liu, K.; Wang, M.; Wang, K.; Fang, L.; Chen, H.; Zhou, J.; Lu, X. Mussel-Inspired Adhesive and Conductive Hydrogel with Long-Lasting Moisture and Extreme Temperature Tolerance. *Adv. Funct. Mater.* **2018**, *28* (3), 1–12.

(30) Barrett, D. G.; Bushnell, G. G.; Messersmith, P. B. Mechanically Robust, Negative-Swelling, Mussel-Inspired Tissue Adhesives. *Adv. Healthc. Mater.* **2013**, *2* (5), 745–755.

(31) Spruijt, E.; Cohen Stuart, M. A.; Van Der Gucht, J. Linear Viscoelasticity of Polyelectrolyte Complex Coacervates. *Macromolecules* **2013**, *46* (4), 1633–1641.

(32) Courtois, J.; Baroudi, I.; Nouvel, N.; Degrandi, E.; Pensec, S.; Ducouret, G.; Chanéac, C.; Bouteiller, L.; Creton, C. Supramolecular Soft Adhesive Materials. *Adv. Funct. Mater.* **2010**, *20* (11), 1803–1811.

(33) Creton, C. Pressure-Sensitive Adhesives: An Introductory Course. *MRS Bull.* **2003**, *28* (June), 434–439.

(34) Philipp, M.; Müller, U.; Jiménez Riobóo, R. J.; Sanctuary, R.; Müller-Buschbaum, P.; Krüger, J. K. Kinetic Processes at the Demixing Transition of PNIPAM Solutions. *Soft Matter* **2013**, *9* (41), 9887–9896.

(35) Ghostine, R. A.; Shamoun, R. F.; Schlenoff, J. B. Doping and Diffusion in an Extruded

Saloplastic Polyelectrolyte Complex. *Macromolecules* **2013**, *46* (10), 4089–4094.

(36) Chollet, B.; Li, M.; Martwong, E.; Bresson, B.; Fretigny, C. Multiscale Surface-Attached Hydrogel Thin Films with Tailored Architecture. *ACS Appl. Mater. Interfaces* **2016**, *8*, 11729–11738.

(37) Marschelke, C.; Raguzin, I.; Matura, A.; Fery, A.; Synytska, A. Controlled and Tunable Design of Polymer Interface for Immobilization of Enzymes: Does Curvature Matter? *Soft Matter* **2017**, *13* (5), 1074–1084.

(38) Sudre, G.; Olanier, L.; Tran, Y.; Hourdet, D.; Creton, C. Reversible Adhesion between a Hydrogel and a Polymer Brush. *Soft Matter* **2012**, *8*, 8184–8193.

(39) Ahagon, a; Gent, an. Effect of Interfacial Bonding on the Strength of Adhesion. *J. Polym. Sci. Polym. …* **1975**, *13*, 1285–1300.

(40) Deplace, F.; Carelli, C.; Mariot, S.; Retsos, H.; Chateauminois, A.; Ouzineb, K.; Creton, C. Fine Tuning the Adhesive Properties of a Soft Nanostructured Adhesive with Rheological Measurements. *J. Adhes.* **2009**, *85* (1), 18–54.

6. General conclusion and further remarks

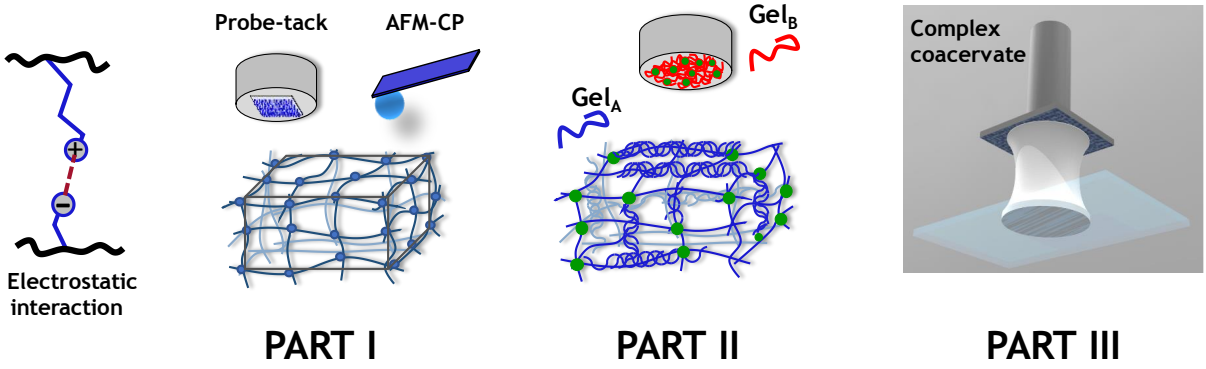

Part I. Model synthetic system

The underwater adhesion between oppositely charged polyelectrolytes swollen materials is a complex multi-parameter problem, and the effect of several of these parameters has been highlighted using a model synthetic system. The synthetic system that we used; an elastic positively charged hydrogel interacting with a negatively charged surface (weak polyacid), highlights the role played by molecular electrostatic interactions and the hydrogel network architecture on the strength of macroscopic adhesion of hydrogels underwater. This synthetic system led us to several conclusions at the macro and the micro scales when linking molecular architectures and electrostatic interactions to underwater adhesion energy:

- Poly(acrylic acid) hydrogel films serve as model system for electrostatic interactions. The fabrication is easy (i.e. less steps than polymer brushes), robust (i.e. homogeneous thickness) and versatile (several thicknesses can be achieved). More notably, these films led us to straightforwardly tune the interfacial areal density of charges and to relate them with macroscopic adhesion without contributing significantly to the dissipated energy.
- The underwater adhesion between hydrogels from electrostatic interactions is a rate-dependent phenomena, since it increases with the logarithm of the pulling rate at both micro

and macro scale when using the probe-tack test and the AFM-colloidal probe technique.

- According to adhesion measurements as a function of different contact times, the kinetics of bond formation is very fast for electrostatic interactions, since only 1 second is enough to measure a significant high macroscopic adhesion ($\sim$0.5 J/m^2).
- Previously, the areal density of interactions at the interface was assumed (of the order of $\Sigma_i \sim 10^{18}$ bonds/m^2). By using the streaming potential measurements, it is possible to make a significantly better estimation of the amount of interactions formed at the interface. The new estimation for our model system at pH 5.5 is of the order of $\Sigma_i \sim 10^{16}$ bonds/m^2.
- The linear dependence of the work of adhesion on the interfacial charge density (Σ_i) is a new result of the thesis. When increasing the pH in the medium, the measured macroscopic and microscopic work of adhesion increases. Qualitatively it is not a surprise that W_a increases with charge density, however, it is notable to conclude that if we double Σ_i we double the work of adhesion. Although such experiments were not carried out, it is possible that for a lower applied pressure during the contact stage ($\ll$3 kPa) or for a higher modulus gel, the density of positive charges available for interactions with the PAA hydrogel thin film will be reduced and that at some point the linear relation will not hold.
- At a constant Σ_i (at both micro and macro scale), the work of adhesion was found to decrease with the elastic modulus of the macroscopic hydrogel. In both, the probe-tack and the AFM-CP measurements, W_a increases up to two orders of magnitude when the elastic modulus of the gel decreases from $\sim$400 kPa to $\sim$100 kPa. This result shows that the rupture of electrostatic interactions between soft swollen materials can be explained semi-quantitatively by comparing to a simple model proposed by Manoj J. Chaudhury for weak adhesion of elastomers. Chaudhury's model, led us to conclude that the adhesion energy can be simplified by a combination of strain rate dependent bond rupture combined with a strong

dependence on the rigidity of the macroscopic hydrogels, particularly on the average number of monomers between crosslinks (N_c). Therefore, according to both Chaudhury's model and the experimental data, by increasing the N_c from ~20 to ~80 monomer units, the macroscopic adhesion increases by almost one order of magnitude from ~0.1 J/m^2 to ~1 J/m^2.

- Finally, we have shown that the measured adhesion energy indeed corresponds to the breaking of electrostatic interactions at the interface since the magnitude (at both micro and macro scale) is highly sensitive to the ionic strength of the medium, i.e the concentration of added salt. This behavior was explained semi-quantitatively by using the Evans model of rupture of single bonds coupled with the Debye-Hückel theory of electrostatic double-layer forces. This model bring us to a description of the debonding process controlled by the kinetic rupture of single ionic bonds as a function of the force pulling rate and the ionic strength of the medium.

We found several encouraging facts when linking molecular electrostatic interactions to macroscopic underwater adhesion. However, it is still necessary to have a better estimate of the areal density of charges for films with different thicknesses (and its effect on macroscopic adhesion), and for films in mediums with different ionic strengths. Finally, Chaudhury's model does not fit our data for a combination of highly crosslinked macroscopic hydrogels and low debonding rates. Therefore, an improvement in this prediction is still necessary, for instance by adding dissipative mechanism of the polymer chains and adding values of non-linear spring constant for the polymer chains.

Part II. Bio-based system

The proposed bio-based system allowed us to measure underwater adhesion between oppositely charged gelatin hydrogels. We found that the concept developed for the synthetic system of controlling and predicting underwater adhesion by tuning the interfacial charge density and the bulk mechanical properties, was transposable to the gelatin-based system. Also, this system led us to several conclusions:

- We succeed in preparing dual crosslink macroscopic hydrogels and thin films based on gelatin using the amidification reaction with the EDC/NHS coupling agent.
- We were able to measure macroscopic underwater adhesion between oppositely charged gelatin gels only by electrostatic interactions and without any contribution of the natural thermoreversible properties of gelatin.
- The new developed gelatin hydrogel thin films serves as a good surface model for mimicking human tissues when testing adhesive systems for medical applications under aqueous environments.
- When adhesive failure occurred, the W_a of Gel_A hydrogels against PAA films was significantly higher than against Gel_B films showing that W_a strongly depends on the interfacial charge density since PAA has a higher density of negative charges than Gel_B, as shown by streaming potential measurements.
- In adhesion experiments between Gel_A and Gel_B, it was possible to tune W_a by changing the pH of the tested medium since the charge level of both Gel_A and Gel_B is pH-dependent.

We showed with this bio-based system, that interfacial charge density and mechanical properties of macroscopic hydrogels are important parameters that permit to control underwater macroscopic adhesion between oppositely charged hydrogels. Moreover, the connection of

molecular architecture and macroscopic adhesion underwater of this gelatin system is not fully understood.

Finally, we presented very briefly a new model system to study the work of adhesion underwater between a gelatin-acrylamide double network hydrogel. Yet, a systematic study of the molecular architecture of this system is necessary to fully understand its connection with the macroscopic underwater adhesion strength.

Part III. Underwater adhesion of complex-coacervates

A new proof of concept for underwater adhesion has been developed in this work. The results show that a complex coacervate with the combination of electrostatic interactions and thermoresponsive domains results in a material system with promising properties as delivery vehicle for underwater injectable adhesives. Moreover, we were able to adapt the underwater probe-tack test to measure, in a reproducible way, the underwater adhesion properties of complex coacervates adhesives after being exposed to either a temperature or a salt switch, or a combination of both setting mechanisms.

We have shown that PNIPAM-reinforced complex coacervates provide an outstanding underwater adhesion performance, in response to different triggers, compared to the unmodified counterpart (homopolymer coacervate). Particularly, when tested with the dual combination of an increase in temperature and a decrease in the salt concentration of the environment. The applications of this novel technology are very broad since it avoids many of the problems of current underwater adhesives. For instance, in biological environments, such as inside the human body (temperature above the LCST and low salt concentration), the proposed technology is an ideal candidate to bond biological tissues. Outside the human body, the complex coacervate prepared at a high salt concentration is a liquid-like material and when

injected inside the body, it can turns into a viscoelastic and sticky material. Therefore, this system will be interested for the unmet surgical adhesives market.

Moreover, the graft copolymer complex coacervate failed cohesively and reached a work of adhesion in the order of 10 J/m^2, which means that the adhesion can indeed be higher by increasing the toughness of the adhesive itself. For instance, it can be improved by changing the architecture of the polyelectrolyte backbones, the length and amount of PNIPAM chains grafted on the backbones or by introducing local reinforcement in the complex coacervate phase, such as incorporating silica nanoparticles.

Annexes

Synthesis of complex coarcervates based polyelectrolytes polymers grafted with PNIPAM.

Materials

Poly(acrylic acid) (PAA, analytical standard, M_n = 239 kg/mol, M_w = 1030 kg/mol), poly(*N*-isopropylacrylamide) amine terminated (PNIPAM-NH_2, average M_n = 5.5 kg/mol), *N*,*N*'-dicyclohexylcarbodiimide (DCC, 99%), acrylic acid (AA, 99%), potassium persulfate (KPS, ≥ 99%), *N*-methyl-2-pyrrolidone (NMP, anhydrous, 99.5%), sodium chloride (NaCl, ≥ 99 %), 1-(3-dimethylaminopropyl)-3-ethyl-carbodiimide hydrochloride (EDC, ≥ 98 %), *N*-hydroxysulfosuccinimide (NHS, 98%), allylamine (98%), toluene (anhydrous, 99.8%), formic acid (≥ 95 %) and 1,4-dithioerythritol (≥ 99 %) were purchased from Sigma-Aldrich. Poly(acrylic acid) (PAA, 25% soln. in water, M_w ≈ 50 kg/mol) was purchased from Polysciences. *N*,*N*-Dimethylaminopropyl acrylamide (DMAPAA, 98%) was purchased from ABCR GmbH. Sodium metabisulfite ($Na_2S_2O_5$, 98%) was purchased from Scharlau. (3-Mercaptopropyl)trimethoxysilane (95 %) was purchased from Alfa Aesar. Methanol (99.9%), tetrahydrofuran (THF, stab./BHT, 99.8%), diethyl ether (stab./BHT AR, 99.5%) and acetonitrile (ACN, AR, 99.8) were purchased from Biosolve. 1.0 M and 0.1 M Sodium Hydroxide solutions (NaOH), 1.0 M and 0.1 M hydrochloric acid (HCl) solutions and CertiPUR® (pH 4.0 buffer solution, citric acid/sodium hydroxide/hydrogen chloride) were purchased from Merck Millipore. Tetradecane (99%) was purchased from TCI Europe. Millipore water was obtained from Milli-Q (Millipore, conductivity: 0.055 $mScm^{-1}$). Silicon wafers were purchased from ACM. Polyvinyl acetate glue (ref. L0196, 20 ml) was purchased from 3M. Cyanoacrylate adhesive (ref. 495) was purchased from Loctite. DMAPAA was

passed through an alumina column to remove the inhibitor. All other products were used as received without further purification.

PAA-g-PNIPAM synthesis

Poly(acrylic acid)-*g*-poly(*N*-isopropylacrylamide) (PAA-*g*-PNIPAM) was synthesized using a "grafting onto" technique according to the method developed by Durand.[1] Briefly, poly(acrylic acid) (PAA) was dissolved in *N*-methyl-2-pyrrolidone (NMP) at 60 °C for 24 hours in a three-neck round-bottom flask equipped with a reflux condenser and a magnetic stirrer. Amine terminated poly(*N*-isopropylacrylamide) (PNIPAM-NH_2), dissolved in NMP, was then added (Figure 1). The mixture was bubbled with nitrogen and, after 2 hours, *N*,*N*'-dicyclohexylcarbodiimide (DCC), previously dissolved in NMP and purged with nitrogen, was added. The ratio between DCC units and amine end groups was set to 10. After 24 hours, the mixture was exposed to air and the flask was immersed in an ice bath.

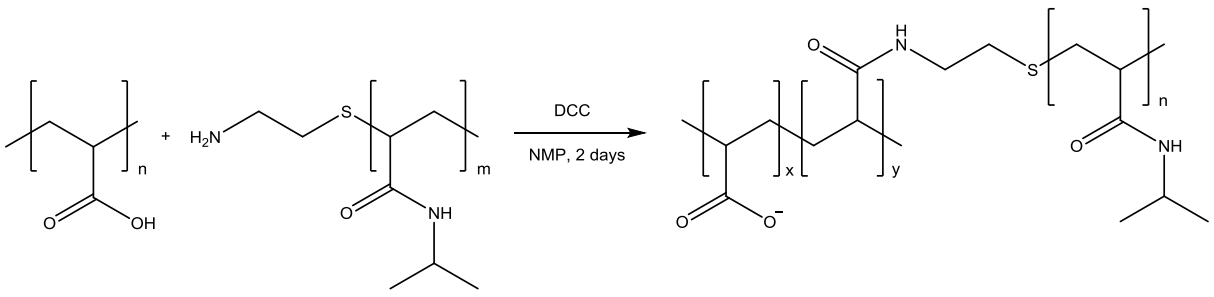

Figure 1. PAA-g-PNIPAM synthesis scheme

Dicyclohexylurea (DCU), by-product of the coupling reaction, precipitated out of the solution and it was removed via centrifugation. PAA-*g*-PNIPAM was then precipitated using a 1.0 M sodium hydroxide (NaOH) solution ([NaOH]/[Acrylic acid units] ≈ 2). The product was washed three times with cold methanol and tetrahydrofuran (THF) and dissolved in Milli-Q water. The residual DCU was removed via centrifugation and the copolymer was dialysed for 1 week against Milli-Q water (membrane cut-off ≈ 10 kg/mol). The final product was recovered by freeze-drying and analysed with ^{1}H-NMR and size exclusion chromatography (SEC).

PAA-*g*-PNIPAM (Figure 2): PAA (^{1}H-NMR, 400 MHz, D_2O, δ (ppm)): 1.46-1.68 (2H,CH_2 backbone), 2.10 (1H, CH backbone). PNIPAM (^{1}H-NMR, 400 MHz, D_2O, δ (ppm)): 1.14 (6H, CH_3), 1.58 (2H, CH_2 backbone), 2.02 (1H, CH backbone), 3.88 (1H, CH).

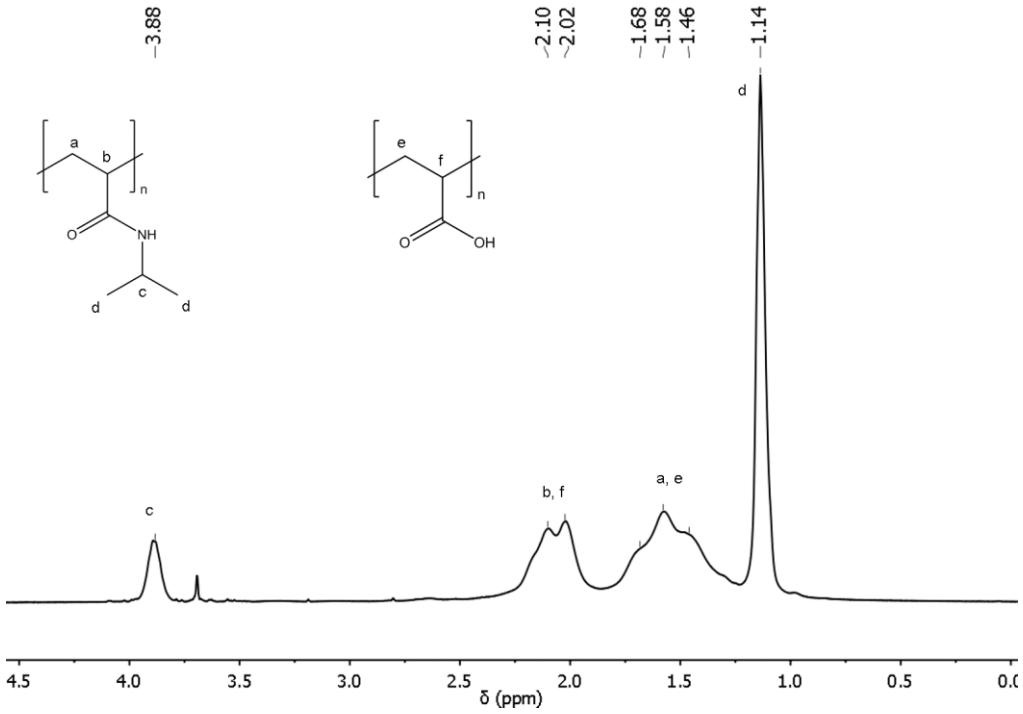

Figure 2. ^{1}H-NMR spectrum of PAA-g-PNIPAM

The molar ratio of PNIPAM sidechains was determined as follows. At first, the area of the peak at 3.88 ppm was set to 1.0. Afterwards, in order to get the PAA contribution to the ^{1}H-NMR spectrum, the area between 1.25 ppm and 2.5 ppm was subtracted by 3.0 (number of hydrogens belonging to the PNIPAM backbone) and successively divided by 3.0 (number of hydrogens belonging to the PAA backbone). The molar ratio of PNIPAM sidechains was then obtained by dividing the area relative to one PNIPAM hydrogen (1.0) by the sum of the areas relative to one PAA hydrogen and one PNIPAM hydrogen. The calculated molar ratio between PAA and PNIPAM is 71:29. Since the M_n of both the backbone and the side chains are known, it is also possible to calculate the total M_n of the copolymer and the number of side chains by ^{1}H-NMR:

the calculated M_n is 400kg /mol, resulting in nearly 28 PNIPAM side chains for every PAA backbone.

M_n of the copolymer was determined by size exclusion chromatography on an Agilent Technologies 1200 system using an Ultrahydrogel 500 column with an Agilent 1200 RI detector. Samples were run using water as eluent containing 100 mM $NaNO_3$ and 10 mM phosphate buffer at pH 7 at a flow rate of 0.5 ml min^{-1}. The calibration was performed using poly(methacrylic acid) standards. M_n as determined by SEC is 403 kg/mol, in good agreement with the ^{1}H-NMR results, with a PDI of 8.5. The high PDI is due to the high polydispersity of the PAA backbone (PDI 4.3) and of the PNIPAM side chains (PDI 3.21), and due to the coupling reaction, which does not allow for control of the number of grafts per backbone.

PDMAPAA-g-PNIPAM synthesis

Poly(*N*,*N*-dimethylaminopropyl acrylamide)-*g*-poly(*N*-isopropylacrylamide) (PDMAPAA-*g*-PNIPAM) was synthesized using a "grafting through" technique. First, a poly(*N*-isopropylacrylamide) macromonomer (macroPNIPAM) was synthesized and subsequently polymerized together with *N*,*N*-dimethylaminopropyl acrylamide (DMAPAA) to obtain the final copolymer.

MacroPNIPAM was prepared according to the method developed by Petit.[2] Briefly, PNIPAM-NH_2 and acrylic acid (AA) were dissolved in NMP in a one-neck round-bottom flask at room temperature and bubbled with nitrogen for 1 hour (**Figure S3**). The ratio between AA units and amino end groups was set to 15. DCC, dissolved in NMP and bubbled with nitrogen, was then added to the mixture ([DCC]/[AA] = 1). The reaction was allowed to proceed for 3 hours under continuous stirring.

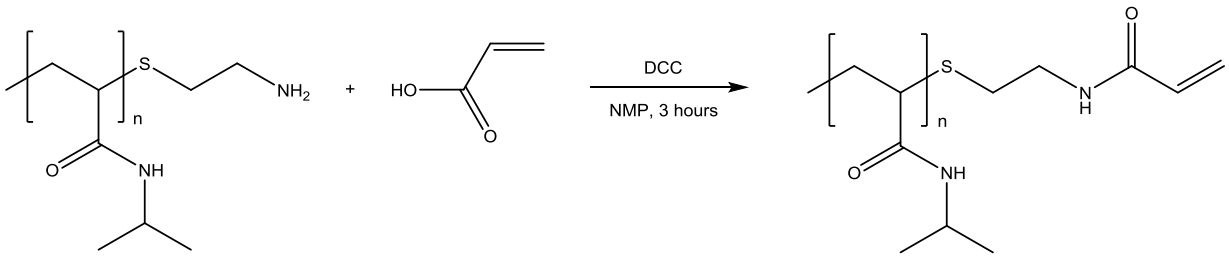

Figure 3. MacroPNIPAM synthesis scheme

DCU was removed via centrifugation and macroPNIPAM was precipitated in cold diethyl ether and washed three times with the non-solvent. The macromonomer was then dialysed against Milli-Q water (membrane cut-off ≈ 2 kg/mol), freeze dried and analysed with ^{1}H-NMR.

MacroPNIPAM (Figure 4): (^{1}H-NMR, 400 MHz, D_2O (solvent peak at 4.70), δ (ppm)): 1.14 (6H, CH_3), 1.58 (2H, CH_2 backbone), 2.01 (1H, CH backbone), 2.63 (2H, CH_2), 3.45 (2H, CH_2), 3.90 (1H, CH), 5.77, 6.20 and 6.38 (3H, end-group).

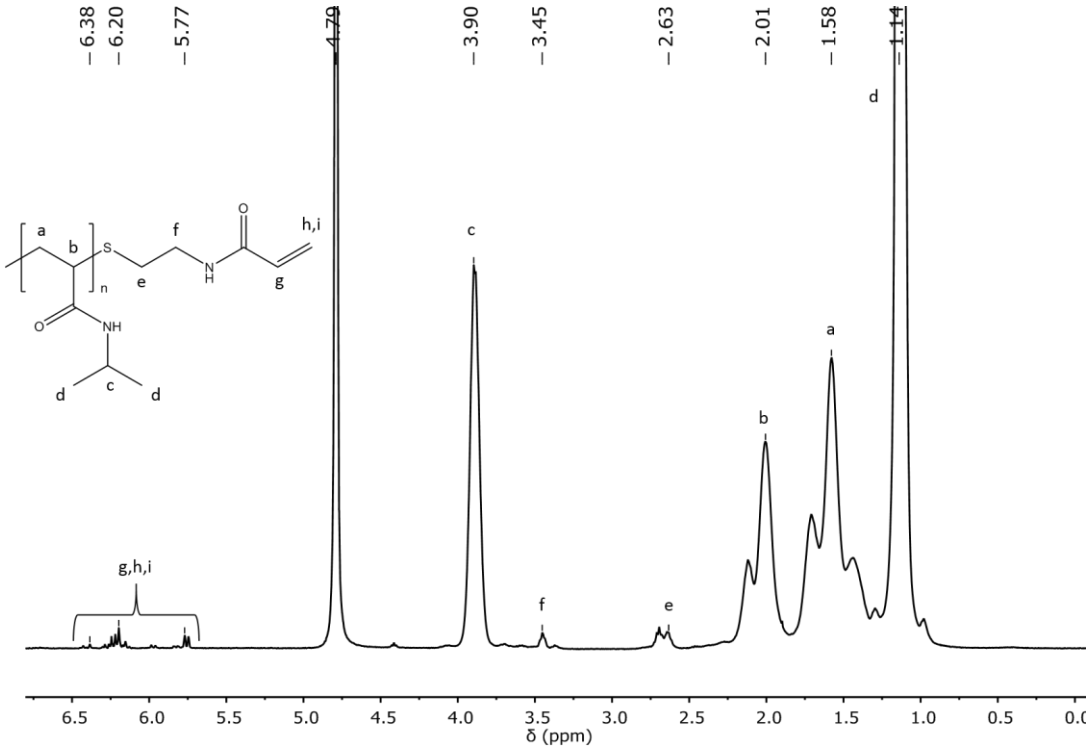

Figure 4. ^{1}H-NMR spectrum of macroPNIPAM

In Figure 4 it is possible to detect the presence of the double bond in the region between 5.5 ppm and 6.5 ppm, which means that the coupling reaction has been performed successfully.

PDMAPAA-*g*-PNIPAM was then obtained by aqueous free radical polymerization: macroPNIPAM and DMAPAA were dissolved at room temperature in a buffer solution at pH = 4 in a three-neck round-bottom flask equipped with a reflux condenser and a magnetic stirrer. The mixture was bubbled with nitrogen for 1 hour; then, sodium metabisulfite ($Na_2S_2O_5$) and potassium persulfate (KPS), previously dissolved in the same buffer solution and purged with nitrogen, were added ([DMAPAA]/[KPS] = 333, [DMAPAA]/[$Na_2S_2O_5$] = 1000) (**Figure S5**). The reaction was allowed to proceed for 4 hours under continuous stirring. The reaction was then stopped exposing the mixture to air and the final product was recovered by precipitation in acetonitrile (ACN).

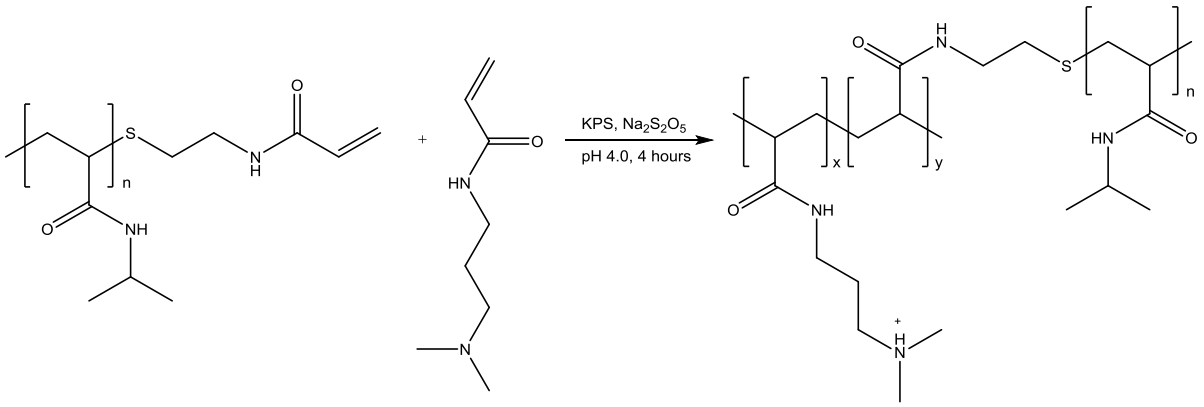

Figure 5. PDMAPAA-g-PNIPAM synthesis scheme

The copolymer was dissolved in the buffer solution and the precipitation in ACN was repeated three times. The final product was then dialysed against Milli-Q water (membrane cut-off ≈ 10 kg/mol) for 1 week. PDMAPAA-*g*-PNIPAM was recovered by freeze drying.

PDMAPAA homopolymer was obtained using the same procedure without adding the PNIPAM macromonomer in the reaction mixture.

PDMAPAA-*g*-PNIPAM (Figure 6): PDMAPAA (^{1}H-NMR, 400 MHz, D_2O, δ (ppm)): 1.63 (1H, CH backbone), 1.91 (2H, CH_2), 2.08 (1H, CH backbone), 2.73 (6H, CH_3), 2.94 (2H, CH_2), 3.25 (2H, CH_2). PNIPAM (^{1}H-NMR, 400 MHz, D_2O, δ (ppm)): 1.20 (6H, CH_3), 1.76(2H, CH_2 backbone), 2.08 (1H, CH backbone), 3.95 (1H, CH).

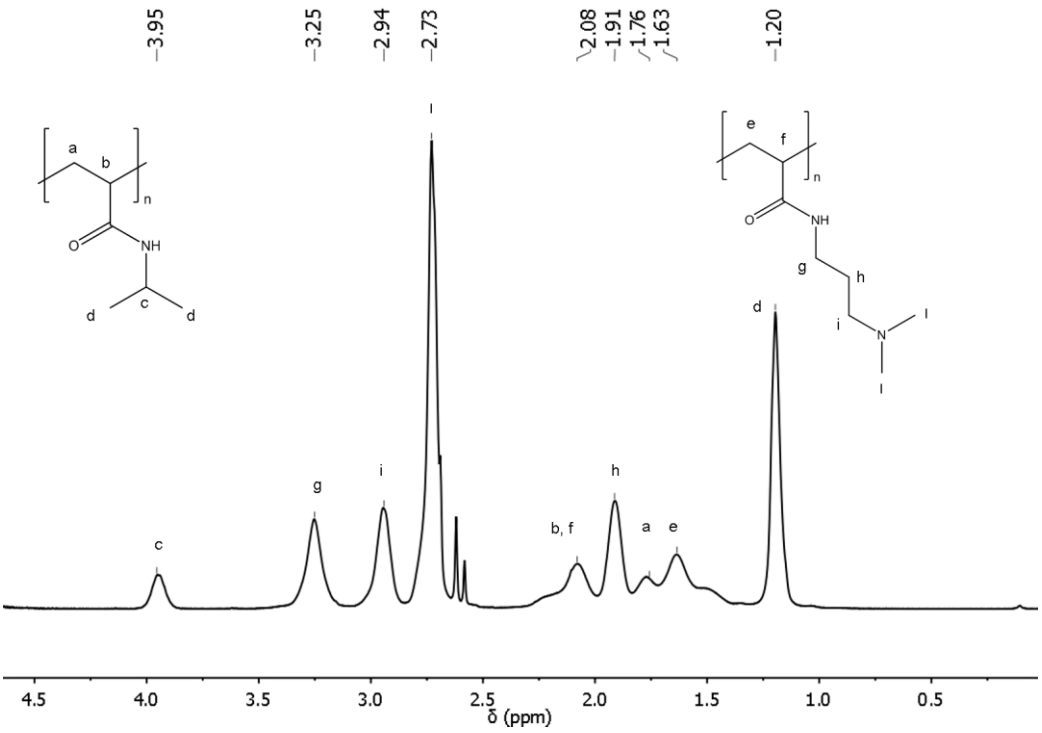

Figure 6. ^{1}H-NMR spectrum of PDMAPAA-g-PNIPAM

The mol% of PNIPAM sidechains was determined as follows. At first, the area of the peak at 1.20 ppm, corresponding to 6 hydrogens in the PNIPAM isopropyl group, was set to 1.0. Afterwards, the area of the peak at 2.73, corresponding to 6 hydrogens in the PDMAPAA dimethylamine group, was determined. The molar ratio of PNIPAM sidechains was then obtained by calculating the ratio between the PNIPAM signal (1.0) and the sum of the PNIPAM and PDMAPAA signals. The calculated molar ratio between PDMAPAA and PNIPAM is 65:35. Since the M_n of the backbone is not known, it is not possible to calculate the total M_n of the copolymer by ^{1}H-NMR.

M_n of the copolymer was determined by size exclusion chromatography on an Agilent Technologies 1260 Infinity II system using a PSS Novema MAX 1000 Å column with an Agilent 1260 RI detector. Samples were run using water as eluent containing 300 mM formic acid at a flow rate of 0.6 ml min^{-1}. The calibration was performed using poly(2-vinylpyridine) standards. M_n of the copolymer is 248 kg/mol, with a PDI of 4.4, which gives an average number molar mass of 186 kg/mol for the PDMAPAA backbone which carry around 12 PNIPAM side-chains. The high PDI is due to the high polydispersity of the PNIPAM side chains (PDI 3.21), to the interactions of the polymer with the column that broaden the molecular weight distribution and to the low molecular weight control due to the free radical polymerization technique. In Table 1, a summary of the characteristics of the polyelectrolytes used in this study is listed.

Polymer	***M_n* NMR (kg/mol)**	***M_n* SEC (kg/mol)**	**PDI**	**Molar (weight) ratio *monomer backbone/PNIPAM side chains* (%)**
PAA	-	239	4.3	-
PAA-*g*-PNIPAM	467	403	8.5	***71:29 (61:39)***
PDMAPAA	-	139	4.6	-
PDMAPAA-*g*-PNIPAM	-	248	4.4	***65:35 (72:28)***

Table 1. Characteristics of polymers used in this study

Optimal mixing conditions

Parameters that strongly affect complex coacervation are the pH, the mixing ratio and the salt concentration.[3,4] In order to obtain a material that could be properly tested in the underwater probe-tack test, the optimal mixing conditions were determined.

Optimal mixing pH

The graft copolymers that were synthesized possess weak polyelectrolyte backbones, which means that the degree of ionization changes as a function of pH. Complex coacervation is

achieved when both the polyelectrolytes are charged and the yield is higher when the degree of ionization of both species is higher. It is important to know, then, what is the optimal pH at which oppositely charged graft copolymer solutions should be mixed. The optimal mixing pH was determined by pH titrations and zeta potential measurements on single polymer solutions.

In order to determine the degree of ionization as a function of pH, pH titrations were performed on single graft copolymers solutions to determine the pK_a and the pK_b. pH titrations were carried out on PAA-*g*-PNIPAM solution, starting from a fully protonated form, and on PDMAPAA-*g*-PNIPAM solution, starting from a fully deprotonated form ([NaCl] = 0.1 M). The concentration of the solution was set to 1.0 g/L. Sodium hydroxide (NaOH) 0.1 M and hydrochloric acid (HCl) 0.1 M solutions were used to modify the pH. The titrations were performed at room temperature using a Schott CG 842 pH meter. The effective pK_a and pK_b were taken as the pH halfway of the equivalence point and could be used to calculate the degree of ionisation as a function of pH (Figure 7), according to the following equations:[3]

$$\alpha_- = \frac{10^{pH-pK_a}}{1+10^{pH-pK_a}}$$

$$\alpha_+ = \frac{10^{pK_b-pH}}{1+10^{pK_b-pH}}$$

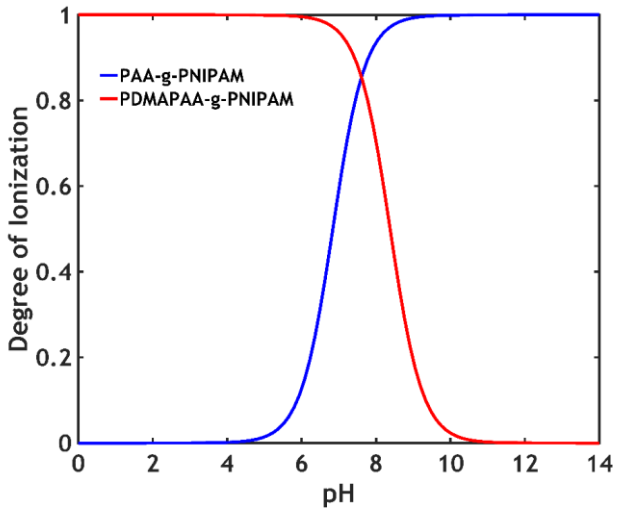

Figure 7. Degree of ionisation of the two graft copolymers as a function of pH

From Figure 7, it is evident that PAA-*g*-PNIPAM acquires a negative charge at pH 4.0 and it becomes fully charged at pH 9.0, while PDMAPAA-*g*-PNIPAM has a positive charge below pH 12.0 and it is fully charged below pH 6.0. The pH at the crossover point is around 7.6.

In addition to that, zeta potential measurements were carried out in order to determine the optimal mixing pH. The analysis were performed on a Malvern Instruments Zetasizer Nano ZS. The electrophoretic mobility was converted into zeta potential values using the Smoluchowsky model. Zeta potential measurements of single graft copolymer solutions were performed as a function of pH (Figure 8). The solutions were prepared at a charged units concentration (moles of PAA/PDMAPAA per unit volume) of 0.01 M and at 0.1 M NaCl. The pH of every sample was adjusted using 0.1 M NaOH and 0.1 M HCl solutions. Experiments were performed in a pH range between 3.5 and 11.5.

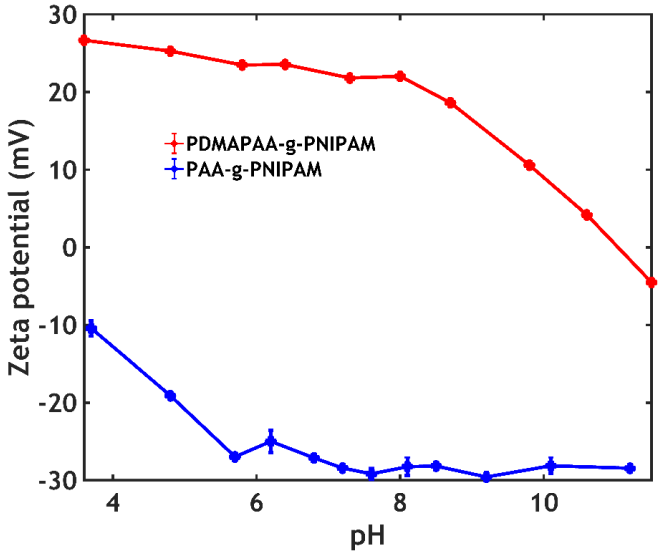

Figure 8. Zeta potential of the two graft copolymer solutions as a function of pH

The trend is similar to the one observed in the titration experiment: PDMAPAA-*g*-PNIPAM is positively charged below pH 11.0 while PAA-*g*-PNIPAM is always negatively charged in the

range analysed. It was not possible to perform experiments at lower pH values because PAA and PNIPAM start to interact at acidic pH, forming complexes which precipitate.

To determine at which pH the oppositely charged polyelectrolytes solutions should be mixed to maximise the interactions and the complex coacervate yield, a strategy commonly used in literature has been used. A third order polynomial line was fitted through the experimental data obtained.[5,6] After that, the product of the absolute values of the zeta potential of the oppositely charged polyelectrolytes at the same pH was calculated. The obtained value is called strength of electrostatic interactions (SEI) and was plotted as a function of pH (Figure 9).

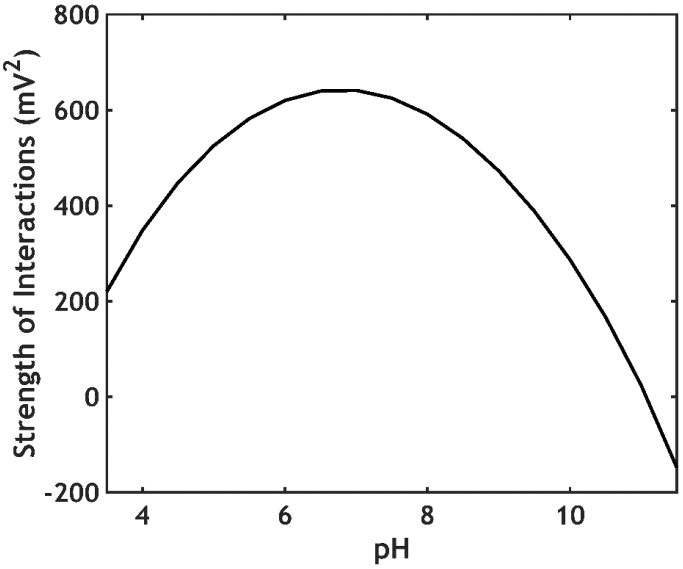

Figure 9. Strength of interactions between the two polyelectrolytes as a function of pH

From this graph, it is clear that the interactions between the graft copolymers are maximised in the pH region around 6.75. After comparing this result to the data obtained from the titration experiments, the optimal mixing pH was set to 7.0.

Optimal mixing ratio

Zeta potential measurements were performed on mixtures of oppositely charged copolymer solutions as a function of the mixing ratio (Figure 10). The mixing ratio is defined as the ratio between positively chargeable units and total chargeable units in the mixture and was calculated according to the information obtained by ^{1}H-NMR. Single graft copolymer solutions were prepared at pH 7.0 and at 0.1 M NaCl. Subsequently, the solutions were mixed at different mixing ratios, keeping the total chargeable monomer concentration (sum of PAA and PDMAPAA moles per unit of volume) constant (0.01 M). The obtained mixtures were centrifuged for 10 minutes at 4000 g to separate any precipitate that could have formed. Zeta potential measurements were then performed on the supernatant as a function of the mixing ratio to check the presence of excess charge in solution.

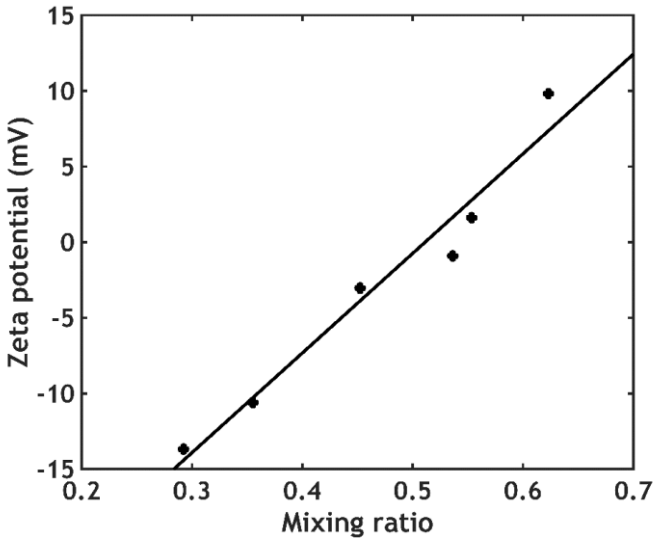

Figure 10. Zeta potential of the dilute phase as a function of the mixing ratio

The graph clearly shows that excess charge is detected in the dilute phase except for a mixing ratio of 0.5, which is when charge balance is achieved. That means that the charges are counterbalanced in the complex coacervate phase and the excess ends up in the dilute phase when the mixing ratio deviates from 0.5. The optimal mixing ratio was then set to 0.5.

Optimal salt concentration

To have good adhesive properties underwater, the material should behave like a fluid when contact is made with the probe and like a stress-bearing solid when the detachment is performed. In order to obtain a material that can easily flow, providing good contact with the surface of interest, the polyelectrolytes should be mixed at a salt concentration close to the critical salt concentration (CSC, concentration at which complexation is suppressed), which is detected slightly above 0.8 M NaCl. For this reason, a salt concentration of 0.75 M NaCl has been chosen in this study. The solidification of the material, required to resist detachment, will then be provided by the formation of stronger electrostatic interactions by immersing the material in a lower ionic strength medium and/or of physical crosslinks between PNIPAM chains above the LCST.

Complex Coacervate formation

Stock solutions of PAA-*g*-PNIPAM and PDMAPAA-*g*-PNIPAM were prepared at a chargeable monomer concentration (PAA/PDMAPAA moles per unit volume) of 0.1 M. The pH of PAA-*g*-PNIPAM solution was adjusted to 7.0 using 0.1 M NaOH and 0.1 M HCl. 3.0 M NaCl was added to the PDMAPAA-*g*-PNIPAM solution to adjust the ionic strength, followed by an adjustment of the pH to 7.0 using 0.1 M NaOH and 0.1 M HCl. Finally, a calculated amount of PAA-*g*-PNIPAM solution was added to the PDMAPAA-g-PNIPAM solution. The final mixture contained a 0.05 M total chargeable monomer concentration, a 0.5 mixing ratio, a 0.75 M NaCl concentration and a pH equal to 7.0. Complex coacervation took place directly after addition of the PAA-*g*-PNIPAM solution. After vigorous shaking, the complex coacervate phase was dispersed throughout the mixture. The mixture was left to equilibrate for 1 day and then it was centrifuged at 4000 g for 1 hour. Two clearly separated phases appeared, with the complex coacervate phase sedimented at the bottom of the centrifuge tube. In addition to that,

complex coacervates were prepared by mixing homopolymers solutions (PAA and PDMAPAA). These samples were obtained using the same procedure and the same parameters described above. The complex coacervates were stored at 4 °C in order to preserve them at a temperature well below the LCST.

Small Angle X-Ray Scattering (SAXS)

SAXS experiments were performed at the European Synchrotron Radiation Facility (ESRF) in Grenoble, France, at the Dutch-Belgian Beamline (BM26B, DUBBLE). A Pilatus 1M detector, a fixed energy of 12 keV and a single detector distance of 2.7 meters were used, covering a total *q*-range from 0.0665 nm^{-1} to 5.23 nm^{-1}. The two dimensional images were radially averaged around the centre of the primary beam to obtain the isotropic SAXS profiles. The scattering pattern from Silver Behenate was used for the calibration of the *q*-range. Eltex was used as reference sample for the intensity calibration in absolute units (cm^{-1}). The data have been normalized to the intensity of the incident beam to correct for primary beam intensity decay. The data were corrected for absorption and background scattering. Two ionization chambers, placed before and after the sample, were utilized for the measurement of the incident and transmitted beams. The background correction was made by subtracting from the total intensity the contribution of density fluctuations evaluated from measuring the blank (0.75 M NaCl solution).The samples were loaded into 2 mm quartz capillaries using Pasteur pipettes and stored at 4 °C before measurements. Before starting the experiment, the samples were placed in a Linkam DSC 600 furnace that allows temperature control. A temperature ramp from 10 °C to 50 °C was performed. SAXS images were recorded every 30 seconds at a fixed temperature, which was kept constant for an interval ranging from 5 to 20 minutes depending

on the temperature selected. When a new temperature was selected, the heating rate was fixed to 10 °C/min.

References

(1) Durand, A.; Hourdet, D. Synthesis and Thermoassociative Properties in Aqueous Solution of Graft Copolymers Containing Poly(N-Isopropylacrylamide) Side Chains. *Polymer (Guildf).* **1999**, *40* (17), 4941–4951.

(2) Petit, L.; Karakasyan, C.; Pantoustier, N.; Hourdet, D. Synthesis of Graft Polyacrylamide with Responsive Self-Assembling Properties in Aqueous Media. *Polymer (Guildf).* **2007**, *48* (24), 7098–7112.

(3) Spruijt, E.; Westphal, A. H.; Borst, J. W.; Cohen Stuart, M. A.; Van Der Gucht, J. Binodal Compositions of Polyelectrolyte Complexes. *Macromolecules* **2010**, *43* (15), 6476–6484.

(4) Gucht, J. van der; Spruijt, E.; Lemmers, M.; Cohen Stuart, M. A. Polyelectrolyte Complexes: Bulk Phases and Colloidal Systems. *J. Colloid Interface Sci.* **2011**, *361* (2), 407–422.

(5) Espinosa-Andrews, H.; Enríquez-Ramírez, K. E.; García-Márquez, E.; Ramírez-Santiago, C.; Lobato-Calleros, C.; Vernon-Carter, J. Interrelationship between the Zeta Potential and Viscoelastic Properties in Coacervates Complexes. *Carbohydr. Polym.* **2013**, *95* (1), 161–166.

(6) Timilsena, Y. P.; Wang, B.; Adhikari, R.; Adhikari, B. Preparation and Characterization of Chia Seed Protein Isolate-Chia Seed Gum Complex Coacervates. *Food Hydrocoll.* **2015**, *52*, 554–563.

Abstract

This work attempts to unravel some of the intricacies of the aqueous adhesion of elastic or viscoelastic highly swollen charged polymers. In Part I the first model synthetic system permitted us to successfully link the molecular architecture of the elastic hydrogels, their interfacial charge density and the ionic strength of the medium with the underwater adhesion properties at a macroscopic level using probe-tack experiments and a microscopic level using atomic force microscopy. In Part II we successfully expanded the synthetic elastic system to measure macroscopic adhesion between oppositely charged gelatin-based hydrogels. Finally, in Part III we developed a synthetic and bio-inspired adhesive based on complex coacervation. This novel adhesive system combines the contribution of electrostatic interactions and thermoresponsive domains resulting in a material with promising properties as an injectable viscoelastic adhesive for medical applications.

Résumé

Ce travail essaie de décortiquer les multiples paramètres régissant l'adhésion en phase aqueuse de polymères chargés. Nous cherchons d'abord à établir un lien entre les interactions électrostatiques moléculaires et les différentes architectures moléculaires de matériaux gonflés élastiques (Parties I et II) ou viscoélastiques (Partie III), avant de nous intéresser à l'adhésion en milieu immergé. (Partie I) Le premier système modèle de matériaux synthétiques nous a permis de corréler l'architecture moléculaire des hydrogels élastiques, la densité de charge interfaciale, et la force ionique du milieu avec les propriétés adhésives en phase aqueuse, à un niveau macroscopique en utilisant la technique du Probe-tack, et également à un niveau microscopique avec la microscopie à force atomique. (Partie II) Par ailleurs, étant inspirés par les systèmes adhésifs naturels, nous avons cherché à étendre ce système modèle à la mesure d'adhésion macroscopique entre hydrogels de gélatine de charges opposées. Nous montrons que le système modèle permettant de contrôler et de prédire l'adhésion en milieu aqueux en modifiant la densité de charge interfaciale et les propriétés mécaniques du matériau est transposable aux systèmes à base de gélatine. (Partie III) Enfin, nous avons développé un adhésif bio-inspiré entièrement synthétique à base de coacervation complexe. Ce nouveau système d'adhésif associe les interactions électrostatiques avec des domaines thermo-sensibles, donnant ainsi naissance à un matériau prometteur pour l'adhésion en milieu immergé.